SURI, Y. 2020. *Numerical simulation of fluid flow, proppant transport and fracture propagation in hydraulic fractures for unconventional reservoirs*. Robert Gordon University, PhD thesis. Hosted on OpenAIR [online]. Available from: https://openair.rgu.ac.uk

Numerical simulation of fluid flow, proppant transport and fracture propagation in hydraulic fractures for unconventional reservoirs.

SURI, Y.

2020

Copyright: the author and Robert Gordon University

OpenAIR @RGU

This document was downloaded from https://openair.rgu.ac.uk

BY NC

Numerical simulation of fluid flow, proppant transport and fracture propagation in hydraulic fractures for unconventional reservoirs

Yatin Suri

A thesis submitted in partial fulfilment of the
requirements of the
Robert Gordon University
for the degree of Doctor of Philosophy
(School of Engineering)

November 2020

Numerical simulation of fluid flow, proppant transport and fracture propagation in hydraulic fractures for unconventional reservoirs

PhD Candidate

Yatin Suri

Supervisory team

Dr. Sheikh Zahidul Islam (Principal Supervisor)

Dr. Mamdud Hossain

School of Engineering, Robert Gordon University, The Sir Ian Wood Building, Garthdee Road, Aberdeen, AB10 7GJ, United Kingdom

Funding organisation

Robert Gordon University, Aberdeen, United Kingdom

Acknowledgements

I would like to take the opportunity to express my gratitude to all who have made substantial contributions to my PhD thesis.

Firstly, I would like to acknowledge and express my heartfelt gratitude to my principal supervisor **Dr. Sheikh Zahidul Islam** and my second supervisor **Dr. Mamdud Hossain** who I describe as academic giants, for their valued guidance, encouragement and constructive feedback throughout my PhD programme. The motivation, support and expertise of my supervisory team helped successfully completing my thesis work. I would like to give thanks to my mentor **Dr. Mathew Nicho**, who inspired me to pursue a PhD and continuously guided me from time to time.

My sincere appreciation to my sponsor **Robert Gordon University, Aberdeen** for funding my PhD programme. I am also grateful to the entire staff at the School of Engineering, Robert Gordon University (RGU) Aberdeen for their support. Very importantly, I must acknowledge the staff at RGU-Library department for their effort in providing materials that were outside my reach. In addition, I would like to thank my research colleagues at the Research hub of the school of engineering for their support and encouragement.

I would like to thank my dear dad Late **Mr. Ranbir Singh Suri** who encouraged and supported me to pursue PhD and left to heavenly place during my second year of PhD. I would like to thank my dear mother **Mrs Anju Suri**, my siblings, **Harshila Suri, Chetan Suri** and my brother-in-law **Inderdeep Singh Purba** for their encouragement, continuous love and support. Finally, I would like to thank my entire family members and friends for their support and encouragement. The words I present here are not enough to express my gratitude to everyone. I thank you all!

Yatin Suri
November 2020

Dedication

This thesis is dedicated to my Father, Late **Mr. Ranbir Singh Suri**, who passed away in the second year of my PhD programme.

Abstract

The distribution of proppant injected in hydraulic fractures significantly affects the fracture conductivity and well performance. The proppant transport and suspension in thin fracturing fluid used in the unconventional reservoirs are considerably different from those of fracturing fluids in the conventional reservoir due to the very low viscosity of fracturing fluids used in the unconventional reservoirs, poor ability to suspend proppants and hence quick deposition of the proppants. This research presents the development of a three-dimensional computational fluid dynamics (CFD) modelling technique for the prediction of proppant-fluid multiphase flow in hydraulic fractures for unconventional reservoirs. The Eulerian-Lagrangian multiphase modelling approach has been applied to model the fluid flow and proppant transport, and the kinetic theory of granular flow is used to model the inter-proppant, fluid-proppant and proppant-wall interactions. The existing proppant transport models ignore the fluid leak-off effect from the fracture side wall and the effect of fracture roughness. Thus, at the interface between the fracture and surrounding porous medium, the mass flow rate from the fracture to porous rock is calculated based on the permeability and porosity of the rock. The leakage mass flow rate is then used to define the mass and momentum source term at the fracture wall as a user-defined function to investigate the proppant transport in hydraulic fractures with fluid leak-off effect. Furthermore, the hydrodynamic and mechanical behaviour of proppant transport on fracture roughness was studied in detail using different rough fracture profiles, and a relationship between the fracture roughness and proppant transport velocity is proposed.

Lastly, an integrated model is developed that simulates the proppant transport in dynamically propagating hydraulic fractures. The existing models either model the proppant transport physics in static predefined fracture geometry or account for the analytical models for defining the fracture propagation using linear elastic fracture mechanics, that limits the fracture propagation model to brittle rocks and neglect plastic deformations. Thus, in the present study, the fracture propagation was modelled using the Extended finite element method (XFEM) and cohesive zone model (CZM) that can model the plastic deformations in the ductile rock. The fracture propagation was coupled with the CFD based proppant transport model to model the fluid flow and proppant transport. The parametric study is then performed to investigate the effect of variation in proppant properties, fracturing fluid properties and geomechanical properties on the proppant transport. This study has enhanced the understanding of the flow and interaction phenomenon between proppant and fracturing fluid and provides a technique with potential application in fracturing design for increasing well productivity. The model can accurately simulate the proppant transport dynamics in hydraulic fracture and the present study propose a solution to a frequent fracture tip screen out challenge faced in the petroleum industry. Thus, the

developed modelling techniques provide the petroleum engineers with a more suitable option for designing the hydraulic fracturing operation, model simultaneously fracture propagation and fluid flow with proppant transport and gain confidence by tracking the distribution of proppants inside the fracture accurately.

Identifying keywords:

Proppant transport, hydraulic fracturing, fracture roughness, computational fluid dynamics, Discrete Element Method, Fracture propagation, Joint roughness coefficient, Fluid leak-off, unconventional reservoirs, fluid flow – fracture propagation coupled model

Table of Contents

Acknowledgements iii
Dedication iv
Abstract v
Identifying keywords: vii
List of figures xii
List of tables xvii
Nomenclature xviii
Chapter 1: Introduction 1
1.1 The motivation for the study 1
1.2 Problem Statement 5
1.3 Research Aims and Objectives 7
1.3.1 Aim 7
1.3.2 Objectives 7
1.4 Study scope 8
1.5 Thesis Outline 8
1.6 Significance 10
Chapter 2: Literature review 11
2.1 Proppant transport in hydraulic fractures 11
2.2 Proppant transport in hydraulic fractures for unconventional reservoirs 13
2.3 Experimental works on Proppant Transport 14
2.4 Numerical methods for modelling proppant transport and distribution 16
2.4.1 Eulerian-Eulerian Method 17
2.4.2 Eulerian-Lagrangian method 18
2.5 Current challenges in numerical modelling 20
2.6 Past fracture propagation and fluid flow models 22
2.7 Key findings from the literature review/Research gap 25
2.8 Contribution to knowledge 27
Chapter 3: Methodology 28
3.1 Computational Fluid Dynamics Methodology 28
3.2 Multiphase flow modelling methods 31
3.2.1 Eulerian-Granular model 31
3.2.1.1 Flow governing equations 32
3.2.1.2 Drag force modelling 34
3.2.1.3 Turbulent dispersion force 35
3.2.1.4 Stress model for the proppant phase 36

3.2.1.5 Granular phase pressure model....36
3.2.1.6 Granular temperature....37
3.2.1.7 Granular bulk viscosity....38
3.2.1.8 Granular shear viscosity....38
3.2.2 Computational Fluid Dynamics - Discrete Element Model (CFD-DEM)....40
3.2.2.1 The governing equations for the particles....40
3.2.2.2 Collision model....42
3.2.3 Dense Discrete Phase Method (DDPM) model....43
3.2.3.1 Flow Governing Equations....44
3.2.3.2 Turbulence modelling....45
3.2.4 Selection of Eulerian-Granular model, CFD-DEM model and DDPM model....50
3.3 Modelling workflow and simulation parameters:....51
3.3.1 Geometry/Computational domain and Meshing....51
3.3.2 Modelling fluid leak-off....53
3.3.2.1 Continuity equation....53
3.3.2.2 Momentum equation....53
3.3.2.3 User-defined function....56
3.3.3 Simulation set up....57
3.4 Methodology for fracture propagation....60
3.5 Extended Finite Element Method (XFEM) Methodology....60
3.5.1 Governing equations....61
3.5.2 Extended finite element method (XFEM) approximation....66
3.5.3 Cohesive zone method....69
3.5.4 Coupling between XFEM and CFD....71
Chapter 4: Development and Comparison of Eulerian-Granular Model and CFD-DEM Model....73
4.1 Brief methodology....73
4.1.1 Eulerian-Granular model....74
4.1.2 Computational fluid dynamics - discrete element model (CFD-DEM)....74
4.2 Numerical modelling parameters....75
4.3 Results and discussion....79
4.3.1 Comparison with the experimental results....79
4.3.2 Results from fluid leak-off modelling....83
4.3.3 Effect of proppant size....85
4.3.4 Effect of fluid viscosity....93
4.3.5 Effect of fracture width....98
4.3.6 Comparison of Eulerian-Granular method with Discrete Element Model....103

4.4 Summary of the key findings 108
Chapter 5: Discussion on the construction of the DDPM model for proppant transport in unconventional hydraulic fractures 109
5.1 Modelling workflow and simulation parameters 110
5.1.1 Geometry/Computational domain 110
5.1.2 Meshing 111
5.1.3 Modelling fluid leak-off 113
5.1.4 Simulation set up 114
5.2 Results and Discussion 115
5.2.1 Comparison with the experimental results 115
5.2.2 Effect of Fracture Roughness 119
5.2.3 Effect of the fluid leak-off rate at fracture wall 122
5.2.4 Effect of injection rate 124
5.2.5 Effect of Proppant Concentration 128
5.2.6 Effect of fracture height 131
5.2.7 Comparison of Foam vs Water as fracturing fluid 134
5.3 Summary of the key findings 138
Chapter 6: Effect of Fracture Roughness on the hydrodynamics of proppant transport in hydraulic fractures 139
6.1 Model development- 139
6.1.1 Problem formulation and Joint Roughness Coefficient profiles 140
6.2 Mathematical model 142
6.2.1 Governing Equations 142
6.2.2 Physical model 142
6.3 Dimensional analysis 146
6.4 Results and Discussion 147
6.4.1 Proppant transport and distribution in smooth fracture 147
6.4.2 Role of fractures roughness on proppant hydrodynamics 149
6.5 Summary of the key findings 162
Chapter 7: Proppant transport in dynamically propagating hydraulic fractures using CFD-XFEM approach 163
7.1 Brief methodology 164
7.1.1 Coupling between XFEM and CFD 164
7.1.2 Numerical modelling parameters 165
7.2 Results and discussion 167
7.2.1 Validation 167
7.2.1.1 Zero toughness plane strain fracture propagation model 167

7.2.1.2 Validation using the real field data 170
7.2.2 Results of the base case 173
7.2.3 Fracture propagation as a function of injection rate 176
7.2.4 The impact of fracturing fluid viscosity on fracture propagation 181
7.2.5 Influence of leak-off coefficient 184
7.2.6 Application in petroleum engineering 187
7.3 Summary of the key findings 188
Chapter 8: Conclusions and Recommendation for Future Work 190
8.1 Conclusions 190
8.2 Recommendations for future work 194
Chapter 9: References 196
Appendix A: User Defined Function (UDF) Code 218
Appendix B: Code for hydraulic fracture propagation using XFEM in Abaqus 225
Appendix C: Comparison of Eulerian-Granular model, CFD-DEM Model and DDPM model with the Experimental study 233
Appendix D: Publications 235

List of figures

Figure 1.1- Hydraulic fracturing in an unconventional reservoir (Siddhamshetty et al. 2018) ...2
Figure 1.2 Particle transport mechanisms (Presley and Tatarko 2009).....3
Figure 2.1 Proppant-fracturing fluid coupled flow (Patankar et al., 2002).....14
Figure 3.1 Energy spectrum of turbulence (Sinha 2013).....30
Figure 3.2 Proppant-proppant collision 43
Figure 3.3 CFD modelling workflow.....52
Figure 3.4 Fracture surrounded by porous rock.....54
Figure 3.5 Fluid Leak-off rate at fracture wall along the fracture length.....56
Figure 3.6. Hydraulic fracture in a porous rock formation (Chen 2013) 62
Figure 3.7. Illustration of the definition of special enriched functions (Wang 2015).....67
Figure 3.8 Illustration of the fracture using the level set method (Modified from Stolarska et al. (2001)) 67
Figure 3.9 illustration of phantom node method.....68
Figure 3.10 Traction–separation relationship (Wang 2015) 70
Figure 3.11 XFEM-CFD coupling workflow 72
Figure 4.1: Computational domain 75
Figure 4.2: Mesh sensitivity study 76
Figure 4.3: Fluid leak-off rate at fracture wall along the fracture length.....78
Figure 4.4: Schematic of the proppant transport fracture slot experiment (Tong and Mohanty 2016) 81
Figure 4.5: Comparison of experimental and numerical results in terms of proppant deposition at the fracture bottom in primary and secondary fracture slots at different time steps.....82
Figure 4.6: Quantitative comparison of numerical results with experimental results.....83
Figure 4.7: Comparison of proppant volume fraction at t=2 s.....84
Figure 4.8: Comparison of proppant horizontal velocity at t=2 s 85
Figure 4.9: Effect of proppant diameter on proppant volume fraction 87
Figure 4.10: Comparison of proppant volume fraction with time for different proppant size....88
Figure 4.11: Effect of proppant diameter on proppant horizontal velocity.....89
Figure 4.12: Variation of proppant horizontal velocity with time for different proppant size....90
Figure 4.13: Effect of multisize proppant injection on the proppant volume fraction.....91
Figure 4.14: Comparison of multisize proppant injection and base case (d = 1 mm).....92
Figure 4.15: Variation of fluid viscosity on the proppant volume fraction.....94
Figure 4.16: Variation of proppant volume fraction with time for different fluid viscosity.....95
Figure 4.17: Effect of fluid viscosity on proppant velocity 96

Figure 4.18: Variation of proppant horizontal velocity for different fluid viscosity vs time 97
Figure 4.19: Variation of fracture width on the proppant volume fraction 99
Figure 4.20: Time evolution of proppant volume fraction for different fracture width 100
Figure 4.21: Contour plot showing the variation of fracture width on the proppant velocity .. 101
Figure 4.22: Variation of proppant horizontal velocity for different fracture width vs time.... 102
Figure 4.23: Comparison of Eulerian-Granular method and DEM 105
Figure 4.24: Comparison of proppant volume fraction for Eulerian-Granular vs DEM model106
Figure 4.25: Comparison of proppant velocity for Eulerian-Granular vs CFD-DEM model... 107
Figure 5.1 Computational domain and boundary conditions used in the study..... 110
Figure 5.2 Histogram showing the normal distribution of fracture height with roughness..... 111
Figure 5.3- Mesh sensitivity study- comparison of numerical results with different mesh sizes a) plot of proppant volume fraction vs fracture height b) plot of proppant axial velocity vs fracture height 112
Figure 5.4 Fluid Leak-off rate at fracture wall along the fracture length 113
Figure 5.5 Comparison of experimental data and numerical result at t=20 s 118
Figure 5.6 Quantitative validation (a) comparison of non-dimensional proppant bed length for experimental study vs current numerical study (b) comparison of non-dimensional proppant bed height for the experimental study vs current numerical study..... 119
Figure 5.7 Comparison of rough and smooth fracture cases at t=2 s 120
Figure 5.8 Comparison of rough and smooth fracture cases at t=2 s 120
Figure 5.9 Comparison of the proppant volume fraction with the non-dimensional fracture height at for smooth and rough fracture case t=3 s..... 121
Figure 5.10 Comparison of vorticity, velocity vector and turbulence kinetic energy plots for smooth vs rough fracture case 122
Figure 5.11 Comparison of Fluid Leak-off case with no leak-off from the fracture wall at 2.5 s 123
Figure 5.12 Contour plot for proppant volume fraction at fracture mid-plane showing three cases of variation in injection velocity 0.1 m/s, 0.5 m/s and 1 m/s..... 125
Figure 5.13 Location of vertical planes at x=0.2 m and x=1.4 m from the inlet to quantitatively analyse the results..... 125
Figure 5.14 Comparison of the proppant volume fraction with the non-dimensional fracture height for injection velocities 0.1 m/s, 0.5 m/s and 1 m/s at two different locations (x=0.2 m and x=1.4 m) inside the fracture..... 126
Figure 5.15 Comparison of the proppant axial velocity with the non-dimensional fracture height for injection velocities 0.1 m/s, 0.5 m/s and 1 m/s at two different locations (x=0.2 m and x=1.4 m) inside the fracture..... 127

Figure 5.16 Contour plot for proppant volume fraction at fracture mid-plane showing three cases of variation in proppant concentration c= 0.10, 0.15 and 0.20 128
Figure 5.17 Comparison of the proppant volume fraction with the non-dimensional fracture height for variation in proppant concentration c= 0.10, 0.15 and 0.20 at two different locations (x=0.2 m and x=1.4 m) inside the fracture.....129
Figure 5.18 Comparison of the proppant axial velocity with the non-dimensional fracture height for variation in proppant concentration c= 0.10, 0.15 and 0.20 at two different locations (x=0.2 m and x=1.4 m) inside the fracture 130
Figure 5.19 Contour plot of the proppant concentration for different fracture height cases H=0.2 m, 0.5 m and 1 m 131
Figure 5.20 Comparison of the proppant volume fraction with the non-dimensional fracture height for different fracture height cases H=0.2 m, 0.5 m and 1 m at two different locations (x=0.2 m and x=1.4 m) inside the fracture 132
Figure 5.21 Comparison of the proppant axial velocity with the non-dimensional fracture height for different fracture height cases H=0.2 m, 0.5 m and 1 m at two different locations (x=0.2 m and x=1.4 m) inside the fracture 133
Figure 5.22 Contour plot showing proppant volume fraction comparison of foam-based fracturing fluid with a water-based fracturing fluid at a different time interval 135
Figure 5.23 Comparison of the proppant volume fraction with the non-dimensional fracture height for foam and water-based fracturing fluid at two different locations (x=0.2 m and x=1.4 m) inside the fracture 136
Figure 5.24 Comparison of the proppant axial velocity with the non-dimensional fracture height for foam and water-based fracturing fluid at two different locations (x=0.2 m and x=1.4 m) inside the fracture 137
Figure 6.1 Rough fracture geometries with different JRC values.....141
Figure 6.2 Histogram for normal distribution of fracture roughness 142
Figure 6.3 Mesh Sensitivity Study a) plot of proppant volume fraction vs fracture height b) plot of proppant axial velocity vs fracture height 143
Figure 6.4 Computational domain 143
Figure 6.5 Fluid leak-off rate at fracture wall along the fracture length.....145
Figure 6.6 variation of slippage velocity with proppant size ratio.....147
Figure 6.7 Log-log plot of correlation between proppant Reynolds number, proppant size ratio and proppant horizontal velocity in smooth fracture 148
Figure 6.8 Comparison of vorticity, velocity vector and proppant volume fraction for different JRC profiles 149
Figure 6.9 Comparison of proppant transport in rough fractures with proppant diameter 0.35 mm and 0.65 mm.....151

Figure 6.10 Comparison of proppant transport in rough fractures with different flow injection velocities 151
Figure 6.11 Comparison of proppant transport in smooth fracture and rough fracture with JRC 16 152
Figure 6.12 Variation of fracture roughness factor with JRC for different injection velocity, and proppant size 153
Figure 6.13 Semi-log plot of fracture roughness factor with Ar/Re 154
Figure 6.14. Variation of fracture roughness factor with JRC and proppant size ratio for Ar/Re<10 156
Figure 6.15. Variation of fracture roughness factor with JRC, proppant size ratio and Ar/Re for Ar/Re>10 156
Figure 6.16. Comparison of the proposed correlation with the previous studies (a) for high viscosity fracturing fluid (b) for low viscosity fracturing fluid 159
Figure 6.17. Proppant transport in industrial-scale hydraulic fracture 161
Figure 7.1 XFEM-CFD coupling workflow 165
Figure 7.2. A typical fracture geometry to investigate proppant transport 166
Figure 7.3. The fluid leak-off rate at different time steps 166
Figure 7.4 Comparison of the current model with an analytical model 169
Figure 7.5 Computational domain and mesh 172
Figure 7.6 Fracture initiation pressure from XFEM model 173
Figure 7.7 Fracture propagation at different time steps 175
Figure 7.8 Proppant transport in dynamic fracture propagation at different time steps 176
Figure 7.9 Proppant transport with dynamic fracture propagation at a varying injection rate . 178
Figure 7.10 Comparison of proppant distribution against fracture height at two different locations for varying injection rates 179
Figure 7.11 Comparison of proppant horizontal velocity against fracture height at two different locations for varying injection rates 179
Figure 7.12 Proppant distribution at different time steps using intermittent injection. 180
Figure 7.13 Comparison of proppant distribution against fracture height at two different locations for intermittent injection at different time steps 181
Figure 7.14 Effect of viscosity on proppant transport 183
Figure 7.15 Effect of fluid viscosity on the proppant volume fraction 183
Figure 7.16 Effect of fluid viscosity on proppant horizontal velocity 183
Figure 7.17 Fluid leak-off profile along fracture length with the different leak-off coefficients 185
Figure 7.18 Fluid leak-off profile along fracture length at different time step 185
Figure 7.19 Proppant distribution with varying leak-off rate constant 186

Figure 7.20 Effect of the fluid leak-off rate constant on the proppant volume fraction 187
Figure 7.21 Effect of the fluid leak-off rate constant on proppant horizontal velocity.....187
Figure C.1 Comparison of Eulerian-Granular Model, DEM Model and DDPM model with Experimental results.....234

List of tables

Table 3.1- Physical properties of proppant and fluid used in the simulation 58
Table 4.1: Physical properties of proppant and fluid used in the simulation..... 79
Table 4.2: Simulation parameters for model validation 81
Table 5.1: Physical properties of proppant and fluid used in the simulation..... 114
Table 5.2: Simulation parameters for comparison with the experimental results 117
Table 5.3: Physical properties of foam as a fracturing fluid used in the simulation..... 135
Table 6.1: Physical properties of proppant and fluid used in the simulation..... 144
Table 6.2: Key physical parameters used in the simulation 161
Table 7.1 Geomechanical and flow properties for comparison with an analytical model..... 169
Table 7.2 Reservoir and geological properties 171
Table 7.3 Fracture propagation at different time steps 174
Table 7.4 Fracture propagation with varying injection rate 177
Table 7.5 Effect of fluid viscosity on fracture propagation..... 181
Table 7.6 Fracture propagation with different leak-off coefficients..... 184

Nomenclature

Symbol	Description	Unit
a_i	Enriched nodal degree of freedom vector	-
A	Area	m^2
$A_0/A_1^{(1)}$	Constants in analytical fracture propagation model	-
b_i^j	Enriched nodal degree of freedom vector at the fracture tip	-
b	Body force	N
$B^{(1)}$	Constant in analytical fracture propagation model	-
c	Proppant concentration	-
C_D	Drag coefficient	-
c_L	Leak-off constant	m/kPa.s
c_t	Rock compressibility	Pa^{-1}
C_v	Constant	-
$\bar{C}$	Pressure equivalent stiffness matrix	-
D	Degradation factor	-
D_H	Hydraulic diameter	m
D_s	Dispersion tensor	-
D_T	Hooke's tensor	Nm^{-2}
$D_{\omega,l}$	Cross-diffusion term	Nms^{-1}
D_ω^+	Positive portion of the cross-diffusion term	Nms^{-1}
d	Particle diameter (size)	m
$\vec{e}_{12}$	Unit vector	-
E	Young's modulus	Nm^{-2}
E'	Plane strain modified elasticity modulus	Nm^{-2}
$\vec{F}$	External body force term	N
$\overrightarrow{F_1}/\overrightarrow{F_2}$	Force on particle 1/particle2	N
F_{1b}/F_{2b}	Blending function in RANS turbulence model	-
$\vec{F}_{drag}$	Drag force	N
$\vec{F}_{gravitation}$	Gravitational force	N
F_i	Source term for the flow through porous media	Nm^{-3}
$\vec{F}_{KTGF}$	Inter-particle interaction force from kinetic theory of granular flow	N
$\vec{F}_l$	Lift force	N
$\vec{F}_{other}$	Additional force term	N
$\vec{F}_{vm}$	Virtual mass force	N

f^p	Equivalent nodal force vector for pressure	N
f^u	Equivalent nodal force vector for displacement	N
$g_{0,ss}$	Radial distribution function	-
g	Acceleration due to gravity	ms^{-2}
G_c	Critical energy release rate	m^2s^{-2}
G^c	Fracture energy due to deformation	m^2s^{-2}
$G_I^c, G_{II}^c, G_{III}^c$	Traction work done in the normal, principle, and second shear directions	m^2s^{-2}
$G_{k,l}$ / $G_{\omega,l}$	Production of turbulence kinetic energy/specific rate of dissipation	Nms^{-1}
$\widetilde{G_{k,l}}$	Model constant in production term of SST k-ω turbulence model	-
H	Fracture height / Height of slot	m
$\overline{H}$	Coupling term due to the fluid pressure	-
$H(x)$	Discontinuous jump function	-
H_o	Height of slurry flow area	m
$\overline{\overline{I}}$	Unit tensor	-
I_D	Deviatoric stress tensor	-
k	Turbulent kinetic energy	m^2s^{-2}
K	Spring constant	Nm^{-1}
$\overline{K}$	Structural stiffness matrix	Nm^{-1}
k_c	Conductivity	m^3/Pa.s
k_D	Dimensionless fracture toughness in the viscosity scaling	-
K_f	Consistency factor for Non-Newtonian fluid	$N.s^n/m^2$
K_I	Stress intensity factor	$Pa\sqrt{m}$
K_{IC}	Critical stress intensity factor	$Pa\sqrt{m}$
K_{ls} /K_{sl}	Momentum exchange coefficient	$Nm^{-1}s$
k_m	Permeability of the rock	mD
k_{Θ_s}	Diffusion coefficient	m^2s^{-1}
$\acute{k}$	Constant	-
K'	Plane strain modified fracture toughness	$Pa.m^{0.5}$
L_s	Length scales of the mean flow	m
$L_{t,l}$	Length scale of the turbulent eddies	m
$l(t)$	Dimensionless fracture length as a function of time	-
$L(t)$	Fracture length scale	m
L_m	Fracture length scale for viscosity scaling	m
$\overrightarrow{M_{ls}}$/ $\overrightarrow{M_{sl}}$	Interfacial momentum transfer	Ns^{-1}
m_1/m_2	Mass of particle 1/particle2	Kg

m_{12}	Reduced mass	Kg
$\dot{m}(x,t)$	Mass flow rate at a particular cell or position and time step	Kg/s
$N_i(x)$	Nodal shape function	-
n	Node	-
n_f	Flow behaviour index for Non-Newtonian fluid	-
$\hat{n}$	Normal unit vector	-
n'	Phantom node	-
N_i^u	Shape function for nodal displacement	-
N_i^p	Shape function for fluid pressure	-
N_i^w	Shape function for crack opening	-
P	Pressure	Nm^{-2}
P_m	Pore pressure	Nm^{-2}
P_{sf}	Solid phase frictional pressure	Nm^{-2}
P_w	Wetted perimeter	m
$p(x,t)$	Dimensionless fluid pressure as a function of distance and time	-
$P(t)$	Dimensionless evolution parameter	-
q_L	Fluid leak-off rate	m^3s^{-1}
q	Fluid flux	ms^{-1}
$q(x,t)$	Volumetric leak-off flow rate as a function of fracture length and time	m^3s^{-1}
q_{tip}	Flow rate at fracture tip	m^3s^{-1}
q_{inlet} / Q_0	Inlet flow rate	m^3s^{-1}
$\bar{Q}$	Coupling term due to the tractions	-
Re_l	Reynolds number for the liquid phase	-
Re_p	Reynolds number for the proppant phase	-
R_{gl}	Reynolds number for the fluid phase based on the channel width	-
R_{gp}	Reynolds number for the proppant phase based on the channel width	-
R_k / R_ω	Constants	-
S	Strain operator	-
S_m	Mass source term	$Kgm^{-3}s^{-1}$
S_u	Momentum source term	Nm^{-3}
t_{coll}	Collision time	s
t_{exp}	Exposure time	s
t_n^0	Tensile strength of rock perpendicular to the interface	Nm^{-2}
t_n	Stress in the normal direction	Nm^{-2}
$\bar{t}_n$	Normal stress for the current separation without damage	Nm^{-2}

t_p	Particle time step	s
t_s^0	Shear strength of rock material in the principle direction	Nm^{-2}
t_s	Stress in principle shear direction	Nm^{-2}
t_t	Stress in the second shear direction	Nm^{-2}
t_t^0	Shear strength of rock material in the second shear	Nm^{-2}
t	Current time step	s
t_c	Traction	N
u	Displacement vector	m
$\vec{v}$	Velocity	ms^{-1}
$\vec{\upsilon}_{dr}$	Drift velocity	ms^{-1}
$\vec{v}_{12}$	Relative velocity between particles	ms^{-1}
v_i	Injection velocity	ms^{-1}
v_r	Velocity in rough fracture	ms^{-1}
v_s	Velocity in a smooth fracture	ms^{-1}
$V(x,t)$	Volume of a cell at a particular time step	m^3
$v(x,t)$	Velocity of the fluid as a function of position and time step	ms^{-1}
w	Fracture width	m
w_s	Width of the slot	m
$\dot{w}$	Rate of change of fracture width with respect to time	m/s
w_{tip}	Fracture width at tip	m
$w(x,t)$	Dimensionless fracture width as a function of distance and time	-
x	Displacement	m
y_w	distance to the next surface	m

Greek symbols:

$\bar{\bar{\tau}}$	Stress-strain tensor	Nm^{-2}
$\in_R$	Fracture roughness factor	-
v_t	Turbulent kinematic viscosity	m^2/s
α^* /α_0^* / α'	Constants in SST k-ω turbulence model	-
$\alpha_{\infty,1}$ / $\alpha_{\infty,2}$	Constants in SST k-ω turbulence model	-
α_∞^* / α_∞	Constants in SST k-ω turbulence model	-
α_p	Poroelastic constant	-
$\alpha_{s,max}$	Maximum packing fraction limit of solids	-
$\alpha_{s,max}$	Maximum volume fraction or packing limit of particle phase	-
$\alpha_{s,min}$	Minimum frictional volume fraction	-

$\alpha_{\omega,1}$/ $\alpha_{\omega,2}$	Constants in SST k-ω turbulence model	-
β^* / β_i	Constants in the turbulent dissipation term	-
β^*_∞	Constants in SST k-ω turbulence model	-
$\beta_{i,1}$/ $\beta_{i,2}$	Constants in SST k-ω turbulence model	-
γ_{Θ_s}	Granular energy dissipation	$Kgm^{-3}s^{-1}$
Γ_c	Crack domain subjected to fluid pressure	-
Γ_F	Domain subjected to traction	-
Γ_u	Domain subjected to displacements	-
δ_n^0	Displacement at the initiation of damage	m
δ_n^f	Displacements at complete failure	m
δ_n^{max}	Maximum value of opening displacement	m
ε_D	Fraction of diameter for allowable overlap	-
ε_m	Dimensionless parameter for viscosity scaling	-
η_{sl}	Ratio between the two characteristic times $\tau_{t,sl}$ and $\tau_{F,sl}$	-
Θ_{JRC}	Joint roughness coefficient	-
Θ_s	Granular temperature	m^2s^{-2}
$\mu_{s,col}$	Collisional viscosity	Pa.s
$\mu_{s,col}$	Granular phase collisional viscosity	Pa.s
$\mu_{s,fr}$	Frictional viscosity	Pa.s
$\mu_{s,fr}$	Granular phase frictional viscosity	Pa.s
$\mu_{s,kin}$	Granular phase kinetic viscosity	Pa.s
$\mu_{s,kin}$	Kinetic viscosity	Pa.s
Π_{kl} / $\Pi_{\omega l}$	Influence term of solid phase turbulence on the liquid phase for k /ω	Nms^{-1}
σ_c	Fracture compressive strength	Nm^{-2}
σ_n	Effective normal stress	Nm^{-2}
σ_{sl}	Dispersion Prandtl number	-
$\sigma_{\omega,1}$ / $\sigma_{\omega,2}$	Constants in SST k-ω turbulence model	-
$\tau_{F,sl}$	The entrainment time of the solid particles by the continuous phase	s
τ_r	Particle relaxation time	s
$\tau_{t,sl}$	Interaction time between particle motion and liquid-phase fluctuations	s
Φ_b	Basic friction angle	-
Φ_{ls}	Interphase granular energy transfer	$Kgm^{-3}s^{-1}$
$\bar{\Omega}_{m0}^{(1)}$	Dimensionless fracture width	-
$\emptyset$ / ψ	Orthogonal signed distance functions	-
$\mu_{t,l}$	Turbulent viscosity	Pa.s

α	Volume fraction	-
γ	Damping coefficient	Nsm^{-1}
$\gamma[P(t)]$	Dimensionless fracture length	-
γ_{Θ_s}	Rate of energy dissipation due to inter-particle collision	$Kgm^{-3}s^{-1}$
δ	Overlap	m
δu	Arbitrary virtual displacement	m
$\delta\boldsymbol{\varepsilon}$	Arbitrary strain	-
ε	Strain	-
$\varepsilon(t)$	Dimensionless parameter	-
η	Coefficient of restitution	-
η_c	Experimental constant	-
θ	Friction angle	-
θ_p	Angle between the mean particle velocity and the mean relative velocity	-
λ	Bulk viscosity	Pa.s
μ	Dynamic viscosity	Pa.s
μ'	Plane strain modified fluid viscosity	Pa.s
ν	Poisson's ratio	-
ξ	Dimensionless length scaling factor	-
ρ	Density	Kgm^{-3}
σ	Total stress	Nm^{-2}
σ'	Effective stress	Nm^{-2}
σ_k / σ_ω	Turbulent Prandtl numbers	-
τ	Maximum shear strength	Nm^{-2}
ϕ	Porosity	-
Ω	Reservoir domain or boundary	-
ω	Specific rate of dissipation	s^{-1}
Γ_ω / Γ_k	Effective diffusivity of specific dissipation rate / turbulent kinetic energy	Pa.s

Subscripts:

f	Fluid phase
i	Phase (liquid or solid)
l	Liquid phase
p	Particle phase
s	Granular phase

Superscripts:

T	Transpose of a matrix

Abbreviations:

2D	Two-dimensional
3D	Three-dimensional
Ar	Archimedes number
CFD	Computational fluid dynamics
CZM	Cohesive zone model
DDM	Displacement discontinuity method
DDPM	Dense discrete phase method
DEM	Discrete element method
DNS	Direct numerical simulation
DPM	Discrete phase method
FEM	Finite element method
FVM	Finite volume method
JCS	Joint wall compressive strength
JRC	Joint roughness coefficient
KGD	Khristianovic-Geertsma-de Klerk model
KTGF	Kinetic theory of granular flow
LEFM	Linear elastic fracture mechanics
P3D	Pseudo-3D model
PC-SIMPLE	Phase-coupled semi-implicit pressure-linked equations
PDE	Partial Differential Equation
PKN	Perkins-Kern-Nordgren model
PL3D	Planar-3D model
RANS	Reynolds-averaged Navier-Stokes
Re	Reynolds number
RSM	Reynolds stress model
SEM	Scanning Electron Microscope
SIMPLE	Semi-implicit pressure-linked equations
SST	Shear stress transport
UDF	User-defined function
XFEM	Extended finite element method

Chapter 1: Introduction

1.1 The motivation for the study

With the rapidly growing energy needs of the world and dwindling hydrocarbon production from conventional reservoirs, the unconventional hydrocarbon reservoirs are gaining great importance. Unconventional reservoirs are essentially any reservoir that has substantially low permeability (<0.1 mD) and require special recovery operations outside the conventional operating practices (Belyadi, Fathi and Belyadi 2019). Unconventional reservoirs include reservoirs such as tight-gas sands, gas and oil shales, coalbed methane, heavy oil and tar sands, and gas-hydrate deposits. These reservoirs require additional recovery solutions such as stimulation treatments (hydraulic fracturing or steam injection), and innovative solutions for economically producing hydrocarbons (Islam 2014). In this present study, the main focus is on unconventional gas reservoirs that are comprised of mainly tight gas sands, coal bed methane, and shale gas. Their shared characteristic is that because of the low matrix permeability (below 0.1 mD), the well stimulation technique like hydraulic fracturing is required to produce hydrocarbons from these reservoirs economically (Lange et al. 2013). Hydraulic fracturing is a process of improving the permeability of a tight rock formation by creating fractures at high pressures (Figure 1.1) (Donaldson, Alam and Begum 2014). It is achieved by injecting a combination of chemicals, water, sand and other additives into the rock formation at high pressures to form cracks or fractures. Once the hydraulic pressure exceeds the tensile strength of the rock, also known as breakdown pressure, the fracture propagates in the direction normal to the least principal stress because it opens and displace the rock against the least resistance and thus it results in tensile failure of the rock (Economides, Hill and Economides 2013). The fractures are kept open by injecting solid particles called proppants (Smith et al. 1997). The prime objective to inject proppant is to assure the fracture do not close against the rock pressure and create the flow path for the hydrocarbon fluids to produce. Hydraulic fracturing, together with proppant placement is a renowned well stimulation technique in the petroleum industry to produce hydrocarbons from the conventional reservoirs (Yew and Weng 2014).

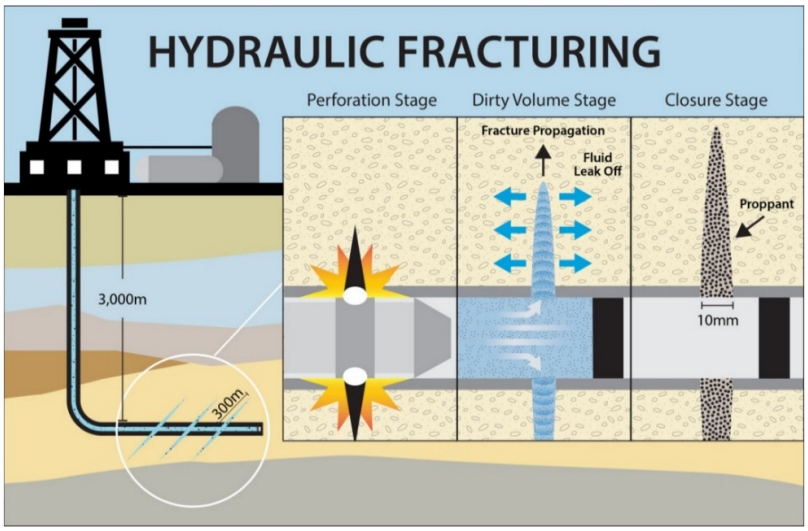

Figure 1.1- Hydraulic fracturing in an unconventional reservoir (Siddhamshetty et al. 2018)

In the last decade the hydraulic fracturing technique has been widely used in the unconventional reservoirs, for example- shale gas and tight gas formation that has substantially low permeability and cannot be economically produced without the stimulation technique (Lange et al. 2013). The hydraulic fracturing in unconventional reservoirs is significantly different from the conventional reservoirs mainly because of the two reasons. Firstly, in conventional reservoirs, the focus of the hydraulic fracture design is to have a large fracture width, whereas, in the low permeability unconventional reservoir, greater fracture length is the prime factor to optimise. In a typical shale gas reservoir, the average fracture width could be less than 5 mm and the average fracture length could be as long as 100 - 300 m (Di and Tang 2018). In contrast, in a typical sandstone moderate permeability reservoir (1-10 mD), the fracture width could be around 10-50 mm, and the fracture half-length could be as long as 20-100 m (Economides, Hill and Economides 2013). Secondly, slick water is commonly used as a fracturing fluid in the unconventional reservoir and due to the low viscosity of slick water and negligible chemical additive, tendency to suspend the proppant greatly decreases (Sahai, Miskimins and Olson 2014). This results in early proppant deposition compared with conventional fracturing fluids (Alotaibi and Miskimins 2015). Therefore, both of these attributes for the unconventional reservoirs, i.e. focus is on creating a longer fracture, and early deposition of the proppants results in the closing of the unpropped section of the fracture when hydraulic pressure is removed and consequently reduced fracture conductivity. This forms the rationale of the current research to enhance the understanding of proppant transport and distribution in unconventional reservoirs with thin fracturing fluids or slick water. The proppant transport and distribution are the complex physical phenomenon resulting from different mechanisms such as (Tsai et al. 2012, Yew and Weng 2014) –

i. Fracturing fluid leak-off from the fracture wall into the reservoir
ii. Gravitational effects resulting in proppant deposition
iii. Rheological properties of the fracturing fluid like fluid density, fluid viscosity, Newtonian and Non-Newtonian flow.
iv. Additional drag force from the rough fracture walls
v. The interaction dynamics between proppants and fluid
vi. Fracture geometry such as fracture width, fracture height and length
vii. Reservoir characteristics like porosity, permeability, and fluid saturation

The transport of proppant in fluid flow depends on the proppant and fluid properties and can be in the form of bedload and/or suspension. Mack, Sun and Khadilkar (2014) described the three proppant transport mechanisms shown in Figure 1.2, namely surface creep, saltation, and suspension. Surface creep refers to when the slurry flow velocity above the bank is greater compared with the critical flow velocity for proppant, and the proppant particles will slide or roll along the surface. Saltation refers to when the flow velocity is further increased, part of the proppant particle is lifted and travel further ahead. Lastly, suspension refers to when the flow velocity is considerably higher and exceeds the critical suspension velocity, and it will result in suspension and transportation of some proppant particles with the liquid.

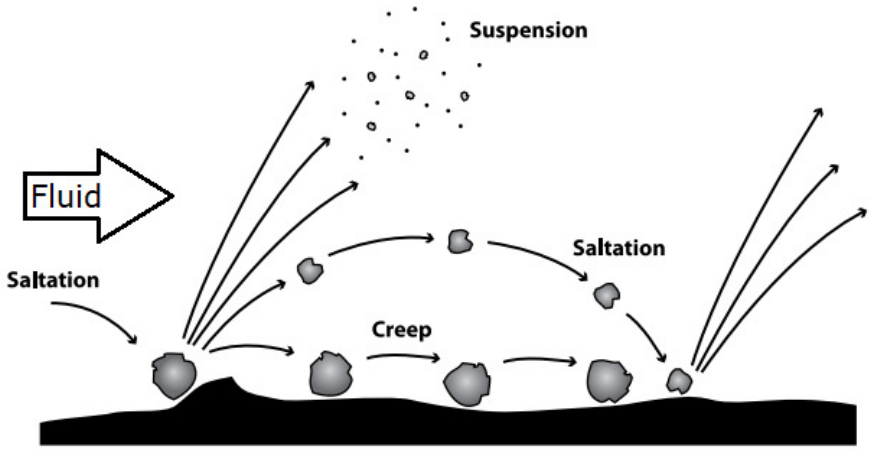

Figure 1.2 Particle transport mechanisms (Presley and Tatarko 2009)

For the proppant transport in fracturing fluid, the discrete phase, i.e. solid or proppant, is suspended in the continuous phase, i.e. fluid, and momentum exchange occurs between both the phases due to the fluid-proppant, proppant-proppant and proppant-wall interactions (Dontsov and Peirce 2014). The typical value of proppant volume fraction in the slick water fracturing fluid slurry varies from 3-20% (Tsai et al. 2012, Bokane et al. 2013, Jain et al. 2013). The three critical physical phenomena that affect the hydrodynamics of particle transport in the fluid are a fluid drag, particle settlement and particle-wall interaction (Patankar and Joseph 2001). For the proppant-fluid two-phase flow, a difference in the velocity of proppant and fluid is present in the fracture that is known as slip velocity. The slip velocity further results in drag force exerted by the continuous phase on the particles (Zhang, Gutierrez and Li 2017). Thus particle-fluid coupling adds complexity to the flow. In addition, with the increase in the particle concentration, the collisions between the particles increases which increases the randomness in the particle motion and significantly increases disturbance of the flow field. The particle random fluctuating velocities are modelled using the granular energy transport equation from Kinetic Theory of Granular Flow (explained in chapter 3) and two-way coupling which means the fluid flow impacts the particle motion and vice versa (Blyton, Gala and Sharma 2015). Thus the randomness in the particle motion can impact the turbulence of the fluid flow as well as the turbulence of the particles. The range of Re in the present study is 990 – 9900 based on the fluid velocity range of 0.1 m/s – 1 m/s (discussed in chapter 3). Lastly, for the slurry flow in rough wall surfaces, the irregular wall results in higher particle-wall interactions and significantly increases the flow disturbance affecting the flow dynamics of solid transport (Zhang et al. 2015). Typically, the fracture aperture is very small (around 3 mm – 10 mm), the fracture walls exert a mechanically induced retardation effect and effects the proppant transport (Zhang et al. 2015). Thus, the frequent proppant-fluid, inter-proppant and proppant-rough wall interactions lead to a complex proppant transport physics in fracturing fluid flow. This complex phenomenon leads to the current research of fracture roughness in the proppant transport model appealing to petroleum engineers and researchers (Deshpande et al. 2013).

In the present work, a numerical model is proposed that solves the mass and momentum conservation equations to model the two-phase flow with fracture fluid, as a continuous phase, and proppants as another phase, to investigate the effect of proppant transport in rough fracture geometry. The reported models (Bokane, Jain and Crespo 2014, Wu and Sharma 2016, Zhang, Gutierrez and Li 2017, Hu et al. 2018, Roostaei et al. 2018) in the literature are described for planar and smooth fracture geometry without fluid leak-off behaviour and limited to the laboratory scale. In the present study, an attempt was made to overcome this challenge by studying solid transport in the fluid to improve the existing models to include the effects of fracture roughness and fluid leak-off from fracture wall on proppant transport, integrate the fluid

flow and proppant transport with dynamic fracture propagation and employ the model for field application.

1.2 Problem Statement

Understanding of the proppant transport and distribution in the fracture network is one of the crucial steps for the success of the hydraulic fracturing (Blyton, Gala and Sharma 2015). After injection, proppant follow the fluid path, the resulting mixture of fluid and proppant has a more significant density, and proppants tend to deposit away from the wellbore based on the physical properties of fluid, proppant and fluid-solid interaction (Tsai et al. 2012). Further, the proppant distribution plays a dominant role to assure the adequate fracture permeability for hydrocarbon fluid production.

The experimental study conducted by Shah, Asadi and Lord (1998), Liu and Sharma (2005) and El-M. Shokir and Al-Quraishi (2009) have identified some of the critical parameters that dominate the slurry movement and proppant distribution namely fluid velocity, fluid rheology, proppant concentration, fracture width, formation characteristics, formation temperature, fracture closure and leak-off. In addition, it was concluded that it is difficult to accurately predict proppant distribution in the field settings based on experimental studies. The proppant placement within the fracture mainly affects the fracture conductivity and well performance, and it is significantly necessary to assess the capability of fracturing fluids for proppant placement at downhole conditions (Shah, Asadi and Lord 1998).

The phenomenon of proppant transport in hydraulic fractures can be numerically modelled, and it involves multi-physics modelling that can account for two-phase flows with particles, fracture rock mechanics, particle-particle interaction and particle micromechanics. Tsai et al. (2012) used numerical modelling using computational fluid dynamics (CFD) to simulate proppant and fracturing fluid distribution. The model identifies the potential for proppant distribution study; however, it fails to incorporate the effect of fracture roughness and fluid leak-off that can greatly affect the proppant distribution.

At present, comparatively limited computational models exist that can comprehensively simulate the whole physics of hydraulic fracturing and proppant distribution (Dontsov and Peirce 2014). The existing proppant transport and fracture simulation models can be categorised into two groups- firstly, models with planar and fixed fracture geometry (Bokane, Jain and Crespo 2014, Wu and Sharma 2016, Zhang, Gutierrez and Li 2017, Hu et al. 2018, Roostaei et al. 2018), and secondly, the fracture geometry predicted from the analytical models, such as KGD, PKN, and

P3D, and coupled with fluid flow and proppant transport (El-M. Shokir and Al-Quraishi 2009, Kong, Fathi and Ameri 2015, Zhan et al. 2016, Izadi et al. 2017, Wang, Elsworth and Denison 2018). The models proposed in the first group are based on pre-determined geometry and for proppant transport model, it ignores the effect of fracture roughness, fracturing fluid leak-off from the fracture wall, and dynamic effects of fracture propagation. Although some of these aspects have been studied separately, an integrated model that can couple the fluid flow, proppant transport and fracture propagation is missing. In the second group of proppant transport and fracture simulation models, where the fracture geometry is predicted from analytical models, and the fluid flow with proppant transport are usually modelled by two-component, interpenetrating continuum, meaning the flow governing equations are specific to the mixture, which cannot provide the accurate description of the particle physics in the slurry flow. Secondly, the effect of fracturing fluid leaking from the fracture-matrix interface on proppant distribution is neglected. Moreover, lastly, in most of the studies, the geometry of the fracture propagation is assumed from the analytical modelling techniques as mentioned earlier, and are based on linear elastic fracture mechanics (LEFM) that limits the fracture propagation to brittle rocks and ignore plastic deformations. In reality, some of the shale rocks are ductile in nature so using LEFM to model fracture propagation provides inaccurate estimation (Wang 2015). However, in the present work, the proppant transport and fluid flow are modelled by solving the flow governing equation for both the phases individually using the CFD technique and the proppant-fluid, proppant-proppant and proppant-wall interactions are modelled using the kinetic theory of granular flow (explained in chapter 3). The model has then integrated to couple the effect of dynamic fracture propagation with the fluid leak-off effects. The effect of dynamic fracture propagation is studied using the Extended Finite Element Method (XFEM) and cohesive zone model (CZM) that can model the plastic deformations in the ductile rock. The CFD, coupled with XFEM approach, offers the advantage of modelling the fracture propagation and investigate the accurate fluid flow and proppant concentration distribution, which may be challenging to obtain experimentally. The proposed three-dimensional integrated fluid flow, proppant transport and fracture propagation model can accurately model the fluid-proppant, proppant-proppant and fracture wall interactions with varying fluid, proppants and geomechanical parameters and fluid leak-off effects.

Furthermore, the hydrodynamics of proppant transport in fractures is a complex process, and the factors like fracture geometry, fracture roughness, and fluid leak-off add additional challenges to model the flow phenomenon numerically. In recent years, several researchers have modelled the proppant transport physics in hydraulic fractures using computational fluid dynamics (CFD) technique. Zhang and Dunn-Norman (2015) examined the proppant distribution at different perforation angle in fractures and compared the pressure drop using CFD. Kou, Moridis and Blasingame (2018) investigated the proppant transport and distribution in the hydraulic fracture

and natural fracture intersection using the discrete element method (DEM). Hu et al. (2018) proposed an idea of using Eulerian-Eulerian proppant transport model for field-scale hydraulic fractures using dimension reduction strategy. The reported studies are limited to the assumption of smooth planar fracture geometry with no leak-off effects from the fracture wall. The fracture roughness, coupled with fluid leak-off, can significantly impact the proppant transport physics. In the current study, firstly, a three-dimensional proppant transport model is developed that accurately models the proppant transport physics and the proppant transport model is validated with the published experimental data. Post that a base case is presented to explain in detail the proppant distribution in a real and rough fracture. Following that, multiple parameters were varied to examine the model with a variation in injection velocity, injection proppant concentration, and fracture height. Next, a detailed analysis of the fracture roughness on the hydrodynamics of proppant transport was carried out, and a relationship between the fracture roughness parameter and flow properties is established. Lastly, the proppant transport in fractures was coupled with dynamic fracture propagation and parametric study of flow and geomechanical parameters of proppant distribution is investigated in detail.

1.3 Research Aims and Objectives

The main focus of this PhD thesis is to develop a three-dimensional model of fluid flow and proppant transport in hydraulic fractures coupled with fracture propagation, fluid leakage and fracture roughness using CFD and XFEM modelling in order to improve the hydraulic fracturing design. The aims and objectives of the PhD work are summarised as follows:

1.3.1 Aim

This work aims to improve the hydraulic fracturing design in unconventional reservoirs by developing an integrated three-dimensional (3D) model that captures the proppant micro-mechanics, fracture roughness, fluid leak-off from the fracture wall and dynamic fracture propagation. The following objectives summarise how the aim of this study is achieved:

1.3.2 Objectives

i. Investigate the numerical modelling techniques and multiphase models that can accurately capture the fluid-proppant and inter-particle interaction in order to predict the various conditions for proppant transport, distribution and deposition in hydraulic fractures.

ii. Investigate the leak-off rate distribution at the sidewalls of the fracture to mimic the fluid leak-off from the fracture to the surrounding porous reservoir by defining a user-defined function in the CFD code and introducing the source terms in the governing equations in order to provide a realistic proppant tracking and more accurate proppant transport.

iii. Validate the results obtained from the CFD simulation model with the published experimental data in order to determine the accuracy of the CFD model.

iv. Investigate the impact of fracture roughness on the hydromechanics of proppant transport in rough fractures in order to calculate a realistic proppant horizontal velocity in rough fractures and better hydraulic fracturing design.

v. Develop the hydraulic fracture propagation model using fracture rock mechanics and finite element techniques and integrate it with the fluid flow and proppant transport model in order to dynamically simulate the realistic phenomenon in unconventional reservoirs and improved hydraulic fracturing design.

vi. Perform a parametric sensitivity study to understand the effect of variation in proppant properties (proppant size), fracturing fluid properties (fluid viscosity) and geomechanical properties (fracture width). Further, investigate the consequence of these parameters on the proppant transport in the hydraulic fractures in order to enhance the understanding of the complex flow phenomenon.

1.4 Study scope

The study is limited to investigating the complex interaction between fluid-proppant, proppant-wall and proppant-proppant with fluid leak-off and dynamic fracture propagation. The proppant transport in complex fracture network is not covered. The emphasis is on understanding the detailed physics involved in proppant transport through rough fractures for optimizing the hydraulic fracturing design parameters.

1.5 Thesis Outline

The outline of the thesis is provided below:

Chapter 1: An introduction to the hydraulic fracturing and role of proppant transport are provided in the first sections. Limitations in current numerical methods are briefly discussed. The aim and objectives of the thesis are described.

Chapter 2: Computational modelling of hydraulic fracturing and proppant transport is a valuable tool for fracturing design optimisation and fracture conductivity as the models provide

information about proppant distribution inside fractures, improving the hydrocarbon recovery with effective fracture treatment, and the effect of operating parameters. A brief literature review of existing hydraulic fracturing and proppant transport modelling work is described in the chapter.

Chapter 3: In this chapter, the governing equations and auxiliary equations for modelling proppant transport in hydraulic fractures are explained. The numerical procedure used for solving the equations is presented. A brief description of the developed user-defined code is also presented. Finally, modelling parameters are provided with appropriate boundary conditions.

Chapter 4: In this chapter, the Eulerian-Granular model is investigated against the Discrete Element Method which is a subtype of Eulerian-Lagrangian model to model the fluid flow and proppant transport inside the planar fracture. Limitations of the Eulerian-Granular model and the Discrete Element Method are discussed. Predicted simulation results are validated with experimental results. A parametric study is performed based on operating conditions, and design parameters are presented.

Chapter 5: In this chapter, a Dense Discrete Phase Method (DDPM) which is another subtype of Eulerian-Lagrangian model is used to simulate proppant distribution in hydraulic fractures. The predicted simulation results were validated against the published experimental study. A realistic fracture geometry is developed with fluid leak-off rate defined along the fracture length to mimic the fluid leak-off from the fracture wall. Additionally, the effect of fracture roughness is included in the model.

Chapter 6: In this chapter, the impact of fracture roughness on the hydrodynamics of proppant transport in rough fractures is investigated in detail. Different Joint Roughness Coefficient (JRC) fracture profiles were used to establish a relationship between fracture roughness parameter and flow properties.

Chapter 7: A hydraulic fracture propagation model using fracture rock mechanics in the unconventional reservoirs and Extended Finite Element Method (XFEM) is proposed. The model is coupled with the fluid flow and proppant transport model discussed in chapter 5.

Chapter 8: The chapter summarizes the outcomes of the thesis. A conclusion and future work are also presented in the chapter.

1.6 Significance

In this research, an attempt has been made to couple the fluid flow through fractures and fracture rock mechanics using numerical methods and contribute to enhancing the knowledge of the mechanical attributes of porous rock under intense injection conditions during the hydraulic fracturing mechanism. The following are the key novelties in the present work or contribution to knowledge -

i. The present study models the effect of dynamic fluid leak-off from the fracture wall in the proppant hydrodynamics in order to accurately simulate the proppant transport in hydraulic fractures.

ii. The present study proposes a 3D proppant transport model that captures the proppant physics in rough fractures using Joint Roughness Coefficient with detailed proppant-wall and inter-proppant interactions using the kinetic theory of granular flow in order to improve the hydraulic fracturing design.

iii. The present study couples the fluid flow and proppant transport with the dynamic fracture propagation using CFD-XFEM method to track the proppants accurately and dynamically simulate the realistic phenomenon for an improved hydraulic fracturing design.

iv. The present model can be used to prevent fracture tip screen out, which is a common failure in hydraulic fracturing design noticed in the oil industry. Fracture tip screen out occurs when proppant in fracturing fluid, create a bridge inside the fracture and prevents any further transport of proppant and fluid, resulting in a rapid increase in pump pressure. Using advanced numerical models like the one proposed in the current study can aid in designing prevention of the fracture tip screen out and model accurately proppant transport physics with dynamic fracture propagation.

Chapter 2: Literature review

In the last decade, the advancements in the technology of horizontal drilling and multistage hydraulic fracturing have resulted in the considerable progress in the hydrocarbon production from unconventional reservoirs, for example, shale gas and tight oil (Warpinski et al. 2009). Both these techniques are closely related to geomechanics, i.e., in order to create a multi transverse hydraulic fracture, wells are drilled horizontally in the direction of minimum horizontal in-situ stress. One conventional method of generating multiple fractures is the plug and perf method, in which multiple fractures are created in stages, and each stage consists of a cluster of perforations (Bokane et al. 2013). As explained earlier in section 1.1 that in order to create hydraulic fractures, highly pressurised fluid is injected at sufficiently high rates (60-100 bbl/min or 0.159-0.265 m^3/s) to initiate and propagate the fractures (Belyadi, Fathi and Belyadi 2019). It is followed by the injection of proppant laden fluid, to ensure that the fracture remains open against the geomechanical stresses and to sustain significant fracture conductivity and permeability to allow the hydrocarbon fluids to flow when the fracturing fluid pressure is reduced (Economides and Nolte 2000, Gaurav, Dao and Mohanty 2010).

The hydraulic fracturing in an unconventional reservoir is considered successful when the long multiple hydraulic fractures are created, uniform proppant transport and distribution in the fractures are obtained, and thus, the long multiple hydraulic fractures with uniform proppant distribution results in the excellent fracture conductivity for the flow of hydrocarbon fluids economically (Gu and Mohanty 2014).

2.1 Proppant transport in hydraulic fractures

Proppant transport plays a vital role in hydraulic fracturing. Proppant particles are dispersed in the fracturing fluid and are injected in the form of slurry in the hydraulic fracture, which is a narrow channel with rough fracture walls making it a particle-fluid two-phase flow problem in a narrow and rough hydraulic fracture (Kostenuk and Browne 2010). The proppant follows the fluid path, momentum exchange occurs between the two phases and the proppant settles down away from the wellbore due to the gravity forces, drag forces, and particle-particle collisions. This is due to two physical mechanisms namely fluid-proppant interaction and proppant-proppant or proppant-wall interaction (Daneshy 2011). There are many factors affecting the proppant transport process, including properties of proppant and fracturing fluid, fracture propagation, fluid leak-off, fluid-proppant interactions, proppant-proppant interactions and proppant-fracture wall interactions (Gadde et al. 2004). Therefore, understanding the proppant transport in

hydraulic fractures constitutes a critical issue. The proppant distribution profile can be categorized into two sections, the suspending region and the packing region (Swan and Brady 2010). In the suspending region, the proppants are suspended in the slurry and are under the influence of drag and gravity forces. The fluid-proppant interaction and inter-proppant interaction are dominant in this region (Boronin and Osiptsov 2010). On the contrary, in the packing region, the friction forces have a greater influence compared to the fluid-proppant and inter-proppant interactions (Deng et al. 2014). Once the proppant deposit at the fracture bottom, the proppant stops moving because the drag forces or relative momentum between the fluid and proppants are not strong enough to overcome the proppant weight, particle cohesion and the wall shear stress from the fracture wall. Especially, when the proppants transport in a low viscous fluid, the tendency of the proppants to settle significantly increases due to the poor ability of the low viscous fluids to suspend proppants and greater influence of inter-proppant and proppant-fracture wall interactions (Deng et al. 2014).

The perf and plug method, as briefly introduced at the beginning of this chapter, are one of the widely used methods for multiple staged hydraulic fracturing, and each stage consists of a cluster of perforations (Bokane et al. 2013). However, Cipolla, Mack and Maxwell (2010) concluded in their study that due to uneven proppant distribution, nearly half of the perforation clusters did not contribute to hydrocarbon production. Further, Daneshy (2011) also observed the similar results of uneven proppant distribution in the perforation clusters and reported that a higher portion of proppant particles entering the last cluster. This behaviour was explained by Daneshy (2011) with a substantial difference in the properties of the proppant and fluid properties. For example-density difference between the fluid and proppants and injecting the fluid-proppant slurry at higher injection rate (100 bbl/min or 0.265 m^3/s) might find it difficult to change direction and thus, will non-uniformly enter the perforations. In addition, Deshpande et al. (2013) conducted a large-scale experimental study to understand proppant distribution in the plug-and-perf method and noticed uneven distribution especially with greater proppant density and lower flow rates. Bokane et al. (2013) used computational fluid dynamics (CFD) numerical modelling method to validate the experimental study by Deshpande et al. (2013) and understand the uneven proppant distribution. However, no quantitative impact of uneven proppant distribution was evaluated by CFD and experimental studies. Uniform proppant distribution in multistage fracturing is often assumed in most reservoir modelling and fracture simulator in the literature (Bokane et al. 2013, Zhan et al. 2016, Wang, Elsworth and Denison 2018), and hence it is essential to include the accurate physics behind proppant transport and distribution on the well performance.

2.2 Proppant transport in hydraulic fractures for unconventional reservoirs

Slick water fracturing fluid is most commonly used in hydraulic fracturing operation in unconventional reservoirs due to the low cost and lower frictional pressure loss during injection (Alotaibi and Miskimins 2015). Additionally, higher injection rate is achieved using slick water (100 bbl/min or 0.265 m^3/s) compared to using conventional fracturing fluid (60 bbl/min or 0.159 m^3/s), and thus a longer and narrow fracture is created using slick water as fracturing fluid in contrast to shorter and wider fracture using conventional fracturing fluid (Belyadi, Fathi and Belyadi 2019). In the slick-water fracturing technique, water, sand, and chemical additives are pumped downhole to create a complex fracture system within the reservoir. The chemical additives used are friction reducers like polyacrylamide, scale inhibitors like ethylene glycol and hydrochloric acid, biocides like methanol and naphthalene to control aerobic bacteria that destroy additives in fracturing fluid, and surfactants like butanol to enhance proppant carrying ability (Wu 2015). The friction reducers like polyacrylamide play a significant role in achieving higher injection rates using slick-water fracturing fluid. The addition of the friction reducers to water reduces friction and makes the water very slick (Speight 2016a). The composition of fracturing fluids in the conventional reservoirs, on the other hand, also includes mixing natural organic thickeners like Guar and Xanthate gums to increase its viscosity and proppant suspension ability. The slick water fracturing fluid has low viscosity when compared with conventional fracturing fluids, and this results in a significant reduction in the capability to transport proppant. Palisch, Vincent and Handren (2010) explained that fluid flow and proppant transportation behaviour show substantial variation using slick water or thin fracturing fluid in comparison with conventional fracturing fluids. Experimental studies carried out by Patankar et al. (2002), Wang et al. (2003), Sahai, Miskimins and Olson (2014) have greatly enhanced the understanding of the proppant distribution in slick water fracturing fluids. It was demonstrated that as the proppants are injected with thin fracturing fluids and due to the very low viscosity of the thin fracturing fluid, the proppant settles quickly and forms a bank in proximity to the wellbore, and the subsequently injected proppant will overpass and deposit ahead as shown in Figure 2.1. The experimental results suggested the proppant transport in fractures with thin fracturing fluid results in flow pattern characterised by three-layers, namely fixed stationary bed, traction carpet and clean fluid layer (Figure 2.1).

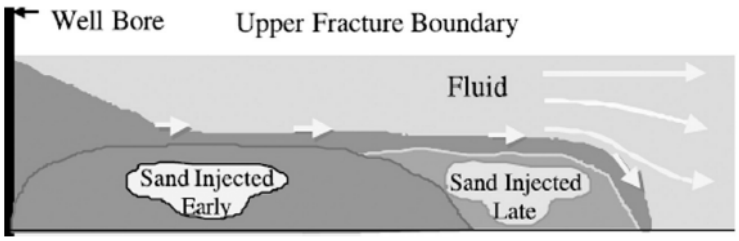

Figure 2.1 Proppant-fracturing fluid coupled flow (Patankar et al., 2002)

Mack, Sun and Khadilkar (2014) described the three proppant transport mechanisms namely surface creep, saltation, and suspension as explained earlier in section 1.1 and shown in Figure 1.2. Tsai et al. (2012) and Tomac and Gutierrez (2014) investigated the fluid-proppant and inter-proppant interactions and modelled the proppant transport in hydraulic fractures. It was proposed that the proppant suspension is the dominant transport mechanism for proppant transport with fracturing fluid due to the higher injection flow rates. One of the critical issues in the proppant transport in hydraulic fractures for unconventional reservoirs is due to the poor proppant suspension ability of the slick water, the proppants deposits quickly after injection close to the wellbore (Sahai, Miskimins and Olson 2014). Thus, as the injection time progress, the proppant bed gradually builds up and form proppant bridge. Proppant bridging is a frequently observed phenomenon seen during hydraulic fracturing that can lead to hydraulic fracturing design failure due to the fracture tip screen out (Dontsov and Peirce 2015). The fracture tip screen out is a condition where the proppant bed forms a bridge and inhibit any further proppant transport into the fracture leading to the unpropped section of the fracture closing down when the hydraulic pressure is removed and consequently results in loss of fracture conductivity (Zhang, Li and Gutierrez 2017). This further result in an abrupt increase in pump pressure leading to hydraulic fracturing operation failure (Sharma and Gadde 2005). The success of a hydraulic fracturing job is governed by the better hydraulic fracturing design, for which correctly modelling the proppant mechanics can play a critical role (Yew and Weng 2014). Numerous experimental and numerical modelling studies have been conducted by researchers and engineers that are discussed in detail in the following sections.

2.3 Experimental works on Proppant Transport

Many experimental studies have been carried out to investigate the proppant transport in hydraulic fractures. In the early studies, the research was mainly focussed on proppant settling velocity and the factors affecting the proppant bank build-up. Kern, Perkins and Wyant (1959) were among the earliest researchers who studied proppant transport and investigated the transport

of sand and water in a vertical slot formed by two parallel Plexiglas plates. It was proposed that during fracturing, the initial sand injected deposits close to the wellbore, and as the injection is progressed the subsequent sand injected transports longer into the fracture. Babcock, Prokop and Kehle (1967) studied the effect of equilibrium velocity and the bank build-up constant on proppant distribution experimentally and proposed a correlation for these two parameters. Schols and Visser (1974) used low viscous fracturing fluid and conducted an experimental study to propose an analytical solution for three different phases of proppant build-up observed during the experiment. It was proposed that the first phase of the proppant bed formation starts at the close to the wellbore. As the proppants settle, the proppant bed gradually increases in height until an equilibrium height is achieved. Schols and Visser (1974) further suggested that the fluid drag forces erode any subsequent proppant deposition than the equilibrium height. Secondly, in the next phase, the proppant distributes over the full length of the fracture and attains an equilibrium height. Lastly, in the final phase, the proppants saltates and increases the length of the proppant bed in the direction of flow. Clark et al. (1977) further investigated the effect of proppant concentration and size, fluid viscosity and flow rate on proppant bed build-up using large vertical slot model.

After 1990, the researchers started investigating the role of convection in proppant transport. Cleary and Fonseca (1992) proposed that downward convection of heavier proppant-laden stages is the dominant phenomenon than settling in vertical fractures and is often neglected in the industrial fracture flow modelling software programs. Barree and Conway (1994) studied proppant distribution experiments to develop a numerical simulation tool and improved the accuracy of the description of slurry transport. It was proposed that vertical particle motion can be modelled by convection or density-driven flow and it is hundreds of time faster than single particle settling velocities. Clark and Zhu (1996) performed a series of slot experiments and proposed a dimensionless group to investigate if convection is an important factor for proppant transport in Newtonian and Non-Newtonian fluids. The dimensionless groups were relationships developed based on the ratios of pressure drop along the fracture slot to the vertical force on the fluids (Newtonian and non-Newtonian). The key properties used in the dimensionless groups were fluid viscosity, density difference between the fluid and proppants, flow rate, gravitational force, fracture slot height and fracture slot width to predict when convection effects would be important in proppant transport. It was proposed by Clark and Zhu (1996) that as the value of the dimensionless group increases, the tendency of the fluid to flow downwards toward the bottom decreases. Al-quraishi and Christiansen (1999) used the small glass models to investigate different flow conditions for proppant transport and proposed that convection plays a dominant role in proppant transport, even with small density differences. Roostaei et al. (2018) accounted

for the dimensionless groups proposed by Clark and Zhu (1996) and convection effects inside fracture slots and proposed a numerical model of proppant transport in hydraulic fractures.

More recently, after 2000, many investigators turned their attention to study the effect of fracture wall effects, turbulence, complex fracture geometry, and fracture networks. Wang et al. (2003) based on the lab data from STIM-LAB, proposed a correlation for proppant flow in fractures with smooth surfaces, fracture wall effects and turbulence. Brannon, Wood and Wheeler (2006) studied the characteristics of proppant slurry transport in a large-scale laboratory experiment and proposed an empirical proppant transport model to define the propped fracture length, based on fracturing fluid and proppant properties. Sahai, Miskimins and Olson (2014) experimentally evaluated proppant distribution in fracture networks with various slot complexity, pumping rate, proppant concentration, and proppant size. Alotaibi and Miskimins (2015) extended this work and highlighted the mechanism of proppant transport during proppant bed development. Furthermore, a scalable correlation is proposed to predict the equilibrium proppant bed height with the variation of flow rates and proppant concentrations. Recently, Tong and Mohanty (2016, 2017) studied proppant transport in complex fractures using water and foam and demonstrated experimentally that foam has the potential of using it as a fracturing fluid and has improved proppant suspension ability than slick water due to higher apparent viscosity. A comprehensive literature review on experimental works of proppant transport in hydraulic fractures suggested that the experiments reported in the literature were mainly focused on the proppant distribution characteristics inside the fracture and investigated the effects of proppant type, fracturing fluid, fracture geometry on the proppant distribution. However, all the slot experiments performed in the literature assumes simple fracture geometry, neglecting the effect of fluid leak off to the surrounding porous media and the effect of fracture roughness. Hence, numerical methods can be used to validate the experimental data and upscale proppant transport physics to the field scale fractures.

2.4 Numerical methods for modelling proppant transport and distribution

The behaviour of proppant transport and distribution has been studied experimentally by numerous researchers, as explained in the previous section. However, some of the challenges from the experimental results are the scale of fracture slots in the laboratory is considerably smaller than the real range, and it is not easy to change the experimental setting. On the contrary, the numerical simulation provides more flexibility in terms of the computational domain and once the physical mechanism for the process is clear, there is no such restriction. To solve this multiphase flow problem of proppant transport in fracturing fluid, there are mainly two kinds of numerical methods, the Eulerian-Eulerian method and the Eulerian-Lagrangian method (Gadde et al. 2004, Chiesa et al. 2005, Tsai et al. 2012). A more detailed discussion on the various

multiphase model approaches and formulation of the numerical frames can be found in Enwald, Peirano and Almstedt (1996) and Tryggvason et al. (2001). The following sections present a brief discussion of the multiphase flow models in the context of liquid-solids flow.

2.4.1 Eulerian-Eulerian Method

The Eulerian-Eulerian method allows the modelling of multiple separate phases that frequently interacts with each other. A specific type of Eulerian-Eulerian model where one of the phases is a solid phase or particle phase and the other phase is fluid is commonly known as the Eulerian-Granular model. In the Eulerian-Granular model, the flow of particle and fluid phase is modelled using continuum medium, meaning both the phases are treated as a continuous phase and mass and momentum conservation equations are solved for both the phases separately. Volume averaging method is used to derive the equations of the Eulerian-Granular model, and the fluid-proppant interaction is modelled using the averaged drag force term in the momentum equation. The averaging introduces a volume fraction function which defines the probability of occurrence of a phase in a fixed control volume in space and time, and their sum is equal to one (Enwald, Peirano and Almstedt 1996). The governing momentum equation for the granular phase includes additional terms to define the properties for granular flow such as a solid pressure and solid stress tensor terms from the application of the kinetic theory of granular flows (Savage and Jeffrey 1981, Jenkins and Savage 1983). The Eulerian-Granular model is based on the Kinetic Theory of Granular Flow (KTGF) which captures the fluid-proppant and proppant-proppant interaction and provides a good approximation of the results in a computationally efficient manner (Clifton and Wang 1988). In Eulerian-Granular model, the volume fraction is used as a parameter to determine how much each phase is present in a control volume (Basu et al. 2015). The fluctuating velocity of the particles is modelled by solving an additional transport equation for the kinetic energy of particles known as the granular energy transport equation. A detailed description of the derivation is presented in Drew (1983) and Ishii and Hibiki (2011). All the terms defining the granular flow properties mentioned above are discussed in detail in chapter 3.

The Eulerian-granular approach is computationally efficient for modelling solid-liquid flow. In proppant transport in fractures, various inter-phase interactions occur like proppant-liquid momentum exchange, proppant-proppant collision and proppant-wall collision. Therefore, all possible interactions between liquid and solids-phase should be accounted for. An additional advantage of Eulerian-granular modelling approach is that it allows for the inclusion of models that are capable of accounting for enduring frictional contact between solids. The frictional inter-particles contact is likely to dominate in stationary proppant bed flow regime, which is a critical flow regime in proppant transport in fractures and of interest in the present study. Some of the

key research studies that describe Eulerian-Eulerian methods in detail are as follows (Gadde et al. 2004, Liu 2006, Kong, McAndrew and Cisternas 2016, Roostaei et al. 2018). Gadde et al. (2004) used the Eulerian-Eulerian approach in order to propose correlations for proppant settling in water frac, taking into account the inertia effects, proppant concentration, turbulence and fracture width. Liu (2006) extended this work in order to experimentally validate it and couple it with the fracture simulator. Kong, McAndrew and Cisternas (2016) applied the Eulerian-Granular model in order to investigate the proppant transport in non-Newtonian fluid and proposed that foam has the potential as an alternative to slick water fracturing fluid in shale-gas reservoirs. Roostaei et al. (2018) applied the Eulerian-Eulerian method and investigated the proppant transport in fixed fracture slots and incorporated the effects of inertia, concentration and fracture wall on the proppant transport in order to track the motion of slurry and proppants. The key limitations of the Eulerian-Granular model are- firstly, in the Eulerian-Granular model only mono-dispersed particle size can be used. Using poly-dispersed proppant size distribution in Eulerian-Granular model would require additional coupling equations for each diameter class. Some of the forces in Eulerian-Granular model depends non-linearly on diameter for instance drag force. These forces will be inaccurate if the arithmetic average of the diameter is used for their computation (Subramaniam 2013, Wang 2020). The second limitation of the Eulerian-Granular model is that the Eulerian-Granular model is not capable of representing the fluxes, associated with two streams of particles moving with different velocities at the same physical location (Subramaniam 2013, Patel et al. 2017). Lastly, the proppant-wall interaction is not accounted in detail in the Eulerian-Granular model (Subramaniam 2013). In the Eulerian-Granular model, the proppant-wall interaction is modelled using the standard Johnson and Jackson (1987) boundary condition with specularity constant and wall restitution coefficient. The specularity constant characterizes the collisional tangential momentum transfer between the solid phase and the wall, and the wall restitution coefficient characterizes the dissipation of collisional kinetic energy transfer between the solid phase and the wall.

2.4.2 Eulerian-Lagrangian method

The Eulerian-Lagrangian method models the liquid or continuous phase by solving the governing equations (mass and momentum conservation equations), while the solid or dispersed phase is modelled by tracking their motion using Newton's second law of motion (Bokane et al. 2013). The solid particles trajectories are computed for each parcel of particles that follow the same trajectory by solving the equation of motion (Patankar and Joseph 2001). It provides a detailed analysis of particle-fluid and particle-particle interaction, and it is computationally costly, which provides a challenge to apply it to the field scale. Unlike Eulerian-Granular model, the Eulerian-Lagrangian method can take into account the proppant size distribution. The proppant-wall

interactions are comprehensively modelled using the reflect boundary condition that models the particles energy and momentum transfer in both normal and tangential direction post-collision. Two most common Eulerian-Lagrangian methods used in the literature are the Discrete Particle Method (DPM) and the Discrete Element Method (DEM) (Tsai et al. 2012, Deng et al. 2014). They differ in the way particle-particle interaction is handled. The DPM model is based on the assumption that that the particle phase is sufficiently dilute (volume fraction <10%) that particle-particle interactions and the effects of the particle volume fraction on the continuous phase fluid are negligible (Zhang, Li and Gutierrez 2016). In the DEM model, the particle-particle/wall interactions are more accurately captured using the soft-sphere approach and unlike the DPM model, it can be used even for the higher proppant volume fraction (10% - 63%) (Deng et al. 2014).

The Discrete Element Method (DEM) is mainly used when a high-volume fraction (10% - 63%) of particles is present, meaning the inter-particle interaction is imperative, such as proppant flow in the fracturing fluid (Wu and Sharma 2016). Cundall and Strack (1979) proposed the DEM method, and it was later coupled with CFD by other researchers to study fluid-solid flow modelling. In this approach, the primary phase is solved using a conventional Eulerian method meaning continuity and momentum equations are solved using CFD, while the solid phase is solved using DEM by tracking every dispersed particle, thus it is a computationally expensive technique. Particles are tracked by calculating and tracking the mass, velocity, and forces acting on a particle using Newton's second law of motion (Zhang, Li and Gutierrez 2017). This is referred to as tracking in the Lagrangian frame in the DEM method (Zhang, Li and Gutierrez 2017). Finally, the drag forces and interphase momentum exchange terms are used to model the interaction, energy dissipation and coupling of both the phases, i.e., continuous and discrete phases (Patankar and Joseph 2001, Tsai et al. 2012). When a particle hits a wall or another particle, the drag force results in lower particle velocities and deceleration occurs. The particles are assumed as rigid. In order to account for accurate particle micro-mechanics and particle collision, it is further assumed that after the collision, the two particles deform and defined by the overlap displacement of the particles. This approach is called the soft-sphere approach that outlined an accurate contact model (Andrews and O'Rourke 1996). The mathematical equations for the soft-sphere approach are explained later in chapter 3.

Accurate proppant distribution in DEM model results in substantially higher computational cost and limits its application for field-scale fractures (Patankar and Joseph 2001, Tsai et al. 2012, Deng et al. 2014, Wu and Sharma 2016). Patankar and Joseph (2001) were among the early researchers who successfully employed the Euler-Lagrangian methods in the study of particle transport. A detailed particle physics involving drag forces, body forces, viscous stresses and

inter-particle interaction were successfully incorporated into the model. The governing equations (continuity and momentum equations) for the fluid phase were solved using continuous Eulerian approach and for the solid phase were solved using the Lagrangian approach (Andrews and O'Rourke 1996). Tsai et al. (2012) used the Euler-Langrangian approach to investigate the proppant transport in water as a fracturing fluid and proposed a 3D model that accounts for detailed proppant-wall and inter-proppant interactions. Furthermore, the proppant settling behaviour with the variation in proppant size, density and flow rates is demonstrated. Deng et al. (2014) used the discrete element method to investigate the interaction between the proppant and surrounding rock (shale) during hydraulic fracturing. The fracture aperture for different conditions of proppant size, Young's modulus of rock and the pressure were calculated. Wu and Sharma (2016) used the CFD-DEM method to investigate the proppant transport through a perforated horizontal casing. An efficiency factor was proposed to evaluate the effectiveness of proppant transport. It was further investigated the perforation orientation plays a critical role in proppant transport efficiency at lower flow rates.

2.5 Current challenges in numerical modelling

The literature review of the experimental and numerical modelling studies for the proppant transport in hydraulic fractures suggested that the prediction of proppant distribution inside the fracture is a multi-physics phenomenon, and some of the factors affecting the dynamics of proppants are- fracture geometry, fracturing fluid properties and proppant properties. Schols and Visser (1974), Clifton and Wang (1988), Ouyang, Carey and Yew (1997), Adachi et al. (2007), Gu and Hoo (2014), and Yang, Siddhamshetty and Kwon (2017) extensively studied the proppant transport in the conventional reservoirs using high viscosity fracturing fluid and neglected the fluid leak-off from the fracture wall. However, in the low viscosity fracturing fluid (like slick water) the proppant suspension is not a primary mechanism and as a result, proppant deposit quickly to form a proppant bed leading to dramatically shorter horizontal distance away from the wellbore. Furthermore, Tsai et al. (2012), Tomac and Gutierrez (2014), Wang, Elsworth and Denison (2018), and Hu et al. (2018) numerically studied the proppant transport and distribution using slick water as fracturing fluid but simplified the model with assuming smooth planar geometry, laboratory-scale model and neglecting fluid leak-off from the fracture wall. To the best of our knowledge, the current numerical models described in the literature are for planar, fixed and smooth fracture geometry. The fluid leak-off effects, where a part of the fracturing fluid leaks into the surrounding rock from the fracture walls, depending upon the reservoir characteristics of the rock is usually neglected in the existing studies for simplifying the proppant physics during the modelling of proppant transport in hydraulic fractures. Furthermore, in terms of computational time, the models described using the Eulerian-Granular method has a faster

computational time but some of the particle physics is simplified, for instance, averaged proppant size or mono-dispersed size proppants and proppant-wall interaction. On the contrary, the models that are described using CFD-DEM can capture the detailed particle physics but are computationally too expensive for its application to large scale or field fractures.

Therefore, in the present study, an attempt has been made to overcome this challenge to capture the proppant physics in rough fracture with a fluid leak-off from the fracture wall and upscale the model for field application. In order to propose a proppant transport model for real fractures or field-scale fractures, a CFD based dense discrete phase method (DDPM) is employed which is a subtype of Eulerian-Lagrangian model (explained in chapter 3). It solves the mass and momentum conservation equations to model the continuous phase, and the proppant phase is modelled in the Lagrangian frame by tracking their motion using the parcel method and applying Newton's second law of motion. A parcel is a group of particles based on similar properties like particle diameter, density, and mass flow rate. In order to save the computational costs in DDPM model, many particles are tracked in each parcel (Patankar and Joseph 2001, Adamczyk et al. 2014). The proppant-fluid interaction is modelled using the interphase momentum exchange term, proppant-proppant and proppant-wall interactions are modelled using the application of KTGF. The DDPM model overcomes the challenges of Eulerian-Granular method and is computationally faster than the DEM model. Like DEM, the DDPM model can be used for higher volume fraction. The current work aims to use the DDPM model and investigate the effect of proppant transport in rough fracture geometry and dynamically couple it with the fracture propagation in unconventional reservoirs. The model also incorporates the fluid leak-off from the fracture walls for slick water and Non-Newtonian fracturing fluid (foam). Kong, McAndrew and Cisternas (2016) described that foam could be used as an alternative to slick water as a fracturing fluid in shale gas reservoirs as it has high apparent viscosity and lower leak off which aids in proppant suspension. Gu and Mohanty (2014) also explained that foam could assist in faster fracture clean-up due to gas expansion and reported that the foam stability depends upon temperature, pressure, gas type, surfactant and concentration. Use of foam as a fracturing fluid has been experimentally studied by many researchers using Hele-Shaw slots in a laboratory-scale model (Tong, Singh and Mohanty 2017, Tong, Singh and Mohanty 2018, Hosseini et al. 2018). In the current study, the proppant distribution for foam as a fracturing fluid is investigated using numerical modelling.

2.6 Past fracture propagation and fluid flow models

Hydraulic fracturing consists of four main processes: (1) the fracture initiation; (2) the fluid flow within the fracture; (3) the fracture growth and propagation; (4) the fluid leak-off from the fracture into the rock formation (Chen et al. 2009). Linear elasticity is usually used to model fracture initiation; Lubrication theory is used to account for the fluid flow within the fracture; linear elastic fracture mechanics (LEFM) theory is adopted as the propagation law, and diffusion of fracturing fluid is used to account for fluid leak-off in the rock formation (Adachi et al. 2007). One of the limitations of the linear elastic fracture mechanics is it assumes rock as brittle material with no ductile or plastic deformations. In reality, some of the shale rocks are ductile in nature so using LEFM to model fracture propagation provides inaccurate estimation (Wang 2015).

The first theoretical mathematical models of hydraulic fracturing were developed in the 1950s. The two main models developed with the assumption of constant height were: the Khristianovic-Geertsma-de Klerk (KGD) model (Zheltov and Khristianovic 1955, Geertsma and De Klerk 1969) and the Perkins-Kern-Nordgren (PKN) model (Nordgren 1972, Perkins and Kern 1961). KGD model is based on the assumption that width of the fracture is a function of length, the fracture is rectangular in shape and best suited for fractures whose height is much greater than its length (Zheltov and Khristianovic 1955, Geertsma and De Klerk 1969), whereas PKN model assumes the width of fracture is a function of height; fracture is elliptical in shape and is applicable when fracture length is much larger than the height (Nordgren 1972, Perkins and Kern 1961). In addition, Yew and Weng (2014) explained that under uniform in-situ stress distribution, the hydraulic fracture is circular in shape and it can be characterised by KGD model, whereas under large and variable in-situ stress distribution, the hydraulic fracture becomes elongated and net wellbore pressure increases, this can be modelled by PKN model.

Simonson, Abou-Sayed and Clifton (1978) developed Pseudo-3D (P3D) models based on PKN model to account for variation in height and examine the fracture propagation. The major difference between the P3D and the two-dimensional (2D) models is the addition of a vertical in-situ stress profile and corresponding fluid flow component. P3D models can further be sub categorised into two main groups: Firstly, cell-based models proposed by Fung et al. (1987) who extended the work of Simonson, Abou-Sayed and Clifton (1978) to multi-layer cases and divided fracture into several discrete and independent cells in the horizontal direction. The model is very reasonable in the central region of the fracture; however, it overestimates the magnitude of fluid pressure along tip region of the fracture and cannot give an accurate description of pressure distribution in fracture. Moreover, secondly lumped models proposed by Cleary, Kavvadas and Lam (1983) which assumes a fractured front consists of two half ellipses combined together.

However, Johnson and Greenstreet (2003) explained that these models cannot model excess leak-off behaviour and cannot simulate fracturing with arbitrary shape. Thus, Planar3D (PL3D) models have been proposed by Advani, Lee and Lee (1990) that assumes the arbitrary shape of hydraulic fracture in a multi-layered formation. In PL3D models, the fractures can be simulated using two approaches: fixed rectangular mesh (Siebrits and Peirce 2002) using Green's function and moving triangular mesh (Advani, Lee and Lee 1990). However, Carter et al. (2000) explained that PL3D model cannot simulate out of plane fractures and deviated wellbore condition and thus, the fully 3D model is required to simulate the hydraulic fracturing process. Settari, Puchyr and Bachman (1990) were among the earliest researchers to propose the concept of partially decoupled fracture modelling and apply it in fracture propagation analysis. Barree and Conway (1994) developed a numerical simulation tool called GOHFER to improve the accuracy of the description of slurry transport and couple it with fracture propagation. However, for the proppant transport, the effect of concentration effects was included, and the effect of wall and inertia was neglected. Further, to couple the fracture propagation and fluid flow the analytical results of fracture width and the pressure were used. Some of the simulation studies based on GOHFER (Al-quraishi and Christiansen 1999, El-M. Shokir and Al-Quraishi 2009) also has the same limitation. Behr et al. (2006) and Shaoul et al. (2007) further developed the work and proposed an approximate model integrating the fracture propagation and reservoir simulation, by importing the propped-fracture geometry in the commercial reservoir simulator. However, only the uniform proppant distribution is assumed in the analysis and the dynamic effects of proppant transport and distribution were neglected in the modelling. Adachi et al. (2007) developed a numerical simulation model for hydraulic fracturing. However, in their work, the proppant settling was assumed to be predominantly by gravity-based, and in the absence of gravity, it was assumed that the fluid and proppant would transport with the same velocity. Further, to couple the fracture propagation and fluid flow the analytical results of fracture width and the pressure were used. Freihauf (2009) in his research, developed a hydraulic fracturing model that couple fluid flow and proppant transport. However, the fracture geometry was modelled using analytical PKN model.

To simulate the 3D real-time fracturing process, Chen et al. (2009) proposed a cohesive element method. Unlike classical fracture mechanics, this model avoids the singularity problems in the crack tip by using traction-separation law. It is implemented by the Finite Element Method (FEM) and pre-assumes a fracture zone. In contrast, Zhang et al. (2010) suggested that this method cannot predict the fracture orientation under complex stress condition, for example-reorientation, because the fracture path is predefined by pre-installing cohesive elements. In order to characterise layered medium in the unconventional reservoir during numerical simulation, Peirce and Siebrits (2001) developed a boundary element-based method for fracture opening in

a layered elastic medium. To improve the method with less simulation cost, Zhou and Hou (2013) introduced an approach to firstly, categorise the elements into three groups: completely fractured, fracture front, unfractured element. Fracture front is the elements in between fractured and unfractured elements. Secondly, weighted fluid pressure was calculated using fracture pressure of completely fractured elements and the pore pressure of unfractured elements. Contrastingly, this method estimated less accurate fracture profile, permeability and stress variation. Further, Yang et al. (2004) used the Weibull's statistical function to characterise and simulate the heterogeneities in the rock properties. Furthermore, the study of Yang et al. (2004) was based on LEFM that assumed rock as a brittle material. However, in this approach, the interfacial behaviour between materials is not considered. Therefore, to simulate the interfacial attributes Fu, Johnson and Carrigan (2013), introduced a coupled model to capture nonlinear interfacial interactions and model the permeability variation. In addition, Finite Volume Method (FVM) together with FEM modelling, was used to simulate fluid flow reservoir deformation. The main challenge in this method is that the crack could only grow along element edges. Gu, Seibrits and Sabourov (2008) proposed another method to simulate the interface behaviour and account for stress shadow effect by using the Displacement Discontinuity Method (DDM) and used interfacial slip based on the P3D model. Weng et al. (2011) expanded this approach and developed Unconventional Fracture Model (UFM) model which is similar to P3D DDM model but also takes into account fracture network and interaction, but to evaluate stress shadow effect it has to be modelled explicitly. Du et al. (2011) used microseismic data and natural fracture intensity to characterise the reservoir and fracture network and proposed a hydraulic fracturing model. However, the simplistic solution of proppant transport was assumed in the model without solving any Partial Differential Equation (PDE). Rebeiro (2013) extended the work of Freihauf (2009) and used the adaptive re-meshing technique but proposed the model only for the fully elastic medium and neglected the plastic deformations in the medium. Recently, Wu (2014) developed a hydraulic fracture propagation model from a horizontal wellbore in a naturally fractured reservoir. The model integrated rock mechanics using Displacement Discontinuity Method (DDM) with fluid mechanics using lubrication theory. However, it does not incorporate proppant distribution in complex fracture networks and assumes a constant height of fractures.

Some other methods to simulate hydraulic fracturing process include the eXtended Finite Element Method (XFEM), and Discrete Element Method (DEM). Taleghani and Olson (2009) used XFEM to study fracture initiation, propagation and interactions between a growing hydraulic fracture and the surrounding natural fracture. Keshavarzi and Mohammadi (2012) extended this work to study the effects of intersection angles between hydraulic fractures and natural fractures. The Finite Element Method (FEM) is extensively used in fracture mechanics to model fracture propagation. However, due to re-meshing required at every time step, the FEM is

computationally expensive (Zienkiewicz, Taylor and Zhu 2013). To overcome this shortcoming of FEM, an improved method Extended Finite Element Method (XFEM) is proposed and used by many researchers recently (Taleghani and Olson 2009, Lecampion 2009, Mohammadnejad and Khoei 2013, Khoei, Vahab and Hirmand 2016, Saberhosseini, Ahangari and Mohammadrezaei 2019). In the XFEM, no re-meshing is required during fracture propagation, and additional enriched degrees of freedom are introduced to model the fracture (Moës, Dolbow and Belytschko 1999, Stolarska et al. 2001, Sukumar and Prévost 2003). In the current research work, the XFEM was used to model the fracture propagation in unconventional hydrocarbon reservoirs, and it is dynamically coupled with the fluid flow and proppant transport model. Sousani et al. (2015) modelled the hydraulic fracturing process using the discrete element method (DEM) and studied the effect of fracture angle on stress and crack propagation. It was shown that with the variation in fracture angle, it results in a change in the internal stress pattern of the model. However, the capillary effects were neglected, and isotropic stress condition was assumed, which become important as fluid flows further away from the wellbore. Additionally, to simulate the DEM to field scale, the simulation cost is substantial. In the DEM, the reservoir is modelled as an arrangement of discrete blocks connected by fractures or faults, and as a result, the fracture propagation is constrained to the edges of discrete blocks. Furthermore, the computational cost of the DEM is extremely expensive.

2.7 Key findings from the literature review/Research gap

From the literature review of the past fracture propagation and fluid flow models, it can be summarised that the fracture propagation has been comprehensively studied by various researchers from 2D analytical models (Geertsma and De Klerk 1969, Nordgren 1972) to 3D advanced numerical XFEM and DEM models (Taleghani and Olson 2009, Marina et al. 2015). However, only a few studies are present in the literature that had integrated the proppant transport and fluid flow with fracture propagation phenomenon (El-M. Shokir and Al-Quraishi 2009, Kong, Fathi and Ameri 2015, Zhan et al. 2016, Izadi et al. 2017, Wang, Jiehao, Elsworth and Denison 2018). In the existing coupled fluid flow and fracture models, the fluid flow and proppant transport are usually modelled by two-component, interpenetrating continuum, meaning the flow governing equations are specific to the mixture, which cannot provide the accurate description of the particle physics in the slurry flow. Secondly, the effect of fracturing fluid leaking from the fracture-matrix interface on proppant distribution is neglected. Moreover, lastly, in most of the studies, the geometry of the fracture propagation is assumed from the analytical modelling techniques and are based on LEFM that limits the fracture propagation to brittle rocks and neglect plastic deformations. In reality, some of the shale rocks are ductile in nature so using LEFM to model fracture propagation provides inaccurate estimation (Wang

2015). In terms of the proppant transport models, the current numerical models are described in the literature for planar, fixed and smooth fracture geometry. As stated previously, the fluid leak-off phenomenon from the fracture walls to the surrounding rock is usually neglected in the existing studies for simplifying the proppant physics during the investigation of proppant transport in hydraulic fractures. Furthermore, in terms of computational time, the models described using the Eulerian-Granular method has a faster computational time but some of the particle physics is simplified, for instance, averaged proppant size or mono-dispersed size proppants and proppant-wall interaction. On the contrary, the models that are described using CFD-DEM can capture the detailed particle physics but are computationally too expensive for its application to large scale or field fractures.

Therefore, to fill this research gap and overcome this challenge, in the present study an attempt has been made to integrate the proppant transport, fluid flow with dynamic fracture propagation using advanced computational modelling techniques for improved hydraulic fracturing design. In the current research, the proppant transport and fluid flow are modelled using the CFD based dense discrete phase method (DDPM) which is a subtype of Eulerian-Lagrangian model that accounts for the multi-size proppant distribution and the interactions between fluid-proppant, proppant-proppant and fracture-wall. It solves the mass and momentum conservation equations to model the continuous phase, and the proppant phase is modelled in the Lagrangian frame by tracking their motion using the parcel method and applying Newton's second law of motion. The proppant-fluid interaction is modelled using the interphase momentum exchange term, proppant-proppant and proppant-wall interactions are modelled using the application of KTGF. It overcomes the challenges of Eulerian-Granular method and is computationally faster than the DEM Model (around 3.5 times faster – see appendix C). Unlike, the models reported in the literature, the present model also incorporates the effect of fluid leak-off from the fracture walls to the surrounding rock in proppant distribution. The proppant transport in fractures was then coupled with dynamic fracture propagation using XFEM and cohesive zone method (CZM) that provides an accurate and computationally inexpensive solution for better proppant tracking and an improved hydraulic fracturing design. The fracture propagation using XFEM and CZM models the rock as a ductile material and overcomes the limitation of the existing fracture propagation models that use LEFM and assumes rock as a brittle material and neglect plastic deformations. The CFD, coupled with XFEM approach, offers the advantage of modelling the fracture propagation and investigate the accurate fluid flow and proppant concentration distribution, which may be challenging to obtain experimentally. The proposed three-dimensional integrated fluid flow, proppant transport and fracture propagation model can accurately model the fluid-proppant, proppant-proppant and fracture wall interactions with

varying fluid, proppants and geomechanical parameters and fluid leak-off effects which will be described in the following chapters.

2.8 Contribution to knowledge

In order to fill some of the research gap identified from the literature review, an attempt has been made in this research to couple the fluid flow with proppant transport in fractures and fracture rock mechanics using numerical methods and contribute to enhancing the knowledge of the mechanical attributes of porous rock under intense injection conditions during the hydraulic fracturing mechanism. The present study models the effect of dynamic fluid leak-off from the fracture wall in the proppant hydrodynamics in order to accurately simulate the proppant transport in hydraulic fractures. Additionally, the present study proposes a 3D proppant transport model that captures the proppant physics in rough fractures using Joint Roughness Coefficient with detailed proppant-wall and inter-proppant interactions in order to improve the hydraulic fracturing design. Finally, the present study couples the fluid flow and proppant transport with the dynamic fracture propagation using CFD-XFEM method to track the proppants accurately and dynamically simulate the realistic phenomenon for an improved hydraulic fracturing design. The existing fracture propagation models use LEFM that assumes rock as a brittle material and neglect plastic deformations. However, some of the rocks are ductile in nature, for instance, shales that show plastic deformation which can be modelled using the XFEM and CZM.

A common failure in hydraulic fracturing design noticed in the oil industry is fracture tip screen out. This happens when proppant in fracturing fluid, create a bridge inside the fracture and prevents any further transport of proppant and fluid, resulting in a rapid increase in pump pressure. Using advanced numerical models like the one proposed in the current study can aid in designing prevention of the fracture tip screen out and model accurately proppant transport physics with dynamic fracture propagation. Furthermore, the numerical modelling results in this research suggests that the reservoir characteristics and flow properties can significantly influence the fracture initiation, fracture length, fracture width and proppant distribution inside the fracture. The coupled phenomenon of fluid flow, fracture propagation, proppant transport, fluid leakage, complex fluid-proppant and inter-proppant interactions can greatly influence the geomechanical stresses in the vicinity of the wellbore. This complex fracture mechanics and hydrodynamics of proppants cannot be modelled using analytical solutions or linear elastic models. Thus, the applicability of the proposed dynamic fracture propagation and fluid flow model with proppant transport and fluid leakage can help petroleum engineers to design the hydraulic fracturing operation with fewer limiting assumptions successfully.

Chapter 3: Methodology

Hydraulic fracturing consists of four main processes: (1) the fracture initiation; (2) the fluid flow within the fracture; (3) the fracture growth and propagation; (4) the fluid leak-off from the fracture into the rock formation (Chen et al. 2009). Thus, the success of a hydraulic fracturing job depends on the accurate design and modelling of an integrated multiphysics phenomenon of fluid flow, proppant transport and fracture propagation. The hydrodynamics of proppant transport is modelled using the computational fluid dynamics and the fracture propagation is modelled using the extended finite element method. The methodology for the computational fluid dynamics and the extended finite element method is discussed in the following sections.

3.1 Computational Fluid Dynamics Methodology

Computational fluid dynamics (CFD) is the branch of fluid mechanics that involves numerically solving a wide range of engineering problems related to fluid flow, the interaction of fluids, heat transfer and related phenomena (Versteeg and Malalasekera 2007). The numerical solutions to the fluid flow engineering problems using CFD mainly involve three steps. The first step consists of pre-processing that involves creating the relevant geometry, generating the appropriate mesh, and specifying boundary conditions to capture the correct physics. The second step is the solution that involves the formulation of the partial differential equations (PDE) that govern the flow based on the conservation laws. It also includes specifying the appropriate numerical method to obtain a solution. The final step is post-processing that involves using the results to analyse the solution (Issa and Oliveira 1993, Xu and Subramaniam 2010).

Depending on the engineering problem, the flow simulation can involve single-phase flow or multiphase flow. The term phase refers to the different physical state of matter, for instance solid, liquid and gas. Some of the examples of multiphase flow are the mixture flow of liquid-solid, gas-liquid, gas-solid or liquid-gas-solid (Blazek 2015). Furthermore, most of the flow phenomenon encountered in engineering applications become unstable above a certain Reynolds number (Re) (Ferziger and Perić 2002). The Reynolds number is the ratio of inertial forces to viscous forces within a fluid and is given by Eq. 3.1.

$$Re = \frac{\rho v L_s}{\mu} \tag{3.1}$$

Where v and L_s are the characteristic velocity and length scales of the mean flow respectively, ρ is the density of the fluid and μ is the dynamic viscosity of the fluid.

The Reynolds number helps predict flow patterns in different fluid flow situations (Blazek 2015). Laminar flow occurs at low Reynolds numbers (Re < 2300), where viscous forces are dominant, and is characterized by smooth, constant fluid motion (Choban et al. 2004). Turbulent flow occurs at high Reynolds numbers (Re > 4000) and is dominated by inertial forces, which tend to produce chaotic eddies, vortices and other flow instabilities (Ferziger and Perić 2002). For fluid flow in a fracture which is a rectangular flow channel and has a rectangular inlet cross-sectional area, the length scale in Eq. 3.1 is given by hydraulic diameter (D_H) and is defined as follows-

$$D_H = \frac{4A}{P_w} \tag{3.2}$$

Where A is the cross-sectional area, and P_w is the wetted perimeter. For a rectangular flow channel with fracture height 0.5 m and fracture width 0.005 m, the D_H equals 9.9×10^{-3} m. Thus, for the fluid density of 1000 kg/m^3, the fluid velocity of 0.5 m/s and fluid viscosity of 0.001 Pa.s, the Re in the present study is 4950, suggesting the nature of flow as turbulent. The range of Re in the present study based on the fluid velocity range of 0.1 m/s – 1 m/s is 990 – 9900 that indicates for the lower fluid velocity (0.1 m/s) the flow is laminar in nature, and as the fluid velocity increases the nature of flow transitions to turbulent flow.

The visualisations of turbulent flow reveal rotational flow structures, called as turbulent eddies, with a wide range of length scales. The largest turbulent eddies interact with and extract energy from the mean flow by a process called vortex stretching (Versteeg and Malalasekera 2007). The large eddies are dominated by inertia effects and viscous effects are negligible. The stretching work done by the mean flow on the large eddies provides the energy which maintains the turbulence (Chung 2010). The smaller eddies are themselves stretched strongly by larger eddies and more weakly with the mean flow. In this way, the kinetic energy is handed down from the larger eddies to progressively smaller and smaller eddies, which is called energy cascading (Sinha 2013). The fluctuating properties of turbulent flow contain energy across a wide range of frequencies or wavenumber and can be explained in terms of energy spectrum or energy cascade diagram which is a plot of spectral energy (kinetic energy per unit mass per unit wavenumber of fluctuation) against wavenumber (Versteeg and Malalasekera 2007). The energy cascade diagram shows that the larger eddies have a low wavenumber and are most energetic. They acquire the energy through strong interactions with the mean flow. This region is called the energy-containing region and eddies here can be represented with the integral scale (Ferziger and Perić 2002). The integral scale can be expressed in terms of kinetic energy and the rate of energy dissipation of a turbulent flow. On the contrary, the spectral energy rapidly decreases as the wavenumber increases. The smaller eddies have a high wave number and lowest energy content. This region is called the dissipation region (Sagaut and Cambon 2008). In the smallest scales

present in the turbulent flow, the inertia and viscous effects are of equal strength, and these scales are named as Kolmogorov scales. The Reynolds number of the smallest eddies based on their characteristic velocity and characteristic length is equal to 1. At the Kolmogorov scales, the energy associated with small scale eddy motion is dissipated and converted into thermal internal energy (Versteeg and Malalasekera 2007). The Kolmogorov scales can be expressed in terms of the rate of energy dissipation of turbulent flow and the fluid viscosity, which is based on the theory that in every turbulent flow the rate of production of turbulent energy has to be in balance with its rate of dissipation. Kolmogorov further proposed that at high mean flow Reynolds number the smallest eddies in a turbulent flow are isotropic in nature, whereas the largest eddies are anisotropic (means the fluctuations are different in different directions) (Peinke et al. 2006). The region in between the energy-containing region and dissipation region is called as inertial subrange region where the size of eddies are intermediate between the large scales and Kolmogorov scales (Versteeg and Malalasekera 2007). Most of the energy transfer from the large size eddies to the smaller size eddies occur in this region. Kolmogorov calculated that the gradient of the line in the energy spectrum diagram against the wavenumber for inertial subrange to be -5/3 (Sagaut and Cambon 2008). A detailed description of the length, time and velocity scales for all the regions in the energy spectrum diagram can be found in Ferziger and Perić (2002) and Versteeg and Malalasekera (2007).

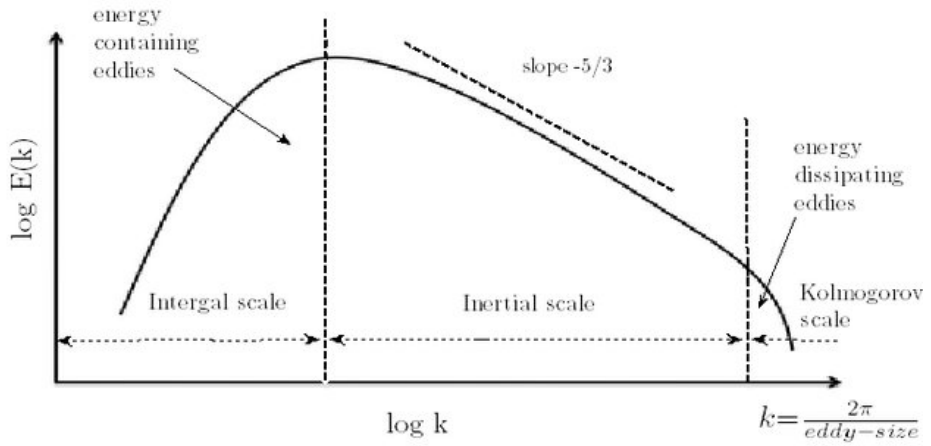

Figure 3.1 Energy spectrum of turbulence (Sinha 2013)

Different methods in CFD are available to resolve the chaotic nature of turbulent flow and velocity fluctuations. The highly accurate method that resolves the entire scale of velocity fluctuations is called direct numerical simulation (DNS) (Elghobashi 1991). However, this method is computationally costly which makes it unsuitable for the practical engineering problems (Moukalled, Mangani and Darwish 2016). Often it is not necessary to predict the detailed flow information of entire turbulence scale in most engineering applications (Drew 1983). The averaging methods are used to average the flow equations and obtain the solution. However, the averaging procedure introduces additional unknown variables in the equations, which necessitate a turbulence model for a solution to be feasible (Versteeg and Malalasekera 2007). This method is known as the Reynolds-averaged Navier-Stokes (RANS) approach for modelling turbulent flows. The RANS method is computationally efficient. It is possible to adopt a coarser mesh structure and a larger time step in the numerical simulation (Jakobsen 2014).

3.2 Multiphase flow modelling methods

Modelling turbulent multiphase flow introduces several challenges compared to single-phase flow. Some of the most demanding problems in multi-phase flow modelling are the effective resolution of fluid turbulence and the simulation of inter-phase interaction (Tryggvason et al. 2001, Ishii and Hibiki 2011). Based on the nature of the multiphase flow, different numerical modelling methodology is used and no general workflow is available (Van Wachem and Almstedt 2003).

The numerical approaches are generally classified into two reference frames for the modelling of solid-liquid multiphase flow. These model frameworks are the Eulerian-Lagrangian model and the Eulerian-Eulerian model approach. In the present research, three different numerical modelling techniques are used to study proppant transport and distribution in hydraulic fractures, namely Eulerian-Granular model, Computational Fluid Dynamics – Discrete Element Model (CFD-DEM), and the DDPM model. The governing equations of all three methods are described in the following sections. The key objective in the present study is to provide a detailed understanding of the proppant transport considering the effect of fluid leak-off from the fracture wall in a planar fracture in the unconventional reservoir.

3.2.1 Eulerian-Granular model

The Eulerian-Granular model is a multiphase flow model in which both phases are defined as a continuous phase. This means the flow governing equations (continuity and momentum equations) are solved separately for each phase. The primary phase is fluid, and the second phase

is defined as granular phase (solid phase). The particle-particle collision or inter-particle interaction is explicitly modelled using a collision model, kinetic theory of granular flow and frictional models (Reuge et al. 2008, Kong, McAndrew and Cisternas 2016). The particle-fluid interaction is defined by interphase exchange coefficients and is modelled using the empirical models (Burns et al. 2004, Reuge et al. 2008, Kong, McAndrew and Cisternas 2016). The governing momentum equation for the granular phase includes additional terms to define the properties for granular flow such as solid pressure and solid stress tensor terms from the application of the kinetic theory of granular flow (Savage and Jeffrey 1981, Jenkins and Savage 1983). The fluctuating velocity of the particles is modelled by solving an additional transport equation for the kinetic energy of particles known as the granular energy transport equation. A key parameter in the granular energy transport equation is granular temperature that represents the particle velocity fluctuations and provides a measure of the kinetic energy associated with solid particles velocity fluctuations, described in detail in section 3.2.1.6. In Eulerian-Granular model, the volume fraction is used as a parameter to determine how much each phase is present in a control volume.

3.2.1.1 Flow governing equations

The governing equations that refer to the equation of conservation of mass and momentum for granular-liquid coupled flow are described below. The equations are based on an assumption of isothermal and incompressible condition for the fracturing fluid. The derivation of the conservation equations can be done by the local instantaneous balance for each of the phases. The detailed derivation of these equations can be found in Anderson and Jackson (1967), Banerjee and Chan (1980), Versteeg and Malalasekera (2007) and Jakobsen (2014).

The mass conservation equation is given by:

$$\rho_i\left(\frac{\partial}{\partial t}\alpha_i + \nabla.\alpha_i\vec{v}_i\right) = 0 \tag{3.3}$$

Where α represents volume fraction, ρ refers to the density, $\vec{v}_i$ refers to instantaneous velocity vector and subscript i refers to phase (liquid or solid). The volume fraction represents the space occupied by each phase, and the laws of conservation of mass (Eq. 3.3) and momentum (Eq. 3.5 and Eq. 3.7) are satisfied by each phase individually. The volume fraction equation is given by Eq. (3.4).

$$\sum_{j=1}^{n} \alpha_j = 1 \tag{3.4}$$

Where n is the total number of phases. In the present study, since there are two phases, solid and liquid, thus n=2.

For the fracturing fluid, the conservation of momentum equation is given by Eq. (3.5)

$$\frac{\partial}{\partial t}(\alpha_l \rho_l \vec{v}_l) + \nabla.(\alpha_l \rho_l \vec{v}_l \vec{v}_l) = -\alpha_l \nabla p + \nabla.\bar{\bar{\tau}}_l + \alpha_l \rho_l g + \overrightarrow{M}_{ls} + S_u \tag{3.5}$$

Where g refers to acceleration due to gravity, the subscript l and s refers to liquid and granular phase respectively, S_u refers to the momentum source term and $\bar{\bar{\tau}}_l$ is the liquid phase stress-strain tensor given by Eq. (3.6).

$$\bar{\bar{\tau}}_l = \alpha_l \mu_l \left(\nabla \vec{v}_l + \nabla \vec{v}_l^{\,T}\right) + \alpha_l (\lambda_l - \frac{2}{3}\mu_l) \nabla.\vec{v}_l \bar{\bar{I}} \tag{3.6}$$

Where λ_l and μ_l refer to the bulk viscosity and dynamic viscosity of continuous phase (fracturing fluid) respectively. The superscript T refers to a transpose of the matrix.

The term $\overrightarrow{M_{ls}}$ in Eq. (3.5) refers to the interfacial momentum exchange between the fluid and granular phase and can be defined by Eq. (3.7). Burns et al. (2004) described that due to the fracturing fluid velocity variation, the motion of granular phase is changed due to the transfer of momentum between the two phases. It is given by Eq. (3.7), where the interfacial momentum exchange between fluid and granular phase can be defined as a combination of the drag force term $\vec{F}_{drag}$, lift force term $\vec{F}_l$ and virtual mass force term $\vec{F}_{vm}$.

$$\overrightarrow{M}_{ls} = \vec{F}_{drag} + \vec{F}_l + \vec{F}_{vm} \tag{3.7}$$

The drag force $\vec{F}_{drag}$ defines the momentum exchange between the solid and liquid phase and is explained in section 3.2.1.2. The lift force is because of the fluid velocity gradient and captures the shearing effect of fluid on the particle.The virtual mass force refers to the force required to accelerate the fluid surrounding the particle (Sankaranarayanan et al. 2002). Issa and Oliveira (1993) and Ekambara et al. (2009) concluded in their study that the lift and virtual mass forces are negligible when the ratio of granular density to fluid density is greater than 1. Thus, only the effect of the drag force is accounted for in this study.

For the granular phase, the conservation of momentum equation is given by Eq. (3.8)

$$\frac{\partial}{\partial t}(\alpha_s \rho_s \vec{v}_s) + \nabla.(\alpha_s \rho_s \vec{v}_s \vec{v}_s) = -\alpha_s \nabla p + \nabla.\bar{\bar{\tau}}_s + \alpha_s \rho_s g + \vec{M}_{sl} \tag{3.8}$$

Where $\overline{\overline{\tau_s}}$ refers to the stress-strain tensor for granular phase, explained in section 0, and $\vec{M}_{sl}$ refers to the interfacial momentum exchange between granular and fluid phase, and is equal in magnitude to $\vec{M}_{ls}$, defined by Eq. (3.7), but opposite in direction.

3.2.1.2 Drag force modelling

The drag force represents the momentum exchange between the phases due to the randomness or disturbance created by each phase. The drag force is described by the Eq. (3.9). Numerous drag force models are available for multiphase flow modelling that differs in the definition of inter-phase momentum exchange coefficient, K_{ls} or K_{sl}.

$$\vec{F}_{drag} = K_{ls}(\vec{v}_l - \vec{v}_s) \tag{3.9}$$

$\vec{v_l} - \vec{v_s}$ is the relative velocity between the phases. Gidaspow (1994) proposed a drag force model which provides the flexibility to use it for a wide application range based on the proppant volume fraction. Gidaspow drag model is a combination of Wen and Yu (1966) drag model and Ergun (1952) drag model. Wen and Yu (1966) proposed a drag model based on the extensive experimental study by Richardson and Zaki (1954) who investigated the solid-liquid interactions in detail and is applicable for the dilute system. Ergun drag model is derived for dense bed and relates to the drag of pressure drop through porous media. At low particle concentration, the Gidaspow drag model acts as Wen and Yu model and at higher particle concentration, it follows the Ergun equation. Thus, the Gidaspow drag model is preferred when a diverse range of solid phase volume fraction is present in the computational domain and the viscous forces dominate the flow. In the current context of proppant transport in hydraulic fracture, a wide range of volume fraction of dispersed proppant can be present in the fracturing fluid slurry, which makes the Gidaspow drag model appropriate for the analysis. Furthermore, Gidaspow drag model has been widely used in the literature for modelling proppant transport in hydraulic fractures (Zhong et al. 2015, Zhang, Li and Gutierrez 2016, Tebowei 2017, Li, Zhang and Lu 2018). Gidaspow drag model is used in the present study as described by Eq. (3.10):

$$K_{sl} = \begin{cases} 150\dfrac{\alpha_s(1-\alpha_l)\mu_l}{\alpha_l d_s^2} + 1.75\dfrac{\rho_l\alpha_s|\vec{v}_s - \vec{v}_l|}{d_s} & \text{if } \alpha_s > 0.2 \\ \dfrac{3}{4}C_D\dfrac{\rho_l\alpha_s\alpha_l|\vec{v}_s - \vec{v}_l|}{d_s}\alpha_l{}^{-2.65} & \text{if } \alpha_s < 0.2 \end{cases} \tag{3.10}$$

Where d_s represents the granular phase diameter and C_D refers to the drag coefficient and calculated by Eq. (3.11).

$$C_D = \begin{cases} \dfrac{24}{\alpha_l.Re_s}[1 + 0.15(\alpha_l.Re_s)^{0.687}] & \text{if } \alpha_l.Re < 1000 \\ 0.44 & \text{if } \alpha_l.Re > 1000 \end{cases} \tag{3.11}$$

Where α_s represents the solid phase volume fraction and can vary from 0-0.63, with 0.63 being the maximum volume fraction or packing limit for the solid phase. α_l represents the liquid phase volume fraction and can vary from 0.37-1. Re_s refers to the Reynolds number of the granular phase and calculated by (3.12).

$$Re_s = \frac{\rho_l d_s|\vec{v}_s - \vec{v}_l|}{\mu_l} \tag{3.12}$$

3.2.1.3 Turbulent dispersion force

Post-injection of the proppants in the hydraulic fractures, the proppant concentration or distribution will vary depending upon the amount of proppant deposition and in suspension. When particles enter a turbulent eddy, it tries to follow it for the time it is crossing the eddy. This effect leads to lateral dispersion, which can be characterized by turbulent dispersion force and is vital to be considered in numerical modelling (Burns et al. 2004, Tebowei 2017).

The interphase momentum exchange is characterized by the drag model as shown in Eq. (3.9), but it fails to account for the effect of turbulent dispersion of the particle phase due to transport by turbulent fluid motion. Burns et al. (2004) described that in order to include turbulent dispersion force, drift velocity can be used that is a result of solid-liquid interaction. The double time-averaging process was proposed to incorporate drift velocity that accounts for the turbulence dispersion force as shown in Eq. (3.13).

$$K_{ls}(\vec{v}_l - \vec{v}_s) = K_{ls}(\vec{V}_l - \vec{V}_s) - K_{ls}\vec{\upsilon}_{dr} \tag{3.13}$$

Where $\vec{\upsilon}_{dr}$ is the drift velocity, $K_{ls}(\vec{V}_l - \vec{V}_s)$ corresponds to the drag force. The term $K_{ls}\vec{\upsilon}_{dr}$ is the turbulent dispersion force. Thus, it can be noted from Eq. (3.13) that mathematically, the turbulent dispersion force adds as a correction to the drag force equation. The drift velocity that corresponds to the turbulence dispersion of solid phase due to velocity fluctuations can be calculated using the Simonin and Viollet (1990) model, described in Eq. (3.14).

$$\vec{\upsilon}_{dr} = D_s\left(\frac{\nabla\alpha_s}{\alpha_s} - \frac{\nabla\alpha_l}{\alpha_l}\right) \tag{3.14}$$

Where $\nabla\alpha_s$and $\nabla\alpha_l$ are the solid phase and liquid phase fluctuations in concentration respectively. D_s corresponds to the dispersion tensor that accounts for the turbulent characteristics of the two phases. D_s can be defined based on the turbulent kinetic energy of the dispersed phase and the ratio of characteristic time of the dispersed phase to the characteristic time of the turbulent eddies, given by Eq. (3.83) in turbulence modelling section 3.2.3.2. A detail derivation of the dispersion tensor can be found in Mudde and Simonin (1999). The equation for the turbulent dispersion force can be written as:

$$F_d = K_{ls}\frac{D_s}{\sigma_{sl}}\left(\frac{\nabla\alpha_s}{\alpha_s} - \frac{\nabla\alpha_l}{\alpha_l}\right) \tag{3.15}$$

Where σ_{sl} is the dispersion Prandtl number and is equal to 0.75 (Tebowei 2017).

3.2.1.4 Stress model for the proppant phase

Savage and Jeffrey (1981) described that the solid stress for the granular phase, $\overline{\overline{\tau_s}}$ (in Eq. (3.8)) is based on the kinetic theory of granular flow (KTGF) models as expressed in Eq. (3.16)

$$\overline{\overline{\tau}}_s = (-P_s + \alpha_s\lambda_s\nabla.\vec{v}_s)\overline{\overline{I}} + \alpha_s\mu_s\left\{[\nabla\vec{v}_s + (\nabla\vec{v}_s)^T] - \frac{2}{3}(\nabla.\vec{v}_s)\overline{\overline{I}}\right\} \tag{3.16}$$

Where $\lambda_s$and μ_s refer to the bulk viscosity and dynamic viscosity of the granular phase respectively, p_s refers to granular phase pressure and $\overline{\overline{I}}$ is the unit tensor.

3.2.1.5 Granular phase pressure model

Granular phase pressure, P_s, is a function of normal force due to particles motion and can be calculated using a correlation from Lun et al. (1984) given by Eq. (3.17). For the granular flow, the granular phase pressure is used in the momentum conservation equation in the form of the granular phase pressure gradient. The granular phase pressure is composed of two parts. The first

part is the kinetic part which is due to the velocity fluctuations and the second part is the collisional part which is due to the inter-proppant collision.

$$P_s = \rho_s \alpha_s \Theta_s + 2\rho_s \alpha_s^2 \Theta_s (1+\eta) g_{0,ss} \tag{3.17}$$

Where η refers to the restitution coefficient from particles collision. The restitution coefficient varies from 0 to 1 for a perfectly elastic collision to a perfectly inelastic collision. The value of the restitution coefficient assumed in the current study is 0.9. The integration between the kinetic part and the collisional part is employed using the radial distribution function, $g_{0,ss}$. The radial distribution function governs the transition from compressible nature of flow to incompressible nature of flow in terms of proppant phase volume fraction and proppant spacing. Lun et al. (1984) proposed the radial distribution function can be calculated using Eq. (3.18)

$$g_{0,ss} = \left[1 - \left(\frac{\alpha_s}{\alpha_{s,max}}\right)^{\frac{1}{3}}\right]^{-1} \tag{3.18}$$

Where, $\alpha_{s,max}$ is the maximum volume fraction or packing limit and a value of 0.63 is used for mono-dispersed particles. The radial distribution function is a correction factor that modifies the probability of collision between the proppants when the proppant phase becomes dense. This can also be interpreted as a non-dimensional distance between the spheres (Gidaspow 1994).

3.2.1.6 Granular temperature

Granular temperature is one of the vital parameters in the granular phase stress model or the granular phase pressure model that are based on KTGF. The particle velocity is decomposed into a mean local velocity and a superimposed fluctuating random velocity. The granular temperature is associated with the random fluctuation velocity. The granular temperature is a quantity that is proportional to the square of the random particle velocity fluctuations about the mean (Biggs et al. 2008). The granular temperature provides a measure of the kinetic energy associated with solid particles velocity fluctuations that aids in the calculation of granular phase stress. The velocity fluctuations of particles are much smaller than their mean velocity and the velocity fluctuations of particles dissipate into heat rather fast as a result of the inter-particle collision (Goldhirsch 2008). Thus, the granular temperature can be referred to as a by-product of flow and defined using Eq. (3.19). It can be obtained by solving an additional transport equation derived from the kinetic theory and known as the granular energy transport equation as shown in Eq. (3.20).

$$\Theta_s = \frac{1}{3}\langle \upsilon_s^2 \rangle \tag{3.19}$$

$$\frac{3}{2}\left[\frac{\partial}{\partial t}(\alpha_s \rho_s \Theta_s) + \nabla \cdot (\alpha_s \rho_s \Theta_s)\vec{v}_s\right] = \left(-P_s\bar{\bar{I}} + \bar{\bar{\tau}}_s\right) : \nabla\vec{v}_s + \nabla \cdot \left(k_{\Theta_s}\nabla\Theta_s\right) - \gamma_{\Theta_s} + \Phi_{ls} \tag{3.20}$$

Where Θ_s, α_s and υ_s refers to the granular temperature, granular phase volume fraction and velocity fluctuation of granular phase respectively. The term $\left(-P_s\bar{\bar{I}} + \bar{\bar{\tau}}_s\right) : \nabla\vec{v}_s$ corresponds to the generation of energy by the solid stress tensor and $k_{\Theta_s}\nabla\Theta_s$ corresponds to the diffusion of energy. k_{Θ_s} is the diffusion coefficient which can be calculated using Eq. (3.21). γ_{Θ_s} represents the rate of energy dissipation within the particle phase due to inter-particle collision and can be calculated using Eq. (3.22). Φ_{ls} represents the transfer of the kinetic energy of random fluctuations in particle velocity from the solids phase to the fluid or solid phase and is given by Eq. (3.23).

$$k_{\Theta_s} = \frac{150\rho_s d_s\sqrt{\Theta_s \pi}}{384(1+\eta)g_{0,ss}}\left[1 + \frac{6}{5}\alpha_s g_{0,ss}(1+\eta)\right]^2 + 2\rho_s {\alpha_s}^2 d_s g_{0,ss}(1+\eta)\sqrt{\frac{\Theta_s}{\pi}} \tag{3.21}$$

$$\gamma_{\Theta_s} = \frac{12(1-\eta^2)g_{0,ss}}{d_s\sqrt{\pi}}\rho_s {\alpha_s}^2 \Theta_s^{3/2} \tag{3.22}$$

$$\Phi_{ls} = -3K_{ls}\Theta_s \tag{3.23}$$

3.2.1.7 Granular bulk viscosity

The granular bulk viscosity denoted by λ_s in Eq. (3.16) is used to calculate the resistance of the granular particles against compression and expansion. Lun et al. (1984) proposed a model to calculate the granular bulk viscosity, as shown in Eq. (3.24).

$$\lambda_s = \frac{4}{3}\alpha_s \rho_s d_s g_{o,ss}(1+\eta)\left(\frac{\Theta_s}{\pi}\right)^{\frac{1}{2}} \tag{3.24}$$

3.2.1.8 Granular shear viscosity

During the proppant transport with the fracturing fluid in the form of a slurry, the proppant undergoes through different types of complex interactions. This complex interaction can be characterized by the granular shear viscosity. The granular shear viscosity is used to model the particle-fluid and particle-particle interaction. The granular shear viscosity is composed of three elements, namely kinetic viscosity $\mu_{s,kin}$, collisional viscosity $\mu_{s,col}$ and frictional viscosity $\mu_{s,fr}$, Eq. (3.25). The kinetic viscosity defines the instantaneous motion of the proppants at different

flow regimes. The collisional viscosity defines the rebounding of proppant post-collision. Furthermore, the frictional viscosity defines the frictional interaction between the proppant phases upon forming of the proppant bed. Once the proppant deposits at the fracture bottom, the frictional forces become dominant. The packing limit for the mono-dispersed size proppants when the frictional forces become dominant is approximately 0.5 (Makkawi, Wright and Ocone 2006).

$$\mu_s = \mu_{s,kin} + \mu_{s,col} + \mu_{s,fr} \tag{3.25}$$

The kinetic viscosity, collisional viscosity, and frictional viscosity can be calculated using the correlations proposed by Gidaspow, Bezburuah and Ding (1991), Gidaspow (1994) and Johnson and Jackson (1987) respectively given in Eq. (3.26), Eq. (3.27) and Eq. (3.28).

$$\mu_{s,kin} = \frac{10\rho_s d_s\sqrt{\Theta_s \pi}}{96\,\alpha_s g_{0,ss}(1+\eta)}\left[1 + \frac{4}{5}\alpha_s g_{0,ss}(1+\eta)\right]^2 \tag{3.26}$$

$$\mu_{s,col} = \frac{4}{5}(1+\eta)\rho_s \alpha_s d_s g_{0,ss}\left(\frac{\Theta_s}{\pi}\right)^{\frac{1}{2}} \tag{3.27}$$

$$\mu_{s,fr} = \frac{P_{sf}\sin\theta}{2\sqrt{I_D}} \tag{3.28}$$

Where θ refers to the friction angle, P_{sf} refers to the friction pressure and I_D is the deviatoric stress tensor. The friction forces, that drive the frictional pressure, become dominant when the effective volume fraction of proppant gets approximately 0.5. Johnson and Jackson (1987) proposed that the friction pressure can be calculated by Eq. (3.29)

$$P_{sf} = F_r \frac{(\alpha_s - \alpha_{s,min})^n}{(\alpha_{s,max} - \alpha_s)^p} \tag{3.29}$$

Where $\alpha_{s,max}$ is the maximum packing limit, $\alpha_{s,min}$ is the volume fraction when the frictional forces become dominant, $F_r = 0.1\alpha_s$. The exponents n and p are constants and the value equal 2 and 5 respectively.

3.2.2 Computational Fluid Dynamics - Discrete Element Model (CFD-DEM)

CFD-DEM is based on Eulerian-Lagrangian method as explained earlier. Unlike other Eulerian-Lagrangian methods, for instance, Discrete Phase Model (DPM) which is applicable only for the low volume fraction of particles (<10%), the Discrete Element Method (DEM) can be used when the higher volume fraction of particles is present (10% - 63%). Thus, CFD-DEM can accurately model the multiphase flow where the inter-particle interaction is imperative, such as proppant flow in the fracturing fluid (Deng et al. 2014). Cundall and Strack (1979) proposed the DEM method, and it was later coupled with CFD by other researchers to study fluid-solid flow modelling (Zhang, Li and Gutierrez 2016). In this approach, the primary phase is solved using a conventional Eulerian method meaning continuity and momentum equations are solved using CFD. However, the solid phase is solved using DEM by tracking every dispersed particle; thus, it is a computationally expensive technique (Wu and Sharma 2016). Particles are tracked by calculating and tracking the mass, velocity, and forces acting on a particle using Newton's second law of motion. This is referred to as tracking in the Lagrangian frame in the DEM method (Zhang, Gutierrez and Li 2017). Finally, the drag forces and interphase momentum exchange terms are used to model the interaction, energy dissipation and coupling of both the phases, i.e., continuous and discrete phases. As mentioned earlier in section 2.4.2 that the particles are assumed as rigid, and in order to account for accurate particle micro-mechanics and particle collision, it is further assumed that after the collision, the two particles deform and defined by the overlap displacement of the particles. This approach is called the soft-sphere approach that outlined an accurate contact model and is explained in section 3.2.2.2.

3.2.2.1 The governing equations for the particles

The distribution of discrete phase particle motion is calculated by integrating the force balance on the particle, which is written in a Lagrangian reference frame. Using Newton's second law of motion, the governing equations of the particle motion can be defined as follows:

$$m\frac{d\overrightarrow{v_p}}{dt} = \vec{F}_{drag} + \vec{F}_{gravitation} + \vec{F}_{other} \tag{3.30}$$

$$\frac{dx_p}{dt} = \overrightarrow{v_p} \tag{3.31}$$

The above equations can be re-written in the following form as

$$\frac{d\overrightarrow{v_p}}{dt} = \frac{\overrightarrow{v_l} - \overrightarrow{v_p}}{\tau_r} + \frac{g(\rho_p - \rho)}{\rho_p} + \vec{F}_{other} \tag{3.32}$$

The velocity and spatial location of discrete particles are calculated using Eq. (3.30) and Eq. (3.31) respectively. The term $\vec{F}_{other}$ refers to other forces such as forces of the collision, cohesion, electrostatic forces, lift forces, magnetic forces and virtual mass forces. The collision model is described in the next section and the forces of cohesion, electrostatic forces, lift forces, magnetic forces and virtual mass forces are not considered in the present study as explained earlier. The variable τ_r is the droplet or particle relaxation time is given by

$$\tau_r = \frac{\rho_p d_p^2}{18\mu} \frac{24}{C_D Re} \tag{3.33}$$

$\frac{\vec{v_l} - \vec{v_p}}{\tau_r}$ is the drag force per unit particle mass, $\vec{v_l}$ and $\vec{v_p}$ is the fluid and particle velocity respectively, μ is the fluid viscosity, ρ and ρ_p are the fluid and particle density respectively, d_p is the particle diameter, and Re is the Reynolds number, defined as

$$Re = \frac{\rho d_p \left|\vec{v_p} - \vec{v_l}\right|}{\mu} \tag{3.34}$$

The Navier-Stokes equations (mass and momentum conservation equations) of the continuous phase are described below:

$$\frac{d\rho\alpha}{dt} + \nabla.(\alpha\rho\vec{v_l}) = 0 \tag{3.35}$$

$$\frac{d(\alpha\rho\vec{v_l})}{dt} + \nabla.(\alpha\rho\vec{v_l}\vec{v_l}) = -\alpha\nabla p + \nabla.\bar{\bar{\tau}} + \alpha\rho\vec{g} + \vec{F} + S_u \tag{3.36}$$

Where S_u refers to the momentum source term and it takes into account the particle motion, $\vec{F}$ represents external body force term, $\bar{\bar{\tau}}$ represents stress tensor, g is the acceleration due to gravity and ρ is the density. In the CFD-DEM method to ensure the numerical stability and converged solution, usually the time step for discrete phase DEM modelling is smaller than continuous phase CFD modelling. This is done to capture the particle micro-mechanics correctly. In the present study, the time step used for the CFD continuous phase flow simulations is 1.0E-3 seconds, and for the discrete phase, DEM simulation is 1.0E-6 seconds, which is three order of magnitude lower. The DEM time step was selected based on the numerical stability and convergence of the solution using the Eq. (3.41), Eq. (3.42) and Eq. (3.44) described in the next section.

3.2.2.2 Collision model

Cundall et al. (1979) proposed the "soft sphere" approach in order to model the collision forces of granular phases in the DEM method. The $\vec{F}_{other}$ term in Eq. (3.30) and Eq. (3.32) accounts for these forces. The granular collision forces are calculated by the deformation, resulting from the overlap between pairs of spheres (Figure 3.2). The spring-dashpot collision model is used in the present study for modelling inter-particle collision.

The force exerted on the proppant due to the collision by another proppant particle is given by Eq. (3.37)

$$\overrightarrow{F_1} = (K\delta + \gamma(\vec{v}_{12}.\vec{e}_{12}))\vec{e}_{12} \tag{3.37}$$

By Newton's third law of motion, the force on the second proppant particle is given by

$$\overrightarrow{F_2} = -\overrightarrow{F_1} \tag{3.38}$$

Where $\vec{e}_{12}$, is the unit vector, γ is the damping coefficient, δ represents the overlap, K represents the spring constant, $\vec{v}_{12}$ is the relative velocity (Issa and Oliveira 1993) and is given by

$$\gamma = -2\frac{m_{12}\ln\eta}{t_{coll}} \tag{3.39}$$

$$\vec{v}_{12} = \vec{v}_2 - \vec{v}_1 \tag{3.40}$$

$$t_{coll} = f_{loss}\sqrt{\frac{m_{12}}{K}} \tag{3.41}$$

$$f_{loss} = \sqrt{\pi^2 + \ln^2\eta} \tag{3.42}$$

$$m_{12} = \frac{m_1 m_2}{m_1 + m_2} \tag{3.43}$$

η is the coefficient of restitution for particles collision, which can vary from 0 to 1 corresponding to from perfectly inelastic to a perfectly elastic collision. The elastic collision with $\eta = 0.9$ is used in this study. K is the spring constant. The spring constant value of 1000 is used in the present study. The particle timestep can be estimated from Eq. (3.44) to get an accurately resolved collision. Thus, the particle time step used was 1.0E-6.

$$\Delta t_p = \frac{1}{20} t_{coll} \tag{3.44}$$

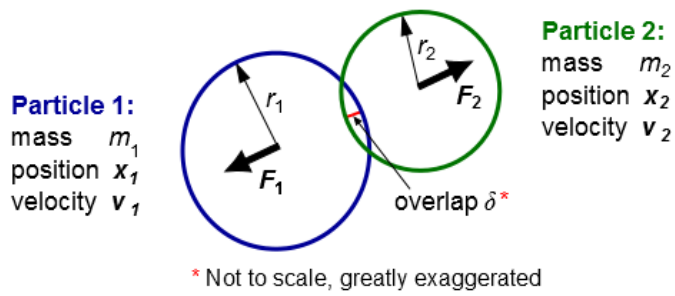

Figure 3.2 Proppant-proppant collision

3.2.3 Dense Discrete Phase Method (DDPM) model

The DDPM model is a subtype of Eulerian-Lagrangian model and combines the advantages of both the models, Eulerian-Granular model and CFD-DEM model. Unlike Eulerian-Granular model, it can take into account the proppant size distribution. The proppant-wall interactions are comprehensively modelled using the reflect boundary condition that models the particles energy and momentum transfer in both normal and tangential direction post-collision. The DDPM model also overcome the limitation of CFD-DEM model that it is computationally cheaper by approximately three times (see appendix C). The DDPM model treats the liquid phase as a continuum by solving the Navier-Stokes equations, while the solid or dispersed phase is modelled by tracking a large number of solid particles using parcel approach as they move through the computational domain. As explained earlier in section 2.5, the parcel is a group of particles based on similar properties like particle diameter, density, and mass flow rate. The proppants are tracked by calculating and tracking the mass, velocity, and forces acting on a particle using Newton's second law of motion. This is referred to as tracking in the Lagrangian frame in the DDPM model. However, the proppants are mapped back to the Eulerian grid. Like CFD-DEM model, the DDPM model can be used for higher volume fraction (10%-63%). The proppant-fluid interaction is modelled using the interphase momentum exchange term, proppant-proppant and proppant-wall interactions are modelled using the application of KTGF. The key objective in the present study is to provide a detailed understanding of the proppant transport considering the effect of fluid leak-off from the fracture wall in a rough fracture geometry in the unconventional reservoir.

3.2.3.1 Flow Governing Equations

Since the DDPM model is a combination of Eulerian-Granular model and CFD-DEM model, some of the governing equations are same as described in the sections 3.2.1 and 3.2.2. However, to explain the governing equations of the DDPM model, the equations previously described will be referenced and only the new equations will be described in this section. The mass conservation equation for the continuous fluid phase and proppant phase based on the volume fraction of the proppants and instantaneous velocity vector is given by Eq. (3.3) as described in section 3.2.1.1. The volume fraction equation is given by Eq. (3.4). For the fracturing fluid, the conservation of momentum equation is given by Eq. (3.5) which is based on the fluid phase stress-strain tensor given by Eq. (3.6) and interphase momentum exchange between the fluid and proppant phase that describes the drag law given by Eq. (3.7) and Eqs. (3.9-3.12). The governing equations of the proppant motion can be defined by Eq. (3.45) using Newton's second law of motion which looks similar to the governing equation of proppants described in Eq. (3.30) except for the term $\vec{F}_{KTGF}$, which refers to inter-particle interaction force from KTGF and can be calculated by Eq. (3.46).

$$m\frac{d\overrightarrow{v_p}}{dt} = \vec{F}_{drag} + \vec{F}_{gravitation} + \vec{F}_{KTGF} \tag{3.45}$$

$$\vec{F}_{KTGF} = -\frac{1}{\alpha_s \rho_s}\nabla.\bar{\bar{\tau}}_s \tag{3.46}$$

The Eq. (3.45) can be re-written in the following form as

$$\frac{d\overrightarrow{v_p}}{dt} = \frac{\overrightarrow{v_l} - \overrightarrow{v_p}}{\tau_r} + \frac{g(\rho_p - \rho)}{\rho_p} + \vec{F}_{KTGF} \tag{3.47}$$

Where $\overline{\overline{\tau_s}}$ refers to the stress-strain tensor for proppant phase and can be calculated based on Eq. (3.16) described earlier in section 0. The variable τ_r is the particle relaxation time and can be calculated based on Eq. (3.33) described earlier in section 3.2.2.1. The drag force modelling, stress terms, granular temperature, granular pressure, and granular shear viscosity equations are as described in section 3.2.1 earlier.

3.2.3.2 Turbulence modelling

Turbulence plays a vital role in the proppant transport phenomenon in hydraulic fractures. Numerous turbulence models are available depending on the flow conditions and nature of randomness or turbulence present (Blazek 2015). The available turbulent models differ by the required number of additional transport equations to be solved, for example- the two-equation models (k−ε, k−ω and k−kl), mixing length model, Reynolds stress model (RSM) and Spalart-Allmaras model (Versteeg and Malalasekera 2007).

Jones and Launder (1972) proposed the standard k−ε turbulence model that is widely used in many practical engineering purposes. However, it applies to a fully developed flow, and provides unreliable results for a variety of flow like near-wall flow, separating flow and adverse pressure gradient flow. On the other hand, the Shear Stress Transport (SST) k-ω turbulence model proposed by (Menter 1993) has the advantage that it shows good behaviour in fully developed flow as well as near-wall flow, adverse pressure gradient and separating flow (Chung 2010). SST k-ω turbulence model blends both k−ε turbulence model and k-ω turbulence model using a blending function and viscosity limiter and provides a much better agreement to experiments with the separated flow (Versteeg and Malalasekera 2007). SST k-ω turbulence model was originally proposed for modelling external aerodynamics flow, but it has also been found to be used in different applications. For modelling solid transport in fluids, the multiphase SST k-ω turbulence model has been widely used in the literature (Bakker, Meyer and Deglon 2009, Nguyen et al. 2014, Alahmadi and Nowakowski 2016, Singh, Kumar and Mohapatra 2017, Zhigarev et al. 2017, Zhang, Wu and Sharma 2019, Yan et al. 2019) which accounts for the fluid phase turbulence effect as well as solid-phase turbulence using turbulent dispersion force as described in the section 3.2.1.3. The Re in the present study is 4950, based on the fluid inlet velocity of 0.5 m/s as mentioned earlier in section 3.1, suggesting the nature of flow as turbulent. The range of Re in the present study based on the fluid velocity range of 0.1 m/s – 1 m/s is 990 – 9900 that indicates for the lower fluid velocity (0.1 m/s) the flow is laminar in nature, and as the fluid velocity increases the nature of flow transitions to turbulent flow. Thus, in the present study, the SST k-ω turbulent dispersed model for modelling the multiphase turbulence of fluid-proppant flow in hydraulic fracture was used and, the corresponding transport equation is given by Eq. (3.48) and Eq. (3.49).

$$\frac{\partial}{\partial t}(\alpha_l \rho_l k_l) + \nabla \cdot (\alpha_l \rho_l k_l \vec{v}_l) = \nabla \cdot \left[\alpha_l \left(\mu + \frac{\mu_{t,l}}{\sigma_k}\right) \nabla k_l\right] + \alpha_l G_{k,l} - \alpha_l \beta^* \rho_l k_l \omega_l + \alpha_l \rho_l \Pi_{kl} \tag{3.48}$$

$$\frac{\partial}{\partial t}(\alpha_l\rho_l\omega_l) + \frac{\partial}{\partial x_i}(\alpha_l\rho_l\omega_l\vec{v}_l) = \nabla\cdot\left[\alpha_l\left(\mu + \frac{\mu_{t,l}}{\sigma_\omega}\right)\nabla\omega_l\right] + \alpha_l G_{\omega,l} - \alpha_l\beta_i\rho_l\omega_l^2 + \alpha_l D_{\omega,l} + \alpha_l\rho_l\Pi_{\omega l} \tag{3.49}$$

Where k represents turbulent kinetic energy, ω represents the specific rate of dissipation, $\vec{v}$ denotes the velocity, α represents the volume fraction, $\mu_{t,l}$ represents the turbulent viscosity and is calculated using Eq. (3.50), the term $G_{k,l}$ describes the production of turbulence kinetic energy and is given by Eq. (3.60), $G_{\omega,l}$ describes the production of ω and can be calculated by Eq. (3.62), $D_{\omega,l}$ serves the cross-diffusion term that plays a vital role in switching between k-ω and k-ε models and can be computed using Eq. (3.72), $\beta^*$and β_i are the constants of the turbulent dissipation term and can be defined by Eq. (3.68) and Eq. (3.69) respectively. Π_{kl} and $\Pi_{\omega l}$ represents the influence of solid phase turbulence on the liquid phase for k and ω, and can be calculated using Eq. (3.70) and Eq. (3.71), respectively. σ_k and σ_ω represents the turbulent Prandtl numbers and can be computed using Eq. (3.51) and Eq. (3.52), respectively.

$$\mu_{t,l} = \frac{\rho_l k_l}{\omega_l}\frac{1}{\max\left[\frac{1}{\alpha^*}, \frac{SF_{2b}}{0.31\omega_l}\right]} \tag{3.50}$$

$$\sigma_k = \frac{1}{\frac{F_{1b}}{1.176} + \frac{1-F_{1b}}{1}} \tag{3.51}$$

$$\sigma_\omega = \frac{1}{\frac{F_{1b}}{2} + \frac{1-F_{1b}}{1.168}} \tag{3.52}$$

Where S is the strain rate magnitude, F_{1b} and F_{2b} are the blending functions and are given by Eq. (3.57) and Eq. (3.53), respectively.

$$F_{2b} = \tanh(\Phi_2^2) \tag{3.53}$$

$$\Phi_2 = \max\left[2\frac{\sqrt{k_l}}{0.09\omega_l y_w}, \frac{500\mu}{\rho y_w^2\omega_l}\right] \tag{3.54}$$

$$\alpha^* = \alpha_\infty^*\left(\frac{\alpha_0^* + Re_t/R_k}{1 + Re_t/R_k}\right) \tag{3.55}$$

$$Re_t = \frac{\rho_l k_l}{\mu\omega_l} \tag{3.56}$$

$$F_{1b} = \tanh(\Phi_1^2) \tag{3.57}$$

$$\Phi_1 = \min\left[\max\left[\frac{\sqrt{k_l}}{0.09\omega_l y_w}, \frac{500\mu}{\rho_l y_w^2 \omega_l}\right], \frac{4\rho_l k_l}{1.168 D_\omega^+ y_w^2}\right] \tag{3.58}$$

$$D_\omega^+ = \max\left[\frac{2\rho_l}{1.168\omega_l}\nabla k_l \nabla\omega_l, 10^{-10}\right] \tag{3.59}$$

Where, α_0^* and $R_k$are constants, $\alpha_0^* = 0.024$. $R_k = 6$. y is the distance to the wall. It is to be noted that in the high-Reynolds number form of the k- ω model, $\alpha^* = \alpha_\infty^* = 1$

The production term for turbulence kinetic energy ($G_{k,l}$) is defined by Eq. (3.60). $G_{k,l}$ can be calculated from Boussinesq hypothesis, which states that $G_{k,l}$ depends on turbulent viscosity, $\mu_{t,l}$ and strain rate, S, as shown in Eq. (3.61).

$$G_{k,l} = -\rho_l \overline{v_i' v_j'} \nabla \vec{v}_l \tag{3.60}$$

$$G_{k,l} = \mu_{t,l} S^2 \tag{3.61}$$

And the production term for ω, $G_{\omega,l}$, is derived by Eq. (3.62):

$$G_{\omega,l} = \frac{\alpha'}{v_t}\widetilde{G_{k,l}} \tag{3.62}$$

$$\widetilde{G_{k,l}} = \min\left(G_{k,l}, 10\rho_l \beta^* k_l \omega_l\right) \tag{3.63}$$

$$\alpha' = \frac{\alpha_\infty}{\alpha^*}\left(\frac{\alpha_0 + Re_t/R_\omega}{1 + Re_t/R_\omega}\right) \tag{3.64}$$

$$\alpha_\infty = F_{1b}\alpha_{\infty,1} + (1 - F_{1b})\alpha_{\infty,2} \tag{3.65}$$

$$\alpha_{\infty,1} = \frac{\beta_{i,1}}{\beta_\infty^*} - \frac{\acute{k}^2}{\alpha_{\omega,1}\sqrt{\beta_\infty^*}} \tag{3.66}$$

$$\alpha_{\infty,2} = \frac{\beta_{i,2}}{\beta_\infty^*} - \frac{\acute{k}^2}{\alpha_{\omega,2}\sqrt{\beta_\infty^*}} \tag{3.67}$$

$$\beta_i = \beta_{i,1} F_{1b} + \beta_{i,2}(1 - F_{1b}) \tag{3.68}$$

$$\beta^* = \beta_\infty^*\left[\frac{4/15 + (Re_t/8)^4}{1 + (Re_t/8)^4}\right] \tag{3.69}$$

Where $\acute{k}$, $\beta_{i,1}$, $\beta_{i,2}$, β_∞^*, $\alpha_{\omega,1}$, $\alpha_{\omega,2}$ and R_ω are constants. $\acute{k} = 0.41$, $\beta_{i,1}$=0.075, $\beta_{i,2}$=0.0828, β_∞^*=0.09 $\alpha_{\omega,1}$=2, $\alpha_{\omega,2}$=1.168 and R_ω=2.95.

The terms Π_{kl} and $\Pi_{\omega l}$ in the Eq. (3.48) and Eq. (3.49), that represents the influence of solid phase turbulence on the liquid phase for k and ω, and can be calculated using Eq. (3.70) and Eq. (3.71) respectively.

$$\Pi_{kl} = \sum_{P=1}^{M} \frac{K_{sl}}{\alpha_l \rho_l} (k_{sl} - 2k_l + \vec{v}_{sl} \cdot \vec{v}_{dr}) \tag{3.70}$$

$$\Pi_{\omega l} = C_{3\omega} \frac{\alpha_l}{k_l} \Pi_{kl} \tag{3.71}$$

Where, k_{sl} is the covariance of velocities of the liquid-phase l and solids-phase s, $\vec{v}_{sl}$ is the relative velocity and $\vec{v}_{dr}$ is the drift velocity.

The cross diffusion term, $D_{\omega,l}$, can be calculated using Eq. (3.72)

$$D_{\omega,l} = \frac{2(1 - F_{1b})\sigma_{\omega,2}\rho_l}{\omega_l} \nabla k_l \nabla \omega_l \tag{3.72}$$

Where $\sigma_{\omega,2}$ is a constant and equals 1.168.

The turbulence in the particle phase is computed as follows:

The characteristic particle relaxation time related to the inertial effect acting on the particle phase is defined as given in Eq (3.73).

$$\tau_{F,sl} = \frac{\alpha_l \rho_l}{k_{sl}} \left(\frac{\rho_s}{\rho_l} + C_V \right) \tag{3.73}$$

The Lagrangian integral time scale calculated along the particle trajectories, mainly affected by the crossing trajectory effect is defined as given in Eq. (3.74)

$$\tau_{t,sl} = \frac{\tau_{t,l}}{\sqrt{1 + c_\beta \xi^2}} \tag{3.74}$$

$$\xi = \frac{|\vec{v}_{sl}| \tau_{t,sl}}{L_{t,l}} \tag{3.75}$$

$$c_\beta = 1.8 - 1.35 \cos^2 \theta_p \tag{3.76}$$

Where θ_p is the angle between the mean particle velocity and the mean relative velocity. The terms $\tau_{t,sl}$ and $\tau_{F,sl}$, represents the time of interaction between solid-particle motion and the liquid-phase fluctuations, and the entrainment of the solid particles by the continuous phase, respectively. $\tau_{t,l}$ is the characteristic time of the turbulent eddies is defined as given in Eq. (3.77) and $L_{t,l}$ is the length scale of the turbulent eddies is defined as given in Eq. (3.78).

$$\tau_{t,l} = \frac{3}{2} \cdot \frac{1}{\omega_l} \tag{3.77}$$

$$L_{t,l} = \sqrt{\frac{3}{2}} \cdot \frac{k_l^{1/2}}{\omega_l} \tag{3.78}$$

The ratio between the two characteristic times, η_{sl} provides a measure of the efficiency of turbulence to entrain solid particles, as given in Eq. (3.79) (Peirano and Leckner 1998, Tebowei 2017).

$$\eta_{sl} = \frac{\tau_{t,sl}}{\tau_{F,sl}} \tag{3.79}$$

The turbulence quantities for the solids-phase are given in Equation (3.80) – (3.84).

$$k_s = k_l \left(\frac{b^2 + \eta_{sl}}{1 + \eta_{sl}} \right) \tag{3.80}$$

$$k_{sl} = 2k_l \left(\frac{b + \eta_{sl}}{1 + \eta_{sl}} \right) \tag{3.81}$$

$$D_{t,sl} = \frac{3}{2} \cdot \frac{1}{\omega_l} \tag{3.82}$$

$$D_s = D_{t,sl} + \left(\frac{2}{3} k_s - b \frac{1}{3} k_{sl} \right) \tau_{F,sl} \tag{3.83}$$

$$b = \frac{(1 + C_V)}{\left(\frac{\rho_s}{\rho_l} + C_V \right)} \tag{3.84}$$

Where C_V is the added mass coefficient and equals 0.5. D_s is the dispersion term which appears in the drift velocity, $\vec{v}_{dr}$ as given in Eq. (3.14) described in section 3.2.1.3.

The drift velocity is computed from Eq. (3.14) when the diffusivities in the liquid and solids phase are assumed to be equal. However, when there exists a significant difference in the diffusivities of the liquid and solids phase, the drift velocity is computed as given in Eq. (3.85).

$$\vec{v}_{dr} = \frac{D_s}{\sigma_{sl}\alpha_s} \nabla \alpha_s - \frac{D_l}{\sigma_{sl}\alpha_s} \nabla \alpha_l \tag{3.85}$$

3.2.4 Selection of Eulerian-Granular model, CFD-DEM model and DDPM model

This section discusses the conditions, limitations and provides suggestions to use the three numerical models discussed in the previous sections for modelling proppant transport in hydraulic fractures.

The Eulerian-Granular model is a reasonable model to simulate the large scale fractures in a computationally efficient manner, but it has the following three limitations as discussed in section 2.4.1. Firstly, only mono-dispersed size proppants can be used in this model. Thus, the calculation of some of the forces that are dependent on the proppant diameter will be inaccurate if multi-size proppant distribution is not used (Subramaniam 2013, Wang 2020). Secondly, the proppant-wall interactions are not modelled in detail in this method unlike the DDPM and CFD-DEM model. The Johnson and Jackson boundary condition method is used to model the particle-wall interaction that uses specularity coefficient and wall restitution coefficient to model the particle-wall interactions. Lastly, the Eulerian-Granular model is not capable of representing the fluxes, associated with two streams of particles moving with different velocities at the same physical location (Subramaniam 2013). Thus when the objective is to have an approximate proppant transport model in hydraulic fracture with uniform size particles and have a quick understanding of the results, the Eulerian-Granular model is recommended.

The CFD-DEM model, on the other hand, uses the Eulerian-Lagrangian method to model the proppant transport and distribution by tracking their trajectories using parcel approach. The particle-particle and particle-wall collisions are modelled using the soft-sphere approach. CFD-DEM model overcomes all the limitations of the Eulerian-granular model in terms of proppant transport dynamics, but it is computationally too expensive to apply it in the large scale fracture. Thus when the objective is to have detailed modelling of proppant dynamics in the laboratory scale fracture models, the CFD-DEM model is recommended.

The DDPM model is another subtype of Eulerian-Lagrangian model. It combines the advantages of both the models, Eulerian-Granular model and CFD-DEM model. It tracks the particle motion using parcel approach similar to CFD-DEM model but used KTGF to model the inter-proppant interactions similar to Eulerian-Granular model. The DDPM model is computationally cheaper than CFD-DEM model (by three times – Appendix C), and can be applicable to the large scale fractures. Thus when the objective is to model the proppant transport with multi-size distribution in a reasonable computational time, the DDPM model is recommended.

3.3 Modelling workflow and simulation parameters:

The CFD modelling of proppant transport in hydraulic fractures was studied using ANSYS FLUENT 18.1. The modelling workflow is shown in Figure 3.3. The first step involves pre-processing, which includes geometry creation and meshing. The second step involves the formulation of the partial differential equations (PDE) that govern the flow based on the conservation laws. It also includes specifying the boundary conditions, fluid and flow properties to capture the correct physics, and defining an appropriate numerical method to obtain the solution. The final step is post-processing that involves using the results to analyse the solution. The modelling workflow along with the simulation parameters used in the study can be summarised in the following steps:

3.3.1 Geometry/Computational domain and Meshing

The hydraulic fracture can be of a variable size from centimetres scale to several meters scale. In the present study, proppant transport and distribution is studied in different fracture geometries (smooth fractures and rough fractures). Thus, detail discussion about the geometry, computational domain, meshing and simulation parameters are discussed in the corresponding chapters 4, 5 and 6.

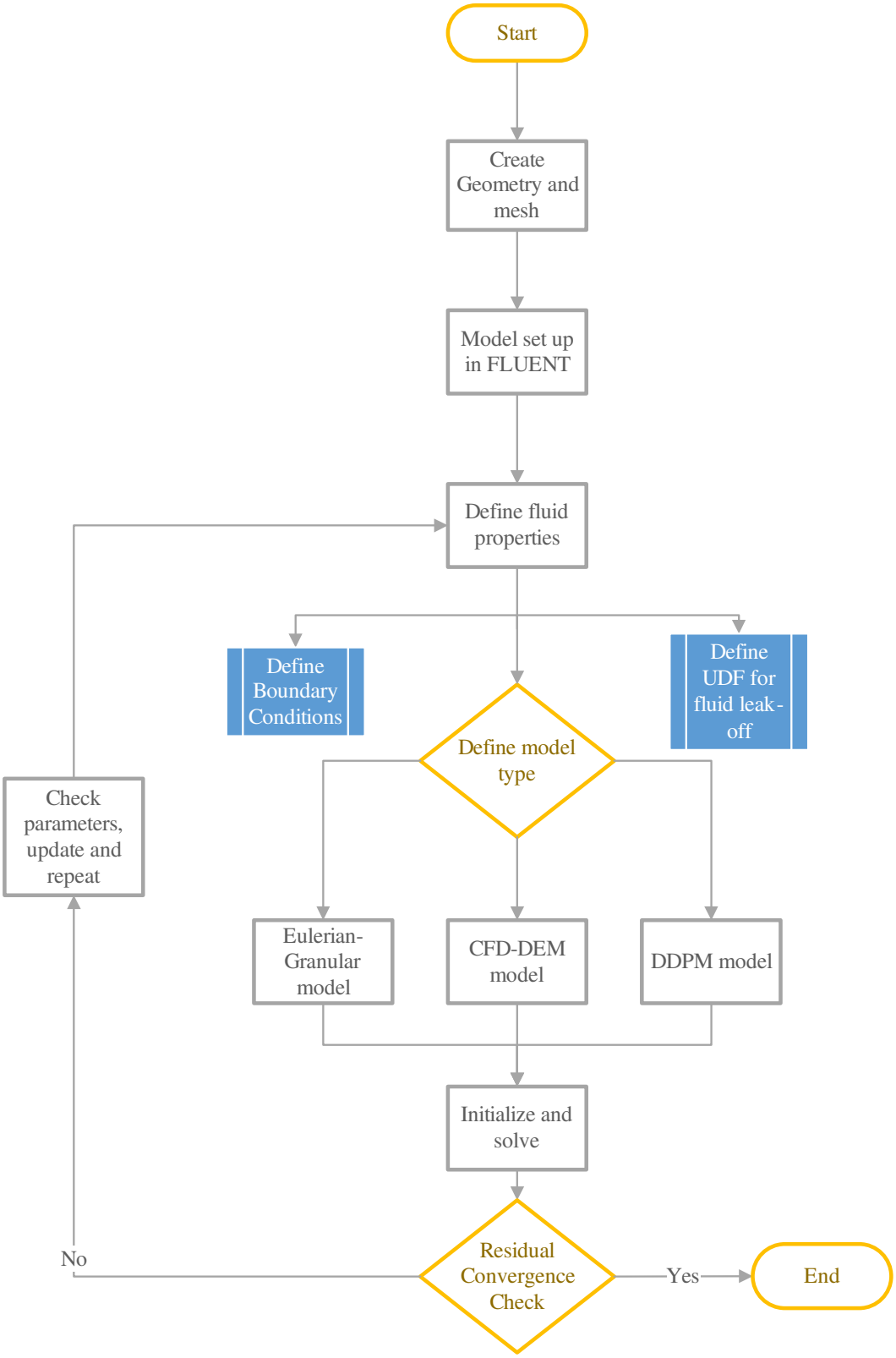

Figure 3.3 CFD modelling workflow

3.3.2 Modelling fluid leak-off

Post-injection of fracturing fluid into the wellbore, the process of fluid flowing from the fracture wall to the surrounding porous rock leaving the proppants in the fracture is called fluid leak-off (Carter 1957). In order to determine the amount of fracturing fluid leak-off at the fracture wall, a separate study was carried out where the fracture domain was surrounded with a porous and permeable rock. At the interface between the fracture and surrounding porous medium, the mass flow rate from the fracture to porous rock is calculated based on the permeability (0.1 mD) and porosity (5%) of rock (Speight 2016b). The leakage mass flow rate at the interface is then used to define the mass and momentum source term at the fracture wall as a user-defined function to investigate the proppant transport and distribution. The fracture surrounded by porous rock is shown in Figure 3.4. It is assumed that the surrounding porous rock is saturated with a single-phase fluid. No effect of interfacial tension and relative permeability due to multiphase flow in a porous medium is accounted for in order to calculate the fluid leakage mass flow rate at the fracture wall. The key governing equations solved for the fluid flow from the fracture to porous media are as follows-

3.3.2.1 Continuity equation

The continuity equation for a steady-state, incompressible and isothermal condition can be defined using Eq. (3.86) (Versteeg and Malalasekera 2007, Noble et al. 2019). It is to be noted that this continuity equation is for a separate fluid leak-off study where the objective is to calculate the water mass flow rate at the fracture-rock interface, based on the injection of single-phase fracturing fluid (water – in this case). The mass flow rate at the fracture-rock interface is then used to define a user-defined function and investigate the proppant transport and distribution in a separate study with a continuity equation defined in the sections 3.2.1-3.2.3.

$$\nabla . v_i = 0 \tag{3.86}$$

Where v_i is the velocity vector.

3.3.2.2 Momentum equation

The Navier-Stokes equation was used to model the momentum change in porous media defined in Eq. (3.87) (Noble et al. 2019). The Eq. (3.86) and Eq. (3.87) are based on isothermal, steady-state, incompressible condition assumptions, and thus the transient terms are neglected. The porosity of the rock was assumed as constant (5%).

$$\rho(v_i.\nabla)v_i = -\nabla P + \mu\nabla^2 v_i + F_i \tag{3.87}$$

where μ is the fluid viscosity, ρ is the fluid density, P is the static pressure, and F_i is the source term to account for the flow through porous media and can be calculated by rearranging the Darcy's Law.

$$F_i = -\frac{\mu}{k_m} v_i \tag{3.88}$$

Where k_m is the permeability of the rock. The surrounding porous rock was assumed to be isotropic, and k was assumed to be homogenous.

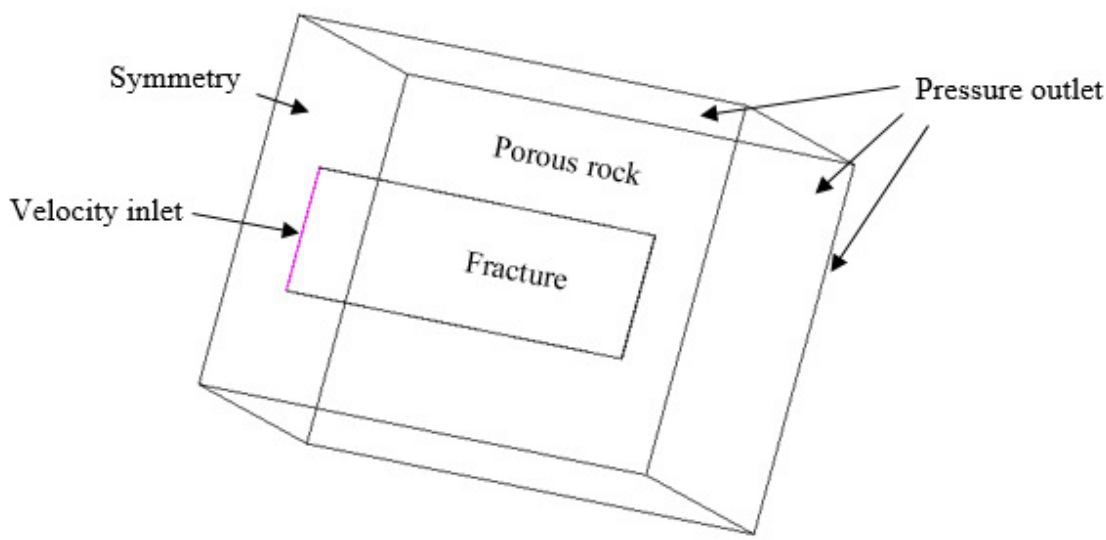

Figure 3.4 Fracture surrounded by porous rock

In order to determine the amount of water mass flow rate at the fracture-rock interface, a 3-D steady-state CFD study was carried out as shown in Figure 3.4. The velocity boundary condition was used at the inlet where water was injected with a specific injection velocity, and pressure boundary condition was used with one atmospheric pressure applied at the outlet (Figure 3.4). The fracture wall was assumed to be an interface between the fracture and surrounding porous and permeable rock. The water mass flow rate from the fracture walls is calculated as a percentage of inlet mass flow rate and plotted along the non-dimensional fracture length, as shown in Figure 3.5. The negative percentage flow rates in Figure 3.5 denotes they are leakage rates. The results in Figure 3.5 shows that for the surrounding rock porosity of 5% and permeability of 0.1 mD, the percentage of injected water mass lost/leaked from the fracture side walls is around 12% for the first 80% of the fracture length, and for the final 20% of the fracture length the leak-off rate as a percentage of injected water mass flow rate rapidly increases from 12% to as high as 65%. This can be explained by the fracture flow domain is like a channel flow, and the surrounding porous medium with such a low permeability (0.1 mD) acts as a flow hindrance. Thus, as the fluid is injected into the fracture domain, it finds it easier to flow longitudinally into the fracture domain in comparison to the leak-off in the lateral direction. Thus the leak-off rate as a percentage of injected water mass flow rate for the first 80% of the fracture length is around 12%. When the fluid reaches the end of the fracture length, it cannot flow further in the longitudinal direction and thus all the fluid leaks off in the lateral direction resulting in an increase of the leak-off rate, as observed in Figure 3.5. The fluid leak-off profile from this study was then used to investigate the proppant transport and distribution with fluid leak-off in a separate study based on the governing equations defined in sections 3.2.1-3.2.3. A user-defined function (UDF) is subsequently defined and written in C++ (section 3.3.2.3) which is interpreted by the CFD solver to model the fluid leak-off and add a mass and momentum source term in the right-hand side of proppant transport governing equations (Eq. (3.3) and Eq. (3.5)). The mass and momentum source terms in the governing equations are defined as zero for all regions of the model except the fracture sidewalls for fluid phase to account for the fluid leakage. Or in other words, the fracture sidewalls were defined as wall boundary condition where the proppants are prevented to leave the computational domain and trapped inside. The fracturing fluid or water (in this case) was lost or leaked based on the mass and momentum source terms (Appendix A). The fluid leakage effect is introduced at the sidewalls of the fracture with the help of user-defined function (UDF). This is done to mimic the fluid leak-off into the porous reservoir, leaving the proppants in the fracture.

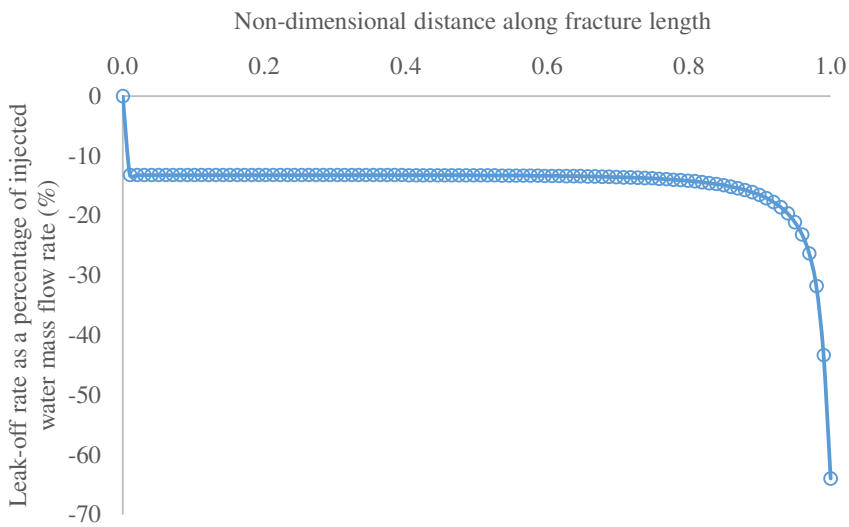

Figure 3.5 Fluid Leak-off rate at fracture wall along the fracture length

3.3.2.3 User-defined function

A user-defined function (UDF) is defined and written in C++ which is interpreted by the CFD solver to model the fluid leak-off and add a mass and momentum source term in the right-hand side of proppant transport governing equations (Eq. (3.3) and Eq. (3.5)). The momentum source term is given by Eq. (3.89) and Eq. (3.90) and the mass source term is given by Eq. (3.91) and Eq. (3.92).

$$S_u = -\frac{\dot{m}(x,t)}{V(x,t)} v(x,t) \tag{3.89}$$

$$S_u = -\frac{\rho_l . q(x,t)}{V(x,t)} v(x,t) \tag{3.90}$$

$$S_m = -\frac{\dot{m}(x,t)}{V(x,t)} \tag{3.91}$$

$$S_m = -\frac{\rho_l . q(x,t)}{V(x,t)} \tag{3.92}$$

Where $\dot{m}(x,t)$ is the mass flow rate at a particular cell or position and time step, $V(x,t)$ is the volume of a cell at a particular time step, $v(x,t)$ is the velocity of the fluid as a function of position and time step, ρ_l is the density of the fluid, $q(x,t)$ is the volumetric fluid leak-off flow rate as a function of fracture length and time. The negative sign indicates the fluid leaking off or the source terms are acting as the mass and momentum sinks in the proppant transport governing equations (Eq. (3.3) and Eq. (3.5)).

The fluid leakage effect is introduced at the sidewalls of the fracture with the help of user-defined function (UDF). The source terms in the governing equations are defined as zero for all regions of the model except the fracture sidewalls. This implies that within the computational domain, when the flowing fluid reaches the fracture wall, then the transport equation will add a mass and momentum sink in the form of source term which is governed by the amount of fluid leak-off rate profile shown in Figure 3.5. This is done to mimic the fluid leak-off into the porous reservoir, leaving the proppant in the fracture. The mass and momentum source terms are calculated using the DEFINE_SOURCE macro. The fluid leak-off rate profile is assigned to the fracture wall using the THREAD_ID(t) function (Fluent 2009). The complete code of the user-defined function is detailed in Appendix A.

3.3.3 Simulation set up

Next, appropriate boundary conditions and simulation properties were defined. Since in the present study, different fracture profiles or computational domain corresponding to smooth fractures and rough fractures are used, the specific values of the inlet, outlet and wall conditions are different based on the type of model. A detailed discussion about the simulation parameters for Eulerian-Granular model, Euler-Lagrangian model and DDPM model can be found in the corresponding chapters 4, 5 and 6. However, a brief description of some of the generic simulation parameters is discussed below.

A velocity inlet boundary condition is used at the inlet where fluid and proppants are injected. The Rosin-Rammler particle size distribution is assumed based on the proppant size. The Rosin-Rammler particle size distribution is a continuous probability distribution function to describe particle size distribution (Brown and Wohletz 1995). The top, bottom walls and fracture tip were specified as no-slip stationary walls for the liquid phase. For the particle phase, the standard Johnson and Jackson (1987) boundary condition with specularity constant and wall restitution coefficient was used to model the particle-wall collision. Benyahia Syamlal and O'Brien (2005), Li and Benyahia (2013) and Tebowei (2017) explained that the specularity constant characterizes the collisional tangential momentum transfer between the solid phase and the wall, and the wall restitution coefficient characterizes the dissipation of collisional kinetic energy transfer between the solid phase and the wall. The value of specularity constant and wall restitution coefficient used is 0.01 and 0.9 respectively based on the study of Ehsani et al. (2015) and Li, Zhang and Lu (2018). In the sidewalls, the fluid leakage effect is introduced with the help of user-defined function (UDF) (See Appendix A). This is done to mimic the fluid leak-off into the porous reservoir, leaving the proppant in the fracture. The momentum and mass source terms are defined

and included in the governing equations through UDFs as described in modelling leak-off section 3.3.2. The fluid leakage rate along the fracture length used in the study is shown in Figure 3.5. A transient state simulation with pressure-based solver and gravitation effects was configured. The pressure-based solver was selected due to the incompressible nature of the studied fluid. The transient state was selected to understand the proppant transport phenomenon with time.

The turbulence model used was the Shear Stress Transport (SST) k-ω model (Menter 1993). The SST k-ω turbulence model is a two-equation eddy-viscosity model, which combines standard k-ω turbulent model in the boundary layer (low-Re region) with the standard k-ε turbulent model in the free-stream (Menter 1993). SST k-ω turbulence model was originally proposed for external aerodynamics application, but due to its applicability in modelling adverse pressure gradients and separating flow, it has been used widely in different applications. As explained earlier in section 3.2.3.2, for modelling solid transport in fluids, the SST k-ω turbulence model has been greatly used in the literature (Bakker, Meyer and Deglon 2009, Nguyen et al. 2014, Alahmadi and Nowakowski 2016, Singh, Kumar and Mohapatra 2017, Zhigarev et al. 2017, Zhang, Wu and Sharma 2019, Yan et al. 2019). Thus, in the current study, the SST k- ω turbulence model is used. The fluid and proppant properties are listed in Table 3.1.

Table 3.1- Physical properties of proppant and fluid used in the simulation

Properties	Value	Reference
Proppant diameter	0.35, 0.50, 0.65 mm	(Li, Zhang and Lu 2018, Zhang and Chao 2018)
Proppant density	2650 kg/m^3	(Izadi et al. 2017)
Fluid density	1000 kg/m^3	(Tong and Mohanty 2016)
Fluid inlet velocity	0.1, 0.25, 0.5 m/s	(Zeng, Li and Zhang 2016, Osiptsov 2017, Hu et al. 2018)
Fluid viscosity	0.0005, 0.001, 0.005, 0.010 Pa-s	(Zhang, Gutierrez and Li 2017, Yi, Wu and Sharma 2018)
Proppant volume fraction	0.10-0.20	(Osiptsov 2017, Hu et al. 2018, Zhang and Chao 2018)

The viscosity of the granular phase is calculated from the Gidaspow (1994) correlation. The primary role of granular viscosity is used to consider the frictional losses. The frictional viscosity refers to the shear viscosity based on the viscous-plastic flow and is calculated using the Johnson and Jackson (1987) correlation. The packing limit defines the maximum volume fraction of the granular phase, which was used as 0.63 based on the study of Basu et al. (2015). Friction packing limit refers to a threshold volume fraction at which the frictional regime becomes dominant, and friction packing limit of 0.5 is used.

In the Eulerian-Granular method, the drag force used to model the interaction between the two phases is based on Gidaspow drag law (1994) and the collision between the proppant particles is modelled using the restitution coefficient as explained in the section 3.2.1.6. The time step used in the simulation was 0.001 s. Finally, the Phase-coupled semi-implicit pressure-linked equations (PC-SIMPLE) algorithm is used as a solution method for a pressure-velocity coupling which is an extension of semi-implicit pressure-linked equations (SIMPLE) algorithm to the multiphase flow problem (Patankar 1980, Versteeg and Malalasekera 2007). In multiphase flow, the phasic momentum equations, the shared pressure, and the phasic volume fraction equations are highly coupled. These equations can be solved in a segregated fashion using a phase-coupled SIMPLE algorithm to couple the shared pressure with the momentum equations (Göktepe, Atalık and Ertürk 2014). In the phase-coupled SIMPLE algorithm, the velocities are solved coupled by phases in a segregated manner. Fluxes are reconstructed at the faces of the control volume and then a pressure correction equation is built based on total continuity (Cokljat et al. 2006). The node-based averaging scheme is used to calculate the gradient (Mahdavi, Sharifpur and Meyer 2015). The node-based averaging calculates the value of the function at the node using weighted averaging and provides a more accurate solution on the unstructured mesh as it does not have a skewness error. The discretisation of momentum, volume fraction, and turbulent kinetic energy was solved by the second-order upwind scheme or linear upwind scheme. In the second-order upwind scheme, the quantities at the cell faces are computed using a multidimensional linear reconstruction approach. It is second-order accurate and depends on the mass flux direction through the face like the upwind scheme. The second-order accuracy is achieved in the linear upwind scheme using gradient limiters that avoids any non-physical solution and instabilities (Versteeg and Malalasekera 2007, Chung 2010).

3.4 Methodology for fracture propagation

Numerically modelling the fluid flow with proppant transport and fracture propagation together are one of the significant technical challenges in hydraulic fracturing of unconventional hydrocarbon reservoirs (Belyadi, Fathi and Belyadi 2019). In the existing coupled fluid flow and fracture models (El-M. Shokir and Al-Quraishi 2009, Kong, Fathi and Ameri 2015, Zhan et al. 2016, Izadi et al. 2017, Wang, Elsworth and Denison 2018), the fluid flow and proppant transport are usually modelled by two-component, interpenetrating continuum, meaning the flow governing equations are specific to the mixture, which cannot provide the accurate description of the particle physics in the slurry flow. Secondly, the effect of fracturing fluid leaking from the fracture-matrix interface on proppant distribution is neglected. Moreover, lastly, in most of the studies, the geometry of the fracture propagation is assumed from the analytical modelling techniques. However, in the present study, the proppant transport and fluid flow are modelled solving the flow governing equation for both the phases individually and the proppant-fluid interaction is explicitly modelled using a CFD based DDPM Model described in section 3.2.3. The model has then integrated to couple the effect of dynamic fracture propagation with the fluid leak-off effects. The existing fracture propagation models use LEFM that assumes rock as a brittle material and neglect plastic deformations. However, some of the rocks are ductile in nature, for instance, shales that show plastic deformation which can be modelled using the XFEM and CZM. The CFD, coupled with XFEM and CZM approach, offers the advantage of modelling the fracture propagation and investigate the accurate fluid flow and proppant concentration distribution, which may be challenging to obtain experimentally. The proposed three-dimensional integrated fluid flow, proppant transport and fracture propagation model can accurately model the fluid-proppant, proppant-proppant and fracture wall interactions with varying fluid, proppants and geomechanical parameters and fluid leak-off effects.

3.5 Extended Finite Element Method (XFEM) Methodology

A fully coupled 3D hydraulic fracturing simulation involves the coupling of fracture mechanics that governs the fracture propagation with the fluid flow and proppant transport modelling that governs the pressure and velocity fields inside the fracture. A cohesive based XFEM technique is applied to calculate the rock stress, fracture initiation, propagation and rock deformation. Following that, a CFD method is applied to model the fluid flow and proppant transport numerically. The key underlying equation describing the cohesive based XFEM is explained below.

3.5.1 Governing equations

The stress inside a poroelastic, isotropic and homogenous medium (Figure 3.6) that is saturated with a single-phase fluid can be described by Eq. (3.93) (Chen 2013, Shi et al. 2017).

$$\begin{gathered} \nabla \cdot \sigma = 0, \text{ on } \Omega \\ \sigma \cdot \hat{n} = F, \text{ on } \Gamma_F \\ \sigma \cdot \hat{n}^- = -\sigma \cdot \hat{n}^+ = -p\,\hat{n}^+ = p\,\hat{n}^-, \text{ on } \Gamma_c \end{gathered} \tag{3.93}$$

where σ is the total stress, F is the external loading, p is the fluid pressure, $\hat{n}$ is the normal unit vector, Ω is the homogenous, isotropic, linear-elastic domain, Γ_F is the domain subjected to traction and Γ_c is the crack domain subjected to fluid pressure. The total stress, σ, can be expressed in terms of the effective stress tensor, σ' and pore pressure, P_m, using poroelasticity theory as defined in Eq. (3.94) (Feng and Gray 2019).

$$\sigma' = \sigma + \alpha_p P_m I \tag{3.94}$$

Where α_p is the poroelastic constant that depends on the rock type and I is the unit tensor.
The strain-displacement equation and crack opening can be defined by Eq. (3.95), assuming small displacements and deformation (Chen 2013)

$$\begin{gathered} \varepsilon = (\nabla u + (\nabla u)^T) / 2 \text{ on } \Omega \\ u = 0 \text{ on } \Gamma_u \\ w = u^+ - u^- \text{ on } \Gamma_c \end{gathered} \tag{3.95}$$

Where ε is the strain, w is the crack opening, and u is the displacement. The linear elastic constitutive law that governs the behaviour of the formation is described by Eq. (3.96)

$$\sigma = D_T : \varepsilon \tag{3.96}$$

where D_T is the Hooke's tensor.

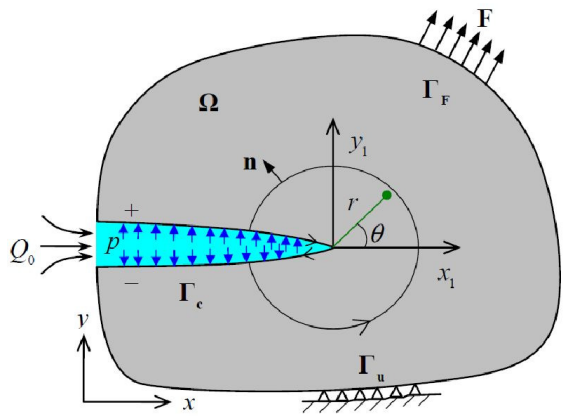

Figure 3.6. Hydraulic fracture in a porous rock formation (Chen 2013)

The continuity equation for pore fluid flow in the porous formation can be expressed as (Feng and Gray 2018)

$$\frac{1}{M}\dot{P_m} + \alpha_p \nabla \cdot \dot{u} + \nabla \cdot v_d = 0 \tag{3.97}$$

Where M is the Biot's modulus, u is the displacement of the solid phase, v_d is the fluid flow velocity of the pore fluid. The fluid flow is assumed to obey Darcy's law as

$$v_d = -\frac{k_m}{\mu}\nabla P_m \tag{3.98}$$

where μ is the viscosity of pore fluid, k_m is the permeability.

For an incompressible fracturing fluid, the mass conservation equation for the fluid flow in the fracture may be expressed as (Chen 2013, Shi et al. 2017)

$$\frac{\partial w}{\partial t} + \frac{\partial q}{\partial x} + c_L = 0 \tag{3.99}$$

where q is the fluid flux inside the fracture, c_L is the fluid leak-off rate from the fracture to the surrounding porous medium, and w is the fracture width. The fluid flow in the fracture is modelled using lubrication theory, given by Poiseuille's law.

$$q = -\frac{w^3}{12\mu}\frac{\partial p}{\partial x} \tag{3.100}$$

Where $\frac{\partial p}{\partial x}$ is the pressure gradient, and μ is the dynamic fracturing fluid viscosity. Substituting Eq. (3.100) into Eq. (3.99) leads to the governing equation for the fluid flow within the fracture

$$\frac{\partial w}{\partial t} - \frac{\partial}{\partial x}\left(k\frac{\partial p}{\partial x}\right) + c_L = 0 \tag{3.101}$$

The general three-dimensional form of Eq. (3.101) can be written as

$$\dot{w} - \nabla^T(k_c \nabla p) + c_L = 0 \tag{3.102}$$

where $k_c = \frac{w^3}{12\mu}$ is the conductivity.

Eq. (3.102) can be solved using the following initial and boundary conditions in the hydraulic fracture,

$$\begin{aligned} q_{inlet} &= Q_0 \\ w_{tip} &= q_{tip} = 0 \end{aligned} \tag{3.103}$$

The equilibrium equation, or Eq. (3.93) can be written in the weak form as (Chen 2013, Shi et al. 2017)

$$\int_\Omega \delta\varepsilon^T \sigma d\Omega - \int_\Omega \delta u^T b d\Omega - \int_{\Gamma_F} \delta u^T t_c d\Gamma_F - \left(\int_{\Gamma_c^+} \delta u_c^{+T} p_c^+ d\Gamma_c + \int_{\Gamma_c^-} \delta u_c^{-T} p_c^- d\Gamma_c\right) = 0 \tag{3.104}$$

Where t_c is the applied traction on the boundary Γ_F, b is the body force, δu and δε are the arbitrary virtual displacement and strain, related by δε = Sδu with S as a strain operator (Chen 2013, Shi et al. 2017).

The fluid pressure on the fracture surfaces and the fracture opening displacement is given by Eq. (3.105) and Eq. (3.106) respectively

$$p = p_c^+ = -p_c^- = p\hat{n}_c = p\hat{n}_c^- = -p\hat{n}_c^+ \tag{3.105}$$

$$w = \hat{n}_c^T.(u_c^+ - u_c^-), \text{or } w = \hat{n}_c \cdot (u_c^+ - u_c^-) \tag{3.106}$$

Thus the equilibrium equation can be written in a simplified weak form as

$$\int_{\Omega} \delta\varepsilon^{T}\sigma d\Omega - \int_{\Omega} \delta u^{T} b d\Omega - \int_{\Gamma_F} \delta u^{T} t d\Gamma_F - \int_{\Gamma_c} \delta w^{T} p d\Gamma_c = 0 \tag{3.107}$$

And the fluid flow governing equation within the fracture can be written in the weak form as

$$\int_{\Gamma_c} \delta p^{T}(\dot{w} - \nabla^{T}(k_c \nabla p) + c_L) d\Gamma_c = 0 \tag{3.108}$$

Eq. (3.108) can further be simplified using integration by parts and the above boundary conditions as (Chen 2013, Shi et al. 2017)

$$\int_{\Gamma_c} \delta p^{T} \dot{w} d\Gamma_c + \int_{\Gamma_c} \nabla^{T}(\delta p) k_c \nabla p d\Gamma_c + \int_{\Gamma_c} \delta p^{T} c_L d\Gamma_c = 0 \tag{3.109}$$

The governing equation of pore fluid flow in porous formation can be written in the weak form as (Feng and Gray 2018)

$$\int_{\Omega} \delta p_m^{T}(\frac{1}{M}\dot{P_m} + \alpha_p \nabla \cdot \dot{u} + \nabla \cdot v_d) d\Omega = 0 \tag{3.110}$$

Using the standard (displacement) discretization method, the displacement vector u, fluid pressure p, and fracture opening displacement w can be approximated as

$$\begin{aligned} u \approx \hat{u} &= \sum_{i=1}^{n} N_i^u u_i = N^u \tilde{u}, \delta u \approx N^u \delta\tilde{u} \\ p \approx \hat{p} &= \sum_{i=1}^{n} N_i^p p_i = N^p \tilde{p}, \delta p \approx N^p \delta\tilde{p} \\ w \approx \hat{w} &= \sum_{i=1}^{n} N_i^w u_i = N^w \tilde{u}, \delta w \approx N^w \delta\tilde{u} \end{aligned} \tag{3.111}$$

where N_i^u , N_i^p and N_i^w are shape functions for nodal displacement (u_i), fluid pressure (p_i), and crack opening respectively. Combining Eq. (3.111), Eq. (3.107), and Eq. (3.96) provides a system of algebraic equations for discrete fracture mechanics described by

$$\overline{K}\tilde{u} - \overline{Q}\tilde{p} - f^{u} = 0 \tag{3.112}$$

Where

$$\overline{K} = \int_{\Omega} B^T D B d\Omega$$

$$f^u = \int_{\Omega} (N^u)^T b d\Omega + \int_{\Gamma_t} (N^u)^T t d\Gamma \tag{3.113}$$

$$\overline{Q} = \int_{\Gamma_c} (N^w)^T n N^p d\Gamma$$

Where $\overline{K}$ is the structural stiffness matrix, $\overline{Q}$ is the coupling term due to the traction on the fracture surface through the matrix, and f^u is the equivalent nodal force vector for displacement. Similarly, combining Eq. (3.111) and Eq. (3.109) provides a system of algebraic equations for discrete fluid dynamics described by

$$\overline{C}\tilde{u} - \overline{H}\tilde{p} - f^p = 0 \tag{3.114}$$

Where

$$\overline{C} = \int_{\Gamma_c} (N^p)^T n^T N^w d\Gamma$$

$$\overline{H} = \int_{\Gamma_c} (\nabla N^p)^T k_c \nabla N^p d\Gamma \tag{3.115}$$

$$f^p = -\int_{\Gamma_c} (N^p)^T g d\Gamma$$

Where $\overline{C}$ is the pressure equivalent stiffness matrix, $\overline{H}$ is the coupling term due to the fluid pressure, and f^p is the equivalent nodal force vector for pressure.

Thus, the discrete governing equations in the matrix form can be written as:

$$\begin{bmatrix} 0 & 0 \\ \overline{C} & 0 \end{bmatrix} \begin{pmatrix} \tilde{u} \\ \tilde{p} \end{pmatrix} + \begin{bmatrix} \overline{K} & -\overline{Q} \\ 0 & \overline{H} \end{bmatrix} \begin{pmatrix} \tilde{u} \\ \tilde{p} \end{pmatrix} = \begin{pmatrix} f^u \\ f^p \end{pmatrix} \tag{3.116}$$

The above equations form a finite element approach for a set of the coupled system of fracture propagation and fluid flow in fracture. The XFEM is adopted to discretize and approximate the displacement field u, as described in the following section (Chen 2013).

3.5.2 Extended finite element method (XFEM) approximation

Belytschko and Black (1999) and Moes, Dolbow and Belytschko (1999) proposed the extended finite element in order to provide a solution to the mesh-independent fracture propagation model. XFEM uses a partition of unity technique from the study of Melenk and Babuska (1996) that extends the conventional FEM approach and model any discontinuities with special enriched functions. XFEM has several advantages over traditional techniques, including simulation of fracture propagation along arbitrary paths independent of the mesh, additional degrees of freedom to model discontinuities and simpler mesh refinement studies. Additionally, it improves the fracture tip solution by avoiding re-meshing during the fracture propagation stage. Using the partition of unity enrichment method, the displacement vector (u) can be described using Eq. (3.117) (Fries and Baydoun 2012).

$$u = \sum_{i=1}^{N} N_i(x)[u_i + H(x)a_i] \tag{3.117}$$

The special enriched functions consist of the discontinuous element $H(x)$ that represents the displacement jump near fracture edges. $N_i(x)$ is the shape function with binary values depending upon the node location. The nodal shape function has a value of one at the node where it is computed and zeroes at other locations. u_i is the displacement that applies to all the nodes and linked to the continuous element. a_i is the enriched degree of freedom at the node. The discontinuous jump function can be defined by Eq. (3.118) (Lecampion 2009, Wang 2015).

$$H(x) = \begin{cases} 1 & \text{if } (x - x^*).n \geq 0 \\ -1 & \text{otherwise} \end{cases} \tag{3.118}$$

Where x and x* are the sample point and the closest point on the crack from the sample point respectively, **n** is the normal unit vector at x*, r and θ are the polar coordinates with the origin located at the fracture tip (Figure 3.7).

One of the significant advantages of the XFEM method over conventional fracture propagation modelling techniques is the description of the fracture. As stated earlier, XFEM aids in fracture propagation by avoiding re-meshing at each time step and thus is computationally attractive technique. Two important fracture propagation modelling techniques incorporated in the XFEM includes a level set method and phantom nodes. The level set method, proposed by Osher and Sethian (1988), is used by XFEM to track the fracture interface and shape. The level set method assumes that two distance functions are required to describe fracture propagation. These distance functions are updated at each iterative time step and represented by $\emptyset$ and ψ. The first function, $\emptyset$, refers to the fracture surface, whereas, ψ refers to the orthogonal fracture surface. The intersection of the surfaces defined by $\emptyset$ and ψ gives crack front. The XFEM fracture modelling mainly relies on the nodal data and is illustrated in Figure 3.8.

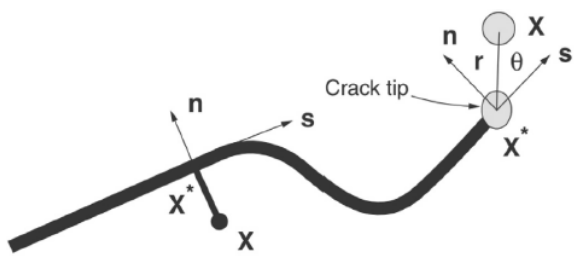

Figure 3.7. Illustration of the definition of special enriched functions (Wang 2015)

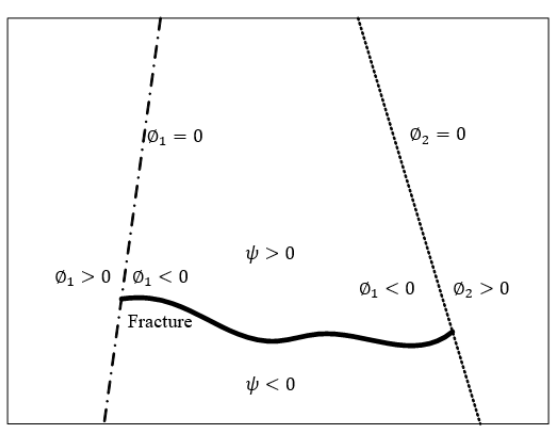

Figure 3.8 Illustration of the fracture using the level set method (Modified from Stolarska et al. (2001))

Secondly, another important tool used to model the fracture discontinuity is using the phantom nodes (Rabczuk et al. 2008). When the formation mesh element is cut through by a fracture, then depending upon the fracture orientation, the cracked element can be split into two parts (Figure 3.9). The phantom nodes can be assigned to the original nodes to model the discontinuity, and thus, the real nodes are no longer secured together and are free to separate apart. This method provides an effective approach for modelling crack growth in solids and provides promising results with mesh independent solution for a sufficiently refined mesh (Duan et al. 2009, Wang 2015). As the fracture initiates, the fracture opening is governed by cohesive law until the fracture opening exceeds the cohesive strength of the element. Following that the phantom nodes and real nodes can separate independently.

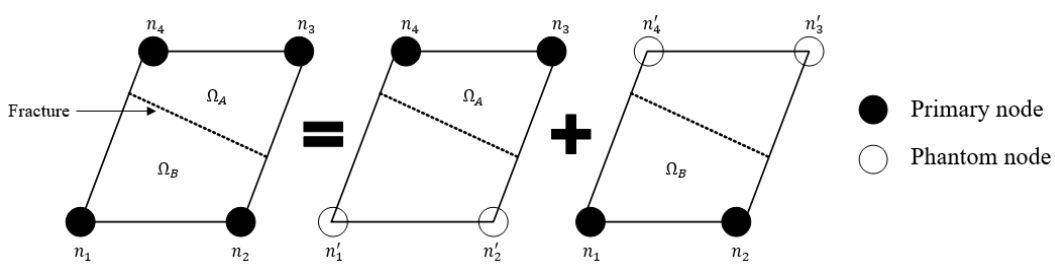

Figure 3.9 illustration of phantom node method

3.5.3 Cohesive zone method

To model the fracture propagation in solid material or rocks requires different conditions or criterion to be defined that governs the advancement of the fracture tip. In fracture mechanics, the fracture can be analysed based on two fundamental approaches, namely energy criterion and stress intensity (Chang 2013). According to the energy criterion approach, fracture propagates when the energy available for fracture propagation overcomes the material resistance. The material resistance is commonly given by the critical energy release rate (G_c) (Wang 2015). On the other hand, the stress intensity approach refers to a parameter known as stress intensity factor, commonly known as K_I that drives fracture propagation. For the linear elastic materials, both the approaches are equivalent. In Linear Elastic Fracture Mechanics (LEFM), the plastic deformation behaviour of the fracture tip region is neglected. Thus, LEFM is capable of modelling the fracture propagation for brittle mode when the K_I is greater than the critical stress intensity factor (K_{IC}). LEFM provides limitations to model the fracture propagation in quasi-brittle materials where the plastic deformation is significant. To overcome that a more robust modelling criterion is required that can model these non-linearities. Barenblatt (1962) proposed a cohesive zone model that captures the plastic deformation non-linear behaviour. The traction–separation relationship is used to describe the constitutive behaviour of the cohesive zone that removes the limitation of singular stress at the fracture tip (Tomar, Zhai and Zhou 2004). The cohesive zone model characterises the cohesive surfaces, which forms when the material elements are pulled apart. According to the traction–separation relationship, the traction value increases with the separation of cohesive surfaces until traction reaches a maximum value. Following that the magnitude of the separation is governed by the cohesive law until the cohesive strength of the fractured element becomes zero, after which the phantom and the real nodes move independently (Chen 2011) (Figure 3.10). The detailed explanation of the traction–separation law with variables in Figure 3.10 can be found in Högberg (2006). The area enclosed in the traction-separation curve defines the energy required for separation, also known as critical fracture energy. The maximum nominal stress ratio criteria (Haddad and Sepehrnoori 2016) are used in the present study that governs the fracture initiation and can be described by Eq.(3.119). When the stress ratios in Eq. (3.119) becomes unity; it marks the fracture initiation (Riccio et al. 2017).

$$\mathrm{Max}\left\{\frac{<t_n>}{t_n^0}, \frac{t_s}{t_s^0}, \frac{t_t}{t_t^0}\right\} = 1 \tag{3.119}$$

The fracture propagation is governed by the amount of degradation in rock stiffness. The amount of degradation is measured by a scalar variable D whose value range from zero (zero damage) to unity (full damage) (Saberhosseini, Ahangari and Mohammadrezaei 2019). Due to the change in

the value of degradation factor, D, the corresponding stress, t_n is also affected and can be described using the following expression:

$$t_n = \begin{cases} (1-D)\bar{t}_n, & \bar{t}_n \geq 0 \\ \bar{t}_n, & \bar{t}_n < 0 \end{cases} \tag{3.120}$$

$$D = \frac{\delta_n^f(\delta_n^{max} - \delta_n^0)}{\delta_n^{max}(\delta_n^f - \delta_n^0)} \tag{3.121}$$

where δ_n^0 is the initial separation or displacement, δ_n^f is the separation at complete failure, δ_n^{max} is the maximum separation, t_n is the stress in the normal direction, t_s is the stress in principle shear direction, and t_t is the stress in the second shear direction. t_n^0, t_s^0 and t_t^0 are the cohesive strengths when the deformation is purely normal to the interface (pure tension), purely in the first shear direction, and purely in the second shear direction. $\bar{t}_n$ is the normal stress predicted by the elastic traction–separation behaviour for the current separation without damage.

Conventionally in the oil and gas industry, the hydraulic fracture modelling is based on the LEFM and assumes only tensile forces for fracture propagation. However, in the formation with ductile properties, the shear forces can play a dominant role in fracture propagation. Depending upon the type of load applied, a fracture or crack can be initiated based on the following three modes. The first type of fracture is called mode I fracture, which is formed mainly due to tensile forces. The mode II fracture is due to the shear forces under sliding, and mode III fracture is due to the shear forces under tearing. Therefore, in the current study, a combined effect of different fracture modes is accounted to outline fracture initiation and propagation criteria.

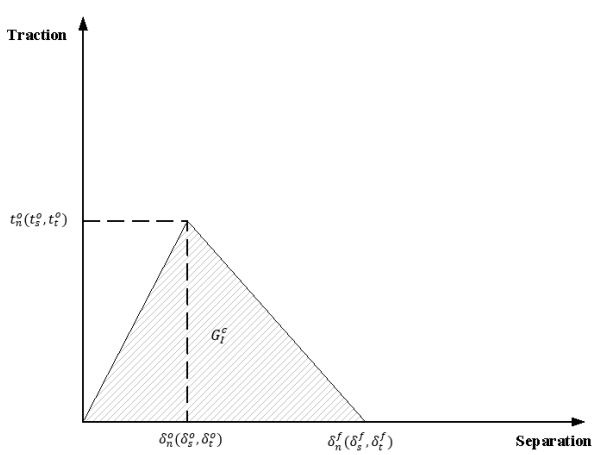

Figure 3.10 Traction–separation relationship (Wang 2015)

In order to account for the mix mode fracture propagation, the criterion proposed by Benzeggagh and Kenane (1996) was used. The fracture energy because of deformation, G^c can be described as

$$G^c = G_I^c + (G_{II}^c - G_I^c)\left(\frac{G_{shear}}{G_{total}}\right)^{\eta_c} \tag{3.122}$$

$$G_{shear} = G_{II}^c + G_{III}^c \tag{3.123}$$

$$G_{total} = G_{shear} + G_I^c \tag{3.124}$$

Where $G_I^c, G_{II}^c, G_{III}^c$ are the fracture energy due to traction-separation in normal, principle and second shear directions. η_c is a constant and can be obtained using the experiment (Benzeggagh and Kenane 1996). The value of η_c =1 is used in the present study because this study is based on the assumption of isotropic formation that the results of fracture propagation due to traction separation law are the same in different modes. Thus, the fracture energy due to deformation, G^c is insensitive to η_c (Wang 2015). It is worth noting that although the current study assumes the fracture energy due to traction-separation in normal, principle and second shear directions are same in all the three directions, but the model is capable of accounting different stresses in the three directions. The numerical model of fracture propagation proposed in the literature by researchers (Chen et al. 2009, Cristian, Paullo and Roehl 2015, Yao, Liu and Keer 2015) use the cohesive zone model, but they require the pre-defined path definition for crack growth. Thus, the XFEM and cohesive zone method can be combined to simulate the fracture propagation without defining the predefined paths and avoids the singularities around the fracture tip (Paul et al. 2018).

3.5.4 Coupling between XFEM and CFD

An explicit coupling simulation approach is used in the present study to integrate the XFEM based fracture propagation model with the CFD-DEM based fluid flow and proppant transport model. Important elements in the current numerical model include the following:

- An XFEM geomechanics solver based on cohesive traction law that models the fracture propagation based on fracture mechanics, geomechanical stress and reservoir properties.
- A CFD based solver for modelling proppant transport inside the fracture with fluid leaking off from the fracture-matrix interface.

Figure 3.11 shows the workflow that was followed in the current numerical model. Firstly, the XFEM model was configured using the available real field reservoir and geomechanical data (discussed in chapter 7 - Table 7.1). Then the simulation run was performed to model the fracture propagation and get the fracture geometry which will then be used as a computational domain

for the proppant transport and fluid flow in the CFD solver. The computational domain was discretized, and the proppant transport and fluid flow analysis were carried out at different time steps with fluid leak-off from the fracture wall, based on the proposed proppant transport model described in section 3.2.3. This is an iterative process where the pressure field and fluid leak-off along the fractures was exchanged at different time steps to model the proppant transport in dynamic fracture propagation, as shown in Figure 3.11. The fluid and proppant mixture is injected at the inlet using velocity inlet boundary condition. To model the fluid leak-off from the fracture wall, a user-defined function is used to add a source term in the continuity and momentum transport equations. The amount of fluid leaking off from the fracture wall is obtained from the XFEM model that was used in the user-defined function. The detailed explanation of the CFD modelling parameters, boundary conditions and user-defined function can be found in section 3.3.

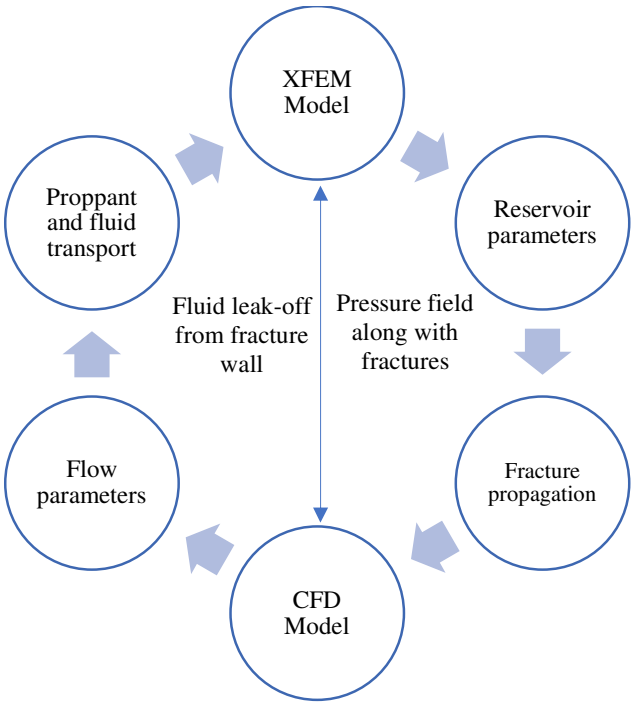

Figure 3.11 XFEM-CFD coupling workflow

Chapter 4: Development and Comparison of Eulerian-Granular Model and CFD-DEM Model[1]

The distribution of proppant injected in hydraulic fractures significantly affects the fracture conductivity and well performance (Yew and Weng 2014). The proppant transport in thin fracturing fluid used during hydraulic fracturing in the unconventional reservoirs is considerably different from fracturing fluids in the conventional reservoir due to the very low viscosity and quick deposition of the proppants (Sahai, Miskimins and Olson 2014). This chapter presents the development of a three-dimensional Computational Fluid Dynamics (CFD) modelling technique for the prediction of proppant-fluid multiphase flow in hydraulic fractures. The proposed model also simulates the fluid leak-off behaviour from the fracture wall (Suri, Islam and Hossain 2020a). The Euler-Granular and CFD-Discrete Element Method (CFD-DEM) multiphase modelling approach has been applied, and the equations defining the fluid-proppant and inter-proppant interaction have been solved using the finite volume technique. The proppant transport in hydraulic fractures has been studied comprehensively, and the computational modelling results of proppant distribution and other flow properties are in good agreement with the published experimental study. Subsequently, a parametric study was performed to critically examine the role of proppant properties (proppant size), fluid properties (fluid viscosity) and geomechanical properties (fracture width) on proppant transport. In addition, the Eulerian-Granular model has been compared with the more accurate Discrete Element Model for proppant flow.

4.1 Brief methodology

In the present study, two different numerical modelling techniques are used to study proppant transport and distribution in hydraulic fractures, namely Eulerian-Granular model and Computational Fluid Dynamics – Discrete Element Model (CFD-DEM), as described in Chapter 3. The key objective in the present study is to provide a detailed understanding of the proppant transport considering the effect of fluid leak-off from the fracture wall in a planar fracture in the unconventional reservoir. Some of the assumptions underlying the current model are as follows: First, the model is a small scale because of the large simulation time in the CFD-DEM model.

---

[1] The results from this chapter are published in the Journal of Fluid Dynamics & Material Processing
Suri Y., Islam, S.Z. and Hossain, M., 2020. Numerical modelling of proppant transport in hydraulic fractures. *Fluid Dynamics & Material Processing*. vol.16, no.2, pp.297-337 https://doi.org/10.32604/fdmp.2020.08421

Second, the slurry is a Newtonian fluid. Third, the fracture geometry is constant and assumed as a cuboid; no dynamic fracture propagation is considered in this study.

4.1.1 Eulerian-Granular model

The Eulerian-Granular model, as described in chapter 3, is a multiphase flow model in which both phases are defined as a continuous phase. This means the flow governing equations (continuity and momentum equations) are solved separately for each phase. The primary phase is fluid, and the secondary phase is defined as granular phase (solid phase). The particle-particle collision or inter-particle interaction is explicitly modelled using a collision model, kinetic theory of granular flow and frictional models (Reuge et al. 2008, Kong, McAndrew and Cisternas 2016). The particle-fluid interaction is defined by interphase exchange coefficients and is modelled using the empirical models (Burns et al. 2004, Reuge et al. 2008, Kong, McAndrew and Cisternas 2016). The governing momentum equation for the granular phase includes additional terms to define the properties for granular flow such as solid pressure and solid stress tensor terms from the application of the kinetic theory of granular flow (Savage and Jeffrey 1981, Jenkins and Savage 1983). A key parameter in the KTGF model for solid-phase stress is a parameter known as granular temperature. The granular temperature provides a measure of the kinetic energy associated with solid particles velocity fluctuations. The granular temperature is a function of the fluctuating velocity of the particles and is obtained using the granular energy transport equation described earlier in section 3.2.1.6. In Eulerian-Granular model, the volume fraction is used as a parameter to determine how much each phase is present in a control volume. The key governing equations corresponding to the Eulerian-Granular model are described in detail in chapter 3.

4.1.2 Computational fluid dynamics - discrete element model (CFD-DEM)

CFD-DEM is based on Eulerian-Lagrangian method as explained earlier. Unlike other Eulerian-Lagrangian methods, for instance, Discrete Phase Model (DPM) which is applicable only for the low volume fraction of particles (<10%), the CFD-DEM can be used when the higher volume fraction of particles is present (10%-63%). Thus, CFD-DEM can accurately model the multiphase flow where the inter-particle interaction is imperative, such as proppant flow in the fracturing fluid (Deng et al. 2014). Cundall and Strack (1979) proposed the DEM method, and it was later coupled with CFD by other researchers to study fluid-solid flow modelling (Zhang, Li and Gutierrez 2016). In this approach, the primary phase is solved using a conventional Eulerian method meaning continuity and momentum equations are solved using CFD. However, the solid phase is solved using DEM by tracking every dispersed particle, thus it is a computationally

expensive technique (Wu and Sharma 2016). Particles are tracked by calculating the mass, velocity, and forces acting on a particle using Newton's second law of motion. This is referred to as tracking in the Lagrangian frame in the DEM method (Zhang, Gutierrez and Li 2017). Finally, the drag forces and interphase momentum exchange terms are used to model the interaction, energy dissipation and coupling of both the phases, i.e., continuous and discrete phases. In order to account for accurate particle micro-mechanics and particle collision, it is further assumed that after the collision, the two particles deform and defined by the overlap displacement of the particles. This approach is called the soft-sphere approach that outlined an accurate contact model and is explained earlier in section 3.2.2.2.

4.2 Numerical modelling parameters

Proppant transport and distribution were investigated in a hydraulic fracture using the CFD technique in ANSYS FLUENT. The geometry or computational domain used in the current study is, as shown in Figure 4.1, with dimensions 1.5 m (length) × 0.05 m (width) × 0.5 m (height). In order to obtain a mesh independent solution, a mesh sensitivity analysis was done by selecting a structured mesh and varying the mesh sizing parameter 0.0025 m, 0.005 m, 0.0075 m, and 0.01 m. The results of the mesh sensitivity analysis were compared against the proppant volume fraction and proppant axial velocity vs fracture height in Figure 4.2. The results from the mesh sensitivity study, suggest that the mesh size of 0.005 m (300×100×10 elements) was reasonably able to provide the mesh independent, numerically converged and computationally efficient solution.

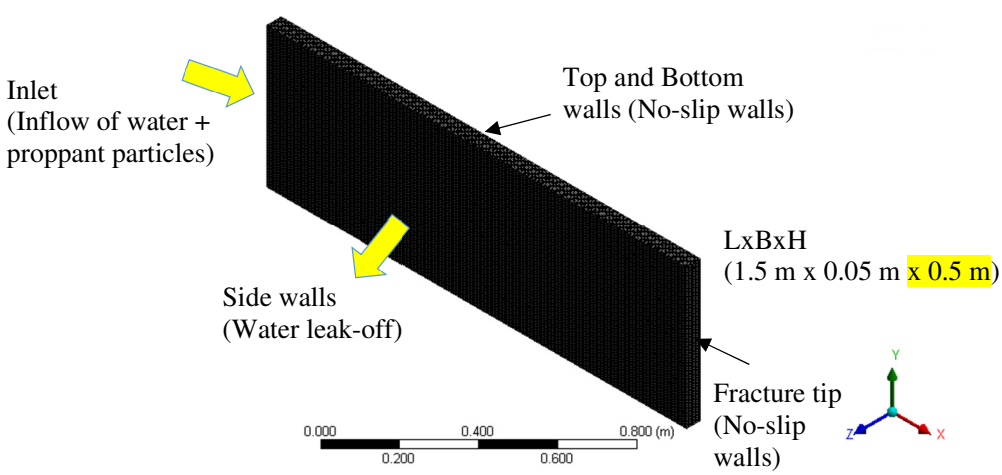

Figure 4.1: Computational domain

a.

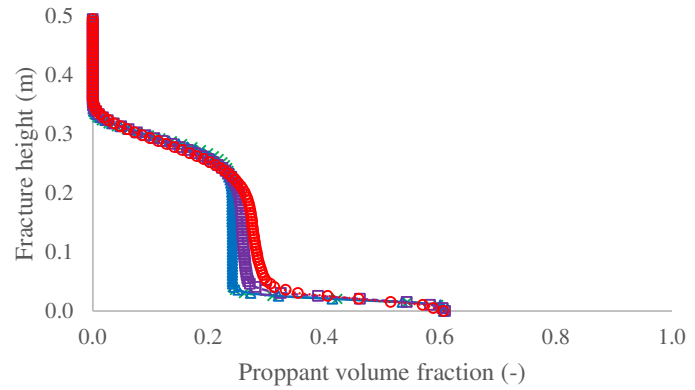

b.

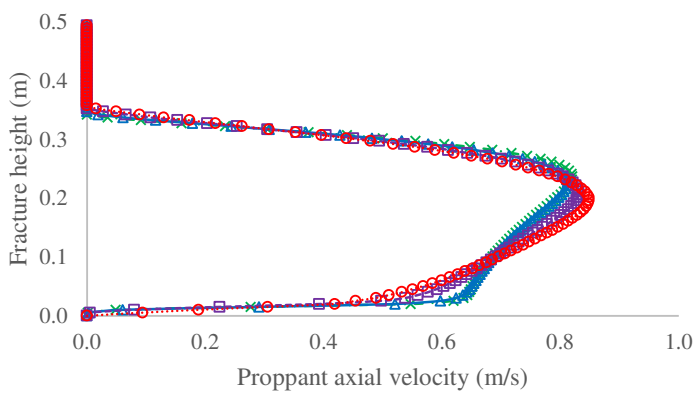

Legend

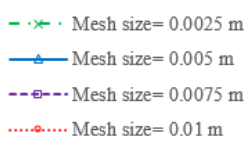

Figure 4.2: Mesh sensitivity study

Next, appropriate boundary conditions, cell zone conditions, and simulation properties were defined. A velocity inlet boundary condition is used at the inlet where fluid and proppants are injected at 0.5 m/s. The particle size distribution is assumed to be of uniform diameter 1 mm. All the walls shown in Figure 4.1 are assumed as no-slip stationary walls for the liquid phase. For the particle phase, the standard Johnson and Jackson (1987) boundary condition with specularity constant and wall restitution coefficient was used to model the particle-wall collision, as explained earlier in section 3.3.3. The value of specularity constant and wall restitution coefficient used is 0.01 and 0.9 respectively based on the study of Ehsani et al. (2015) and Li, Zhang and Lu (2018). In order to mimic the fluid leak-off into the surrounding porous rock, the fluid leakage effect is modelled through the fracture sidewalls with the help of a user-defined function (Appendix A) as discussed earlier in the section 3.3.2.3. The momentum and mass source terms are defined and included in the governing transport equations through UDF been written in C++, which is interpreted by the CFD solver, ANSYS FLUENT 18.1. In order to obtain

the fluid leakage rate, an explicit CFD study was carried out to calculate the water leaking off rate along the fracture sidewall. The underlying equations describing the source terms and UDF used to model the fluid leak-off is explained earlier in section 3.3.2. The fluid leak-off profile along the fracture length to a surrounding porous rock with porosity 5% and permeability 1 mD used in the current study is shown in Figure 4.3.

The pressure-based solver with gravitational effects was used to solve the governing proppant transport equations as described earlier in section 3.3.3. In order to model the turbulence, the Shear Stress Transport (SST) k-ω model (Menter 1993) was used, as described earlier in section 3.2.3.2, due to its wide application in the literature for modelling solid transport in fluid (Bakker, Meyer and Deglon 2009, Nguyen et al. 2014, Alahmadi and Nowakowski 2016, Singh, Kumar and Mohapatra 2017, Zhigarev et al. 2017, Zhang, Wu and Sharma 2019, Yan et al. 2019). Two different models were studied for proppant transport in fracture – Eulerian-Granular model (or Eulerian Two-fluid model) and Discrete Element model (CFD-DEM Model). The fluid and solid properties are listed in Table 4.1. The typical value of proppant volume fraction in the slick water fracturing fluid slurry varies from 3-20% (Tsai et al. 2012, Bokane et al. 2013, Jain et al. 2013). Thus, in the current study, the proppant volume fraction of 20% is used to model the inter-proppant interaction. The proppant diameter used in the present study is 1 mm, as shown in Table 4.1. In a dispersed multiphase flow, once the particle fluid interaction in CFD-DEM and Eulerian-Granular models are defined as empirical models for sub-grid particles (e.g.: Gidaspow Drag Model), the particle diameter must be much smaller than cell size to account the interaction between phases accurately (Chu et al. 2017, Nikolopoulos et al. 2017). It is recommended in the literature (Loth 2010, Chu et al. 2017, Nikolopoulos et al. 2017) that for CFD-DEM the mesh size should be larger than particle diameter to avoid granular volume fraction larger than 1, and for the Eulerian-Granular model, the mesh size should be as large as 10 times the particle size.

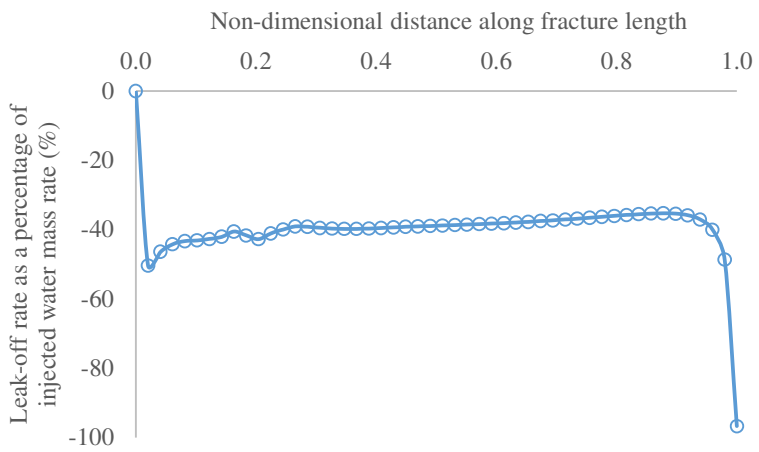

Figure 4.3: Fluid leak-off rate at fracture wall along the fracture length

The viscosity of the granular phase is calculated from the Gidaspow, Bezburuah and Ding (1991) correlation as described earlier in section 0. The primary role of granular viscosity is used to consider the frictional losses. The frictional viscosity refers to the shear viscosity based on the viscous-plastic flow and is calculated using the Johnson and Jackson (1987) correlation (section 0). The packing limit defines the maximum volume fraction of the granular phase. For the uniform proppant size, this value is equal to 0.63. Friction packing limit refers to a threshold volume fraction at which the frictional regime becomes dominant, and friction packing limit of 0.5 is used. In the Eulerian-Granular method, the drag force used to model the interaction between the two phases is based on Gidaspow drag law, as described in section 3.2.1.2. The collision between the proppant particles is modelled using the restitution coefficient and KTGF, as explained earlier in sections 3.2.1.5-3.2.1.8.

Table 4.1: Physical properties of proppant and fluid used in the simulation

Properties	Value
Proppant diameter	1 mm
Proppant density	2650 kg/m^3
Fluid density	1000 kg/m^3
Fluid inlet velocity	0.5 m/s
Fluid viscosity	0.001 Pa-s (1 cP)
Proppant volume fraction	0.20

On the other hand, for CFD-DEM modelling, the time step used for continuous phase CFD modelling was 1.0E-3 s, and for discrete phase was 1.0E-6 s, which is three orders of magnitude higher. Thus, this approach is computationally expensive. The time step was selected based on the numerical stability and convergence of the solution using the Eq. (3.41), Eq. (3.42) and Eq. (3.44) described earlier in section 3.2.2.2. To accurately model the inter-particle collision, DEM collision with the spring-dashpot model was used in the normal and tangential direction as explained earlier. The top, bottom walls and fracture tip were specified as no-slip stationary walls for the liquid phase, as shown in Figure 4.1. For the particle phase, the reflect boundary condition with specularity constant of 0.01 and wall reflection coefficient of 0.9 in both normal and tangential directions was used to model the particle-wall collision (Benyahia, Syamlal and O'Brien 2005, Ehsani et al. 2015, Li, Zhang and Lu 2018). Finally, the Phase-coupled SIMPLE algorithm is used as a solution method for the pressure-velocity coupling (section 3.3.3). The discretisation of momentum, volume fraction, and turbulent kinetic energy was solved by the second-order upwind scheme, as explained earlier in section 3.3.3.

4.3 Results and discussion

4.3.1 Comparison with the experimental results

The present simulation model was compared against the experimental study of Tong and Mohanty (2016). Tong and Mohanty (2016) performed an experimental study of proppant transport in fracture slots. The experiment consisted of two transparent fracture slots, as shown in Figure 4.4. The main fracture slot is called as a primary fracture slot, and the bypass fracture slot is called as a secondary fracture slot. The slick water slurry with the suspended proppants is injected using a progressive cavity pump and sand funnel through the inlet located at the right end of the main fracture slot, as shown in Figure 4.4. The fracturing fluid slurry (water +

proppants) is injected at the inlet. Water is used as a fracturing fluid with viscosity 1 cP and density 1000 kg/m^3. The proppant transport was monitored and recorded with cameras as shown in Figure 4.4. The simulation was performed with the geometry similar to the experimental setup. All the modelling parameters are presented in Table 4.2, which are similar to experimental parameters. Eulerian-Granular multi-phase flow model was used. Fracturing fluid (water, in this case) along with the proppant is injected at the inlet.

Figure 4.5 shows a comparison of experimental and simulation results in terms of proppant deposition at the fracture bottom in primary and secondary fracture slots at three different time periods after the start of injection. The results from Figure 4.5 show that the current numerical model simulates the proppant distribution similar to the experimental results. In order to quantitatively compare the results, two dimensionless parameters were calculated namely, non-dimensional proppant equilibrium height and non-dimensional proppant bed length. The non-dimensional proppant equilibrium height is the normalized proppant bed height and the non-dimensional proppant bed length is the normalized proppant bed length calculated at the centre of proppant bed. The results between numerical modelling study and experimental study were compared in terms of non-dimensional proppant equilibrium height and non-dimensional proppant bed length at the centre and plotted in Figure 4.6. The results from Figure 4.5 and Figure 4.6 suggests a reasonable match between the experimental study and the current model. The average error calculated is 5.8% and 7.5% for non-dimensional proppant equilibrium height and non-dimensional proppant bed length respectively, which suggests an overall good match and the simulation model can be used to perform further analysis of proppant distribution in the slick water fracturing fluid.

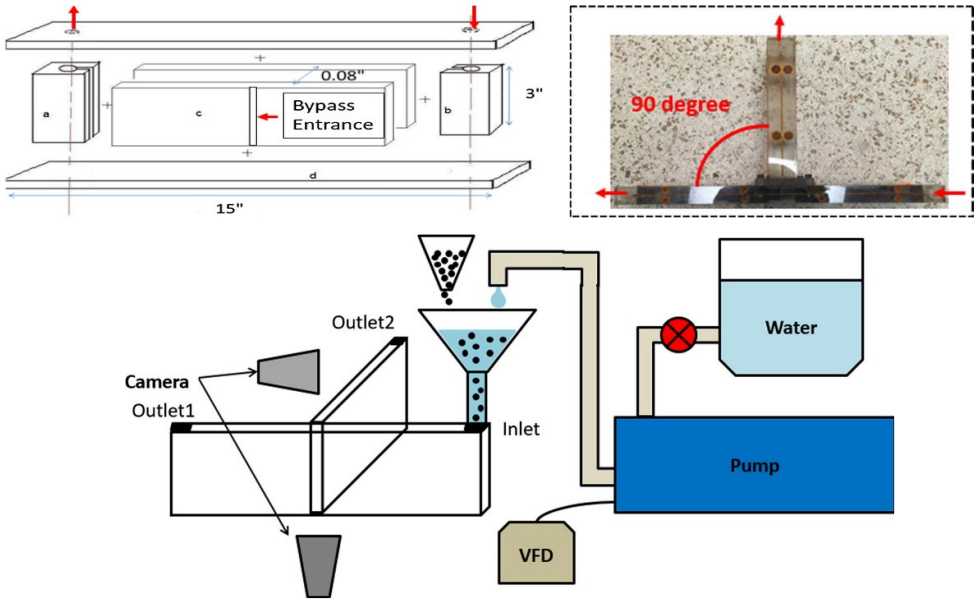

Figure 4.4: Schematic of the proppant transport fracture slot experiment (Tong and Mohanty 2016)

Table 4.2: Simulation parameters for model validation

Simulation parameters	Value
Fracture dimensions, L×W×H (m)	0.381 × 0.0762 × 0.002 (primary slot) 0.1905 × 0.002 × 0.0762 (secondary slot)
Proppant diameter (µm)	600
Proppant density (kg/m^3)	2650
Fluid density (kg/m^3)	1000
Fluid inlet velocity (m/s)	0.2
Fluid viscosity (cP)	1
Injection time (s)	20,40,60

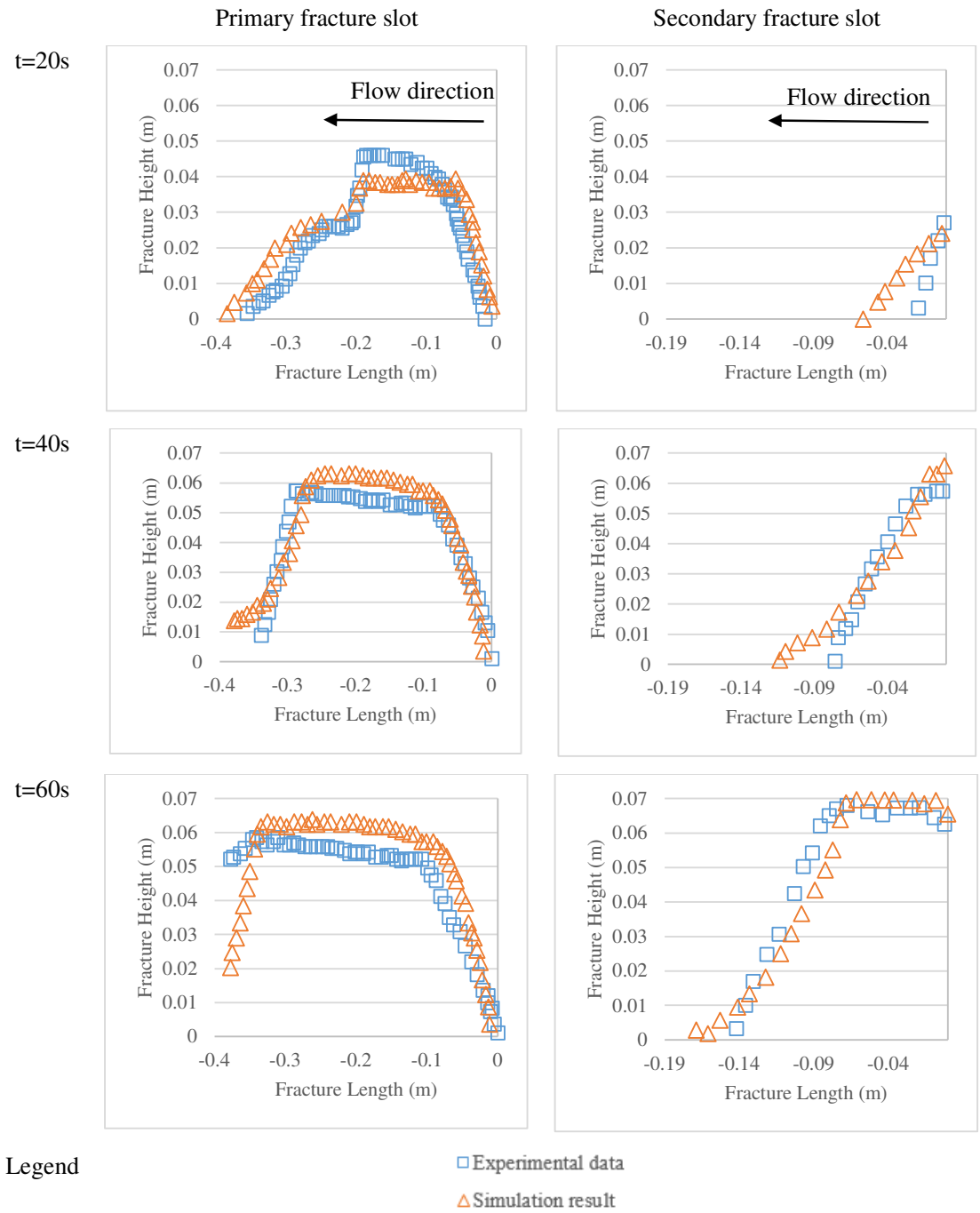

Figure 4.5: Comparison of experimental and numerical results in terms of proppant deposition at the fracture bottom in primary and secondary fracture slots at different time steps

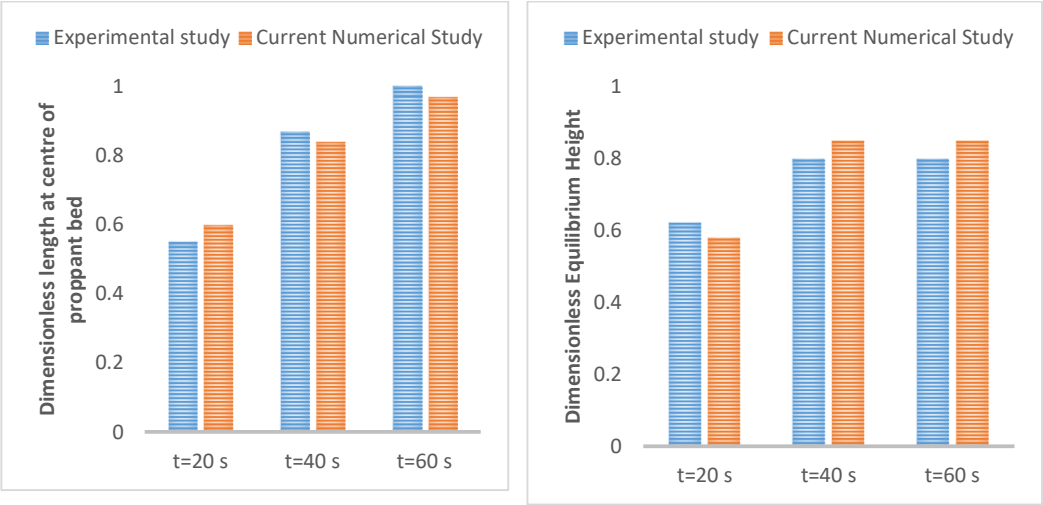

Figure 4.6: Quantitative comparison of numerical results with experimental results

4.3.2 Results from fluid leak-off modelling

Fluid leak-off is one of the critical phenomena that govern the proppant suspension in the slurry. As the fracturing fluid slurry is injected in the fracture, the fracturing fluid leaks off from the fracture wall to the surrounding porous rock at a rate depending upon the reservoir characteristics. The remaining proppants in the slurry have a tendency to deposit and form proppant bed at the fracture bottom. The higher leak-off rate can result in a greater flow of thin fracturing fluid to the surrounding reservoir rock, leaving behind the proppant in the remaining slurry and consequently early deposition of the proppants. The fluid leak-off depends on the reservoir characteristics (porosity and permeability). The simplest model to take into account the fluid leak-off is defined by Carter (1957), which describes the leak-off rate depends on a mathematical constant and elapsed time. Leak off effects play a vital role in shale reservoirs where due to the use of thin fracturing fluid, the ability to suspend the proppants is considerably low. Furthermore, greater fluid leak-off from the fracture wall will increase the rate of proppant bed formation and early fracture tip screen out, which is a common failure in hydraulic fracturing design noticed in the oil industry. Fracture tip screen out occurs when proppant in fracturing fluid, create a bridge inside the fracture and prevents any further transport of proppant and fluid, resulting in a rapid increase in pump pressure. The fracture tip screen out inhibits any further proppant transport into the fracture, and the unpropped section of the fracture will close down, resulting in loss of fracture conductivity. The fracturing fluid leak-off from the fracture wall is ignored in the existing numerical proppant transport modelling studies, as explained earlier in chapter 2, resulting in inaccurate flow and transport properties of proppants.

The effect of fluid leak-off from the fracture wall in the proppant distribution was investigated by comparing it with a simulation case with no fluid leak-off effect. The results were compared based on the variation of proppant volume fraction and proppant horizontal velocity, as shown in Figure 4.7 and Figure 4.8. The proppant volume fraction and proppant horizontal velocity were calculated at two different longitudinal locations from the inlet x=0.25 m and x= 1.2 m and results were plotted against the fracture height at t=2 s (Figure 4.7 and Figure 4.8). The results show that as the fluid leaks off the fracture wall, leaving the proppants in the remaining slurry, it increases the tendency for the proppants to settle at fracture bottom and forms a bed. Thus, comparatively greater proppant bed height is noticed in the fluid leak-off case against the no leak-off case. Furthermore, comparing the proppant horizontal velocity suggests that the lower value of the horizontal velocity of proppants is noticed in the fluid leak-off case against the no fluid leak-off case. This can be explained by the greater tendency of the proppants to settle down at the fracture bottom and thus have lower horizontal transport velocity. The comparison study of fluid leak-off effect with no fluid leak-off effect suggests that the proppant bed height will be under predicted by 10-50% if the leak-off effects are ignored in the proppant transport model and can significantly impact the hydraulic fracture design.

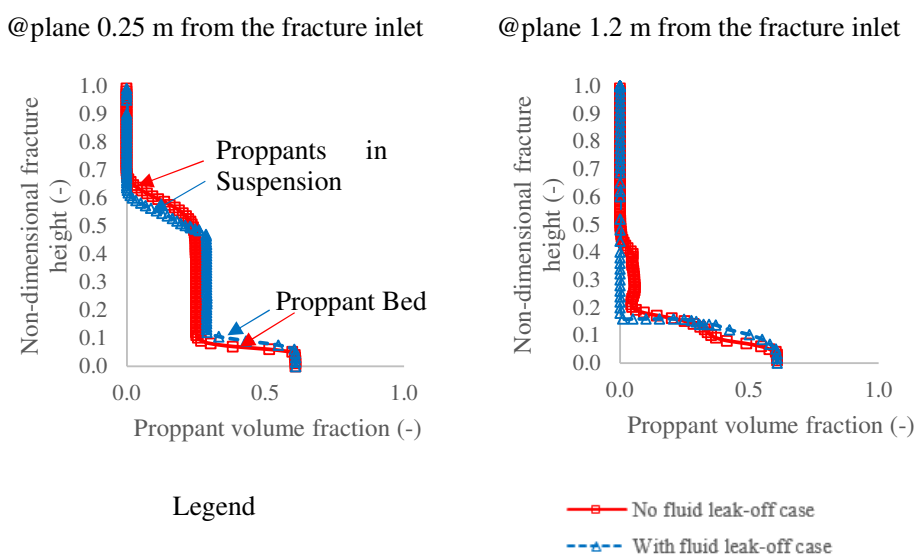

Figure 4.7: Comparison of proppant volume fraction at t=2 s

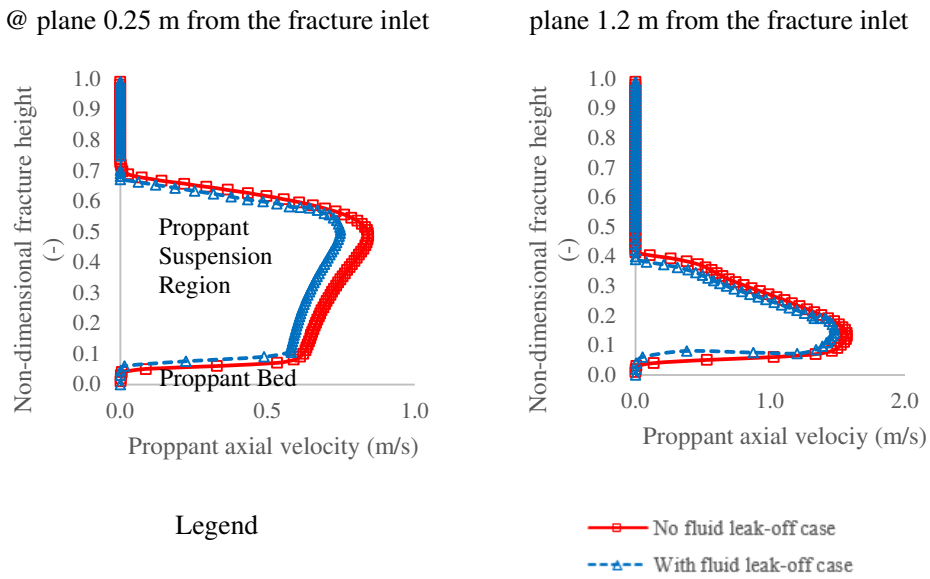

Figure 4.8: Comparison of proppant horizontal velocity at t=2 s

4.3.3 Effect of proppant size

The proppant size was varied, keeping all the other parameters constant, and simulation run was performed. The three cases of variation in proppant diameter studied are diameter = 0.3 mm, 0.5 mm and 1 mm. Figure 4.9 and Figure 4.11 are the contour plots of proppant volume fraction and proppant horizontal velocity respectively at fracture mid-plane for different time step and all the three cases of variation in proppant sizes. It shows the difference in proppant distribution inside the fracture with time. It can be interpreted from Figure 4.9 that greater particle deposition is noticed for proppants with greater size, or in other words, the greater size proppants tends to settle more quickly. This is due to as the proppant size increases, it increases vertical settling velocity, thus as the particles get larger, the tendency for deposition increases. On the other hand, the smaller size proppants have a lower settling velocity in the vertical direction and occupy greater volume in the suspending region.

Next, the proppant volume fraction and proppant horizontal velocity were calculated at two different locations in the longitudinal direction from the inlet at 0.25 m and 0.8 m. The results were plotted with the fracture height to investigate the advancement of proppant volume fraction with time (Figure 4.10 and Figure 4.12). The results from Figure 4.10 show that the proppant volume fraction is identical for all the cases at the beginning, but later with time, the smaller size proppant particles (0.3 mm and 0.5 mm) are more suspended and fill a larger volume of the fracture, while the bigger size particles show greater deposition. The results from Figure 4.12 show that the proppant horizontal velocity profiles initially at t=0.5 s is similar for all the three

cases. However, later with the progression of time, close to the wellbore (x=0.25 m from inlet), the greater size proppants are moving with higher velocity. However, away from the wellbore (x=0.8 m from inlet), the greater size proppants appear to move slowly compared to the smaller size proppants. This velocity lag of greater size proppants away from the wellbore can be attributed to the higher drag forces experienced in comparison to the smaller size proppants. Consequently, the smaller size proppants are transported to a more considerable distance with the fluid flow. The reverse flow in the velocity profiles is due to the proppants after colliding with the fracture wall, moves in the reverse direction. Thus, the greater reverse flow velocity of smaller size proppants observed in Figure 4.11 explains that a higher number of smaller size proppants colliding the fracture wall with higher velocity and rebounding back in the suspension layer.

The parametric study of the proppant distribution to particle diameter suggests that it can play a significant role in optimising fracture conductivity. One effective approach, for low viscosity fluid-like slick water, could be injecting the smaller size proppant particles first in the slurry displaced by larger size proppant particles for distributing the higher volume of the fracture with proppants. To understand the effect of multisize proppant injection, smaller proppants with diameter 0.3 mm were injected for 0-1 s followed by 0.5 mm proppant diameter for 1-2 s and 1 mm proppant diameter for 2-3 s respectively (Figure 4.13-Figure 4.14). It can be observed that as the smaller proppant has a greater tendency for suspension and are injected prior to the larger proppant, thus multisize proppant injection results in improved distribution and can lead to more uniform fracture conductivity. Tsai et al. (2012) also reported similar observations in their study with different proppant size.

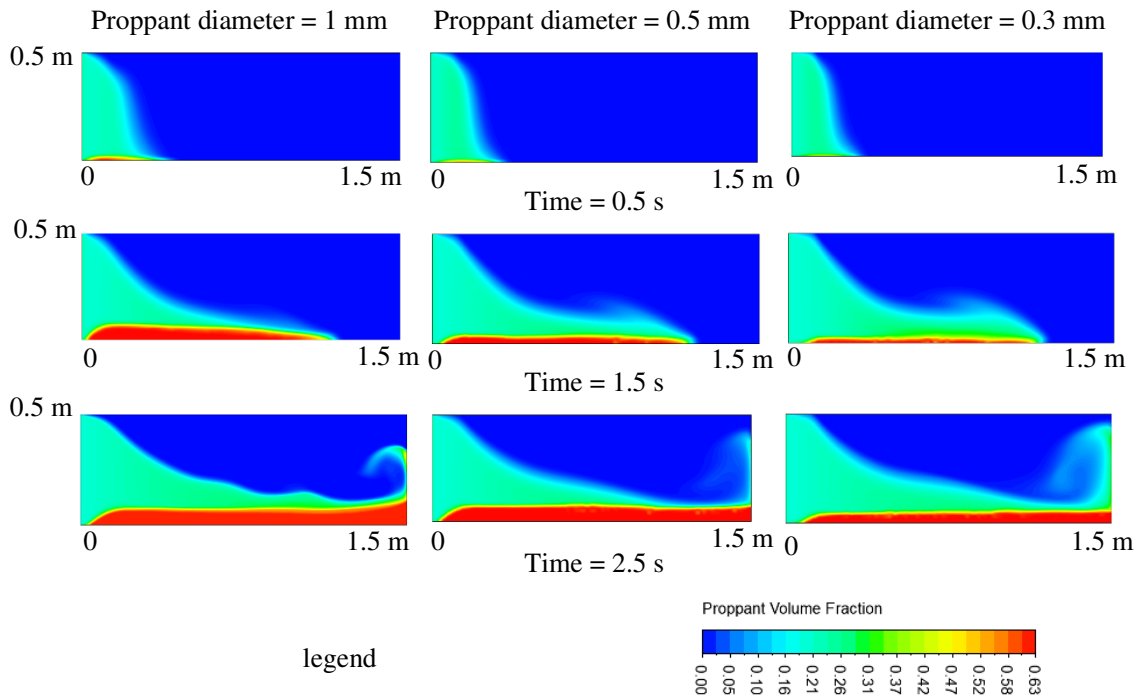

Figure 4.9: Effect of proppant diameter on proppant volume fraction

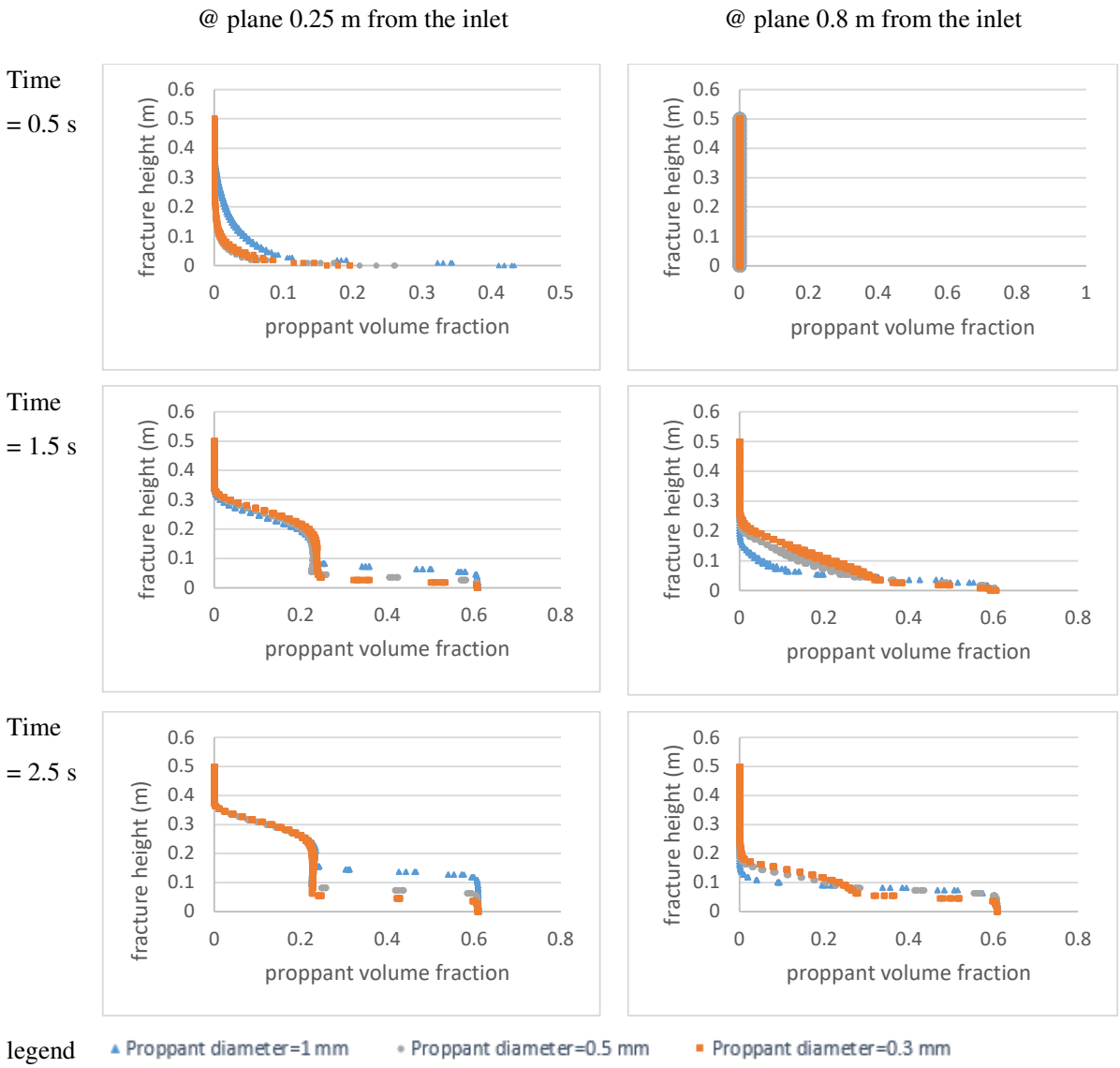

Figure 4.10: Comparison of proppant volume fraction with time for different proppant size

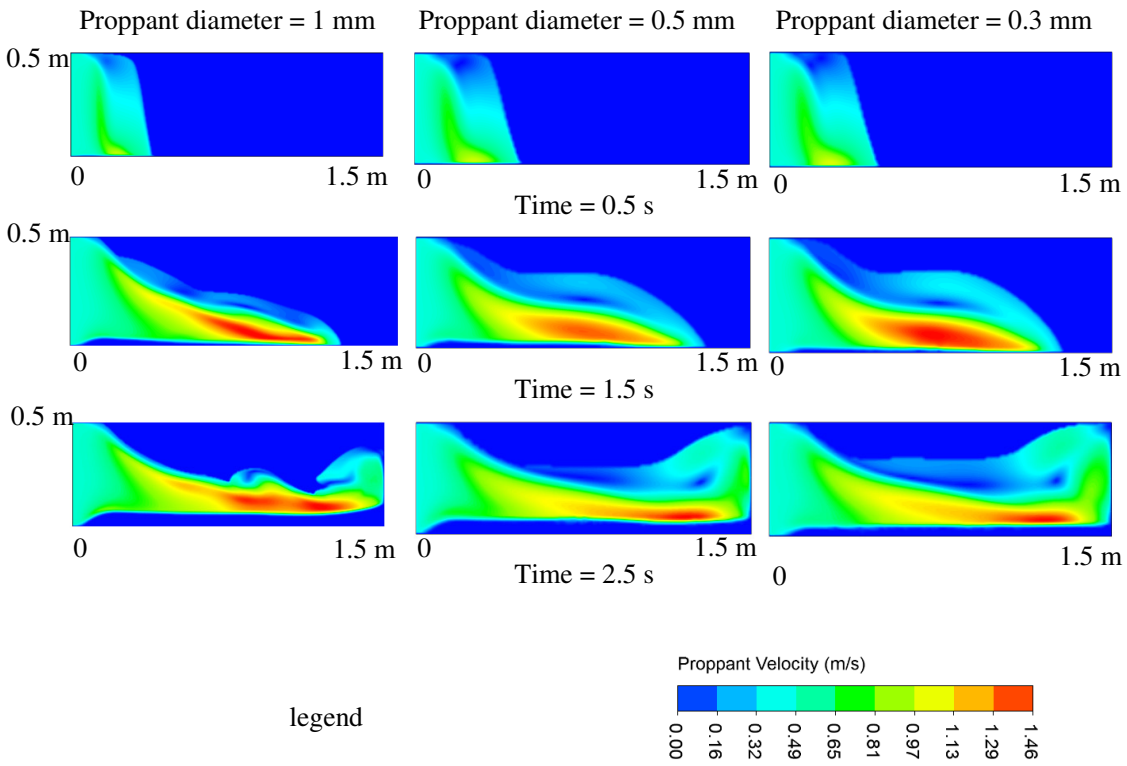

Figure 4.11: Effect of proppant diameter on proppant horizontal velocity

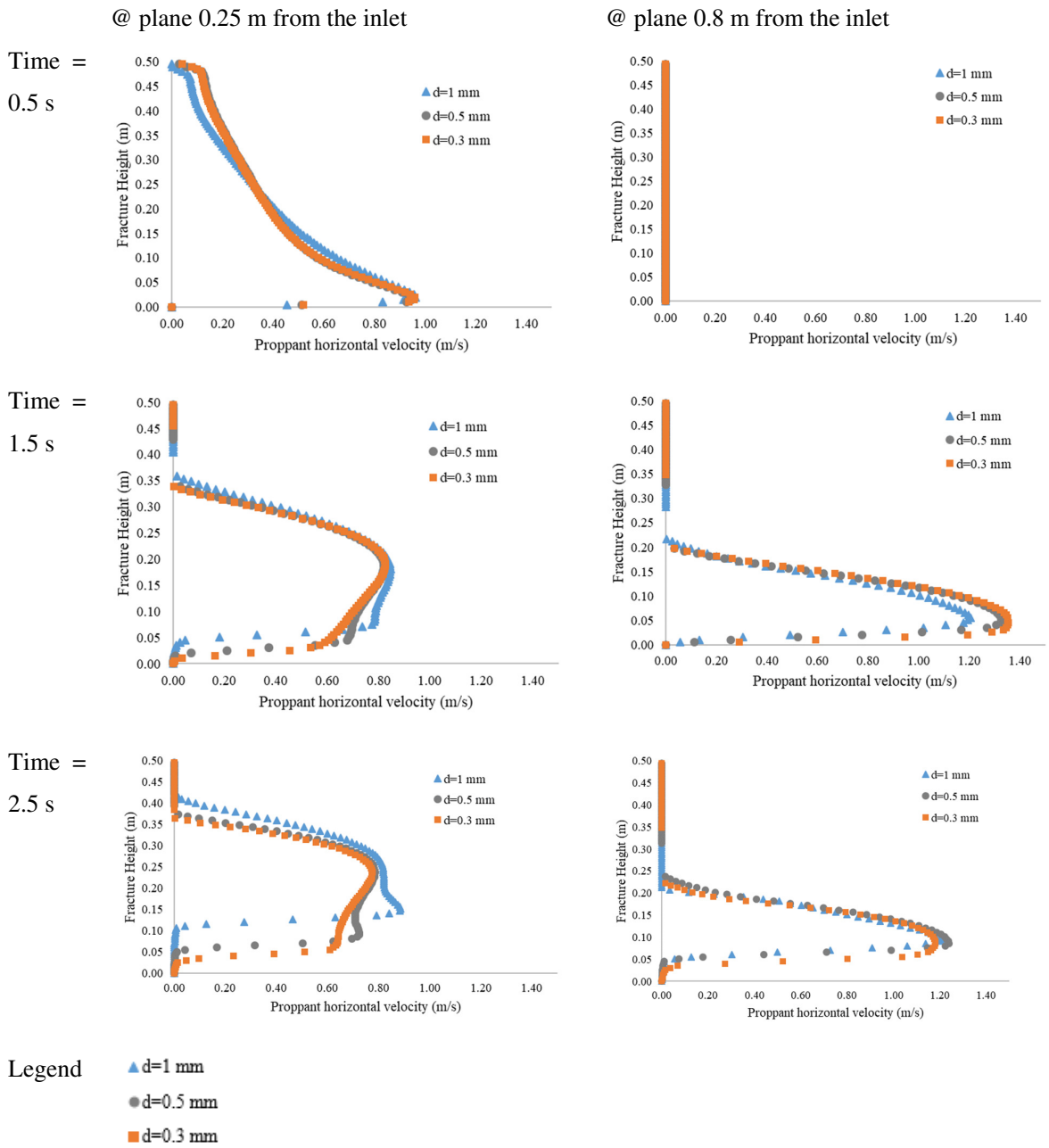

Figure 4.12: Variation of proppant horizontal velocity with time for different proppant size

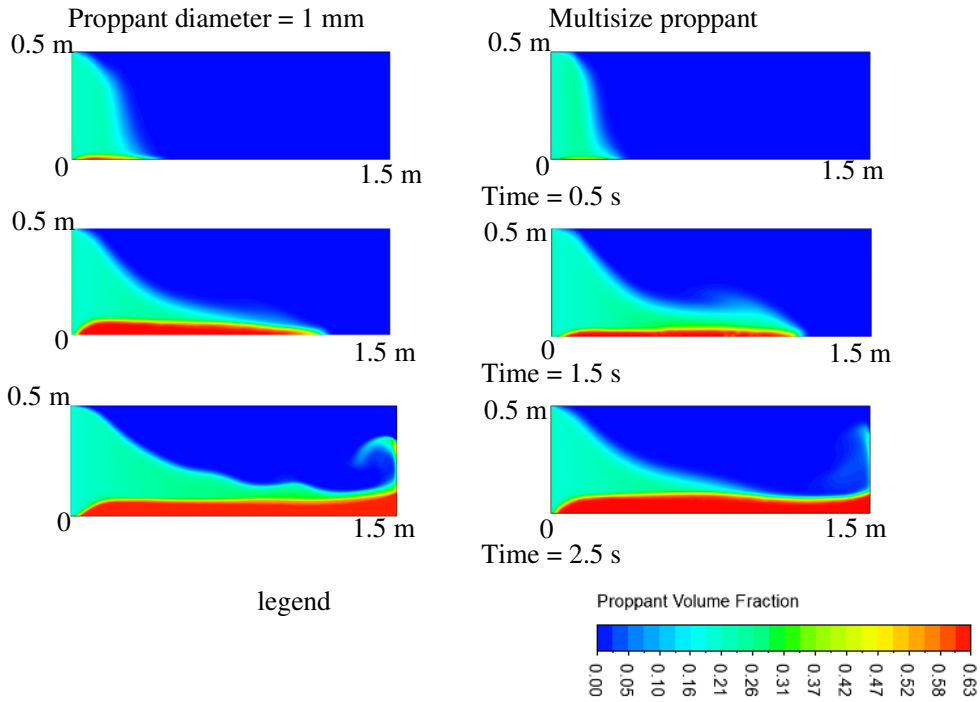

Figure 4.13: Effect of multisize proppant injection on the proppant volume fraction

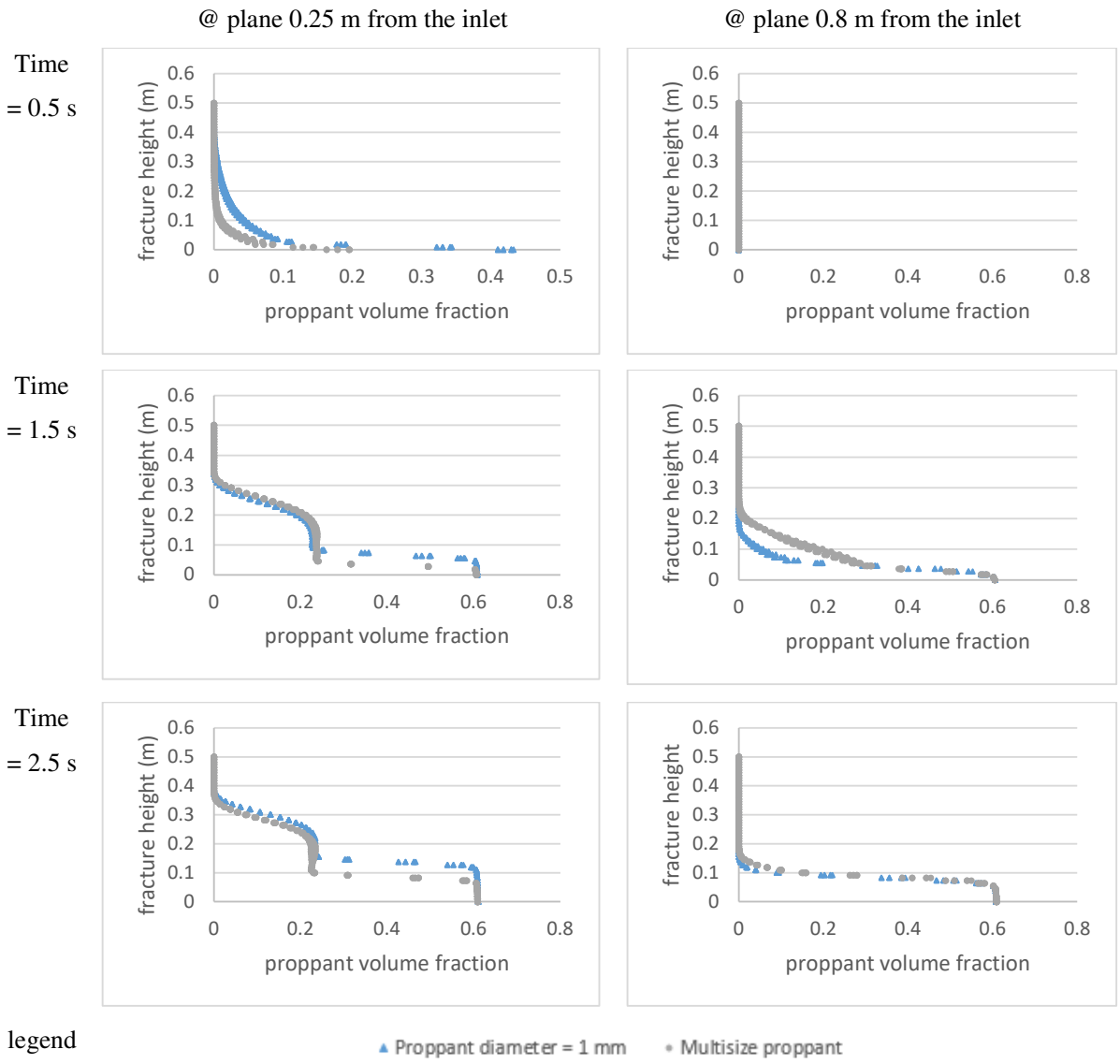

Figure 4.14: Comparison of multisize proppant injection and base case (d = 1 mm)

4.3.4 Effect of fluid viscosity

In the next study, the fluid viscosity was varied, keeping all the other parameters constant, and simulation run was performed. The three cases of variation in fluid viscosity studied are μ= 1 cP, 10 cP and 100 cP. Figure 4.15 and Figure 4.17 are the contour plots of proppant volume fraction and proppant horizontal velocity respectively at fracture mid-plane for different time step showing all the three cases of variation in fluid viscosity. It can be interpreted from the contour plots that particle deposition is much dependent on the fluid rheological property. With the increase in the viscosity of the fracturing fluid, the percentage of the proppant deposition decreases substantially. This is due to the increasing viscous forces that provide more flow resistance and drag force on the proppant particles. As a consequence, higher viscosity fracturing fluid prevents proppant particles from depositing. This observation is evident in Figure 4.15 that for the simulation case of 100 cP fracturing fluid viscosity, the proppants deposition is considerably low.

Next, the proppant volume fraction and proppant horizontal velocity were plotted with the fracture height and the advancement of proppant volume fraction with time at the two-different vertical planes was analysed (Figure 4.16 and Figure 4.18). The results from Figure 4.16 show that the proppant volume fraction is identical for all the cases at the beginning, but later with time, low viscosity fracturing fluids result in greater proppant deposition compared with high viscosity fracturing fluids. The results from Figure 4.18 show that the proppant velocity profile is significantly dependent on the fracturing fluid viscosity. With the progress of time, closer to the wellbore (0.25 m from inlet), the proppant flow in high viscous fracturing fluid lags behind compared to the low viscous fracturing fluid. This can be attributed to the higher viscous resistance force provided by the high viscosity fracturing fluid, which promotes the suspension ability of the proppants and retards the proppant deposition. Whereas, far from the inlet, the proppant horizontal velocity with high viscosity fracturing fluid is slightly greater than the low viscosity fracturing fluid, which suggests the higher tendency of the high viscosity fracturing fluid to transport proppant to a longer distance. This parametric study results in an important conclusion that the proppant transport, distribution and settling is substantially dependent on the fracturing fluid viscosity. Highly viscous fracturing fluids impede the proppant deposition.

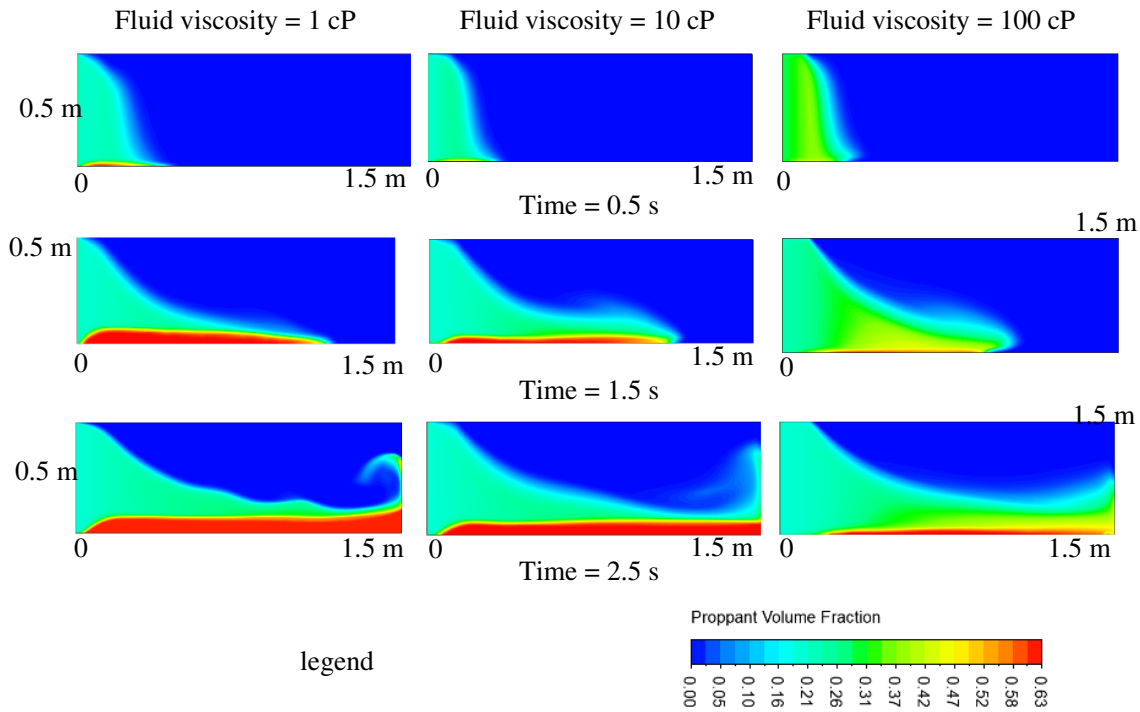

Figure 4.15: Variation of fluid viscosity on the proppant volume fraction

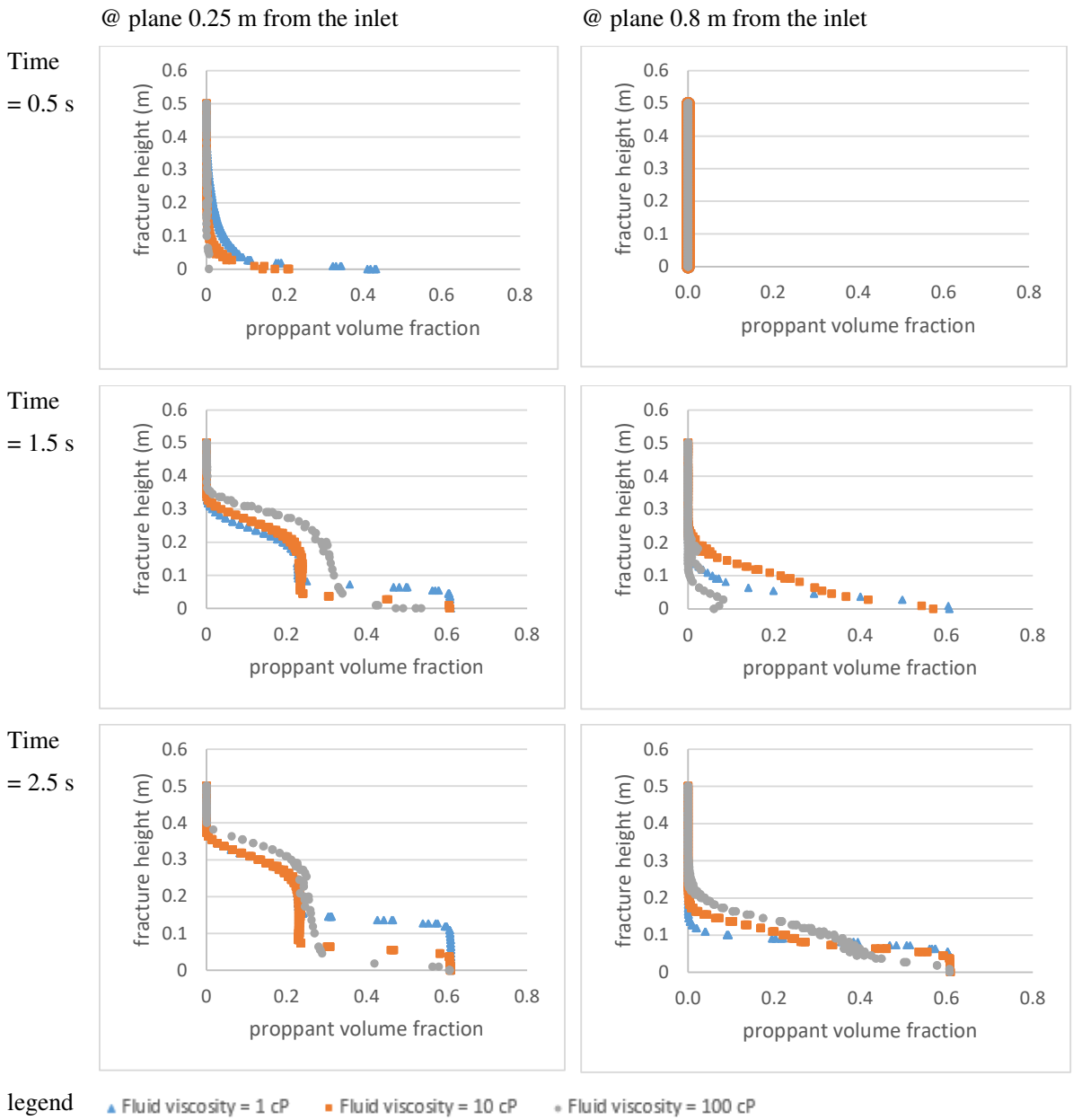

Figure 4.16: Variation of proppant volume fraction with time for different fluid viscosity

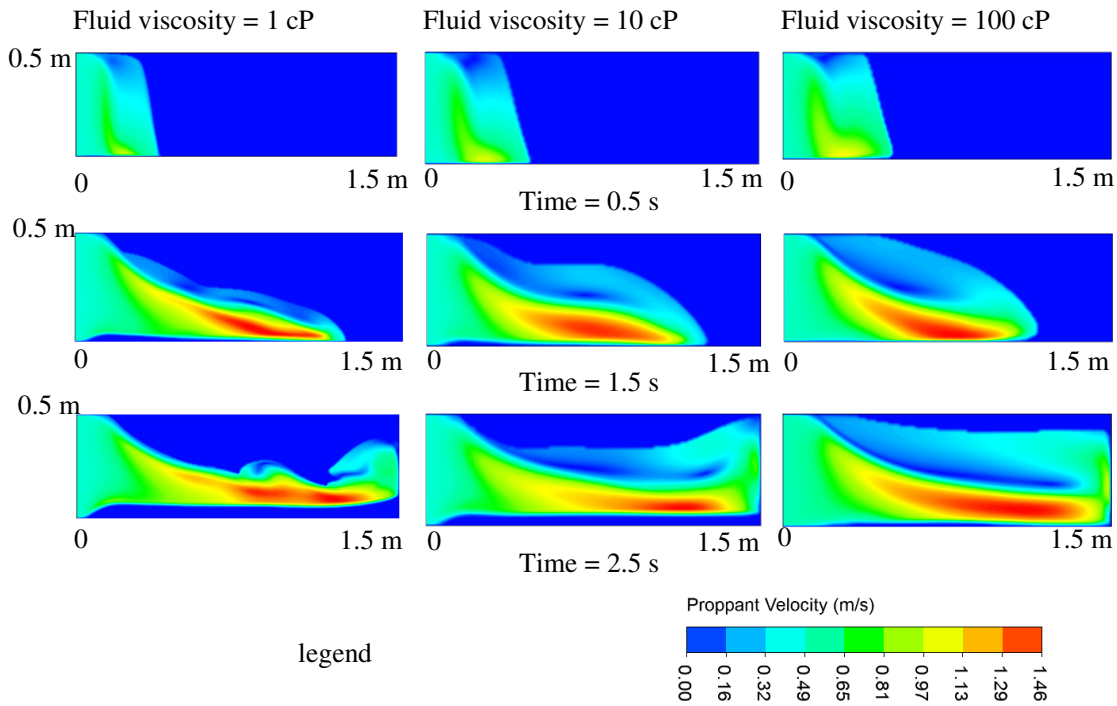

Figure 4.17: Effect of fluid viscosity on proppant velocity

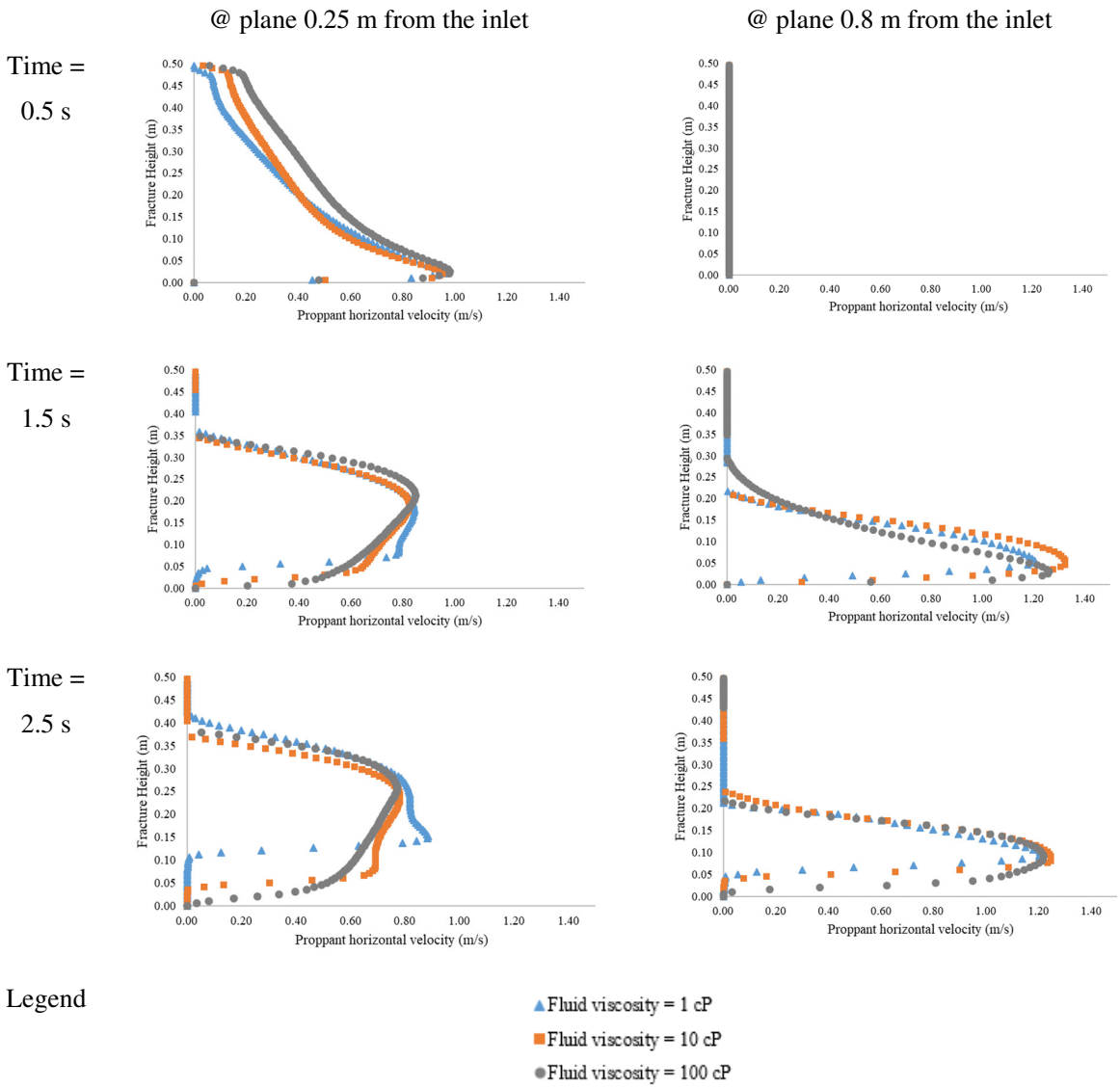

Figure 4.18: Variation of proppant horizontal velocity for different fluid viscosity vs time

4.3.5 Effect of fracture width

In the next study, the fracture width was varied, keeping all the other parameters constant, and simulation run was performed. The three cases of variation in fracture width studied are width= 0.01 m, 0.05 m and 0.005 m. Figure 4.19 and Figure 4.21 are the contour plots of proppant volume fraction and proppant horizontal velocity respectively at fracture mid-plane for different time step and shows all the three cases of variation in fracture width.

Two important observations can be made. Firstly, the difference in proppant distribution is less pronounced initially at time=0.5 s, and the effect of the fracture width is visible only at later times as the flow progresses. And secondly, the smaller width leads to greater wall resistance to the flow. As a result, the proppant in the lower fracture width case tends to deposit quickly, leading to a greater height of the dune formation. On the other hand, for the greater fracture width results in lower wall resistance, leading to the proppant particles travelling farthest and covers maximum volume.

Next, the time evolution of proppant volume fraction and proppant horizontal velocity was plotted with the fracture height and shown in Figure 4.20 and Figure 4.22. An important observation that can be noticed in Figure 4.20 is that for the cross-section of 0.25 m from the inlet and lower fracture width case (0.005 m), higher proppant deposition and suspension characteristics is observed. This is because the lower fracture width due to greater wall resistance tends to form higher particle dune. On the contrary, for the cross-section of 0.8 m from the inlet and lower fracture width case (0.005 m), lower proppant deposition characteristics are noticed. This is due to unlike higher fracture width case, the proppant in lower fracture width do not tend to spread to the higher volume of the fracture, thus resulting in lower concentration away from the wellbore. The results from Figure 4.22 show that the fracture width plays a significant role in the proppant velocity profile. The proppant velocity for the lower fracture width is considerably lower compared with greater fracture width. At t=1.5 s, away from the wellbore (0.8 m from inlet), the proppant horizontal velocity is almost three times higher for fracture width=0.05 m compared with fracture width of 0.005 m. This can be attributed to the lower fracture width results in greater wall resistance and consequently, higher proppant deposition.

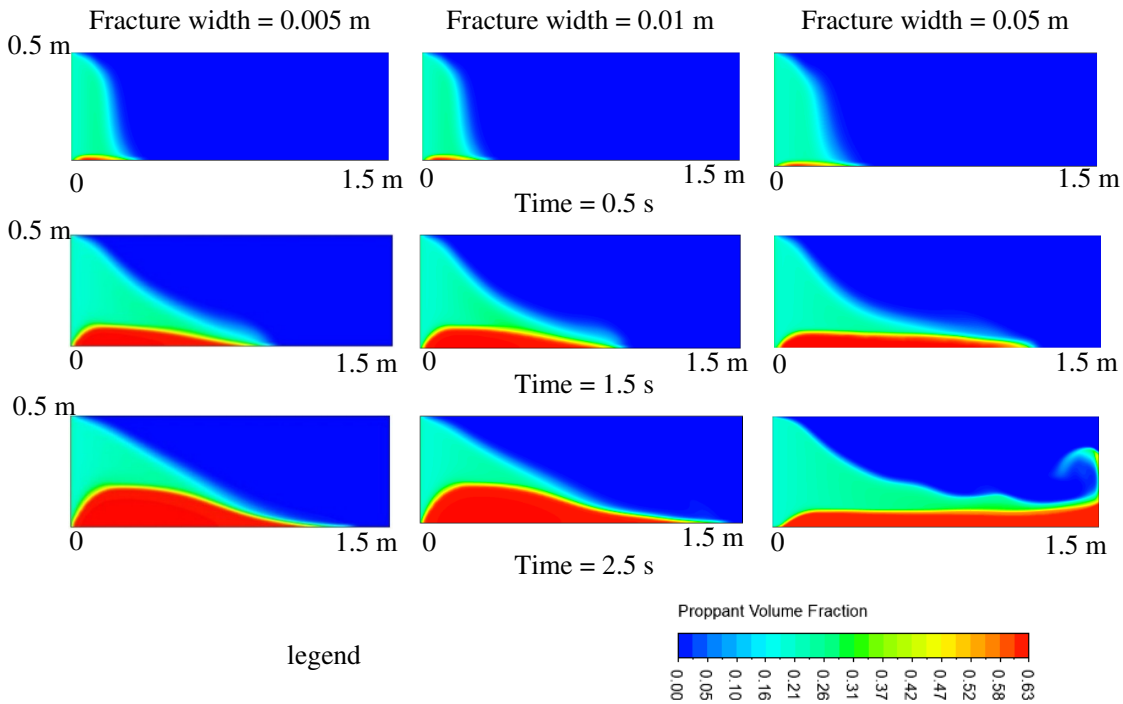

Figure 4.19: Variation of fracture width on the proppant volume fraction

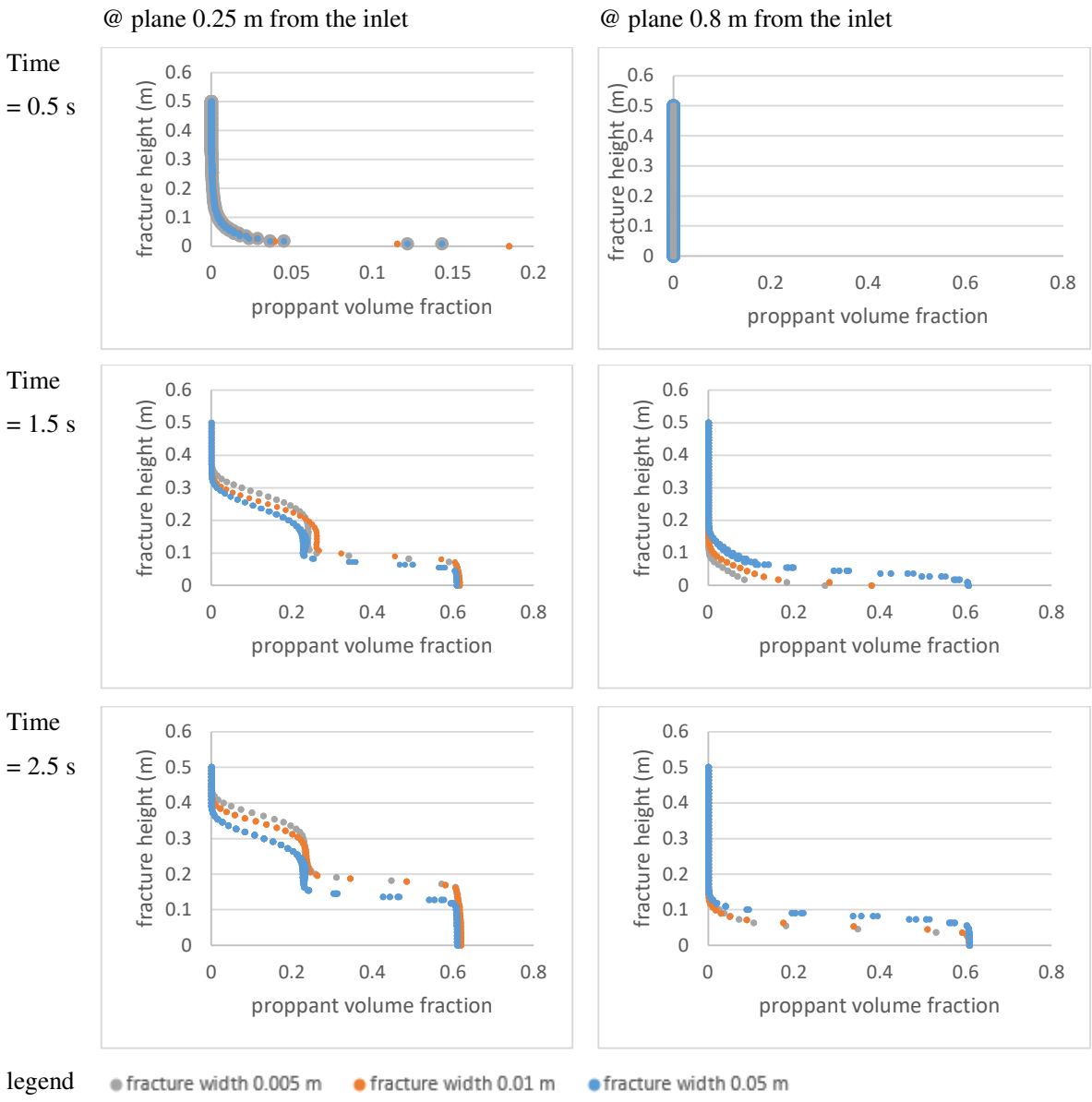

Figure 4.20: Time evolution of proppant volume fraction for different fracture width

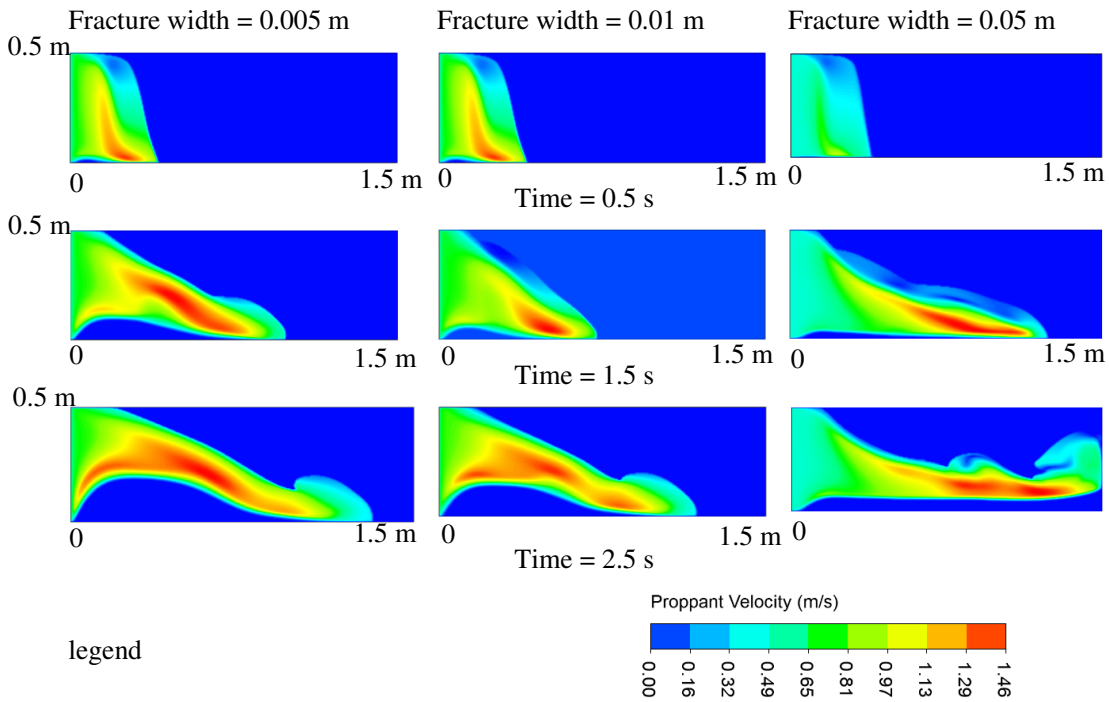

Figure 4.21: Contour plot showing the variation of fracture width on the proppant velocity

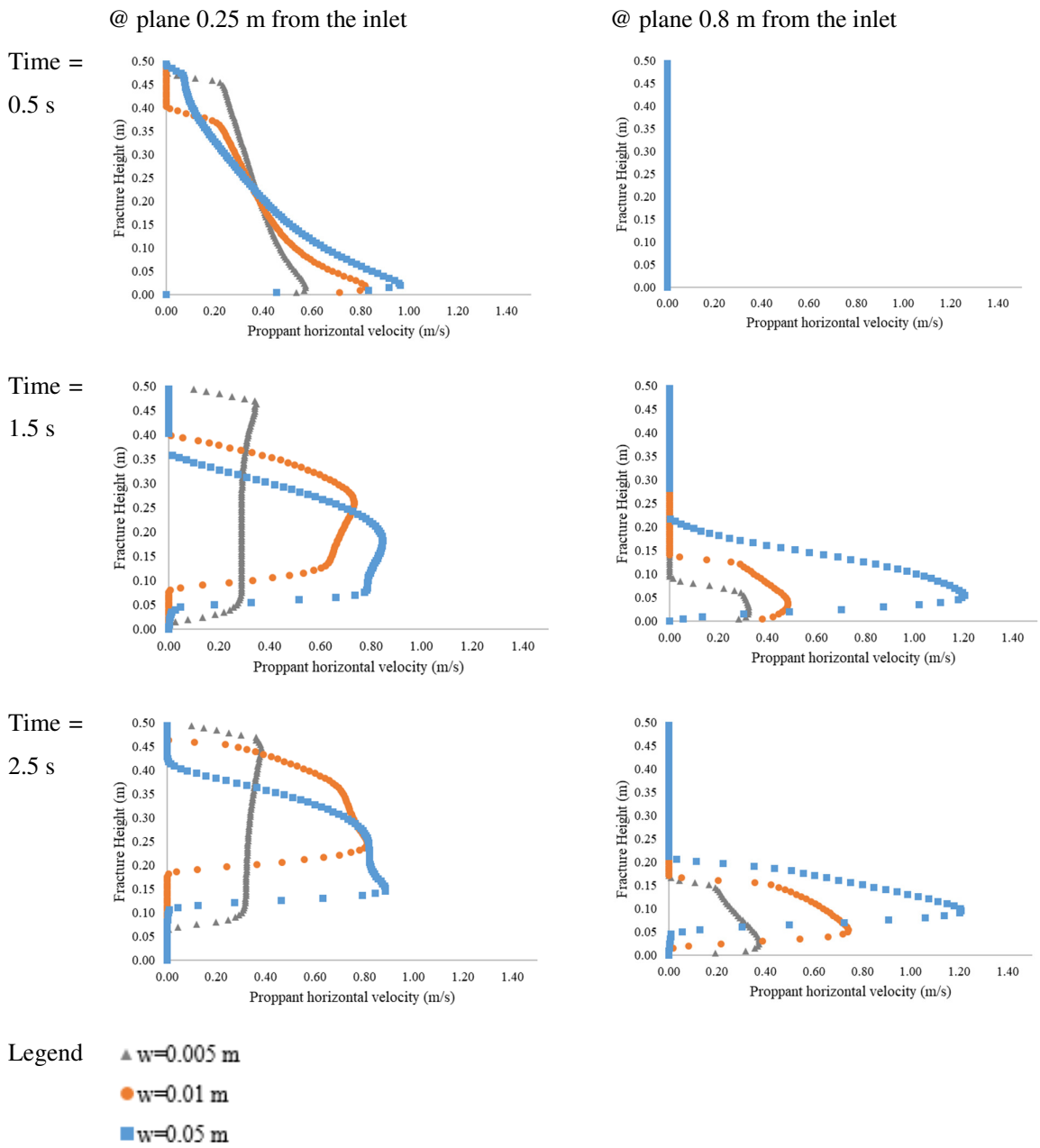

Figure 4.22: Variation of proppant horizontal velocity for different fracture width vs time

4.3.6 Comparison of Eulerian-Granular method with Discrete Element Model

To understand the difference in proppant distribution between Eulerian-Granular method and CFD-DEM method, a separate study was carried out using an inlet velocity of 0.1 m/s and proppant volume fraction of 0.15. All the other simulation parameters were the same as described earlier in Table 4.1. Figure 4.23 shows the comparison of Eulerian-Granular and DEM methods. The DEM model as explained in chapter 3, tracks the proppant trajectory at each iteration and implicitly calculates the inter-proppant interaction and proppant-fluid interaction to capture a detailed proppant micromechanics. On the other hand, Eulerian-Granular method provides proppant volume fraction, which can act as a substitute for the proppant position, and it uses a semi-empirical relationship to calculate the inter-proppant and fluid-proppant interaction. One of the most significant advantages of using Eulerian-Granular method in proppant transport is that it is computationally economical compared with the DEM model. The time step used in the Eulerian-Granular model was 1.0E-3 s and in DEM model was 1.0E-6 s. In terms of simulation time, for investigation of proppant transport after 5 s of injection, the Eulerian-Granular model required 1 day to solve. On the contrary, the DEM model required 45 days to complete the simulation.

Figure 4.23 compares both the approaches and shows that the particle distribution rate at the suspension layer and fracture bottom in Eulerian-Granular method is significantly different from the DEM method. This can be explained by the different ways in which particle-particle and particle-wall interaction is captured in both these approaches. DEM method models the particle motion explicitly with a detailed inter-proppant and proppant-wall interaction and tends to capture the physical phenomenon comprehensively. On the other hand, the Eulerian-Granular method is based on KTGF and considers the granular particles as continuous media. Thus, it describes more fluid-like behaviour for the proppants and results in higher particle distribution rate at fracture bottom. Proppants modelled using DEM has a greater tendency to collide and suspend in the slurry, resulting in transporting proppant to a longer length, whereas, in the Eulerian-Granular method, the proppant tends to settle quickly and form relatively greater proppant bed.

Figure 4.24 shows the quantitative comparison of Eulerian-Granular and CFD-DEM methods. The proppant volume fraction and axial proppant velocity were plotted with the fracture height, and the time evolution of proppant volume fraction and axial proppant velocity at the vertical cross-section of x=0.25 m and x= 0.8 m from inlet was analysed. It can be observed from Figure 4.25 that the proppant suspension layer for the DEM method is considerably greater at both the cross-section suggesting that the proppant transport using DEM method tends to suspend greater

proppants and can transport proppants to a long distance away from the wellbore, compared with the Eulerian-Granular method. This can be explained by explicit treatment of frictional viscosity and inter-particle interaction in CFD-DEM method, which provides an accurate prediction of proppant distribution inside the fracture. Whereas, as explained earlier, the Eulerian-Granular method considers the granular particles as a continuous phase with a high viscosity. Thus, it describes more fluid-like behaviour for the proppants.

On close observation from the Figure 4.25, which is the plot of proppant horizontal velocity vs fracture height, it shows that at the fracture bottom, the greater proppant velocity observed in Eulerian-Granular method relates to the greater tendency of the proppant to travel away from the inlet and deposit. This can be noticed by the greater proppant deposition in the form of a bed at the fracture bottom in the contour plot for the Eulerian-Granular method (Figure 4.23). On the contrary, the proppant velocity for the DEM method is relatively lower and more uniform in the suspension region compared with the Eulerian-Granular method. This suggests that the suspended proppants due to comparatively more uniform velocity profile possess greater tendency to remain suspended and consequently longer proppant bed length, as evident in the proppant volume fraction contour plot (Figure 4.23). This physical observation can again be explained by the difference in proppant physics between the two methods. The DEM method models the particle motion explicitly with a detailed inter-proppant and proppant-wall interaction and thus results in a greater amount of proppants in the suspension region. The Eulerian-Granular method uses KTGF and considers the granular particles as continuum media. Thus, it describes more fluid-like behaviour for the proppants with a greater tendency to deposit and form a proppant bed. Proppants modelled using DEM has a greater tendency to collide and suspend in the slurry, resulting in transporting proppant to a longer length, whereas, in the Eulerian-Granular method, the proppant tends to settle quickly and form relatively greater proppant bed. In general, from the comparison of both the techniques, it can be interpreted that Eulerian-Granular method provides a reasonable approximation to the proppant particle physics inside the fracture. Considering the significant simulation time required for the DEM method, and applicability for upscaling the model to field-scale hydraulic fractures, this comparison study suggests that Eulerian-Granular method can be used for practical problems of petroleum engineering interests for proppant distribution and settling.

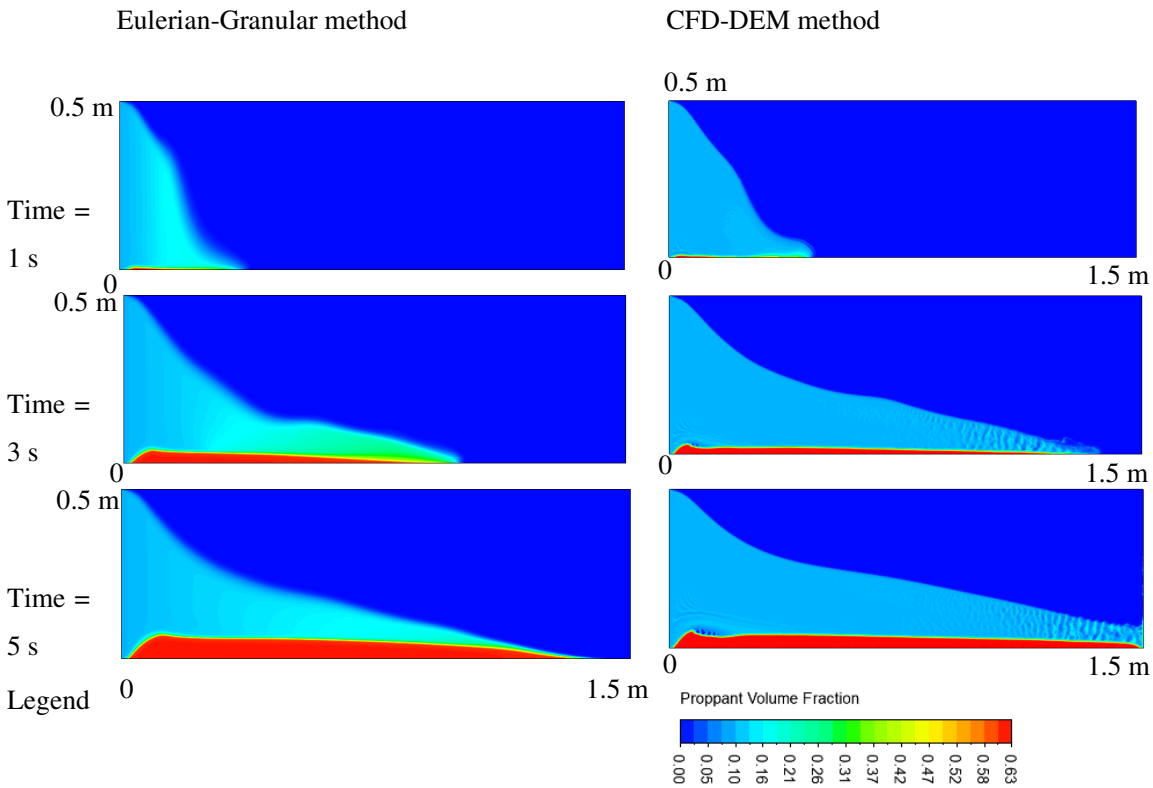

Figure 4.23: Comparison of Eulerian-Granular method and DEM

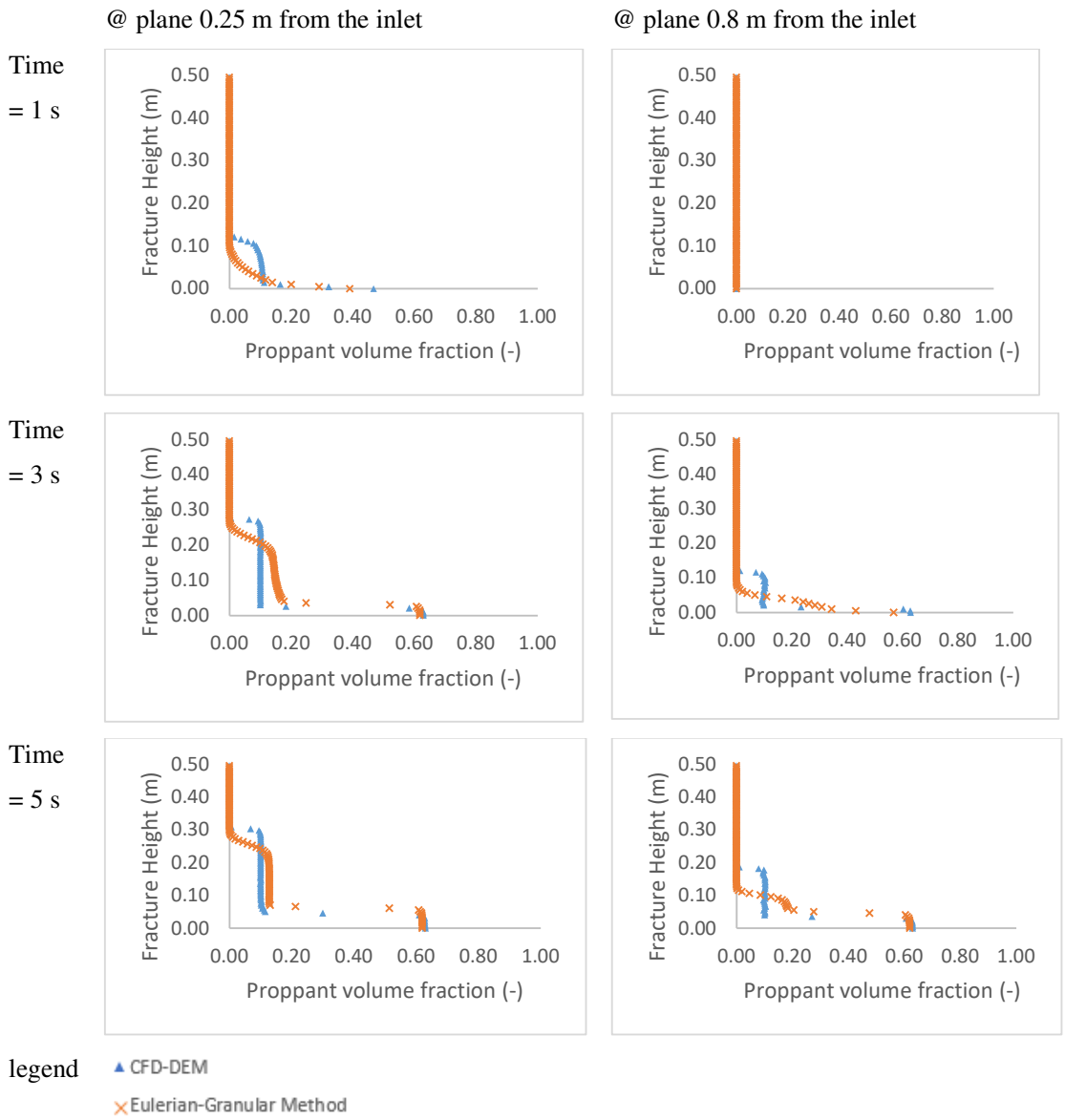

Figure 4.24: Comparison of proppant volume fraction for Eulerian-Granular vs DEM model

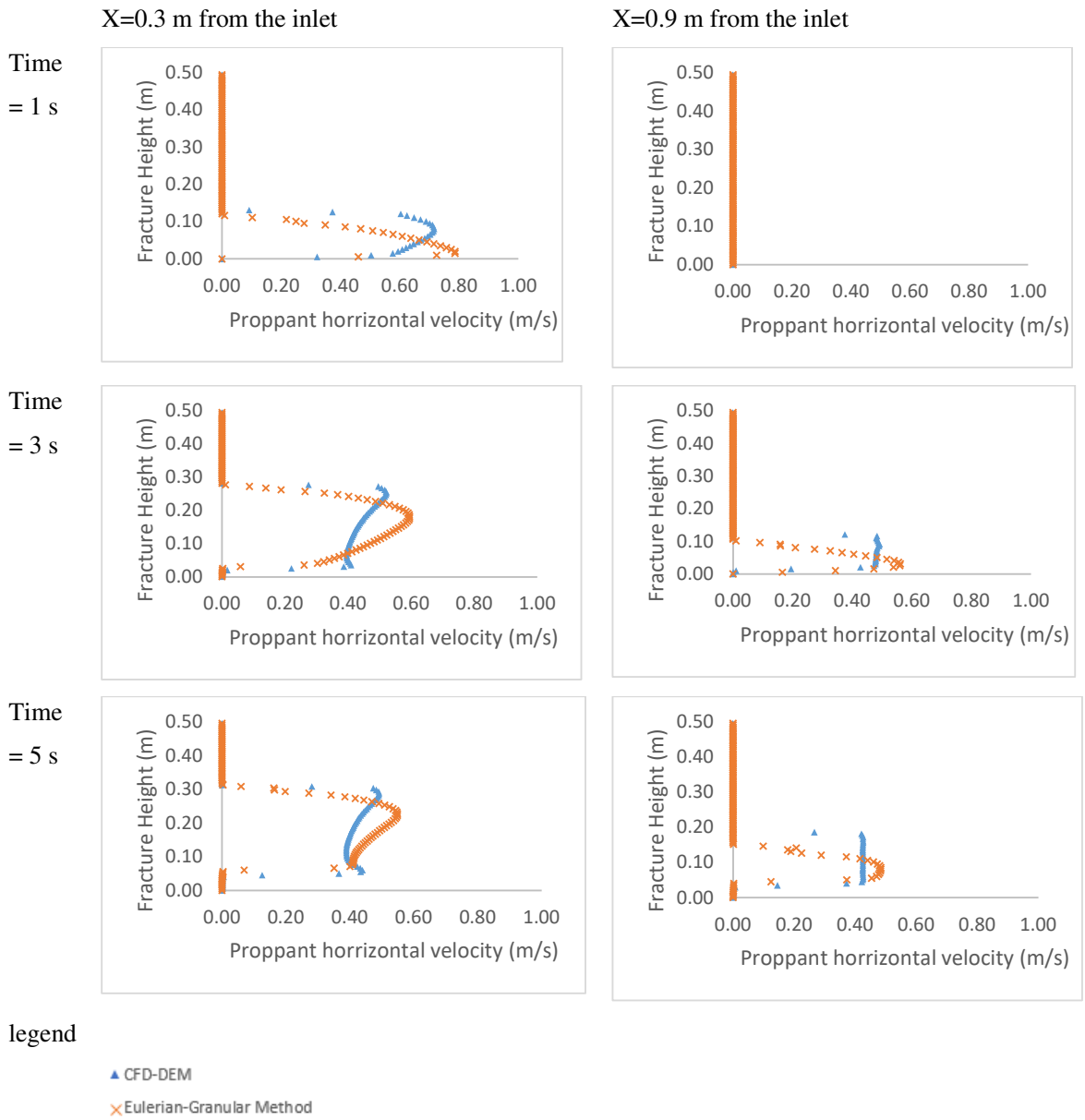

Figure 4.25: Comparison of proppant velocity for Eulerian-Granular vs CFD-DEM model

4.4 Summary of the key findings

Proppant transport study in hydraulic fractures was conducted using the advanced numerical flow modelling methods, namely, Eulerian-Granular method and Discrete Element Method in commercial computational fluid dynamics (CFD) software, ANSYS FLUENT. A user-defined function was defined in order to mimic and model the fluid leak-off rate in the porous reservoir through the hydraulic fracture. It was established by adding the momentum and mass source terms in the flow governing equations.

The results were validated with the reported experimental study and show good agreement. The parametric study was performed to understand the proppant settling and transport mechanism by the variation in proppant properties (proppant diameter), fluid property (fluid viscosity) and geomechanical property (fracture width). The results show that proppant distribution is significantly affected by these properties. Small diameter proppant tends to remain suspended in the slurry, and larger diameter proppant tends to settle down quickly. Secondly, highly viscous fluids prevent the proppants from depositing due to the significant increase in the drag forces and proppants with lower fracture width tends to form deposition dune quickly.

Finally, the comparison of the Eulerian-Granular method was made with the DEM method. The Eulerian-Granular method provides an approximate match with the DEM; however, the particle distribution rate in the Eulerian-Granular method is relatively higher than the DEM method. This was explained by the different ways in which particle-particle interaction is captured, and particle physics is handled in both these approaches. DEM provides a more accurate particle physics, but the computational time required is significantly higher. Considering the significant simulation time required for the DEM method, and applicability for upscaling the model to field-scale hydraulic fractures, the current study suggests that Eulerian-Granular method can be used for practical problems of petroleum engineering interests for proppant distribution and settling. The current study has enhanced the understanding of complex proppant transport phenomenon in hydraulic fractures with fluid leak-off by capturing the proppant-fracturing fluid interaction and inter-particle physics accurately using the advanced computational methods.

Chapter 5: Discussion on the construction of the DDPM model for proppant transport in unconventional hydraulic fractures[2]

For hydraulic fracturing design in unconventional reservoirs, it is of vital importance to accurately predict proppant distribution in fractures, as the distribution of proppant affects fracture conductivity (Donaldson, Alam and Begum 2014). As discussed in chapter 2, the existing proppant transport models (Adachi et al. 2007, Tsai et al. 2012, Gu and Hoo 2014, Yang, Siddhamshetty and Kwon 2017, Wang, Elsworth and Denison 2018) ignore the fluid leak-off effect from the fracture side wall and the effect of fracture roughness. In this chapter, a CFD based DDPM model is used which is a combination of CFD-DEM and Eulerian Granular method. It solves the mass and momentum conservation equations to model the continuous phase, and the proppant phase is modelled in the Lagrangian frame by tracking their motion using Newton's second law of motion (Suri, Islam and Hossain 2019). However, the proppants are mapped back to the Eulerian grid. The inter-proppant interaction is modelled by KTGF, and the proppant-wall interaction is modelled using the Lagrangian method. It overcomes the challenges of Eulerian-Granular method and is computationally faster than Eulerian-Lagrangian methods. Like CFD-DEM model, the DDPM model can be used for higher volume fraction. The current work aims to use the DDPM model and investigate the effect of proppant transport in rough fracture geometry. The reported models in the literature (Tomac and Gutierrez 2014, Zhang, Li and Gutierrez 2016, Hu et al. 2018) are described for planar and smooth fracture geometry without fluid leak-off behaviour. In the present study, an attempt has been made to overcome this challenge to capture proppant physics in a rough fracture. The model also incorporates the fluid leak-off from the fracture walls for slick water and Non-Newtonian fracturing fluid (foam). First, the proppant model is validated with the published experimental results. Subsequently, a base case simulation of the proppant transport and distribution in a real and rough fracture geometry is presented with fluid leak-off. Then, a series of case studies are designed to evaluate the impact of using Non-Newtonian fluid (foam), variation in injection velocity, injection proppant concentration, and fracture height. The key governing equations corresponding to the DDPM model are described in detail in chapter 3.

---

[2] The results from this chapter are published in the Journal of Natural Gas Science and Engineering.
Suri, Y., Islam, S.Z. and Hossain, M., 2019. A new CFD approach for proppant transport in unconventional hydraulic fractures. *Journal of Natural Gas Science and Engineering*, *70*, p.102951. https://doi.org/10.1016/j.jngse.2019.102951

5.1 Modelling workflow and simulation parameters

The CFD modelling of proppant transport in hydraulic fractures was studied using ANSYS FLUENT 18.1. The modelling workflow along with the simulation parameters used in the study can be summarised in the following steps:

5.1.1 Geometry/Computational domain

The hydraulic fracture can be of a variable size from centimetres scale to several meters scale. In the present study, the computational domain involves a three-dimensional rough fracture with dimensions 1.5 m × 0.005 m × 0.5 m, length × width × height respectively, as shown in Figure 5.1. The two-dimensional rough fracture profile in x-y direction was created using SynFrac software (Ogilvie, Isakov and Glover 2006) which followed the normal distribution fracture height with a mean of 0.5 m and a standard deviation of 2 mm. Then, the fracture surface was created using the two-dimensional rough fracture profile in x-y direction and mean fracture aperture of 5 mm. The fracture surface was extruded in the fracture height or y direction to create a three-dimensional rough fracture geometry. The method from Briggs, Karney and Sleep (2017) was used to generate a rough fracture model. The fracture profile is shown in Figure 5.1 and the histogram showing the normal distribution of the fracture height is shown in Figure 5.2.

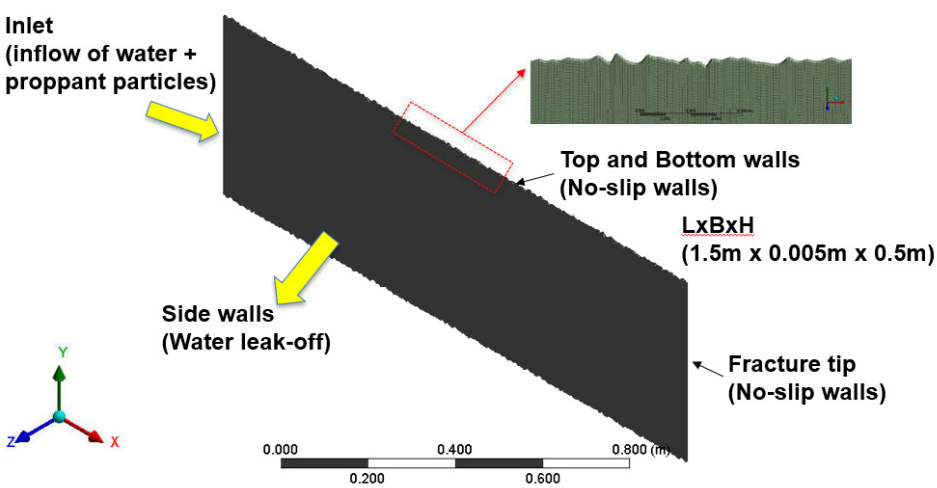

Figure 5.1 Computational domain and boundary conditions used in the study

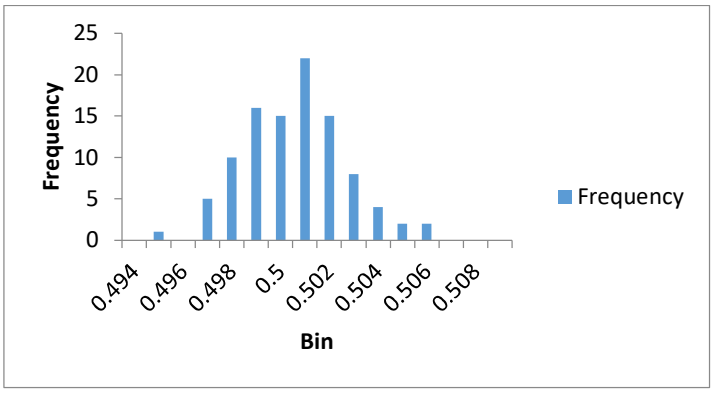

Figure 5.2 Histogram showing the normal distribution of fracture height with roughness

5.1.2 Meshing

The mesh sensitivity study was carried out to investigate the mesh independent solution by selecting a structured mesh with mesh sizes 0.002 m, 0.0025 m, 0.003 m, and 0.004 m. Three inflation layers with the first layer thickness 0.0005 m and growth ratio 1.2 were added in all the fracture geometries to account for the fracture roughness. The results are presented in Figure 5.3a and Figure 5.3b showing the proppant volume fraction vs fracture height and proppant axial velocity vs fracture height at a cross-section of 0.1 m from the inlet. The mesh sensitivity results suggest that the mesh with sizing parameter 0.0025 m can reasonably provide mesh independent solution with a percentage error of ±5% compared against the mesh sizing of 0.002 m, as shown in Figure 5.3. Based on the mesh sensitivity study, the mesh was generated in the computational grid evenly distributed in all direction with size 0.0025 m (600×200×8 elements). The computational mesh was selected to provide good quality mesh, numerically converged and mesh independent solution with a reasonable computational cost. To include the fracture roughness along the side walls of the fracture, wall surface roughness height and roughness constant were modified to 0.0005 m and 0.5 respectively based on the study of Blocken, Carmeliet and Stathopoulos (2007).

a.

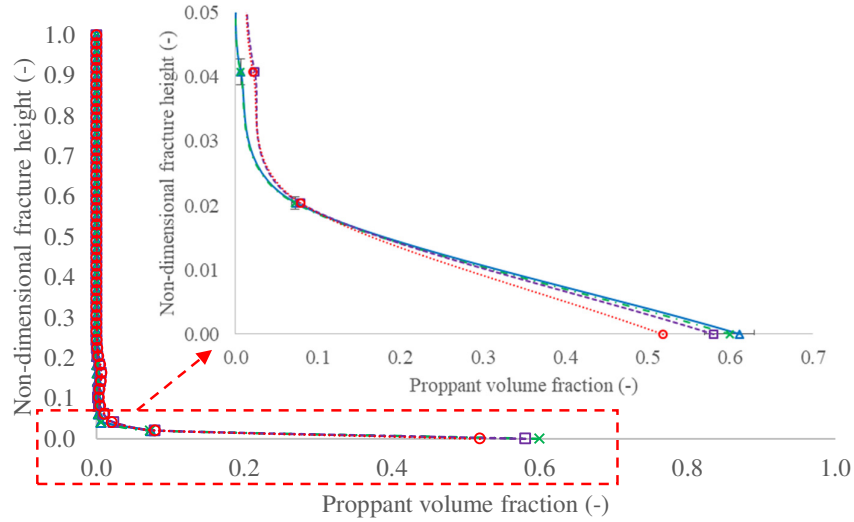

b.

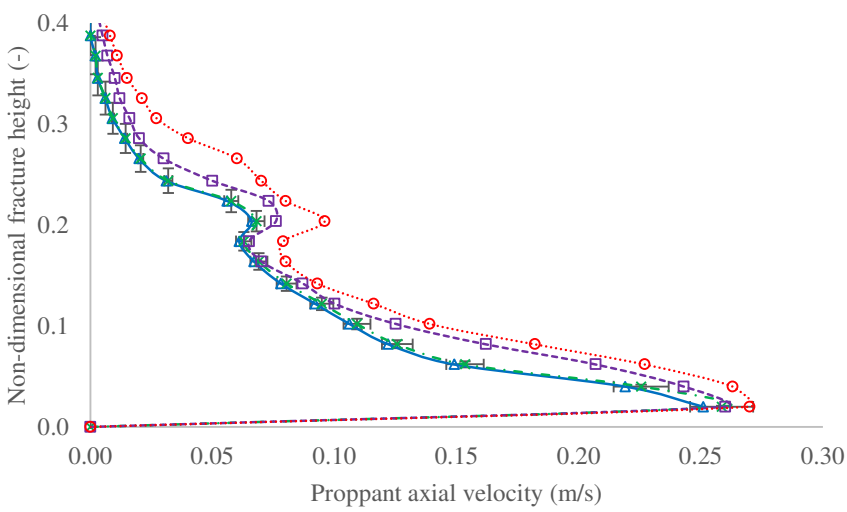

Legend

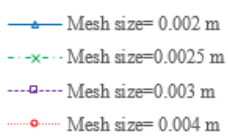

Figure 5.3- Mesh sensitivity study- comparison of numerical results with different mesh sizes a) plot of proppant volume fraction vs fracture height b) plot of proppant axial velocity vs fracture height

5.1.3 Modelling fluid leak-off

Post-injection of fracturing fluid into the wellbore, the process of fluid flowing from the fracture wall to the surrounding porous rock is called fluid leak-off, as explained earlier in section 3.3.2. In order to determine the amount of fracturing fluid leak-off at the fracture wall, a separate study was carried out where the fracture domain was surrounded with a porous and permeable rock, as discussed in chapter 3 section 3.3.2. A similar fracture configuration, as described in section 5.1, is used and is surrounded by a porous and permeable shale rock with porosity 5% and permeability 0.1 mD (Speight 2016b), as shown in Figure 3.4 earlier. The key governing equations solved for the fluid flow from the fracture to porous media are described in chapter 3. The velocity boundary condition was used at the inlet where water was injected with an injection velocity of 0.5 m/s. All the other boundary conditions and the leakage mechanisms are explained in section 3.3.2. The fluid leak-off rate profile or the fluid leak-off rate as a percentage of injected water mass flow rate from the fracture side walls is calculated along the fracture length and shown in Figure 5.4. The fluid leak-off profile in Figure 5.4 was then used to investigate the proppant transport and distribution based on the governing equations defined in sections 3.2.1-3.2.3. A user-defined function (UDF) is subsequently defined and written in C++ (section 3.3.2.3) which is interpreted by the CFD solver to model the fluid leak-off and add a mass and momentum source term in the right-hand side of proppant transport governing equations (Eq. (3.3) and Eq. (3.5)), as discussed earlier in section 3.3.2. In the fracture geometry of Figure 5.1, at the side walls, the fluid leakage effect is introduced with the help of user-defined function (UDF) (See Appendix A). This is done to mimic the fluid leak-off into the porous reservoir, leaving the proppant in the fracture.

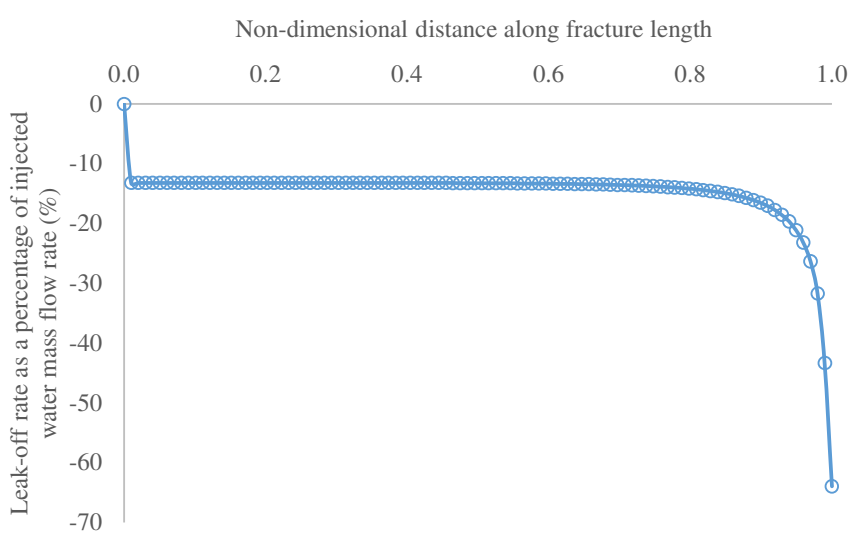

Figure 5.4 Fluid Leak-off rate at fracture wall along the fracture length

5.1.4 Simulation set up

Next, appropriate boundary conditions and simulation properties were defined. A velocity inlet boundary condition is used at the inlet where fluid and proppants are injected at 0.5 m/s. The Rosin-Rammler particle size distribution is assumed based on the 20/40 size sand. The Rosin-Rammler particle size distribution is a continuous probability distribution function to describe particle size distribution (Brown and Wohletz 1995). The top, bottom walls and fracture tip were specified as no-slip stationary walls for the liquid phase, as shown in Figure 5.1. For the particle phase, the reflect boundary condition with specularity constant of 0.01 and wall reflection coefficient of 0.9 in both normal and tangential directions was used to model the particle-wall collision (Benyahia, Syamlal and O'Brien 2005, Ehsani et al. 2015, Li, Zhang and Lu 2018). In the side walls, the fluid leakage effect is introduced with the help of user-defined function (UDF). This is done to mimic the fluid leak-off into the porous reservoir, leaving the proppant in the fracture. The momentum and mass source terms are defined and included in the governing equations through UDFs as described in modelling leak-off section. The fluid leakage rate along the fracture length used in the study is shown in Figure 5.4.

A transient state simulation with pressure-based solver and gravitation effects was configured, as described earlier in section 3.3.3. The turbulence model used was the Shear Stress Transport (SST) k-ω model, as explained earlier in section 3.2.3.2. The SST k-ω turbulence model is a two-equation eddy-viscosity model, which combines standard k-ω turbulent model in the boundary layer (low-Re region) with the standard k-ε turbulent model in the free-stream (Menter 1993). The fluid and proppant properties are listed in Table 5.1.

Table 5.1: Physical properties of proppant and fluid used in the simulation

Property	Value
Proppant diameter	20/40 size sand
Proppant density	2650 kg/m^3
Fluid density	1000 kg/m^3
Fluid inlet velocity	0.5 m/s
Fluid viscosity	0.001 Pa-s (1cP)
Proppant volume fraction	0.20

The viscosity of the granular phase is calculated from the Gidaspow (1994) correlation as discussed earlier in section 0. The primary role of granular viscosity is used to consider the frictional losses. The frictional viscosity refers to the shear viscosity based on the viscous-plastic flow and is calculated using the Johnson and Jackson (1987) correlation (section 0). The packing limit defines the maximum volume fraction of the granular phase, which was used as 0.63 based on the study of Basu et al. (2015). Friction packing limit refers to a threshold volume fraction at which the frictional regime becomes dominant, and friction packing limit of 0.5 is used, as explained earlier in section 3.3.3.

In the DDPM model, the drag force used to model the interaction between the two phases is based on Gidaspow drag law (1994) and the collision between the proppant particles is modelled using the restitution coefficient and KTGF, as explained in chapter 3 (sections 3.2.1.5-3.2.1.8). The time step used in the simulation was 0.001 s. The reflect DPM boundary condition used at walls so that the particles will reflect after the collision with the wall.

Finally, the Phase-coupled SIMPLE algorithm is used as a solution method for the pressure-velocity coupling (section 3.3.3). The node-based averaging scheme is used to calculate the gradient and the discretisation of momentum, volume fraction, and turbulent kinetic energy was solved by the second-order upwind scheme, as explained earlier in section 3.3.3.

5.2 Results and Discussion

5.2.1 Comparison with the experimental results

The present simulation model was compared against the experimental study of Tong and Mohanty (2016) described earlier in section 4.3.1. Tong and Mohanty (2016) performed an experimental study of proppant transport in fracture slots at different injection rates. The experiment set-up consisted of two transparent fracture slots is shown in Figure 4.4 and described earlier in section 4.3.1. The main fracture slot is called as a primary fracture slot, and the bypass fracture slot is called as a secondary fracture slot. The fracturing fluid slurry (water + proppants) is injected at the inlet at different flow rates or injection velocities (0.1, 0.2 and 0.3 m/s) and proppant concentration (0.038, 0.019, and 0.013). 20/40 size sand is used as a proppant with a density of 2650 kg/m^3. Water is used as a fracturing fluid with viscosity 1 cP and density 1000 kg/m^3. The proppant transport was monitored and recorded with cameras as shown in Figure 4.4. The simulation was performed with the geometry similar to the experimental setup. All the modelling parameters are presented in Table 5.2, which are similar to experimental parameters.

The DDPM model was used to model the fluid flow and proppant distribution. Fracturing fluid (water, in this case) along with the proppant is injected at the inlet. The proppant bed deposition after 20 s of injection for different flow rates (or injection velocities) is compared for both the numerical and experimental results and are shown in Figure 5.5. The results from Figure 5.5 show that the current numerical model simulates the proppant distribution similar to the experimental results. To quantitatively compare the results, dimensionless equilibrium height and dimensionless length at the centre of proppant bed are plotted in Figure 5.6 for all the cases.

The results of dimensionless equilibrium height are also compared with an analytical model by Wang et al. (2003) described as follows-

$$\frac{\mathrm{H-Ho}}{\mathrm{w}_s} = [-2.3 \times 10^{-4} \ln(\mathrm{R_{gp}}) + 2.92 \times 10^{-3}] \times \mathrm{Re_l}^{1.2-1.26\times10^{-3}\mathrm{R_{gl}}^{-0.428}[15.2-\ln(\mathrm{R_{gp}})]} \times \mathrm{Re_p}^{[-0.0172\ln(\mathrm{R_{gp}})-0.12]} \quad (5.1)$$

Where H, $\mathrm{H_o}$ and w_s are the height of slot, the height of slurry flow area and the width of slot respectively. $\mathrm{Re_l}$ and $\mathrm{Re_p}$ are the Reynolds number for the fluid and proppant phase respectively. The $\mathrm{R_{gl}}$ and $\mathrm{R_{gp}}$ are the Reynolds number for the fluid and proppant phase based on the channel width respectively. Detailed definition of. $\mathrm{Re_l}$, . $\mathrm{Re_p}$, $\mathrm{R_{gl}}$ and $\mathrm{R_{gp}}$ can be found in Wang et al. (2003).

Figure 5.5 and Figure 5.6 shows a good match among the experimental study and the current simulation. The average error in dimensionless equilibrium height and dimensionless length at the centre of proppant bed is 3.2% and 3% respectively between the current simulation and the experiment, which suggests a reasonable match with the experiment. The average error in dimensionless equilibrium height, between the current model and the analytical model by Wang et al. (2003), is 25%. This error can be attributed to the analytical model by Wang et al. is proposed for long fracture slot (Wang et al. 2003). Using the analytical model for smaller fracture overestimates the equilibrium height. Thus, an overall good match of the simulation result with the experiment suggests that the simulation model can be used to perform further analysis of proppant distribution in the slick water fracturing fluid. Furthermore, a detailed comparison of the Eulerian-Granular model, CFD-DEM and the DDPM model with the experimental results of Tong and Mohanty (2016) is done and explained in Appendix C. The comparison results of all the numerical models with the experimental results suggest that the DDPM model provides a reasonable approximation to the proppant particle physics inside the fracture in a reasonable

computational time and can be used for practical problems of petroleum engineering interests for proppant distribution and settling.

Table 5.2: Simulation parameters for comparison with the experimental results

Property	Value
Fracture dimensions, L×W×H (m)	0.381 × 0.0762 × 0.002 (primary slot) 0.1905 × 0.002 × 0.0762 (secondary slot)
Proppant diameter	20/40 sand
Proppant density (kg/m^3)	2650
Fluid density (kg/m^3)	1000
Fluid inlet velocity (m/s)	0.1, 0.2, 0.3
Fluid viscosity (cP)	1
Proppant volume fraction	0.038, 0.019, 0.013
Injection time (s)	20

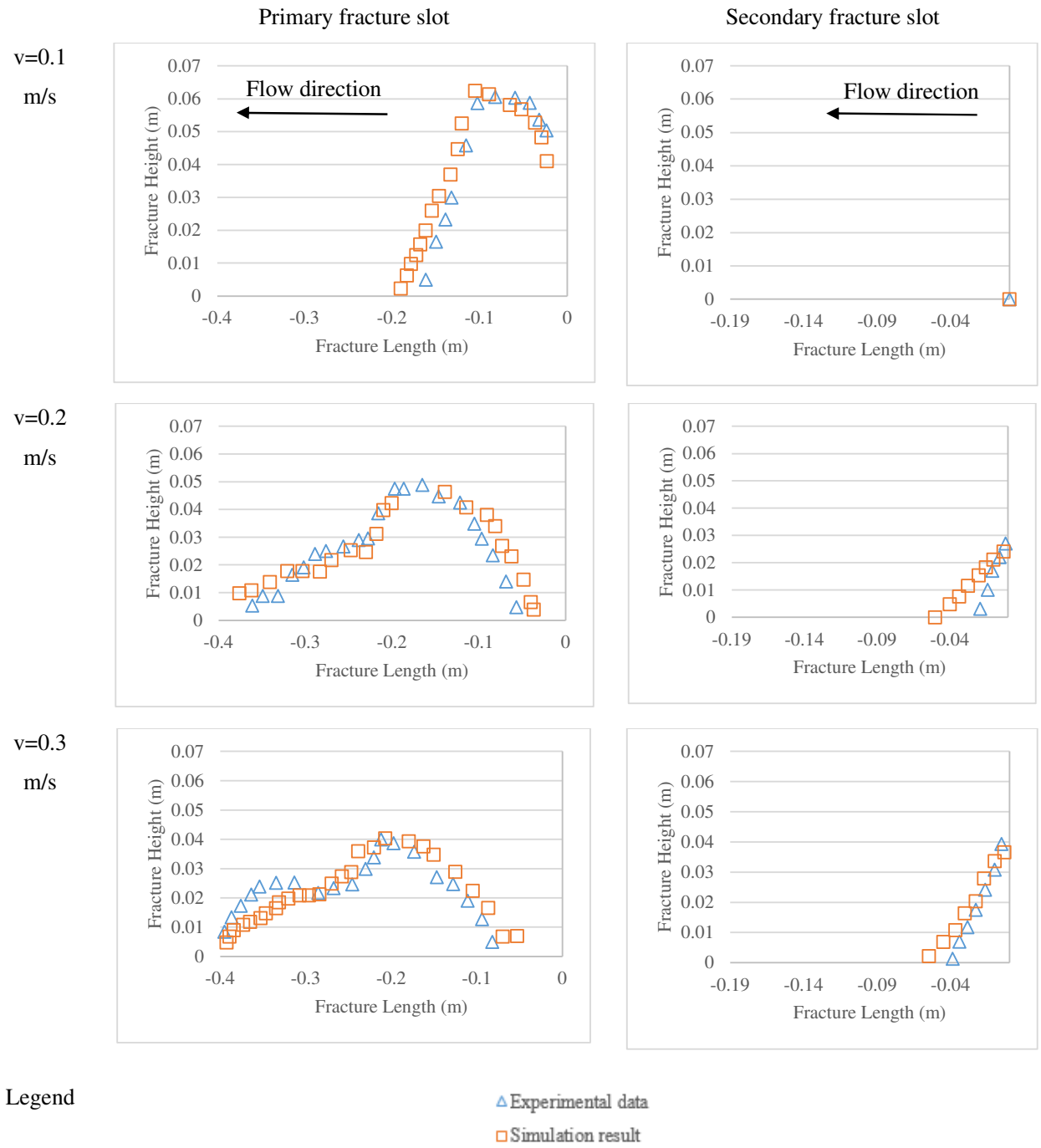

Figure 5.5 Comparison of experimental data and numerical result at t=20 s

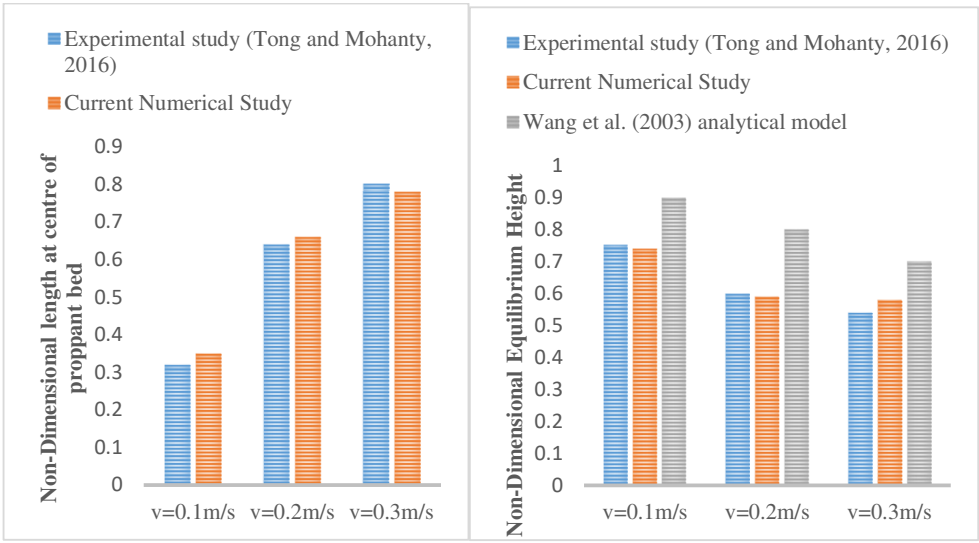

Figure 5.6 Quantitative validation (a) comparison of non-dimensional proppant bed length for experimental study vs current numerical study (b) comparison of non-dimensional proppant bed height for the experimental study vs current numerical study

5.2.2 Effect of Fracture Roughness

An investigation was carried out to understand the role of fracture wall roughness in proppant distribution. A comparison is made between the rough fracture case described in the geometry section earlier with the smooth fracture case with no fracture roughness. Figure 5.7 and Figure 5.8 shows the contour plot of proppant volume fraction for both the cases and their comparison respectively. It can be interpreted from Figure 5.8 that, the fracture wall roughness provides additional drag resistance force near the fracture wall and thus, it resulted in shorter proppant bed length compared with the smooth wall fracture. Conversely, neglecting the fracture roughness in the proppant transport model can result in over predicting the proppant bed length. The proppant volume fraction was plotted with the non-dimensional fracture height at two vertical cross-sectional planes at 0.2 m and 1.4 m from the inlet in the longitudinal direction (Figure 5.9). The results show that, away from the wellbore, in the case with fracture roughness, greater proppant particles in suspension is noticed compared with the smooth wall fracture case. This can be explained by the fracture roughness causes more turbulence in the flow and the increase in turbulence results in a more significant amount of proppants in the suspension region. The smooth fracture can be underpredicting the proppant transport by 10-15% in the proppant suspension layer.

In order to investigate in detail, the role of turbulence caused by the rough fracture surfaces on the flow field and proppant transport, a comparison of vorticity, velocity vector and turbulent kinetic energy was made between rough fracture and smooth fracture cases in Figure 5.10. It is noticed that the rough fracture surface induces a high vortex region resulting in higher turbulence (Figure 5.10a). This can further be supported by the high turbulent kinetic energy observed especially near the fracture wall, that aids in the greater suspension of the proppants in the fracturing fluid (Figure 5.10c). Figure 5.10b shows the zoomed view of the velocity vector field of the continuous phase at the fracture wall, and it can be noticed that including the fracture roughness into the model disrupts the continuous velocity vector field in the smooth fracture wall case into vortices in the rough fracture wall case that can significantly affect the proppant transport and distribution. Thus, the comparison results explain that inclusion of the fracture roughness in the proppant transport model is vital in proppant distribution study, and assuming the fracture wall as smooth can underpredict the proppant transport in the proppant suspension layer and overpredict the proppant bed length.

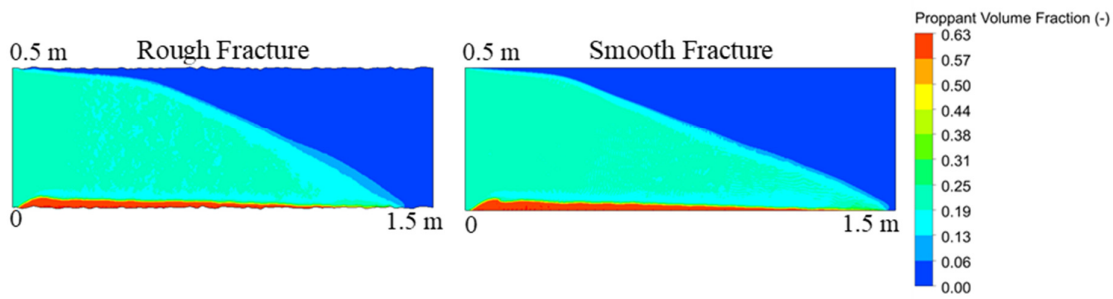

Figure 5.7 Comparison of rough and smooth fracture cases at t=2 s

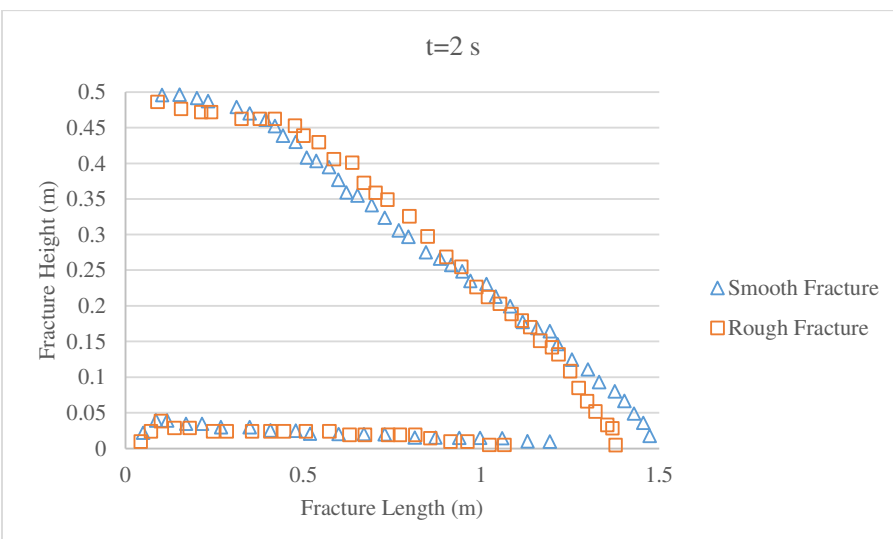

Figure 5.8 Comparison of rough and smooth fracture cases at t=2 s

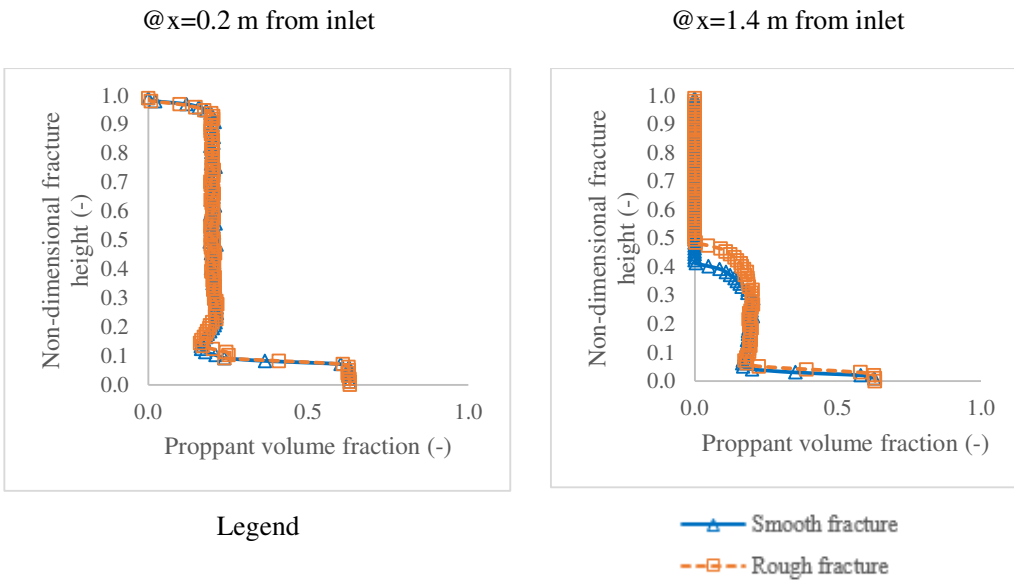

Figure 5.9 Comparison of the proppant volume fraction with the non-dimensional fracture height at for smooth and rough fracture case t=3 s

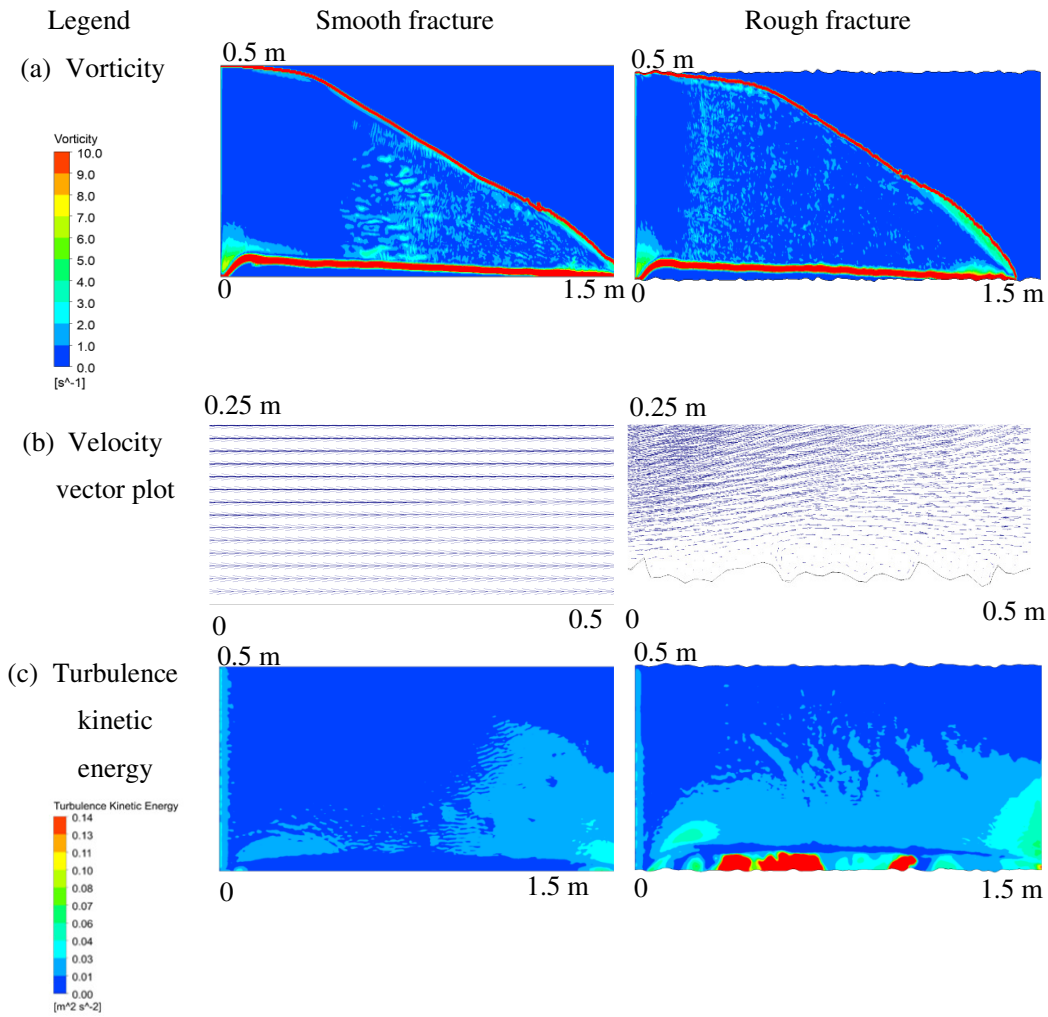

Figure 5.10 Comparison of vorticity, velocity vector and turbulence kinetic energy plots for smooth vs rough fracture case

5.2.3 Effect of the fluid leak-off rate at fracture wall

As explained in chapter 4, fluid leak-off is one of the critical phenomena that govern the proppant suspension in the slurry. As the fracturing fluid slurry is injected in the fracture, the fracturing fluid leaks off from the fracture wall to the surrounding porous rock at a rate depending upon the reservoir characteristics. The remaining proppants in the slurry have a tendency to deposit and form proppant bed at the fracture bottom. The higher leak-off rate can result in a greater flow of thin fracturing fluid to the surrounding reservoir rock, leaving behind the proppant in the remaining slurry and consequently early deposition of the proppants.

Next, an analysis was carried out to understand the effect of fluid leak-off at the fracture wall on proppant distribution. A comparison is made between the fluid leak-off from the fracture wall and neglecting the fluid leak-off, as shown in Figure 5.11. The proppant volume fraction was plotted with the fracture height at t=2.5 s after the start of injection at two vertical cross-sectional planes at 0.2 m and 1.4 m from the inlet in the longitudinal direction (Figure 5.11). Leak off effects plays a vital role in shale reservoirs where due to the use of thin fracturing fluid, the ability to suspend the proppants is considerably low. Furthermore, greater fluid leak-off from the fracture wall will increase the rate of proppant bed formation and early fracture tip screen out. The fracture tip screen out will then inhibit any further proppant transport into the fracture, and the unpropped section of the fracture will close down, resulting in loss of fracture conductivity. The results show that neglecting the fluid leak-off phenomenon at the fracture wall in the proppant transport study can have a significant impact on the proppant distribution inside the fracture. As the fluid leaks off the fracture wall, the proppants tends to deposit at the fracture bottom and thus greater proppant bed height is noticed in fluid leak-off case compared with the no leak-off case. Neglecting the leak-off effects can result in under predicting the proppant bed height by 10-50% and over predicting the suspension layer by 10-50%.

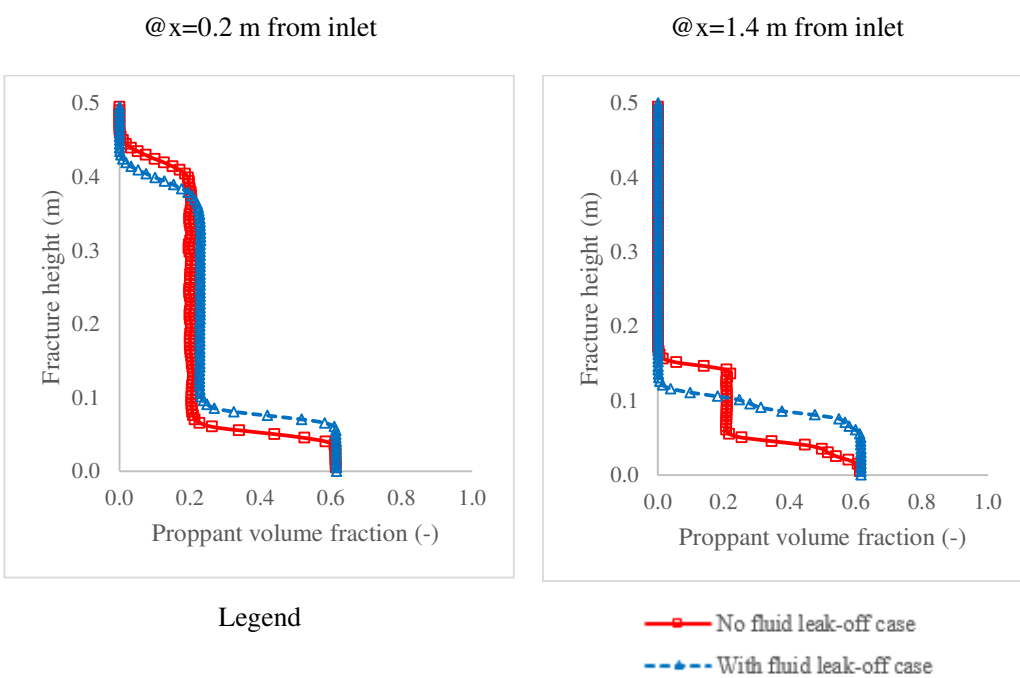

Figure 5.11 Comparison of Fluid Leak-off case with no leak-off from the fracture wall at 2.5 s

5.2.4 Effect of injection rate

In this section, the effect of variation in injection rate was investigated on the proppant transport and distribution. Since the present study is based on the fixed fracture geometry with a constant inlet cross-section area of 0.0025 m^2, the volumetric flow rate is described in terms of injection velocity. The injection velocity was varied, keeping all the other parameters constant, and simulation run was performed. The three cases of variation in injection velocity studied are v = 0.1 m/s, 0.5 m/s and 1 m/s that refers to a fluid injection rate of 0.00025 m^3/s, 0.00125 m^3/s, and 0.0025 m^3/s respectively. Figure 5.12 is the contour plots of proppant volume fraction at fracture mid-plane for different time step and all the three cases of variation in injection velocity. It shows the difference in proppant distribution inside the fracture with time. It can be interpreted from the contour plots that as the injection velocity is increased, it results in a greater proppant deposition away from the wellbore. The higher amount of proppant is in the suspension layer with the increase of injection velocity and results in proppant being transported longer.

Next, to analyse the proppant bed height, comparing the case of v =0.5 m/s @2 s and v =1 m/s @1 s shows that increasing the injection velocity results in a reduction in proppant bed height. The proppants tend to suspend and are transported further. Similar observation is also seen comparing case of v =0.1 m/s @3 s and v =0.5 m/s @1 s.

To quantitatively understand these results, two vertical cross-sectional planes were selected at 0.2 m and 1.4 m from the inlet in the longitudinal direction (Figure 5.13). The proppant volume fraction and proppant axial velocity were plotted with the non-dimensional fracture height at these planes and the advancement of proppant volume fraction and proppant axial velocity with time was analysed (Figure 5.14 and Figure 5.15). The results show that the increase in injection velocity provides greater energy for the proppant to remain in the suspension layer and as a result transport the proppants deeper inside the fracture.

The parametric study of the proppant distribution to injection velocity suggests that it can play a significant role in optimising proppant distribution and hence the fracture conductivity. One practical approach, for low viscosity fluid like slick water, could be injecting the proppant at higher injection rates to enhance the proppant transport in fractures.

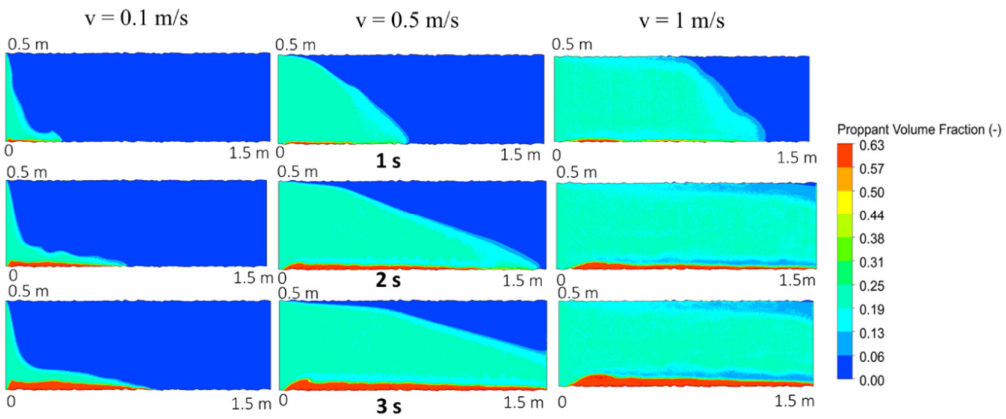

Figure 5.12 Contour plot for proppant volume fraction at fracture mid-plane showing three cases of variation in injection velocity 0.1 m/s, 0.5 m/s and 1 m/s

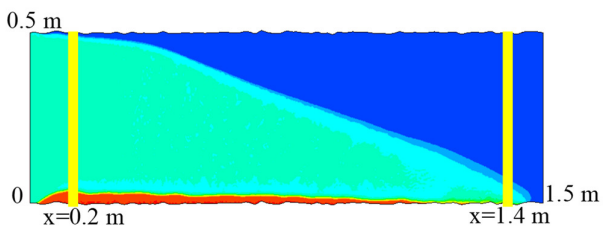

Figure 5.13 Location of vertical planes at x=0.2 m and x=1.4 m from the inlet to quantitatively analyse the results

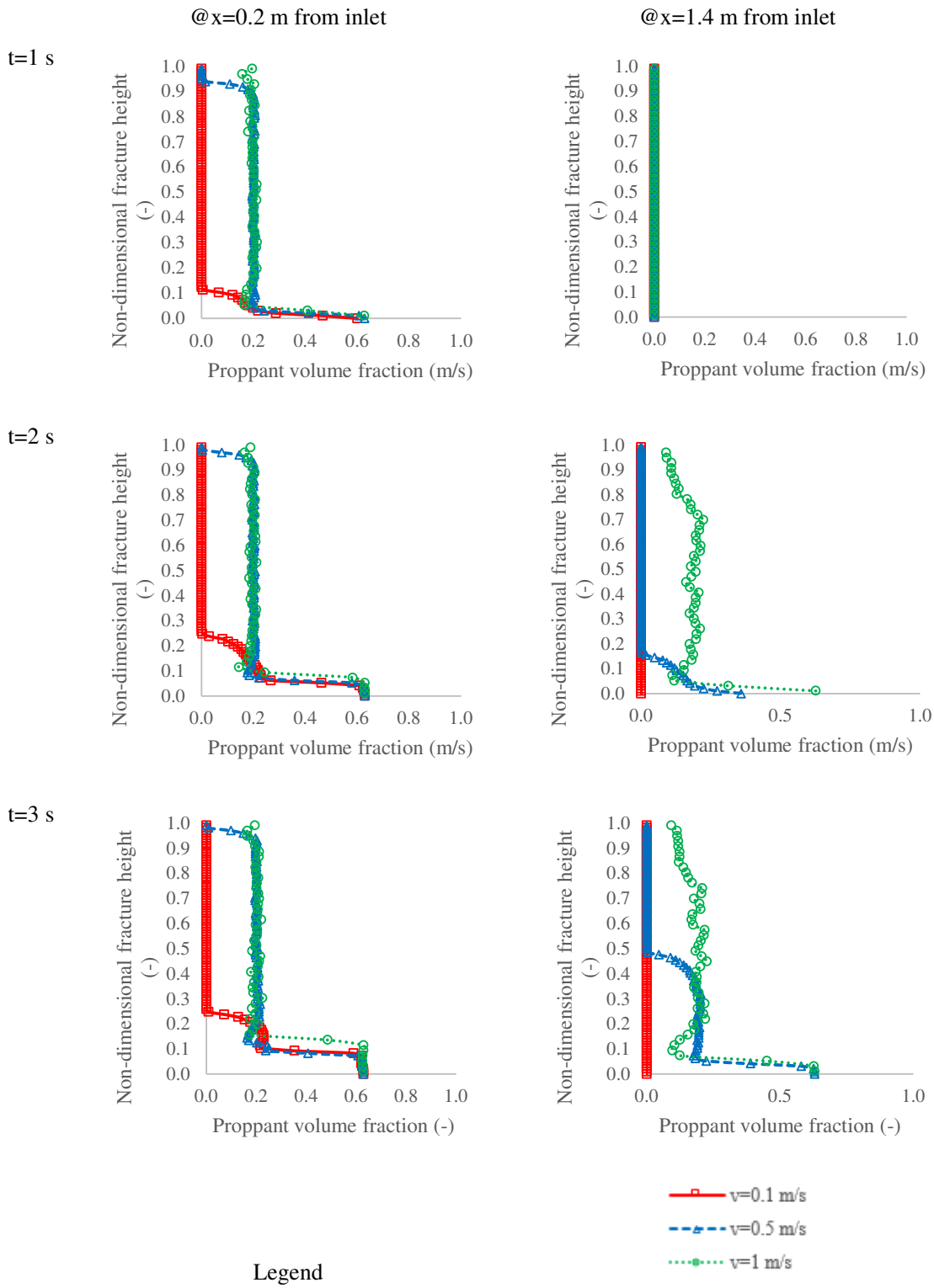

Figure 5.14 Comparison of the proppant volume fraction with the non-dimensional fracture height for injection velocities 0.1 m/s, 0.5 m/s and 1 m/s at two different locations (x=0.2 m and x=1.4 m) inside the fracture

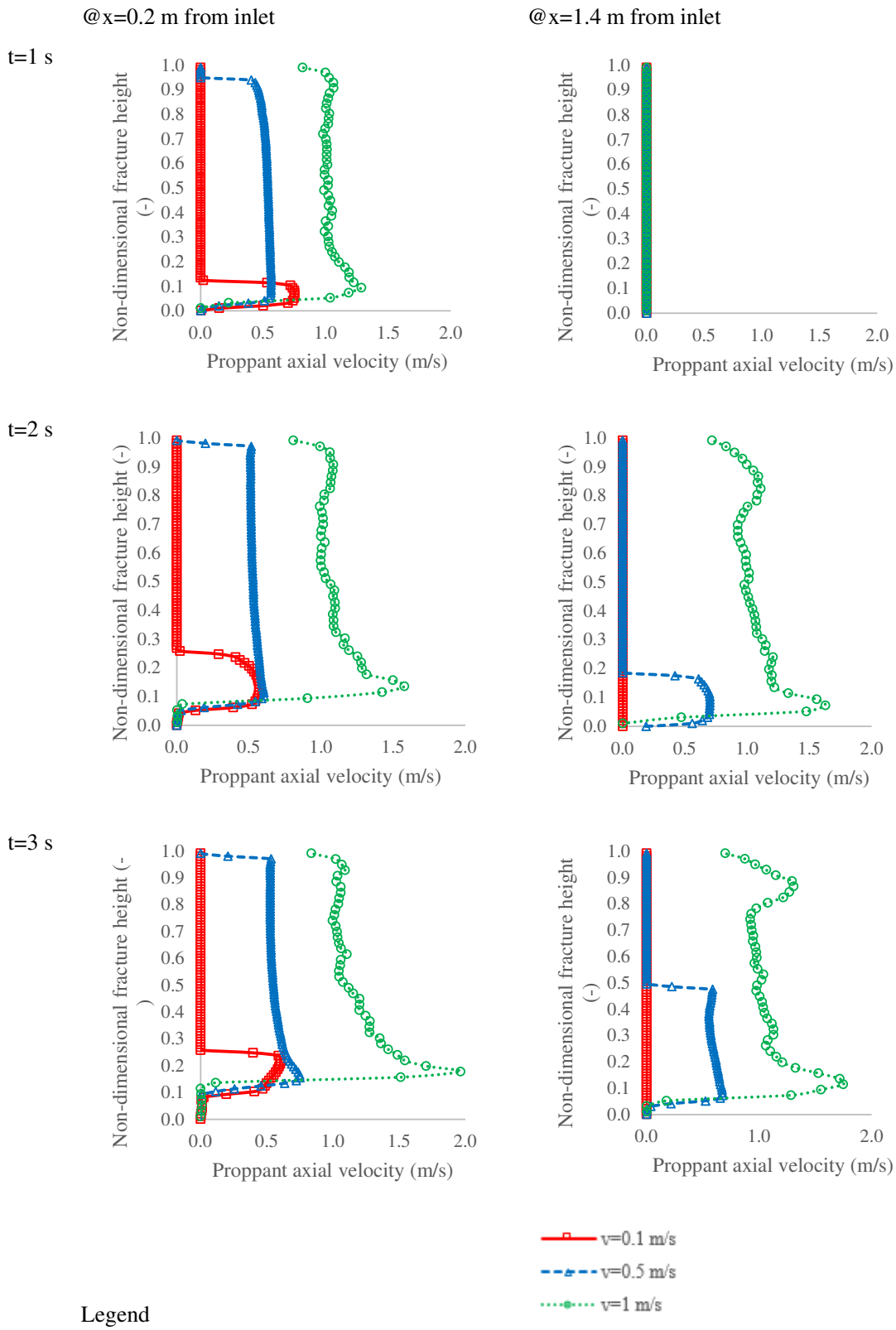

Figure 5.15 Comparison of the proppant axial velocity with the non-dimensional fracture height for injection velocities 0.1 m/s, 0.5 m/s and 1 m/s at two different locations (x=0.2 m and x=1.4 m) inside the fracture

5.2.5 Effect of Proppant Concentration

In the next study, the proppant concentration was varied keeping all the other parameters constant, and simulation run was performed. The three cases of variation in proppant concentration studied are c= 0.10, 0.15 and 0.20. Figure 5.16 is the contour plots of proppant volume fraction at fracture mid-plane for different time step showing all the three cases of variation in proppant volume fraction. It can be interpreted from the contour plots that the proppant concentration has a complex effect on proppant transport, such as proppant settling velocity, the rate of proppant bed build-up. The higher proppant concentration can help in transporting proppant to a longer distance and greater proppant bed height.

Next, the proppant volume fraction and proppant axial velocity was plotted with the fracture height and the advancement of proppant volume fraction with time at the two-different vertical planes was analysed (Figure 5.17 and Figure 5.18). The results show that the case with c=0.20 having higher proppant concentration tends to transport proppant to the longer distance (@x=1.4 m t=2 s; t=3 s) which is the primary objective in the shale gas reservoirs and also has higher proppant velocity in the longitudinal direction. Often the significant challenge using slick water fracturing fluid in shale gas reservoir is the quick deposition of proppants with shorter proppant bed length. This parametric study results in an important conclusion that the proppant transport, distribution and settling is substantially dependent on the proppant concentration. Higher proppant concentration can assist in achieving longer proppant bed length.

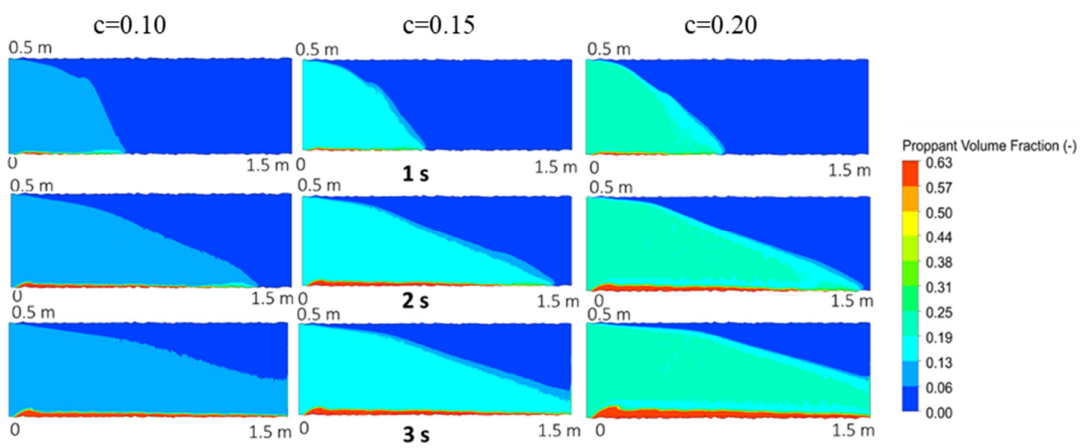

Figure 5.16 Contour plot for proppant volume fraction at fracture mid-plane showing three cases of variation in proppant concentration c= 0.10, 0.15 and 0.20

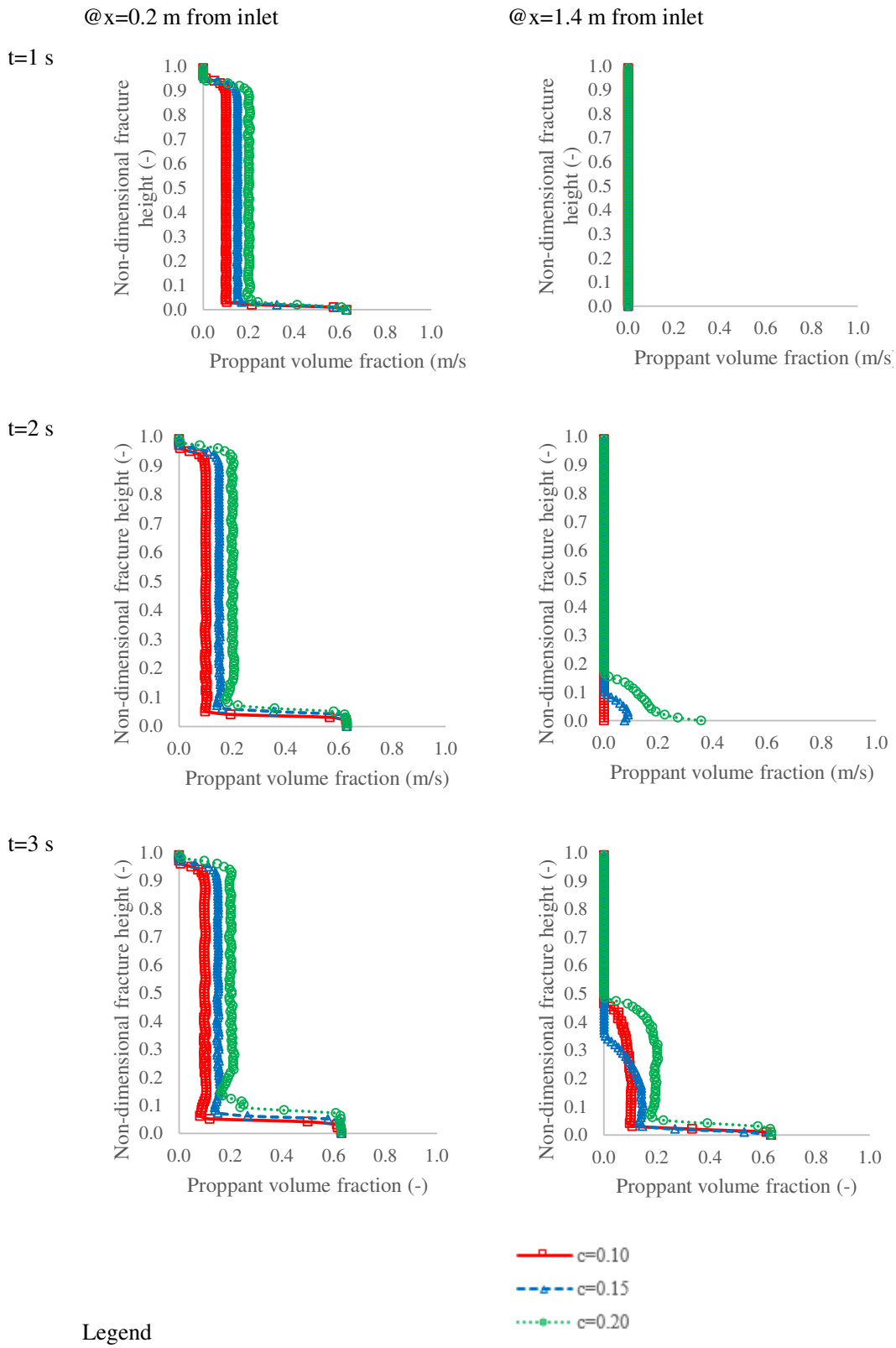

Figure 5.17 Comparison of the proppant volume fraction with the non-dimensional fracture height for variation in proppant concentration c= 0.10, 0.15 and 0.20 at two different locations (x=0.2 m and x=1.4 m) inside the fracture

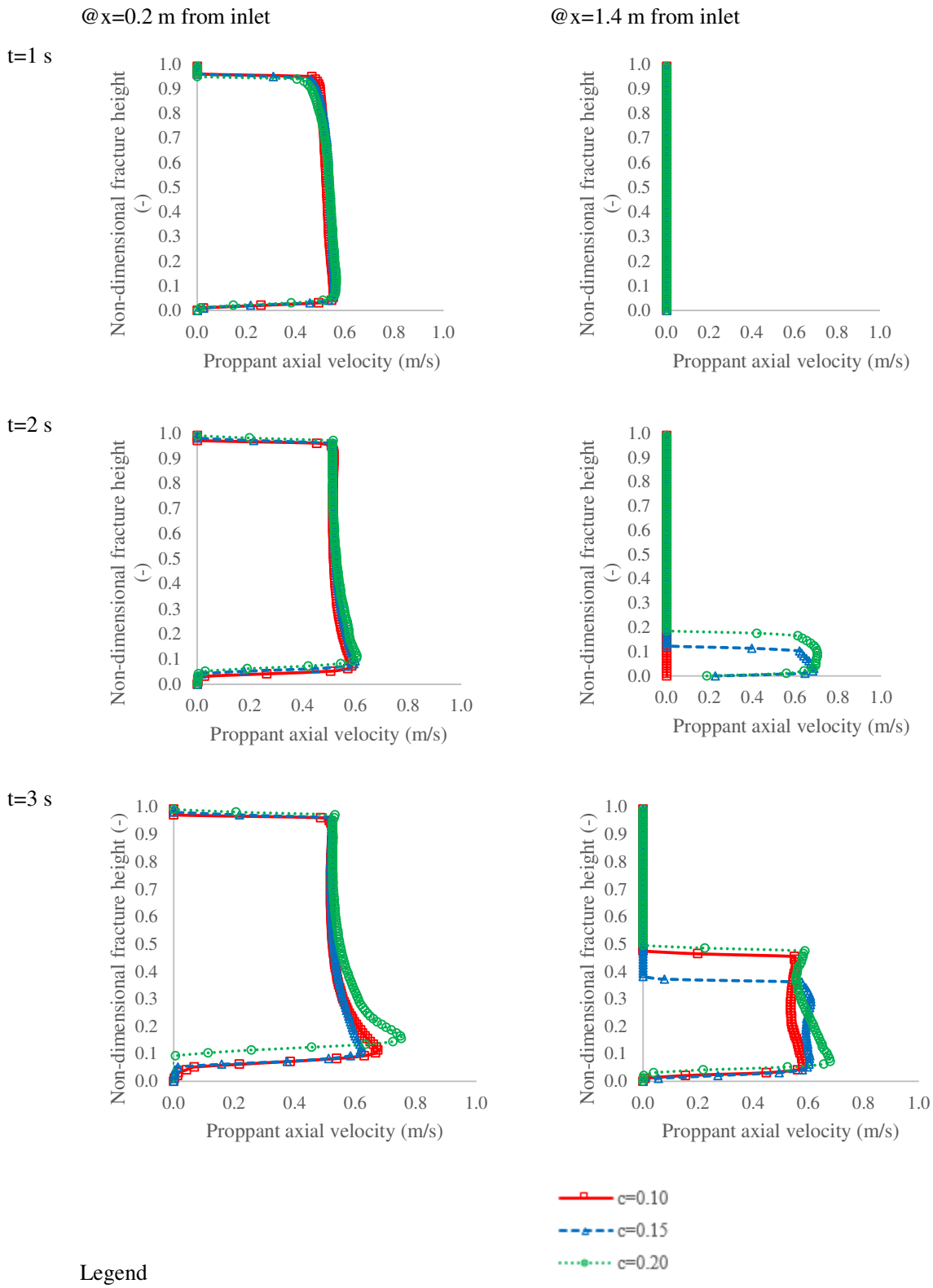

Figure 5.18 Comparison of the proppant axial velocity with the non-dimensional fracture height for variation in proppant concentration c= 0.10, 0.15 and 0.20 at two different locations (x=0.2 m and x=1.4 m) inside the fracture

5.2.6 Effect of fracture height

In the next study, the fracture height was varied keeping all the other parameters constant, and simulation run was performed. The three cases of variation in fracture height studied are h= 0.2 m, 0.5 m and 1 m. Figure 5.19 is the contour plots of proppant volume fraction at fracture mid-plane for different time step and shows all the three cases of variation in fracture height. The contour plot shows that the fracture height has a significant role in proppant transport. The higher fracture tends to suspend greater proppants in the slurry and transport proppants to a longer distance. To understand the results quantitatively, the proppant volume fraction was plotted with the normalised (dimensionless) fracture height and the time evolution of proppant volume fraction at the two-different vertical cross-sections x=0.2 m, and x=1.4 m from inlet was analysed (Figure 5.20). Figure 5.20 shows that at time=2 s and 3 s, greater fracture height is helping to transport proppants to a greater distance by suspending more proppants. At x=0.2 m, although lower proppant bed height is obtained for H=1 m case, the greater height can transport the proppant to longer length as evident at plane x=1.4 m. Conversely, smaller fracture height results in greater proppant deposition. Comparing the proppant axial velocity (Figure 5.21), it can be observed that away from the wellbore the proppants velocities are higher for the greater fracture height case, which is helping to have higher proppant bed length. This is significantly important for hydraulic fractures in the shale gas reservoirs.

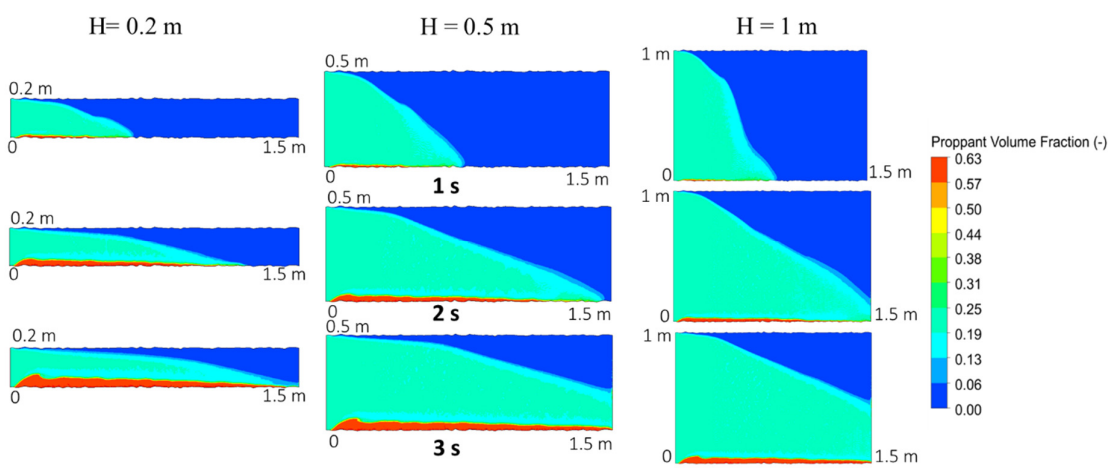

Figure 5.19 Contour plot of the proppant concentration for different fracture height cases H=0.2 m, 0.5 m and 1 m

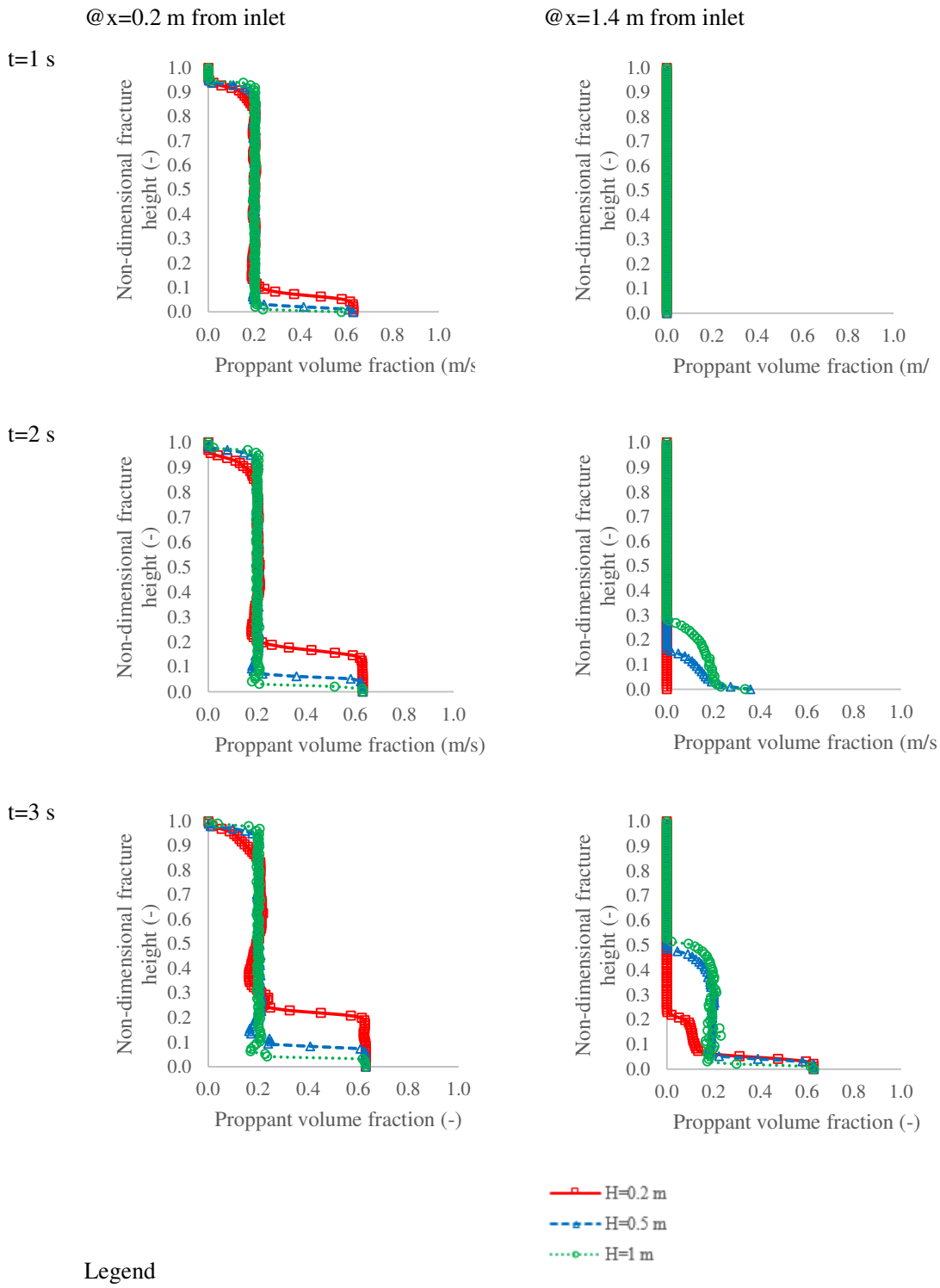

Figure 5.20 Comparison of the proppant volume fraction with the non-dimensional fracture height for different fracture height cases H=0.2 m, 0.5 m and 1 m at two different locations (x=0.2 m and x=1.4 m) inside the fracture

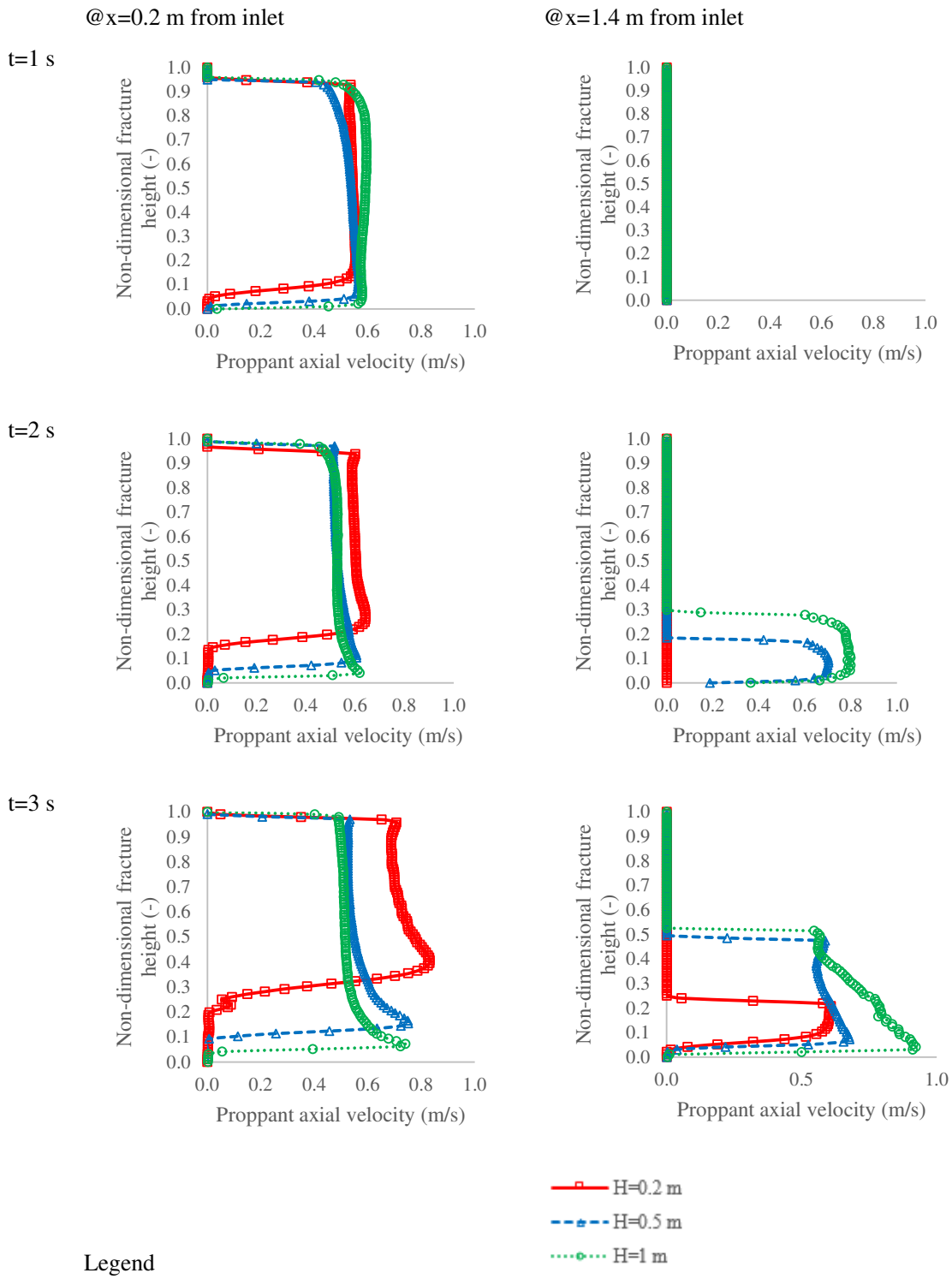

Figure 5.21 Comparison of the proppant axial velocity with the non-dimensional fracture height for different fracture height cases H=0.2 m, 0.5 m and 1 m at two different locations (x=0.2 m and x=1.4 m) inside the fracture

5.2.7 Comparison of Foam vs Water as fracturing fluid

One of the significant problems faced in the shale gas reservoirs during proppant transport is the quick deposition of the proppant due to the low viscosity and lower capability to suspend the proppants for slick water. A case study is designed to simulate Non-Newtonian fluid (Foam) that in the experiment has been reported to have better suspension capability than slick water, due to higher apparent viscosity. Some of the assumptions used to numerically model foam injection in the DDPM model are as follows-

i. High quality and uniform foam (dry foam) is assumed. No effect of foam drainage and foam microstructure is accounted for in the model.
ii. Laminar flow for foam has been assumed with Isothermal condition.
iii. The experimental data for foam is used from the experimental study of Tong, Singh and Mohanty (2017)
iv. Herschel Bulkley model is used to account for the rheological properties of the foam.

The key properties used to model foam injection in the current study are summarised in Table 5.3. Figure 5.22 is the contour plots of proppant volume fraction at fracture mid-plane for different time step and shows the comparison of foam vs water-based fracturing fluid. Figure 5.22 shows that as reported in the experiment, the foam has improved capability to suspend proppants, and the proppant bed height and bed length is lower for the foam injection, with greater proppant suspension layer, compared with the water injection.

The time evolution plot (Figure 5.23 and Figure 5.24) for the proppant volume fraction and proppant axial velocity with the non-dimensional fracture height at the two vertical cross-sections x=0.2 m and 1.4 m from the inlet show that the proppant suspension layer for the foam case is significantly higher compared with the water case, which enhances the ability for the fracturing fluid to transport proppants to a more considerable distance inside fractures. Moreover, with time the suspended proppants deposits and forms proppant bed. This comparison study further suggests that using foam as a fracturing fluid have the potential to mitigate the challenge of quick deposition of proppant in shale gas reservoirs.

Table 5.3: Physical properties of foam as a fracturing fluid used in the simulation

Property	Value
Specific gravity	0.3
Fluid inlet velocity	0.5 m/s
Viscosity	Herschel Bulkley model
Consistency factor (K_f)	1.77 $N.s^n/m^2$ (Gu and Mohanty, 2015) @T=308 K, P=9.65 MPa
Flow behaviour index (n_f)	0.45
Proppant volume fraction	0.20

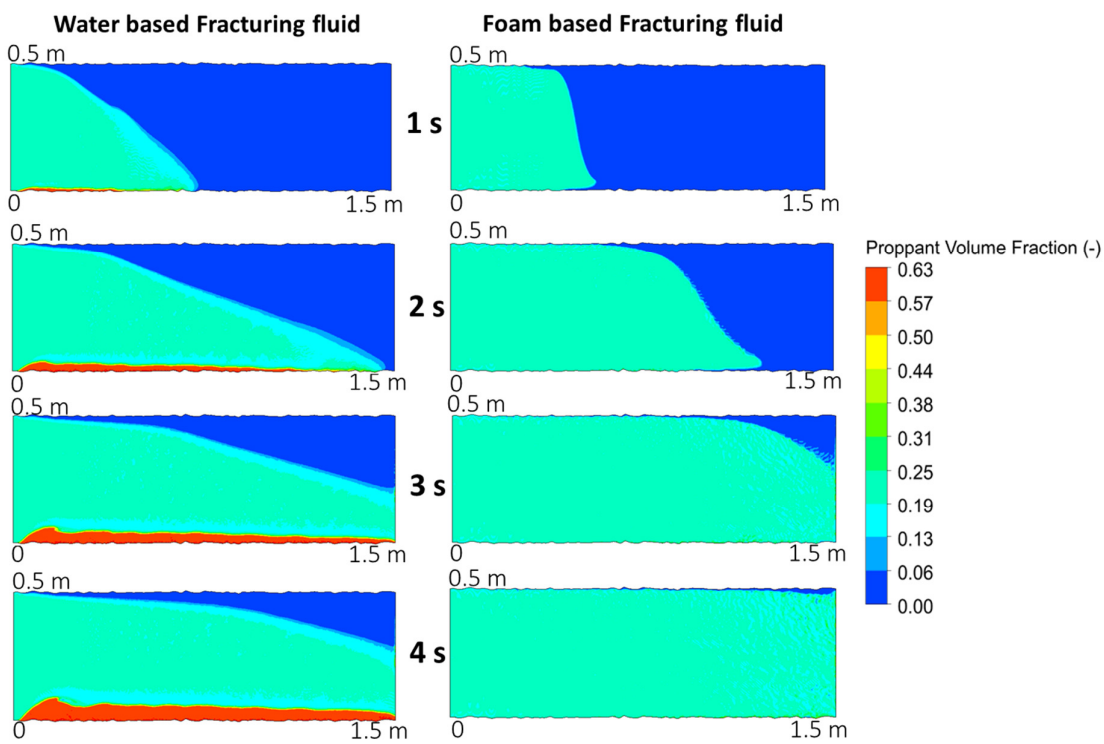

Figure 5.22 Contour plot showing proppant volume fraction comparison of foam-based fracturing fluid with a water-based fracturing fluid at a different time interval

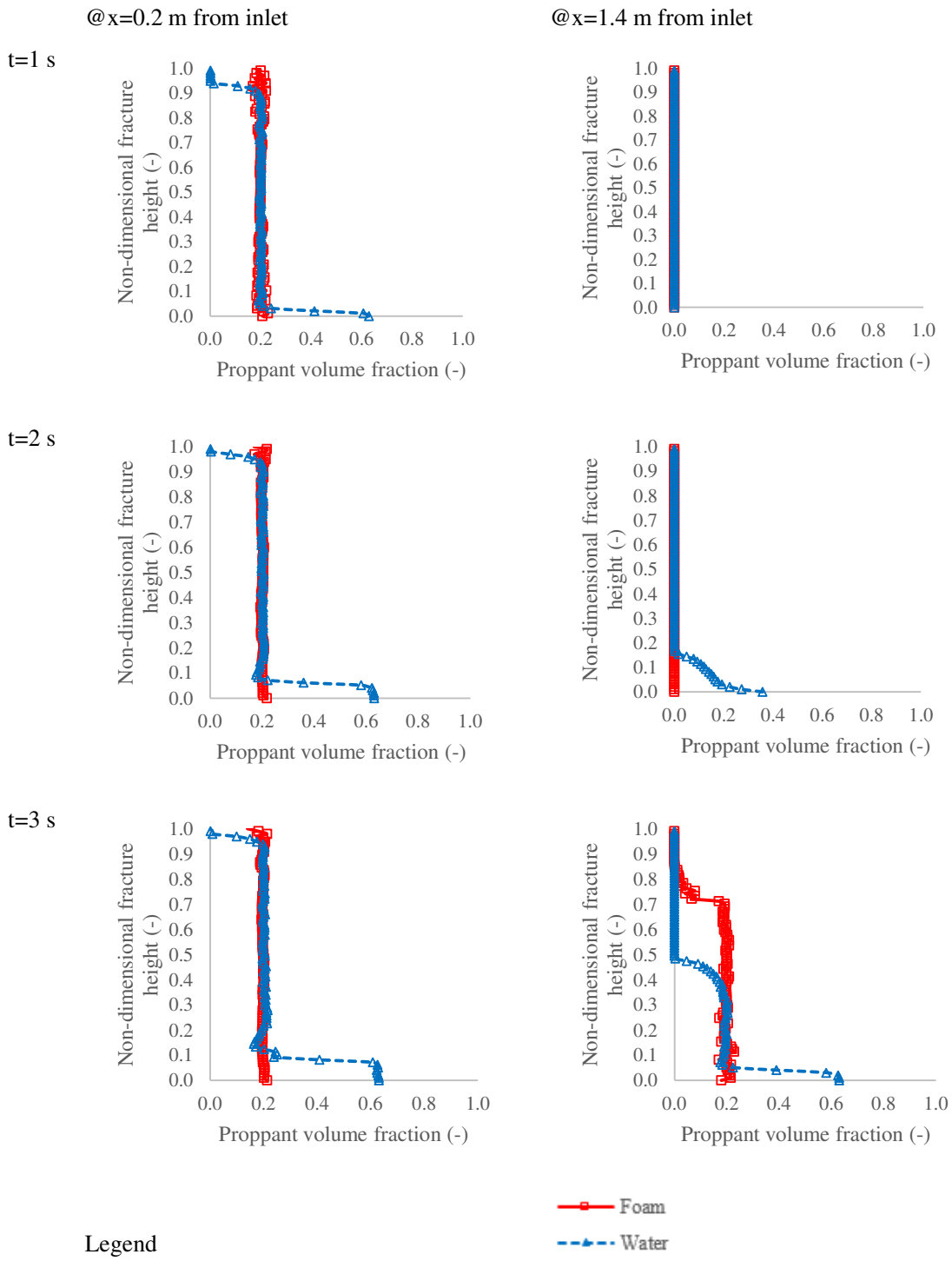

Figure 5.23 Comparison of the proppant volume fraction with the non-dimensional fracture height for foam and water-based fracturing fluid at two different locations (x=0.2 m and x=1.4 m) inside the fracture

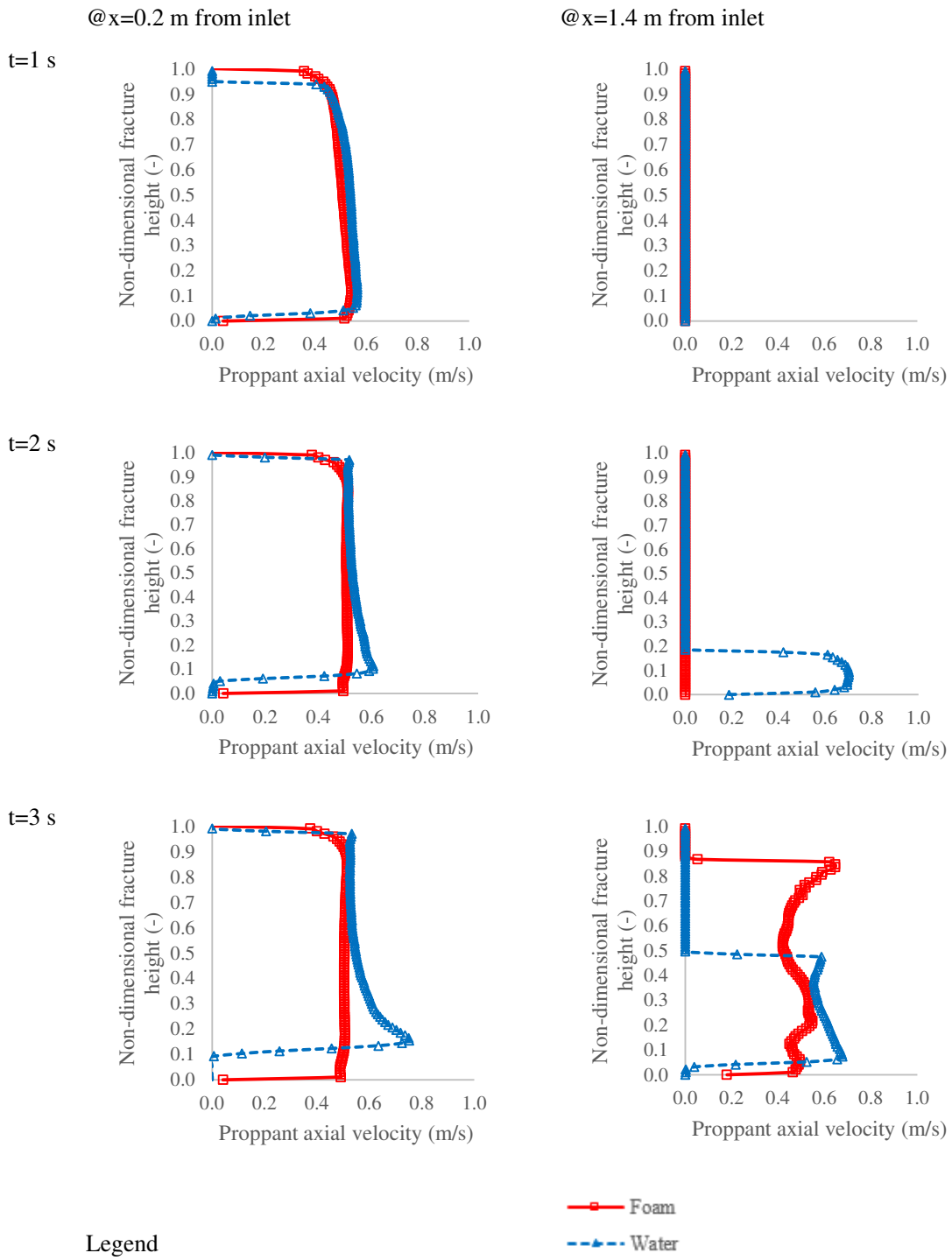

Figure 5.24 Comparison of the proppant axial velocity with the non-dimensional fracture height for foam and water-based fracturing fluid at two different locations (x=0.2 m and x=1.4 m) inside the fracture

5.3 Summary of the key findings

Numerical simulation of proppant movement is studied within the hydraulic fracture using the DDPM model in which leak-off from the fracture wall and fracture roughness are modelled together. The model was validated with the reported experimental study and show good agreement. The simulation results suggest that neglecting the fracture roughness in the proppant transport model can result in over predicting the proppant bed length and underpredicting the proppant suspension layer by 10-15%. Furthermore, neglecting the fluid leak-off effect can result in under predicting the proppant bed height by 10-50% and over predicting the proppant suspension layer by 10-50%. The parametric study was performed to understand the proppant settling and transport mechanism by the variation in injection velocity, proppant concentration, fracture height, and use of foam as fracturing fluid. The sensitivity analysis of injection velocity shows that it is one of the key factors during Hydraulic Fracturing design. For low viscosity fluid like slick water, higher injection velocity can have higher proppant concentration in the suspension and result in transporting proppant to a greater distance inside the fracture. The sensitivity analysis of proppant concentration shows that proppant concentration has a complex effect on proppant transport, such as proppant settling velocity, the rate of proppant bed build-up. The higher proppant concentration can help to reach the equilibrium height quickly, higher proppant velocity in the longitudinal direction and longer proppant bed length.

The comparison of foam injection with water injection shows that foam has improved capability to suspend proppants and using foam as a fracturing fluid have the potential to mitigate the challenge of quick deposition of proppant in shale gas reservoirs. Considering the applicability of the DDPM model for rough fractures, the current study suggests that the DDPM model can be used for practical problems of petroleum engineering interests for proppant distribution and settling. The current study has enhanced the understanding of complex proppant transport phenomenon in hydraulic fractures with fluid leak-off by capturing the proppant-fracturing fluid interaction and inter-particle physics accurately using the advanced computational methods.

Chapter 6: Effect of Fracture Roughness on the hydrodynamics of proppant transport in hydraulic fractures[3]

In this chapter, the DDPM model discussed in Chapter 5, which is a combination of CFD-DEM and Eulerian Granular method is used to investigate in detail the effect of fracture roughness on the hydrodynamics of proppant transport in rough fractures. It solves the mass and momentum conservation equations to model the continuous phase, and the proppant phase is modelled in the Lagrangian frame by tracking their motion using Newton's second law of motion (Suri, Islam and Hossain 2019). The inter-proppant interaction is modelled by KTGF, and the proppant-wall interaction is modelled using the Lagrangian method (Suri, Islam and Hossain 2020b). It overcomes the challenges of Eulerian-Granular method and is computationally faster than Eulerian-Lagrangian methods. Like CFD-DEM, the DDPM model can be used for higher volume fraction. The reported models in the literature (Tomac and Gutierrez 2014, Zhang, Li and Gutierrez 2016, Hu et al. 2018) are described for planar, and smooth fracture geometry without fluid leak-off behaviour and limited to the 2D. In the present study, an attempt has been made to overcome this challenge to capture the proppant physics in rough fracture with a fluid leak-off from the fracture wall and propose a 3D proppant transport model. The model also incorporates the fluid leak-off from the fracture walls for slick water. First, the proppant transport and distribution in smooth fractures is studied. Subsequently, proppant transport and distribution in real and rough fracture geometry is presented with fluid leak-off, and a detailed analysis is presented.

6.1 Model development-

The key aim of the present work is to extensively investigate the impact of fracture roughness on the hydrodynamics of proppant transport and distribution in hydraulic fractures. A CFD based DDPM numerical model is used to solve this multiphase flow problem coupled with fluid leak-off from the fracture wall in a rough fracture geometry in the unconventional reservoir.

---

[3] The results from this chapter are submitted and under review in the Journal of Natural Gas Science and Engineering

Suri, Y., Islam, S.Z. and Hossain, M., 2020. Effect of Fracture Roughness on the hydrodynamics of proppant transport in hydraulic fractures. *Journal of Natural Gas Science and Engineering, 80*, p.103401. https://doi.org/10.1016/j.jngse.2020.103401

6.1.1 Problem formulation and Joint Roughness Coefficient profiles

Barton and Choubey (1977) were among the early researchers who studied the fracture roughness in detail and proposed a parameter called Joint Roughness Coefficient (JRC), denoted by Θ_{JRC}, to differentiate the rough fractures. JRC has been widely used in the literature to generate rough fracture profiles and investigate the fluid flow in rough fracture (Olsson and Barton 2001, Giacomini et al. 2008, Crandall, Ahmadi and Smith 2010, Rasouli and Hosseinian 2011, Briggs, Karney and Sleep 2017). The equation for JRC is defined by Eq. (6.1).

$$\Theta_{JRC} = \frac{\tan^{-1}\left(\frac{\tau}{\sigma_n}\right) - \Phi_b}{log\left(\frac{JCS}{\sigma_n}\right)} \tag{6.1}$$

Where τ is the maximum shear strength; σ_n is the effective stress in the normal direction; Φ_b is the angle of friction; and σ_c is fracture compressive strength, JCS is the joint wall compressive strength. The fracture profiles with different JRC values are shown in Figure 6.1. Barton and Choubey (1977) calculated the value of JRC for different rock types. The JRC value for calcareous shale was calculated as 8.2. More recently, Kassis and Sondergeld (2010) extracted the Scanning Electron Microscope (SEM) image of a Barnett shale core sample in order to investigate the fracture roughness. The fracture roughness for the Barnett shale sample can be related to the JRC scale of Barton and Choubey (1977) in between 10-11. Furthermore, some of the smooth rock types analysed by Barton and Choubey (1977) are Slate and Gneiss whose JRC values range in between 2-6.

In the present study, three different rough fractures were created with JRC values 4, 8 and 16 using the published data by Barton and Choubey (1977) and SynFrac software. However, it was ensured to have a normalised distribution for the fracture geometry with a mean fracture aperture of 5 mm. The hydraulic fracture can be of a variable size from centimetres scale to several meters scale. In the present study, the computational domain involves a three-dimensional rough fracture with dimensions 1.5 m x 0.005 m x 0.5 m, length x width x height, respectively, as shown in Figure 6.1. The two-dimensional rough fracture profile in y-z direction was created using SynFrac software (Ogilvie, Isakov and Glover 2006) which followed the normal distribution fracture aperture with a mean of 5 mm and a standard deviation of 1 mm. Then, the fracture surface was created using the two-dimensional rough fracture profile in y-z direction and mean fracture aperture of 5 mm. The fracture surface was extruded in the fracture length or x-direction to create a three-dimensional rough fracture geometry. The method from Briggs, Karney and Sleep (2017) was used to generate the rough fracture model. The fracture profile is shown in

Figure 6.1 and the histogram showing the normal distribution of the fracture height with a mean aperture of 5 mm is shown in

Figure 6.2. One of the key assumptions underlying the current model is that no dynamic fracture propagation is considered in this study.

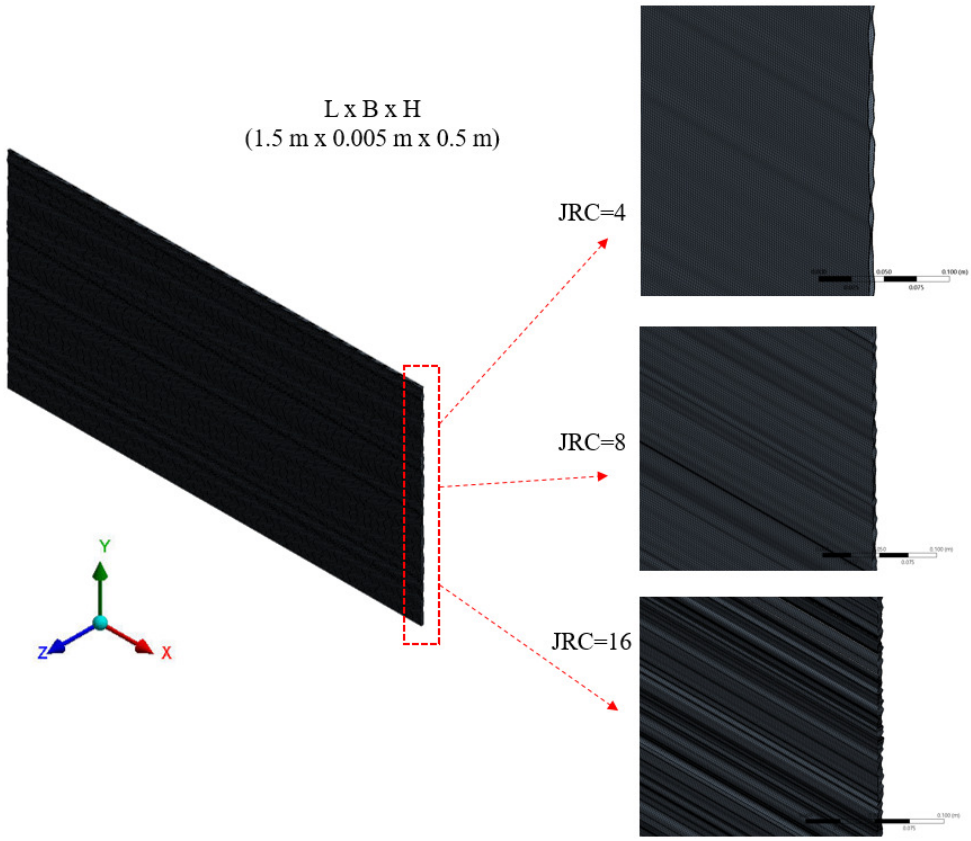

Figure 6.1 Rough fracture geometries with different JRC values

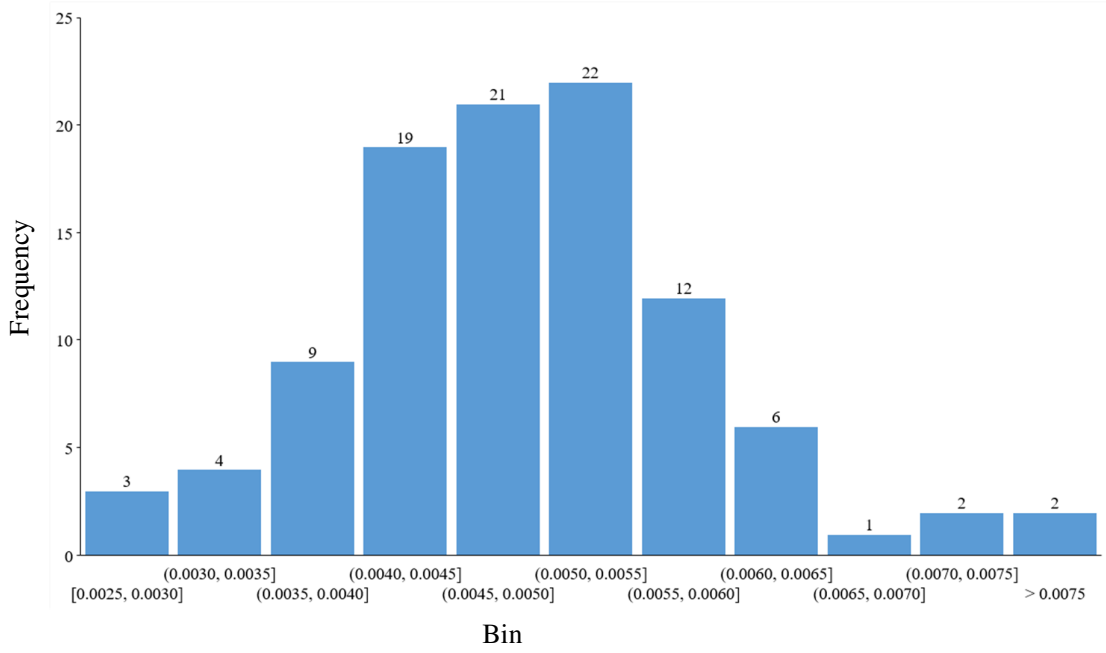

Figure 6.2 Histogram for normal distribution of fracture roughness

6.2 Mathematical model

6.2.1 Governing Equations

As discussed earlier in chapter 3, the proppant transport and fluid flow in the hydraulic fracture can be numerically modelled using mainly two methods- Eulerian-Granular method and Eulerian-Langrangian method (or CFD-DEM). In the present work, the DDPM model is used, which is a combination of CFD-DEM and Eulerian-Granular method, as discussed earlier in chapters 3 and 5. It solves the mass and momentum conservation equations to model the continuous phase, and the proppant is tracked by calculating and tracking the mass, velocity, and forces acting on a particle using Newton's second law of motion. This is referred to as tracking in the Lagrangian frame in the DDPM model. It overcomes the challenges of Eulerian-Granular method and is computationally faster than CFD-DEM (section 3.2.3). The key governing equations are discussed in chapter 3.

6.2.2 Physical model

Proppant transport and distribution were investigated in a hydraulic fracture using the CFD technique in ANSYS FLUENT. The geometry or computational domain used in the current study is, as shown in Figure 6.1, with dimensions 1.5 m (length) × 0.005 m (width) × 0.5 m (height).

In order to obtain a mesh independent solution, a mesh sensitivity analysis was done by selecting a structured mesh with mesh sizes parameter 0.002 m, 0.0025 m, 0.003 m, and 0.005 m. Three inflation layers with the first layer thickness 0.0005 m and growth rate of 1.2 were added in all the fracture geometries to account for the fracture roughness. The results of the mesh sensitivity analysis were compared against the proppant volume fraction and proppant axial velocity vs fracture height at a cross-section of 0.5 m from the inlet (Figure 6.3). The results from the mesh sensitivity study, suggest that the mesh size of 0.0025 m (600×200×8 elements) was reasonably able to provide the mesh independent, numerically converged and computationally efficient solution.

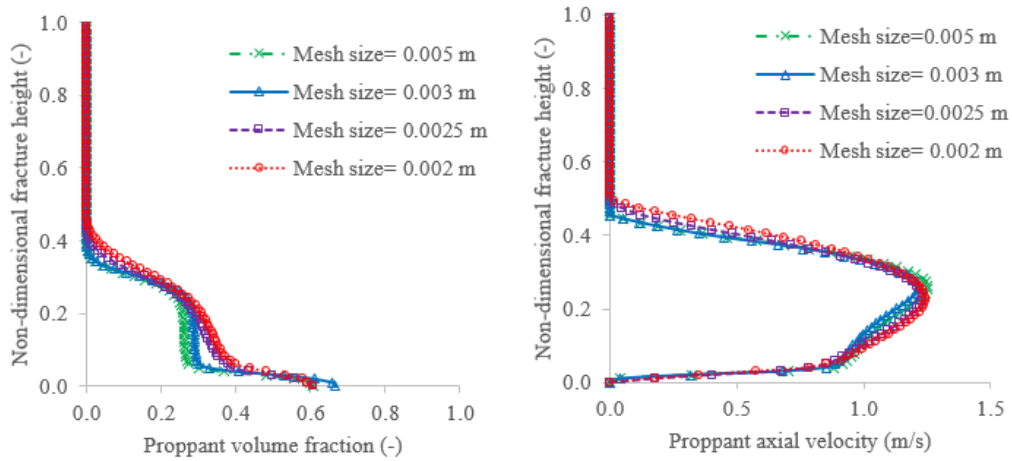

Figure 6.3 Mesh Sensitivity Study a) plot of proppant volume fraction vs fracture height b) plot of proppant axial velocity vs fracture height

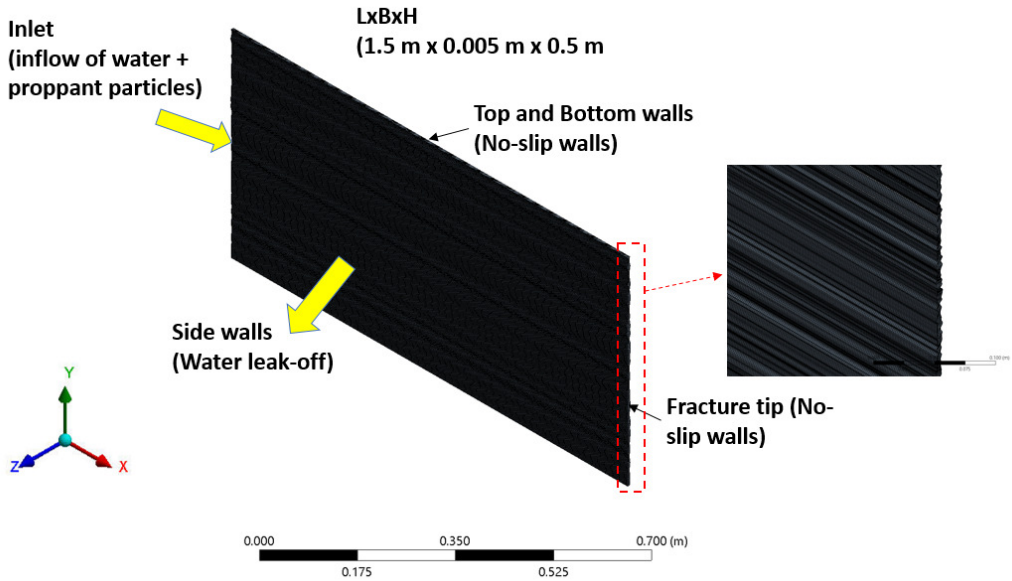

Figure 6.4 Computational domain

Next, appropriate boundary conditions and simulation properties were defined. A velocity inlet boundary condition is used at the inlet where fluid and proppants are injected together, as shown in Figure 6.4. The proppant size, injection rate (or injection velocity), fluid viscosity and fracture width were varied for different JRC values, as shown in Table 6.1. The top, bottom walls and fracture tip were specified as no-slip stationary walls for the liquid phase, as shown in Figure 6.4. For the particle phase, the reflect boundary condition with specularity constant of 0.01 and wall reflection coefficient of 0.9 in both normal and tangential directions was used to model the particle-wall collision, as discussed earlier in section 3.3.3. In order to mimic the fluid leak-off into the surrounding porous rock, the fluid leakage effect is modelled through the fracture sidewalls with the help of a UDF, as explained earlier in section 3.3.2. In order to obtain the fluid leakage rate, an explicit CFD study was carried out to calculate the water leaking off rate along the fracture sidewall. The underlying equations describing the source terms and UDF used to model the fluid leak-off is explained in detail in chapter 3. The fluid leak-off profile along the fracture length to a surrounding porous rock with porosity 5% and permeability 0.5 mD used in the current study is shown in Figure 6.5.

Table 6.1: Physical properties of proppant and fluid used in the simulation

Properties	Value
Proppant diameter	0.35, 0.50, 0.65 mm
Proppant density	2650 kg/m^3
Fluid density	1000 kg/m^3
Fluid inlet velocity	0.1, 0.25, 0.5 m/s
Fluid viscosity	0.0005, 0.001, 0.005, 0.010 Pa-s
Proppant volume fraction	0.15
Fracture width	3, 5, 10 mm
JRC	0 (Smooth), 4, 8, 16

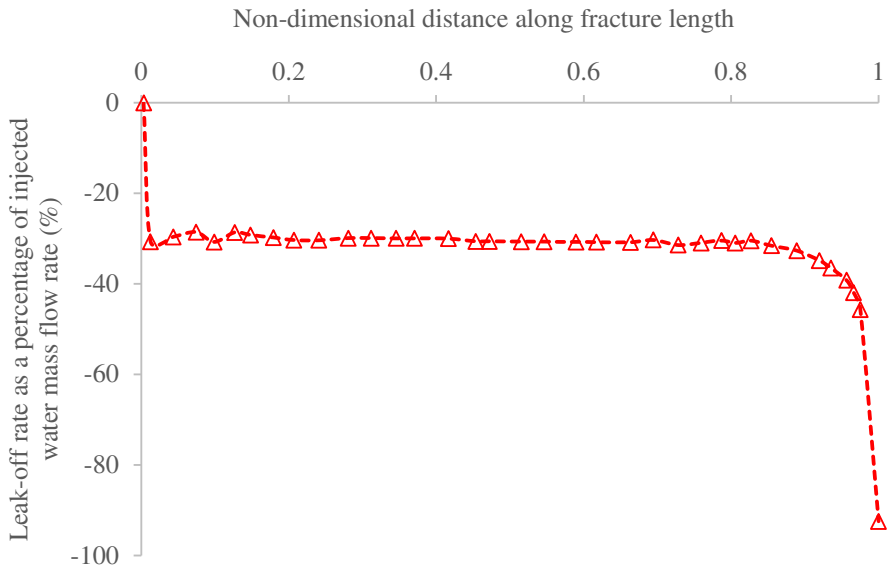

Figure 6.5 Fluid leak-off rate at fracture wall along the fracture length

The pressure-based solver with gravitational effects was used to solve the governing proppant transport equations as described earlier in section 3.3.3. The turbulence model used was the Shear Stress Transport (SST) k-ω model, as explained earlier in section 3.2.3.2. The typical value of proppant volume fraction in the slick water fracturing fluid slurry varies from 3-20% (Tsai et al. 2012, Bokane et al. 2013, Jain et al. 2013). Thus, in the current study, the proppant volume fraction of 15% is used to model the inter-proppant interaction. The viscosity of the granular phase is calculated from the Gidaspow, Bezburuah and Ding (1991) correlation as discussed earlier in section 0. The primary role of granular viscosity is used to consider the frictional losses. The frictional viscosity refers to the shear viscosity based on the viscous-plastic flow and is calculated using the Johnson and Jackson (1987) correlation (section 0). The drag force used to model the interaction between the two phases is based on Gidaspow (1994) drag law (section 0). The collision between the proppant particles is modelled using the restitution coefficient and KTGF, as explained earlier in chapter 3 (sections 3.2.1.5-3.2.1.8).

The time step used in the simulation was 1.0E-3 s. The reflect DPM boundary condition used at walls so that the particles will reflect after the collision with the wall. Finally, the Phase-coupled SIMPLE algorithm is used as a solution method for the pressure-velocity coupling (section 3.3.3). The node-based averaging scheme is used to calculate the gradient and the discretisation of momentum, volume fraction, and turbulent kinetic energy was solved by the second-order upwind scheme, as explained earlier in section 3.3.3.

6.3 Dimensional analysis

Non-dimensional parameters used in the present study were derived using the dimensional analysis (Tan 2011). The key parameters that affect the proppant transport and fluid flow in hydraulic fractures are- Proppant properties (proppant size or proppant diameter d_p, proppant density d_p), fracturing fluid properties (fluid viscosity μ_i, fluid density ρ_l , injection flow rate or injection velocity v_i), geo-mechanical parameters (fracture width w, fracture roughness Θ_{JRC}, fluid leak-off rate $c_{L,}$) (Li, Zhang and Lu 2018). Thus, the proppant distribution, velocity and pressure at any position can be expressed in the following function:

$$(\alpha, v, P) = f(d_p, \rho_{p,} \rho_{l,} v_{i,} \mu_{i,} w, c_{L,} \Theta_{JRC}) \tag{6.2}$$

Eq. (6.2) can be written in the non-dimensional form by using proppant diameter d_p, injection velocity v_i and fracturing fluid density ρ_l

$$\left(\alpha, \frac{v}{v_{i,}}, \frac{P}{\rho_l \,.\, v_i^2}\right) = f(\frac{d_p}{w}, \frac{\rho_p}{\rho_l}, \frac{v_s}{v_r}, \frac{\rho_l . v_{i,} . d_p}{\mu_i}, \frac{(\rho_p - \rho_l)\rho_l d_p^3 g}{\mu_i^2}, c_{L,} \Theta_{JRC}) \tag{6.3}$$

Where, $\frac{\rho_l . v_{i,} . d_p}{\mu_i}$ is the Reynolds number that describes the ratio of inertia effect to viscous effects, and $\frac{(\rho_p - \rho_l)\rho_l d_p^3 g}{\mu_i^2}$ is the Archimedes number that describes the ratio of inertia effects to gravity effects.

The density ratio of proppant-to-fluid is constant, and the leak-off rate depends on the reservoir characteristics (porosity and permeability), which are also assumed as constant for a given porosity and permeability. Therefore, Eq. (6.3) can be re-written as-

$$\left(\alpha, \frac{v}{v_{i,}}, \frac{P}{\rho_l \,.\, v_i^2}\right) = f(\frac{d_p}{w}, \frac{v_s}{v_r}, Re, Ar, \Theta_{JRC}) \tag{6.4}$$

A series of simulation run was performed by varying the injection velocity, proppant diameter, fluid viscosity, and fracture roughness one at a time. A detailed investigation of the effects of the dimensionless parameters on the proppant transport and flow characteristics was carried out and explained in the following section.

6.4 Results and Discussion

6.4.1 Proppant transport and distribution in smooth fracture

In the slurry flow, the fracturing fluid carries the proppants inside the fracture, and the fracturing fluid also exerts a drag force on the proppants. Due to the drag force and the energy dissipation, the proppant travels slowly compared to the fluid, and this results in slippage velocity. The proppant motion with fluid can be characterised by the slippage velocity, which is a difference in the fluid and proppant velocity. The slippage velocity depends upon the proppant size and fracturing fluid rheology. Furthermore, when the proppant transport in the hydraulic fractures, the interaction between the proppants and fracture wall affects the horizontal motion. The flow velocity at the centre of the fracture is highest resulting in proppants to transport faster and is smallest near the walls due to non-slip walls, and high shear-induced forces.

To understand the effect of slippage velocity and proppant size ratio on proppant transport, a normalised graph is plotted against variables $\frac{v_p - v_l}{v}$ and $\frac{d}{w}$ as shown in
Figure 6.6. Where, $v_p - v_l$ represents the slippage velocity, v is the characteristic velocity and can be defined by $\sqrt{gd}$, d is the proppant diameter and w is the fracture width. It can be interpreted from the figure that as the fracture width decreases or proppant diameter increases, the size ratio $\left(\frac{d}{w}\right)$ increases. It results in greater fracture wall retardation effect on proppant motion and consequently decreases in the proppant horizontal transport velocity or slippage velocity.

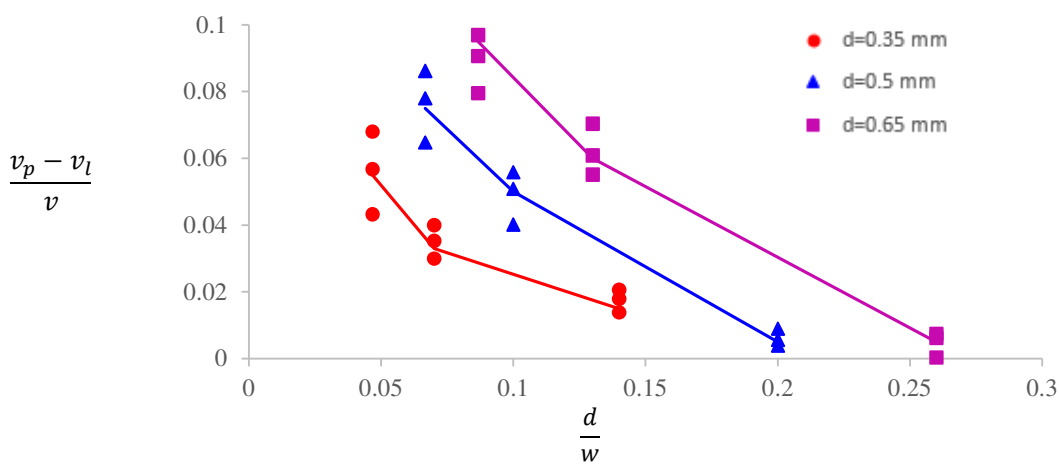

Figure 6.6 variation of slippage velocity with proppant size ratio

The slippage velocity depends on the injection velocity, proppant size and proppant Reynolds number. Thus, to understand the role of slippage velocity on proppant and fluid properties, two non-dimensional variables were evaluated $Re.\frac{d}{w}$ and $Re\sqrt{\frac{v_p}{v_i}}$. $Re.\frac{d}{w}$ is a function of proppant size and $Re\sqrt{\frac{v_p}{v_i}}$ depends on the slippage velocity. The simulation results of all the cases in Table 6.1 with a smooth fracture profile are plotted on a log-log scale in Figure 6.7. It can be interpreted that $Re.\frac{d}{w}$ and $Re\sqrt{\frac{v_p}{v_i}}$ varies linearly in a log-log scale and the power law correlation was defined using the curve fitting, which can be directly used in the fracture simulators to determine the average horizontal velocity of proppants in smooth fractures.

$$Re.\frac{d}{w} = 0.07\left(Re\sqrt{\frac{v_p}{v_i}}\right)^{1.1} \tag{6.5}$$

Where v_i is the injection velocity in m/s.

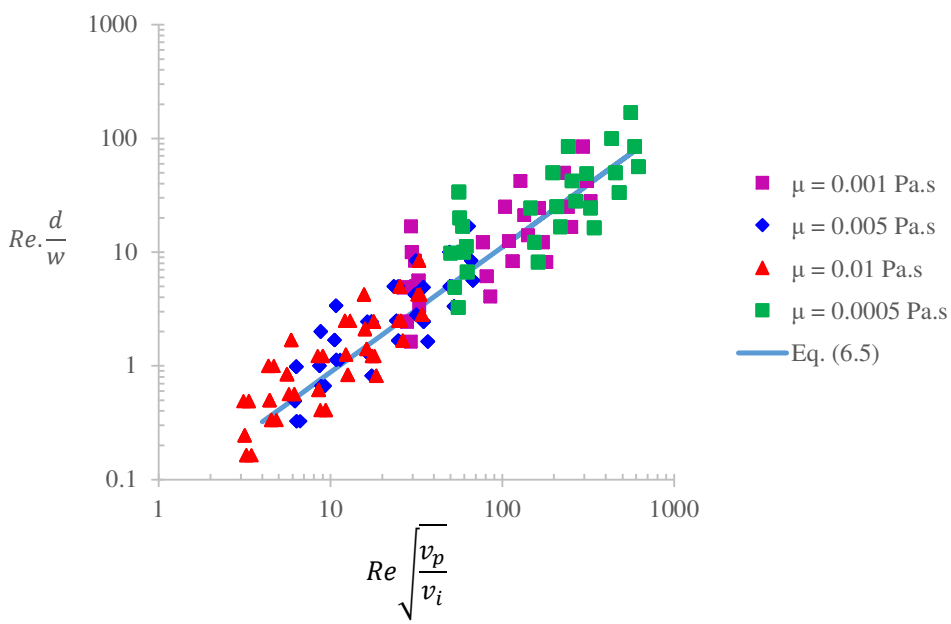

Figure 6.7 Log-log plot of correlation between proppant Reynolds number, proppant size ratio and proppant horizontal velocity in smooth fracture

6.4.2 Role of fractures roughness on proppant hydrodynamics

The fracture roughness or the irregular wall surfaces can aid in greater inter-proppant interactions and proppant-fracture wall interaction, which consequently influence the proppant transport and distribution. In order to investigate in detail, the role of fracture roughness in proppant transport regime, understanding of the different fracture roughness and flow parameters is prerequisite. As mentioned earlier, Barton and Choubey (1977) were among the early researchers who studied the fracture roughness in detail and proposed a parameter called Joint Roughness Coefficient to differentiate different rough fractures. The equation for JRC is defined in Eq. (6.1). In the present study, the rough fractures were created using the JRC profiles from the study of Barton and Choubey (1977) using different JRC profiles and SynFrac software as described earlier. However, the fracture geometries using JRC profiles were created such that it followed a normalised distribution with a mean aperture equal to fracture width. Then the proppant transport was modelled in the rough fractures using the DDPM model (CFD-DEM) described earlier, and the simulation results in the form of contour plots are shown in Figure 6.8. The results in Figure 6.8 suggest that fracture roughness plays a significant role in proppant transport. As the JRC increases, it escalates the inter-proppant and proppant-fracture wall interaction. Consequently, it adds that the degree of randomness in the flow to make it more turbulent and complex.

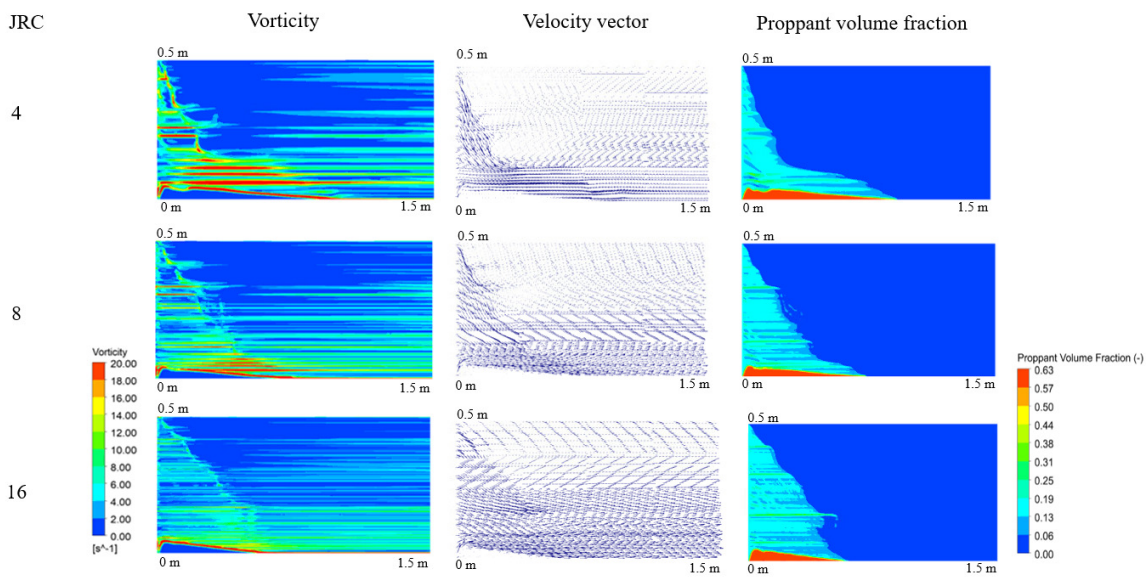

Figure 6.8 Comparison of vorticity, velocity vector and proppant volume fraction for different JRC profiles

The fracture roughness further affects the hydrodynamic and mechanical behaviours of the proppant flow. The turbulence in the flow due to the fracture roughness increases the ability of proppants to suspend in the fluid and support the proppant to transport longer distance into the fracture. Figure 6.8 shows the comparison of vorticity, velocity vector plot and proppant volume fraction plot for different JRC fracture profiles. It can be interpreted from the comparison that with the increase in JRC, it increases the vorticity in the flow due to higher turbulence and flow instability caused by the proppant-wall and inter-proppant collisions. Notably, at the fracture wall, the high vortex region is evident where the proppant frequently collides with the rough fractures leading to higher turbulent kinetic energy and randomness in the flow. It can be noticed from Figure 6.8 that the fracture with JRC=16 has significantly greater vorticity in some region inside the fracture domain where the fracture with JRC=4 has no vorticity. This roughness induced turbulence is also evident in the velocity vector plot for different JRC profiles. On comparison of proppant volume fraction contour plot for different JRC profiles, two important observations can be noticed. Firstly, with the increase in JRC value, the increase in the amount of proppant suspension is evident in Figure 6.8 by the size of the proppant suspension layer. This suggests that with time, the suspended proppant can be transported further inside the fracture. Thus, neglecting the JRC or effect of fracture roughness could lead to inaccurate estimation of the proppant and fluid velocity into the hydraulic fracturing design. Secondly, for the lower value of JRC or relatively smooth fractures, the fracture wall exerts an additional force or mechanical retardation force on proppants, which slows down the suspended proppants and results in more proppant deposition. This is evident in Figure 6.8, where the proppant bed observed in JRC 4 is greater than JRC 8 and JRC 16 fracture profiles. The mechanical retardation effect becomes more dominant, especially in the low viscosity fracturing fluid, like slick water, commonly used in shale gas reservoirs. In the high viscosity fracturing fluid, the effect is less dominant.

Next, to investigate the impact of fractures with different JRC profiles on flow regimes, the proppant size and injection rate were varied and compared in Figure 6.9 and Figure 6.10 respectively. It can be interpreted from Figure 6.9 proppant volume fraction plots that proppant particles with greater size form a larger proppant bed compared to smaller size proppants. On the contrary, in terms of proppant suspension, the proppants with smaller size is noted to have a larger suspension region in Figure 6.9 proppant volume fraction plot compared to the larger size proppants. This can be explained by the proppants with greater size due to its comparatively heavier weight has a higher vertical settling velocity and thus greater tendency to deposit. Conversely, the smaller size proppants due to the lower settling velocity is easily carried away by the flowing fluid and thus resulting in more suspended proppant particles.

Figure 6.10 shows that as the injection rate or injection velocity is increased, less proppant deposition is seen in the volume fraction contour plot. This can be explained by the increase in

injection velocity results in the increase in the ability of the proppant to suspend and creates randomness in the flow. This further leads to high vorticity in the flow. Thus, a higher number of suspended proppants due to increase in injection velocity can aid in more extended proppant transport.

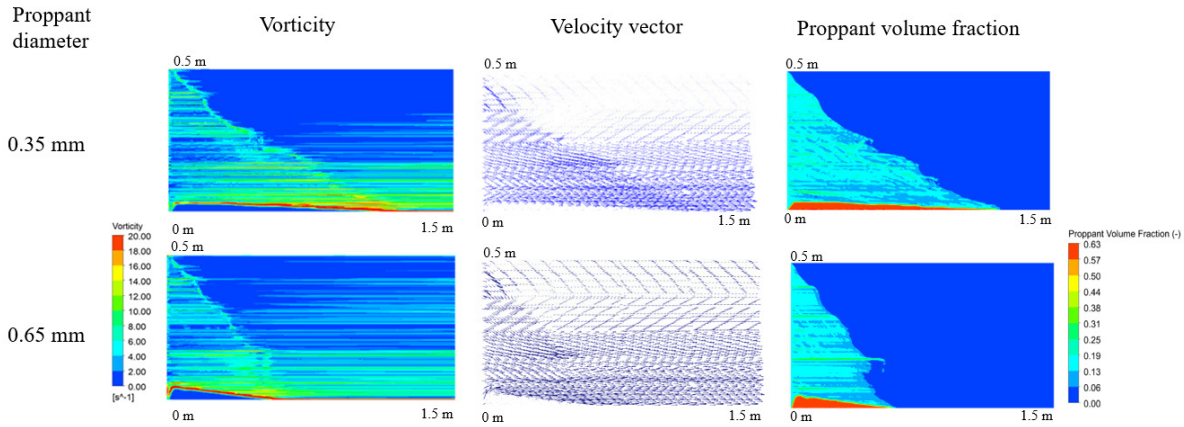

Figure 6.9 Comparison of proppant transport in rough fractures with proppant diameter 0.35 mm and 0.65 mm

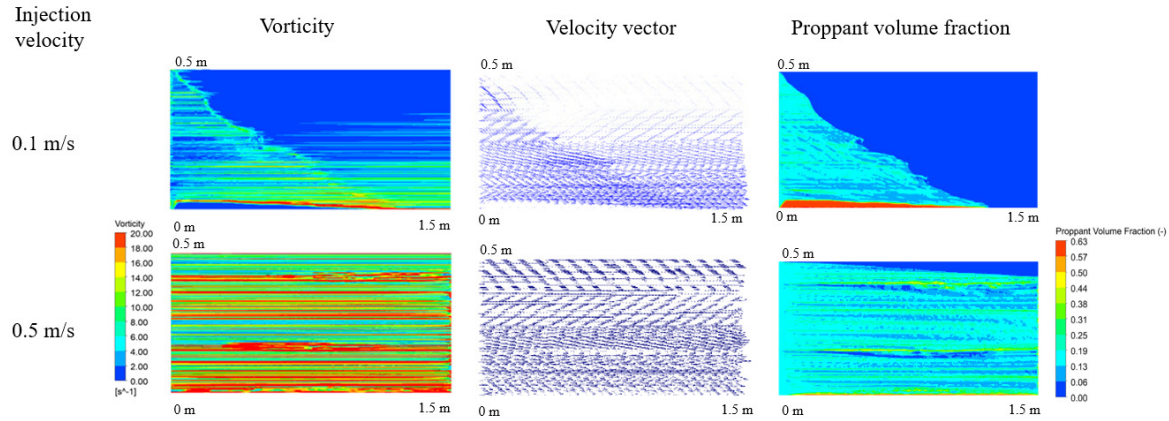

Figure 6.10 Comparison of proppant transport in rough fractures with different flow injection velocities

Next, a comparison is made between proppant transport in smooth and rough fracture case with JRC of 16, proppant diameter of 0.65 mm, fluid viscosity of 1 cP and injection velocity of 0.1 m/s. As explained earlier, it is evident from Figure 6.11 that due to the rough fracture wall, the mechanical interaction between the proppant-fracture wall increases and it significantly impacts the vorticity and turbulence in the flow. The increase in the vorticity leads to the higher ability of the slurry to suspend proppants and consequently less deposition of the proppants is seen in terms of proppant bed.

As analysed above, the fracture roughness plays a significant role in the hydrodynamics of proppant transport, and qualitative comparison of vorticity, longitudinal velocity and volume fraction is shown in Figure 6.8-6.11. Next, to quantitatively investigate the effect of fracture roughness on the proppant transport and distribution, a fracture roughness factor is introduced which is defined as $\in_R = (v_s/v_r)$. The fracture roughness factor is the ratio of proppant axial velocity in a smooth fracture (v_s) to that in the rough fracture (v_r). A detailed analysis was carried out to investigate the impact of JRC on proppant transport. Different proppant transport simulations were run using the DDPM model with varying proppant properties (proppant diameter), flow properties (injection rate and fluid viscosity) and geomechanical properties (fracture roughness JRC and fracture width) one at a time as summarized in Table 6.1.

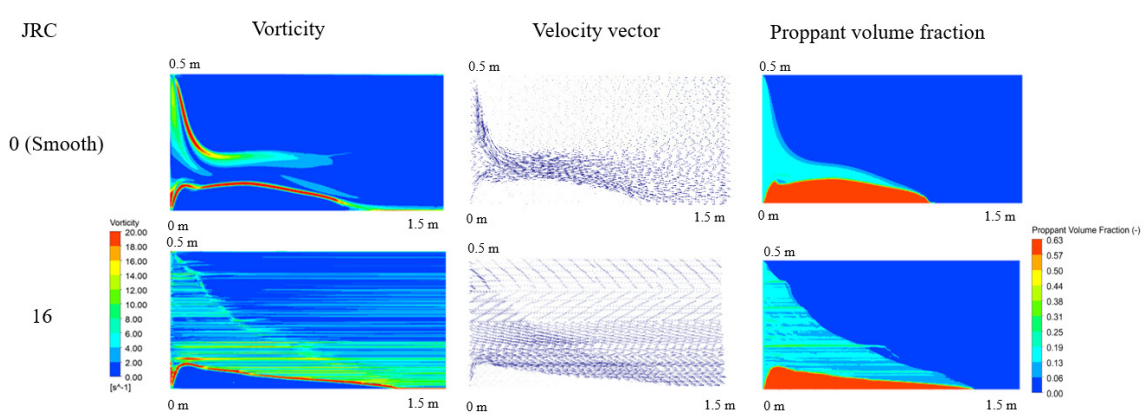

Figure 6.11 Comparison of proppant transport in smooth fracture and rough fracture with JRC 16

Firstly, the effect of JRC fracture profiles on the roughness factor was analysed (Figure 6.12). It can be interpreted from Figure 6.12 that with the increase in JRC, the roughness factor decreases. This is particularly true under the influence of low injection velocities and higher diameter proppant size (Figure 6.12(a-f)). This is due to the increase in fracture roughness results in an increase in the inter-proppant and proppant-fracture wall interactions. Thus, strong mechanical interactions cause more randomness in the flow and accelerate the proppants axial velocity, resulting in the roughness factor $\in_R$ below 1. However, during the proppant transport in high viscosity fluid, the mechanical interaction-induced flow effects do not play a dominant role in proppant horizontal transport, which causes $\in_R \approx 1$ and can be ignored, as shown in Figure 6.12. Thus, the mechanical interaction-induced effects are strongly dependent on proppant transport regimes (injection velocity, proppant size and fluid viscosity).

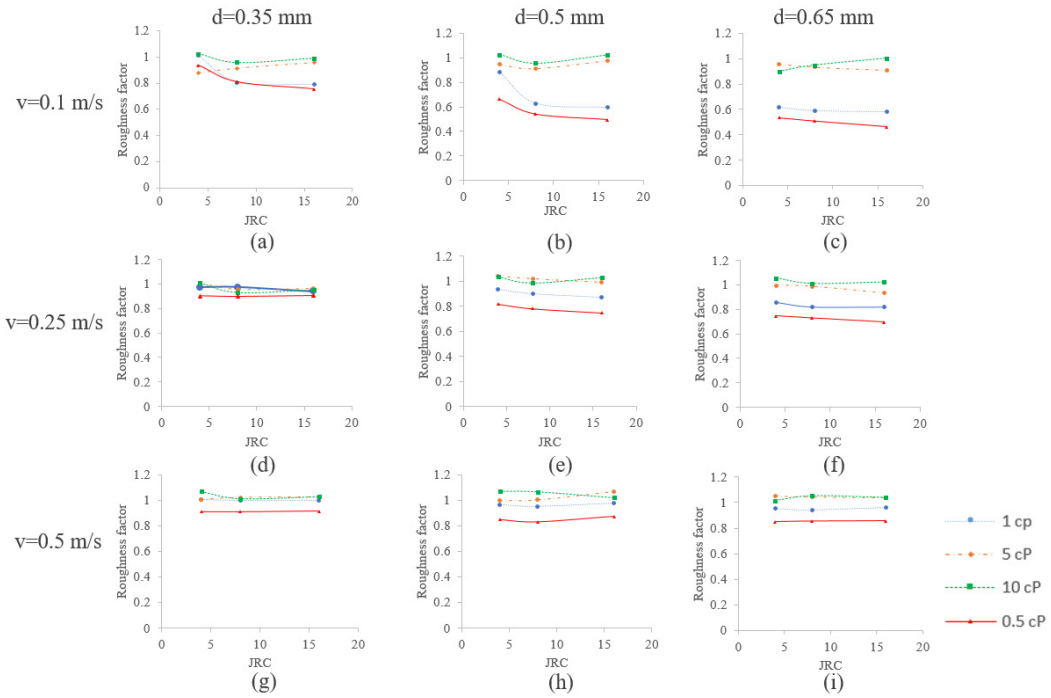

Figure 6.12 Variation of fracture roughness factor with JRC for different injection velocity, and proppant size

Because of the strong dependence of proppant transport in different flow regime, the transport regions should be defined. A dimensionless composite parameter is introduced (Ar/Re) which is a ratio of Archimedes number and Reynolds number. The Archimedes number denotes the ratio of buoyancy force to inertia force. Figure 6.13 shows the plot between the fracture roughness factor $\in_R$ and Ar/Re, which suggests that for a low value of Ar/Re, the fracture roughness factor varies mostly independent of Ar/Re. Conversely, when the ratio of Ar/Re>10, the fracture roughness factor significantly decreases. This can be explained by when proppants are transported with high-viscous fracturing fluids; the proppant Reynolds number is small. This results in a relatively stable flow field inside the fracture and consequently, low mechanical interaction flow effects. However, when the proppants are transported with low-viscous fluids, the proppant Reynolds number is higher. This results in significantly higher inter-proppant and proppant-wall interactions and consequently increased mechanical interaction flow effects. Thus, proppant horizontal transport is greatly dependent on the fracture roughness and the ratio of Ar/Re.

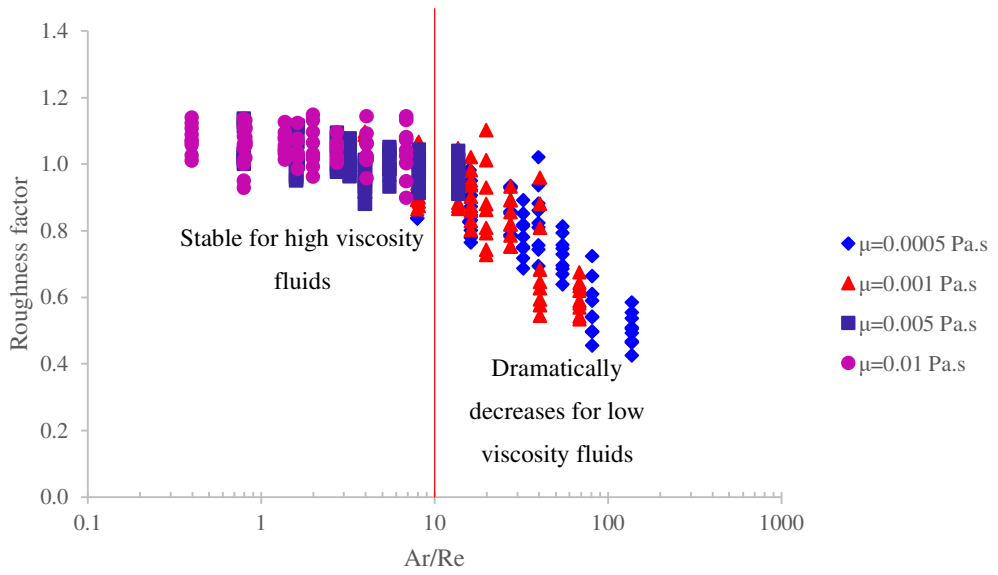

Figure 6.13 Semi-log plot of fracture roughness factor with Ar/Re

Figure 6.13 is categorised into two regions based on the variation of fracture roughness factor. In the first region, the fracture roughness factor is almost constant and does not vary much against Ar/Re for the range of Ar/Re between 0.3 and 10. The fracture roughness factor can be regarded as primarily dependent on JRC, proppant size ratio and injection rate or velocity in this region, and independent of the ratio of Ar/Re. Thus, a non-dimensional parameter $\Theta_{JRC}\left(\frac{d}{w}\right)$ is proposed, and the plot of the roughness factor $\in_R$ against the variation in the non-dimensional parameter is shown in Figure 6.14. Figure 6.14 shows that fracture roughness factor varies linearly with the change of non-dimensional parameter $\Theta_{JRC}\left(\frac{d}{w}\right)$ and Eq. (6.6) captures the variation of fracture roughness factor against JRC and proppant size ratio for the range of Ar/Re between 0.3 and 10.

$$\frac{v_s}{v_r} = 1 - 0.0007 * \Theta_{JRC}\frac{d}{w} \qquad 0.3 \leq \frac{Ar}{Re} \leq 10 \tag{6.6}$$

From Figure 6.13, the second region can be defined where the fracture roughness factor drastically declines as $\frac{Ar}{Re}$ increases. This can be explained by when the proppant transport with low viscosity fracturing fluids, the inter-proppant and proppant-wall interactions significantly increases, resulting in higher mechanical interaction flow effects. The increase in fracture roughness further adds to mechanical interactions and consequently, the mechanical interaction flow effects become dominant and gradually governs the proppant transport. Thus, in this region, the fracture roughness factor is dependent upon particle Reynolds number and Archimedes number along with JRC, proppant size ratio and injection rate or velocity. A non-dimensional variable that incorporates the effect of JRC, Ar/Re, and d/w is proposed, $\frac{Re}{\Theta_{JRC}.Ar}\left(\frac{w}{d}\right)$, and the plot of the roughness factor $\in_R$ against the variation in non-dimensional parameter is shown in Figure 6.15. Figure 6.15(a) shows that with the increase of the proposed non-dimensional parameter, due to the flow instabilities caused by the fracture roughness and mechanical interaction flow effects, the fracture roughness factor efficaciously increases initially and progressively stabilises to $\in_R = 1$. To gain a better understanding of the results at lower value of non-dimensional parameter, the results are plotted in a semi-log scale in Figure 6.15(b). To encompass the effect of variation of fracture roughness factor on JRC, Ar/Re, proppant size ratio and injection velocity, a new relationship is obtained and shown in Eq. (6.7) that can aid the petroleum engineers to model the proppant transport in rough fractures.

$$\frac{v_s}{v_r} = 1 - 0.13 * \left[\Theta_{JRC}.\frac{d}{w}\frac{Ar}{Re}\right]^{0.3} \qquad 11 \leq \frac{Ar}{Re} \leq 120 \tag{6.7}$$

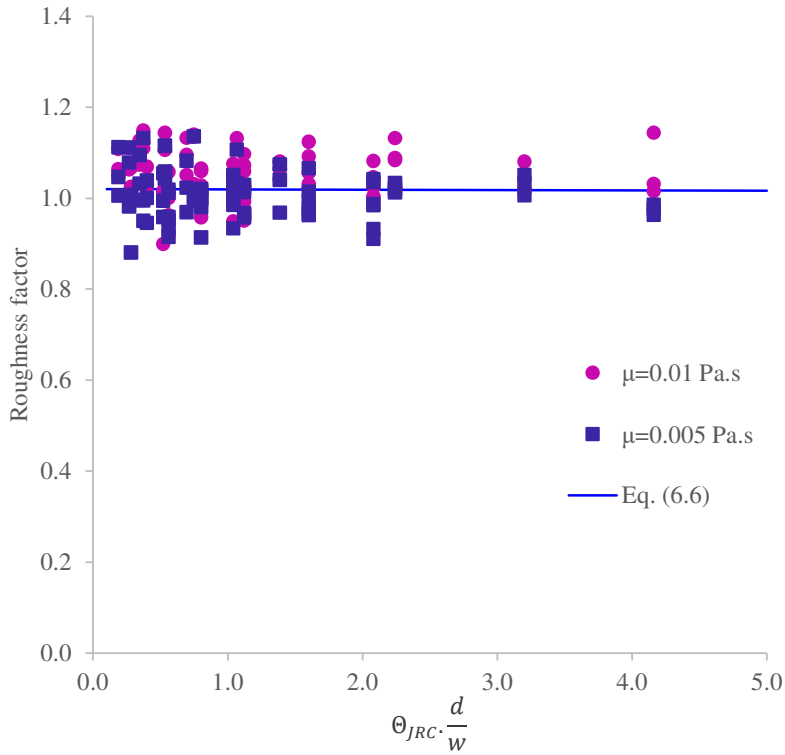

Figure 6.14. Variation of fracture roughness factor with JRC and proppant size ratio for Ar/Re<10

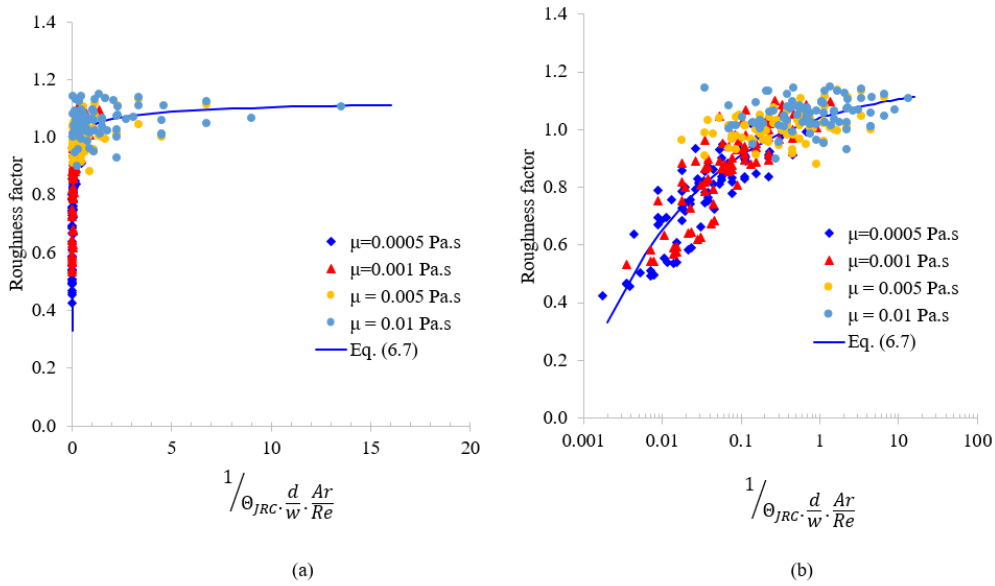

Figure 6.15. Variation of fracture roughness factor with JRC, proppant size ratio and Ar/Re for Ar/Re>10

The correlation developed in the current study from Eq. (6.6) and Eq. (6.7) relates to the proppant horizontal transport velocity against the fracture roughness (JRC), flow regime (Ar/Re), fluid leak-off effects and proppant size ratio (d/w) in 3D fractures. A common assumption widely used during the hydraulic fracturing simulation in shale gas reservoirs and modelling of proppant transport is that the average proppant transport velocity is equal to the carrier fracturing fluid velocity, and the proppant settling velocity follows Stokes' law (Blyton, Gala and Sharma 2018). However, to accurately model the proppant transport and distribution, the effects of fracture roughness, fluid leak-off, drag forces, gravity forces, inter-proppant and proppant-fracture wall interactions are required to be incorporated not included together in previous assumptions. The proposed correlation was compared against the existing studies, namely Zhang, Gutierrez and Chao (2019) and Blyton, Gala and Sharma (2015). Zhang, Gutierrez and Chao (2019) investigated the Joint Roughness Coefficient (JRC) fracture profiles and proposed a proppant transport model in rough fractures. However, the model is limited to two-dimensional fracture geometry, and gravitational effects along with fluid-leak off effects were ignored. The correlation proposed by Zhang, Gutierrez and Chao (2019) is shown in Eq. (6.8). On the other hand, Blyton, Gala and Sharma (2015) comprehensively investigated the proppant transport in hydraulic fractures using CFD-DEM method and proposed a correlation for proppant settling velocity against different proppant size ratio. However, the effect of fracture roughness was ignored in the proppant hydrodynamics. The correlation proposed by Blyton, Gala and Sharma (2015) is shown in Eq. (6.9).

$$\frac{v_r}{v_s} = \begin{cases} 1 - 0.0066.\Theta_{JRC}\dfrac{d}{w}\dfrac{v_i}{\sqrt{gd}} & 0.78 \leq \dfrac{Ar}{Re} \leq 11.15 \\ 1 - \dfrac{\Theta_{JRC}.\dfrac{d}{w}\dfrac{v_i}{\sqrt{gd}}}{\Theta_{JRC}.\dfrac{d}{w}\dfrac{v_i}{\sqrt{gd}} + 238.56\dfrac{Re}{Ar}} & 11.15 \leq \dfrac{Ar}{Re} \leq 394.92 \end{cases} \tag{6.8}$$

$$\frac{v_p}{v_f} = \begin{cases} 1 & \dfrac{d}{w} < 0.4 \\ -1.73\left(\dfrac{d}{w}\right)^3 + 2.45\left(\dfrac{d}{w}\right)^2 - 0.69\left(\dfrac{d}{w}\right) + 1 & 0.4 < \dfrac{d}{w} < 0.95 \\ -21.45\left(\dfrac{d}{w}\right) + 21.45 & \dfrac{d}{w} > 0.95 \end{cases} \tag{6.9}$$

Figure 6.16 shows a comparison of the correlation proposed in Eq. (6.6) and Eq. (6.7) in the current study with the previous studies of Zhang, Gutierrez and Chao (2019) and Blyton, Gala and Sharma (2015). Figure 6.16(a) shows the effect of fracture roughness on proppant transport under the influence of high viscosity fracturing fluid. As discussed earlier, when the proppants are transported with high-viscous fracturing fluids; the proppant Reynolds number is small. This results in a relatively stable flow field inside the fracture and consequently, low mechanical interaction flow effects. Thus, under the influence of high viscosity fracturing fluid, no significant variation in terms of roughness factor is noticed on comparison of the proposed correlation with the study of Zhang, Gutierrez and Chao (2019) and Blyton, Gala and Sharma (2015). On the other hand, Figure 6.16(b) shows the effect of fracture roughness on proppant transport under the influence of low viscosity fracturing fluid like slick water, which is commonly used in hydraulic fracturing of shale gas reservoirs. When the proppants are transported with low-viscous fluids, the proppant Reynolds number is higher. This results in significantly higher inter-proppant and proppant-wall interactions and consequently increased mechanical interaction flow effects. Thus, on comparison of the proposed correlation in the current study with the study of Zhang, Gutierrez and Chao (2019) and Blyton, Gala and Sharma (2015) shows that since Blyton, Gala and Sharma (2015) ignored the effect of fracture roughness, the turbulence and mechanical interaction flow effects caused due to the increased proppant-fracture rough wall interactions were missed in the proppant transport prediction. The proppant transport model proposed by Zhang, Gutierrez and Chao (2019) on the other hand, although included the effects of fracture roughness and is able to capture the mechanical interaction flow effects, but is limited to two-dimensional fracture geometry with no gravitational and fluid leak-off effects. On comparison of the current model with the results proposed by Zhang, Gutierrez and Chao (2019) in Figure 6.16(b) suggests that the results from Zhang, Gutierrez and Chao (2019) underpredict by approximately 20% the proppant transport and distribution due to the assumption of no fluid-leak off, no gravitational effects, and two-dimensional fracture geometry which significantly affects the inter-proppant and proppant-fracture wall interactions. Thus, the applicability of the proposed proppant transport model with fluid leakage and fracture roughness can help petroleum engineers to design the hydraulic fracturing operation with fewer limiting assumptions successfully.

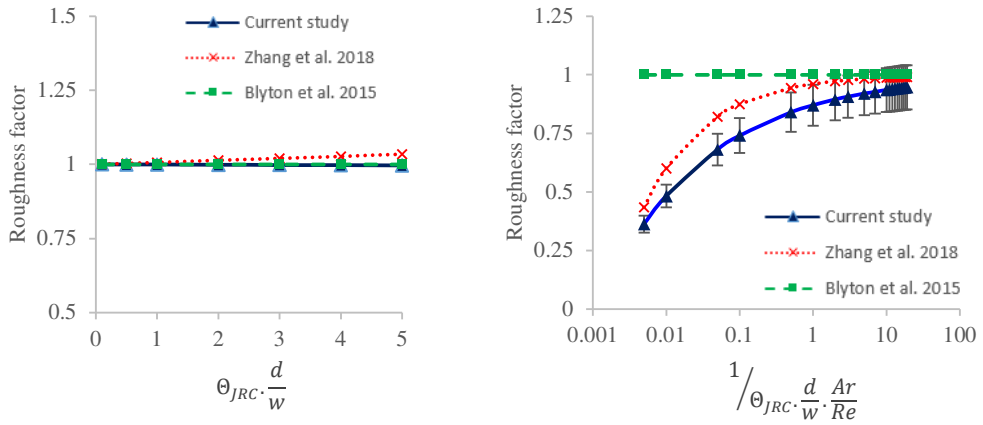

(a) (b)

Figure 6.16. Comparison of the proposed correlation with the previous studies (a) for high viscosity fracturing fluid (b) for low viscosity fracturing fluid

The proppant transport in the current study accounts for the effect of fracture roughness, fluid leak-off from the fracture walls, inter-proppant and proppant-fracture wall interactions. As mentioned previously, no dynamic fracture propagation and fracture mechanics is considered in the current model. However, the proppant transport model developed accounting the integrated effects of fracture roughness, fluid leak-off, inter-proppant and proppant-fracture wall interactions can be incorporated into a complete 3D hydraulic fracture simulation study of shale gas reservoirs. The 3D complete hydraulic fracturing simulation study in shale gas reservoirs will couple the fracture geomechanics, fluid flow and proppant transport in hydraulic fractures to more accurately determine the pressure drop, fluid flow and production efficiency in shale gas reservoirs (Zhang and Sun, 2019).

In order to investigate the applicability of the current proppant transport model with the real fractures, the current model was compared with the field observations from the hydraulic fracturing in shale gas reservoir. Raterman et al. (2018) investigated the hydraulic fracture propagation from the coring results extracted from a pilot well offset from an adjacent hydraulically fractured well. It was reported that although the stimulated hydraulic fractures were more than 1,000 ft (305 m), the proppant transport distribution was inefficient and limited to merely 75 ft (23 m) from the wellbore. Secondly, Kurison, Kuleli and Mubarak (2019) validated long hydraulic fractures in a carbonate-rich ultra-low permeability reservoir using fracture modelling and observations from chemical tracers, microseismic, pressure interference and reservoir simulation. Furthermore, Kurison et al. (2019) used data analytics approach to correlate well production performance with hydraulic fracturing stimulation parameters for wells in Eagle

Ford and Utica shale reservoirs. Thus, the hydraulic fracture geometry was derived from the Kurison, Kuleli and Mubarak (2019) study of fracture half-length 800 ft (245 m) and fracture height of 125 ft (38 m) to investigate the proppant transport. The fracture width was assumed as 10 mm. Kurison et al. (2019) provided estimates of average volumes of hydraulic fracturing cluster stimulation for two shale plays. The typical field average for hydraulic fracturing fluid volumes for single perforation clusters in a single wing of the bi-wing fracture is approximately 1500 bbls (equivalent to 3000 bbls fluid volume for a bi-wing fracture). The typical injection time is 60 min, which translates to the fluid flow rate of 36,000 bbl/d (0.06625 m^3/s). The proppants injected per cluster estimated by Kurison et al (2019) is 50,000 lbs for a single wing fracture (equivalent to 100,000 lbs for a bi-wing fracture). This translates to the proppant concentration of 0.794 lbs/gal. Thus, using this proppant concentration and typical proppant density of 2650 kg/m^3, the proppant volume fraction calculated and used in the model is 3.6%. The key physical properties used in the simulation are detailed in Table 6.2 which are based on the study of Raterman et al. (2018) and Kurison et al. (2019). The current hybrid proppant transport model with an assumed JRC of 4 based on the fracture and core images from Raterman et al. (2018) was used in the simulation. The injection time used is 60 min. Figure 6.17 shows the result of proppant distribution after 60 min of injection. The proppant volume fraction plot in Figure 6.17 shows that the proppant deposits at the fracture bottom and forms a proppant bed. For the injection time of 60 min, the proppant laterally extends to the entire length of the hydraulic fracture of 245 m. However, in terms of proppant bed height, the average proppant bed height formed after 60 min of injection is approximately 5.5 m. It is to be noted that once the injection of fracturing fluid stops, the unpropped section of the hydraulic fracture closes down due to the surrounding geomechanical stresses and reservoir pressure. The fracture closure post-injection is not modelled as it is out of the scope of the current study. Additionally, the average proppant horizontal transport velocity is calculated from the numerical simulation at 35 m from the inlet and compared with the velocity predicted from the Eq. (6.6) based on the ratio of Ar/Re. The average proppant horizontal transport velocity from the numerical simulation is 0.21 m/s and from the Eq. (6.6) is 0.205 m/s, which shows a good agreement and applicability of the current model in simulating the real fractures.

Table 6.2: Key physical parameters used in the simulation

Property	**Value**
Fracture dimension	245 m × 38 m × 0.01 m
Injection rate	0.06625 m^3/s (3600 bbl/d)
Proppant size	0.284 mm (40/70 size sand)
Proppant concentration	0.794 lbs/gal
Proppant density	2650 kg/m^3
Proppant volume fraction	0.036
Slick water density	1000 kg/m^3
Assumed fluid viscosity	0.001 Pa.s
JRC	4

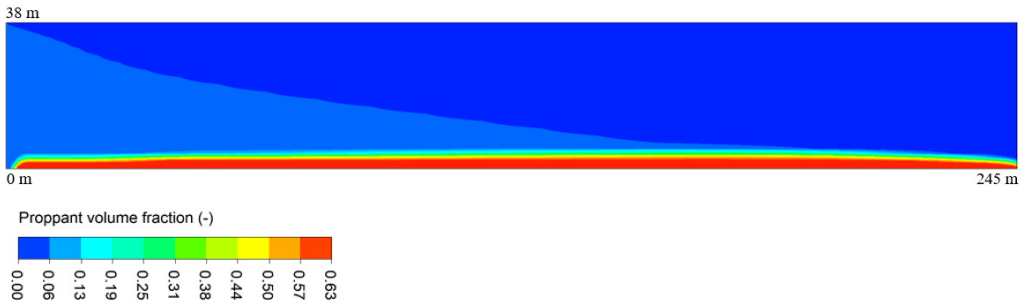

Figure 6.17. Proppant transport in industrial-scale hydraulic fracture

The proppant transport and distribution in a hydraulic fracture depends on a combination of multiple physical parameters. A detailed discussion of the parametric study about the role of proppant size, injection rate, fluid viscosity and proppant concentration in improving the proppant distribution can be found in chapters 4 and 5. In order to improve the proppant transport efficiency firstly, the proppant injection time has to be sufficient enough so that the proppant can successfully distribute to the maximum stimulated hydraulic fracture volume. This can be achieved by correctly modelling the proppant transport physics as detailed in the current model. Secondly, another important parameter that significantly improves the proppant transport and distribution is injecting proppants with varying size. It is explained earlier in section 4.3.3 that one of the effective approaches for improving the proppant transport efficiency in the fracture is injecting the fracturing fluid slurry with smaller size proppants followed by larger size proppant particles. This is particularly true for the low viscosity fracturing fluid such as slick water which is commonly used in hydraulic fracturing of shale reservoirs. The smaller size proppants possess a greater suspension ability in the fracturing fluid, and thus injecting the proppant with variation

in size results in improved proppant sweep efficiency and can lead to more uniform fracture conductivity (Suri, Islam and Hossain 2020a). Lastly, the fracturing fluid viscosity plays an important role in improving the efficiency of proppant transport. The higher viscosity fracturing fluid due to its better proppant suspension ability can suspend the proppants for a longer period and thus resulting in more extended proppant transport inside the fracture. Thus, it can be summarised from the above discussion that the proppant transport efficiency in the hydraulic fracture can be improved using an appropriate combination of injection rate, proppant size, injection time, and fracturing fluid viscosity. The current proppant transport model described in this study can be used to successfully simulate the proppant transport physics by varying different parameters and can aid the petroleum engineers to improve the hydraulic fracturing design.

6.5 Summary of the key findings

Proppant transport and distribution is studied in the rough hydraulic fractures using the CFD based DDPM model. The effect of fracture Joint Roughness Coefficient was quantitatively investigated on proppant motion. For the fluid flow and proppant transport in smooth fractures, the fracture walls employ substantial mechanical retardation effects on proppants resulting in a decrease of proppant horizontal transport velocity and greater proppant deposition. In contrast, when the proppants are transported in rough fractures, with the increase in fracture roughness the inter proppant and proppant -wall interactions dramatically increase, and consequently higher amount of proppant is suspended in the slurry resulting in greater proppant horizontal transport velocity. Furthermore, in terms of horizontal motion, proppants are inclined to transport a long distance away from the wellbore with the increase in fracture roughness. The mechanical interaction flow effects were found to be dependent on the proppant transport regime. When the proppant transport in high viscosity fluids (i.e. at low proppant Reynolds number), no significant effect of fracture roughness in proppant transport is noticed. In contrast, for proppant transport in low viscosity fluids (i.e. at high proppant Reynolds number), the mechanical interaction effects become dominant with roughness and significantly increases proppant horizontal transport velocity.

Chapter 7: Proppant transport in dynamically propagating hydraulic fractures using CFD-XFEM approach[4]

Numerically modelling the fluid flow with proppant transport and fracture propagation together are one of the significant technical challenges in hydraulic fracturing of unconventional hydrocarbon reservoirs (Belyadi, Fathi and Belyadi 2019). In the existing coupled fluid flow and fracture models (El-M. Shokir and Al-Quraishi 2009, Kong, Fathi and Ameri 2015, Zhan et al. 2016, Izadi et al. 2017, Wang, Elsworth and Denison 2018), the fluid flow and proppant transport are usually modelled by two-component, interpenetrating continuum, meaning the flow governing equations are specific to the mixture, which cannot provide the accurate description of the particle physics in the slurry flow. Secondly, the effect of fracturing fluid leaking from the fracture-matrix interface on proppant distribution is neglected. Moreover, lastly, in most of the studies, the geometry of the fracture propagation is assumed from the analytical modelling techniques that are based on LEFM and assumes rock as a brittle material with no plastic deformations. However, some of the rocks are ductile in nature, for instance, shales that show plastic deformation which can be modelled using the XFEM and CZM, as discussed earlier in chapter 3 (section 3.5.3). In the present study, the proppant transport and fluid flow are modelled solving the flow governing equation for both the phases individually and the proppant-fluid interaction is explicitly modelled using a CFD based DDPM model described in section 3.2.3 (Suri, Islam and Hossain 2019). The model has then integrated to couple the effect of dynamic fracture propagation with the fluid leak-off effects (Suri, Islam and Hossain 2020c). The CFD, coupled with XFEM approach, offers the advantage of modelling the fracture propagation and investigate the accurate fluid flow and proppant concentration distribution, which may be challenging to obtain experimentally. The proposed three-dimensional integrated fluid flow, proppant transport and fracture propagation model can accurately model the fluid-proppant, proppant-proppant and fracture wall interactions with varying fluid, proppants and geomechanical parameters and fluid leak-off effects.

---

[4] The results from this chapter are to be published (in press) in the International Journal of Rock Mechanics and Mining Sciences.

Suri, Y., Islam, S.Z. and Hossain, M., 2020. Proppant transport in dynamically propagating hydraulic fractures using CFD-XFEM approach. *International Journal of Rock Mechanics and Mining Sciences, 131*, p.104356. https://doi.org/10.1016/j.ijrmms.2020.104356

7.1 Brief methodology

A fully coupled 3D hydraulic fracturing simulation involves the coupling of fracture mechanics that governs the fracture propagation with the fluid flow and proppant transport modelling that governs the pressure and velocity fields inside the fracture. A cohesive based XFEM technique is applied to calculate the rock stress, fracture initiation, propagation and rock deformation. Following that, a CFD method is applied to model the fluid flow and proppant transport numerically. The key underlying equation describing the cohesive based XFEM and finite volume based CFD-DEM is explained earlier in chapter 3.

7.1.1 Coupling between XFEM and CFD

An explicit coupling simulation approach is used in the present study to integrate the XFEM based fracture propagation model with the CFD-DEM based fluid flow and proppant transport model. Important elements in the current numerical model include the following:

- An XFEM geomechanics solver based on cohesive traction law that models the fracture propagation based on fracture mechanics, geomechanical stress and reservoir properties.
- A CFD based solver for modelling proppant transport inside the fracture with fluid leaking off from the fracture-matrix interface.

Figure 7.1 shows the workflow that was followed in the current numerical model. Firstly, the XFEM model was configured using the available real field reservoir and geomechanical data, as shown in Table 7.1. Then the simulation run was performed to model the fracture propagation and get the fracture geometry which will then be used as a computational domain for the proppant transport and fluid flow in the CFD solver. The computational domain was discretized, and the proppant transport and fluid flow analysis were carried out at different time steps with fluid leak-off from the fracture wall, based on the proposed proppant transport model described in chapter 3 and 5. This is an iterative process where the pressure field and fluid leak-off along the fractures was exchanged at each time step to model the proppant transport in dynamic fracture propagation, as shown in Figure 7.1. The fluid and proppant mixture is injected at the inlet using velocity inlet boundary condition. To model the fluid leak-off from the fracture wall, a user-defined function is used to add a source term in the continuity and momentum transport equations. The amount of fluid leaking off from the fracture wall is obtained from the XFEM model that was used in the user-defined function. The detailed explanation of the CFD modelling parameters, boundary conditions and user-defined function is discussed in chapter 3 and 5.

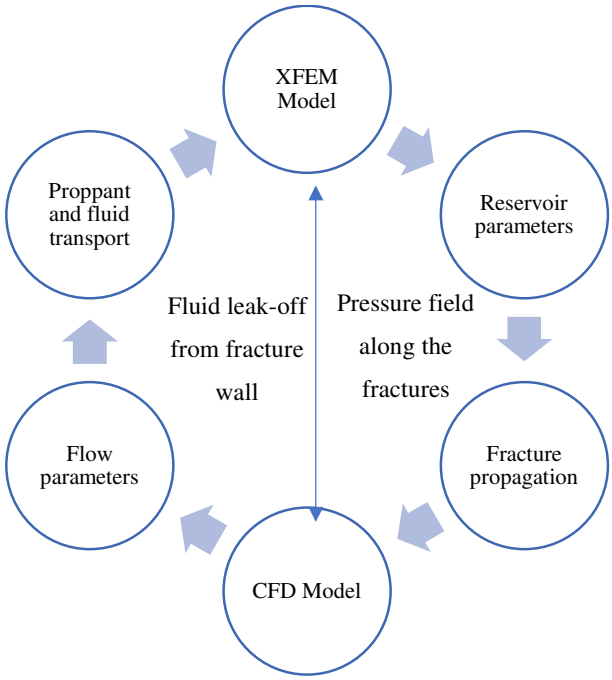

Figure 7.1 XFEM-CFD coupling workflow

7.1.2 Numerical modelling parameters

Proppant transport and distribution were investigated in a hydraulic fracture using the CFD based DDPM model described earlier in section 3.2.3. As the fracture propagates with time, the fracture geometry varies with time steps. The fracture geometry at different time step was imported into the CFD model from the XFEM model to study proppant transport. A typical fracture geometry or computational domain at a particular time step is shown in Figure 7.2 that illustrates the boundary condition used in the current study. Firstly, the mesh of the fracture geometry is created so that it reasonably provides the mesh independent, numerically converged and computationally efficient solution. The fracturing fluid and proppants were injected together at the inlet with the volumetric inlet flow rate of 0.0025 m^3/s. The density and viscosity of the fracturing fluid are assumed as 1000 kg/m^3 and 1 cP (0.001 Pa-s). The density of proppants assumed is 2650 kg/m^3 with proppant size based on 20/40 sand and proppant volume fraction of 0.10. The no-slip wall condition was used at the top wall, bottom wall and fracture tip for the liquid phase, as shown in Figure 7.2. For the particle phase, the reflect boundary condition with specularity constant of 0.01 and wall reflection coefficient of 0.9 in both normal and tangential directions was used to model the particle-wall collision, as discussed earlier in section 3.3.3. In order to mimic the fluid leak-off into the surrounding porous rock, the fluid leakage effect is modelled through the fracture sidewalls with the help of a user-defined function (UDF). The momentum and mass source terms are explicitly defined in the governing transport equations through UDF. The

underlying equations describing the source terms and UDF used to model the fluid leak-off is explained earlier in chapter-3. The fluid leak-off profile along the fracture length to a surrounding porous medium obtained from the XFEM model at different time steps is shown in Figure 7.3.

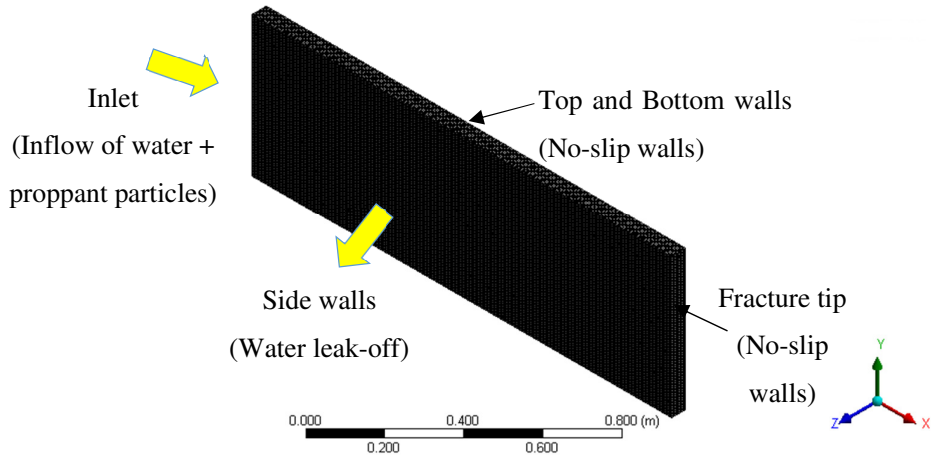

Figure 7.2. A typical fracture geometry to investigate proppant transport

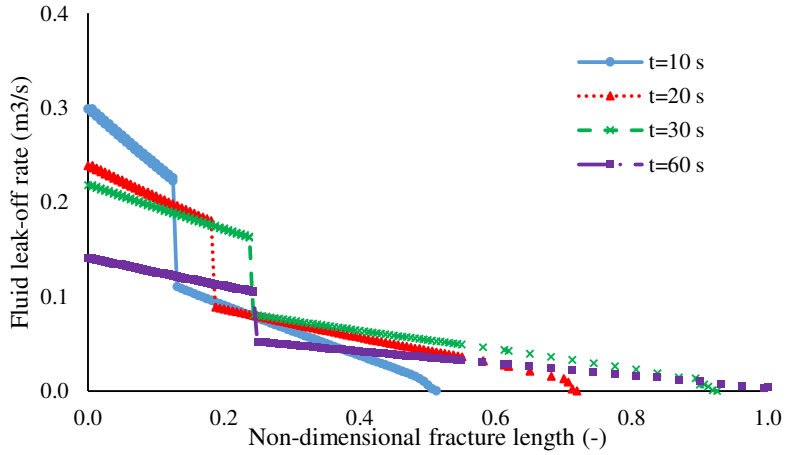

Figure 7.3. The fluid leak-off rate at different time steps

The pressure-based solver with transient state simulation was used to solve the proppant transport equations. The effect of gravity was included in the simulation. In order to model the turbulence in the flow, the Shear Stress Transport (SST) k-ω model (Menter 1993) was used that blends the standard k-ω turbulent model near the wall with the standard k-ε turbulent model in the free-stream (Versteeg and Malalasekera 2007) and widely used in the literature for modelling solid transport in fluids, as discussed earlier in section 3.2.3.2. The simulation time step used was 0.001 s. The phase-coupled SIMPLE algorithm and the node-based averaging scheme is used as a solution method for the pressure-velocity coupling (Patankar 1980, Versteeg and Malalasekera 2007) and to calculate the gradient, respectively (Mahdavi, Sharifpur and Meyer 2015). Lastly, the second-order upwind scheme was used to discretize and solve the governing equations, ad discussed earlier in section 3.3.3.

7.2 Results and discussion

7.2.1 Validation

The proposed XFEM model in the current study is validated using the two different approaches. Firstly, using the zero-toughness plane strain analytical model (Adachi 2002) and secondly, using the real field data. The validation using the analytical model is described in section 7.2.1.1, and the validation using the real field data is described in section 7.2.1.2.

7.2.1.1 Zero toughness plane strain fracture propagation model

The fracture propagation using the XFEM model was compared against the analytical results from the zero-toughness plane strain model from Adachi (2002) using the geomechanical properties, as shown in Table 7.1. The solution from plane strain model assumes impermeable elastic medium with negligible fracture toughness. Adachi (2002) proposed the dimensionless variables of fracture width, $w(x,t)$, defined by Eq. (7.1), fracture length, $l(t)$, defined by Eq. (7.2), net fluid pressure, $p(x,t)$, defined by Eq. (7.3) and flow rate, Q_0, to derive the zero-toughness solution of 2D hydraulic fracture propagation using the first-order approximation. Adachi (2002) described that the proposed analytical model could successfully model the asymptotic behaviour of fracture opening and fluid pressure in the near tip region.

$$w(x,t) = \varepsilon(t)L(t)\Omega[\xi, P(t)] = \varepsilon(t)L(t)\gamma[P(t)]\overline{\Omega}(\xi) \tag{7.1}$$

$$l(t) = \gamma[P(t)]L(t) \tag{7.2}$$

$$p(x,t) = \varepsilon(t)E'\Pi[\xi, P(t)] \tag{7.3}$$

Where $\varepsilon(t)$ is a small dimensionless parameter (Eq. (7.5)), $L(t)$ denotes a length scale of the same order as the fracture length $l(t)$ (Eq. (7.6)), $P(t)$ is the dimensionless evolution parameter, $\gamma[P(t)]$ is the dimensionless fracture length and $\xi = x/l(t)$ is the scaled coordinate ($0 \leq \xi \leq 1$). The evolution parameter can be considered as a dimensionless toughness in the viscosity scaling.

$$k_D = \frac{K'}{(E'^3 \mu' Q_0)^{1/4}} \tag{7.4}$$

For the viscosity scaling, denoted by a subscript m, the small parameter and length scale take the explicit forms, as shown in Eq. (7.5) and Eq. (7.6) respectively.

$$\varepsilon_m = \left(\frac{\mu'}{E't}\right)^{1/3} \tag{7.5}$$

$$L_m = \left(\frac{E't^4 Q_0^3}{\mu'}\right)^{1/6} \tag{7.6}$$

Where E' the plane strain modified elasticity modulus and is defined by Eq. (7.7), K' the plane strain modified fracture toughness and is defined by Eq. (7.8), and μ' is the plane strain modified fluid viscosity and is defined by Eq. (7.9).

$$E' = \frac{E}{1 - \upsilon^2} \tag{7.7}$$

$$K' = \left(\frac{32}{\pi}\right)^{\frac{1}{2}} K_{IC} \tag{7.8}$$

$$\mu' = 12\mu \tag{7.9}$$

Where K_{IC} is the fracture toughness or critical stress intensity factor. E and ν are the elastic modulus and Poisson's ratio respectively.

Adachi (2002) derived the zero-toughness solution of 2D hydraulic fracture propagation using the first-order approximation as shown in Eq. (7.10).

$$\bar{\Omega}_{m0}^{(1)} = A_0(1 - \xi^2)^{2/3} + A_1^{(1)}(1 - \xi^2)^{5/3} + B^{(1)}\left[4\sqrt{1 - \xi^2} + 2\xi^2 \ln\left|\frac{1 - \sqrt{1 - \xi^2}}{1 + \sqrt{1 - \xi^2}}\right|\right] \tag{7.10}$$

Where A_0, $A_1^{(1)}$ and $B^{(1)}$ are constants and the value equals $3^{1/2}$, -0.156 and 0.0663 respectively. ξ is the length scaling factor. $\bar{\Omega}_{m0}^{(1)}$ is the dimensionless fracture width. The detailed derivation and explanation of the zero-toughness model can be found in Adachi (2002) and Adachi and Detournay (2002).

The geomechanical and flow properties used in the comparison of current XFEM based simulation and an analytical model is detailed in Table 7.1. Figure 7.4 shows the fracture propagation after 20 s of injection in terms of fracture width or fracture aperture and fracture half-length. The graph shows a reasonable match with a percentage error of ±5% between the XFEM based numerical model and the zero-toughness analytical model. The results suggest that the XFEM model can be used for a detailed analysis of fracture propagation in porous media.

Table 7.1 Geomechanical and flow properties for comparison with an analytical model

Parameter	**Value**
Elastic modulus	30 GPa
Poisson's ratio	0.3
Stress intensity factor	0.956 MPa.m$^{1/2}$
Fluid viscosity	5.0 Pa.s
Fluid injection rate	0.001 m^3/s

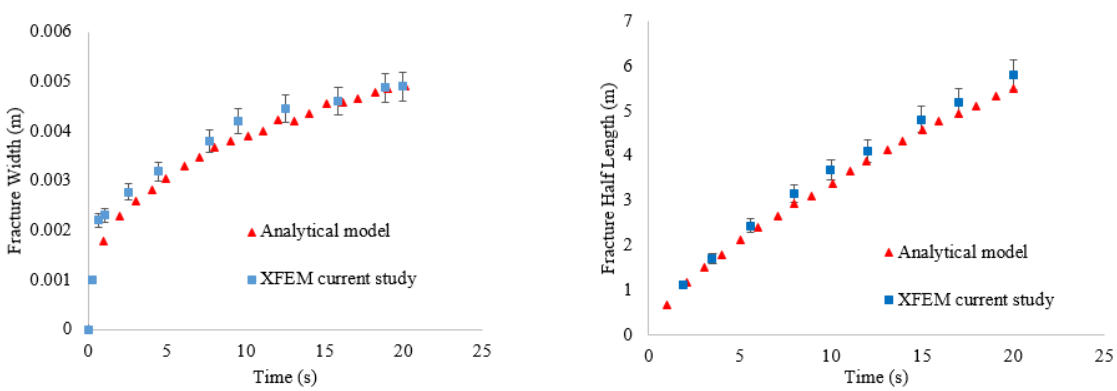

Figure 7.4 Comparison of the current model with an analytical model

7.2.1.2 Validation using the real field data

In order to study the dynamic fracture propagation with fluid flow and proppant transport, the real field data was used by Saberhosseini, Ahangari and Mohammadrezaei (2019). The field is located offshore in the Persian Gulf and consists of a tight limestone oil reservoir. The reservoir and geological properties used in the current study are detailed in Table 7.2. A detailed description of geology and reservoir characteristics can be found in Saberhosseini, Ahangari and Mohammadrezaei (2019).

The semi-circular reservoir geometry with a diameter of 160 m is used in the current study, as shown in Figure 7.5. The height of the reservoir is assumed as constant 20 m. The perforation or the initial location of the crack was defined using the XFEM method in Abaqus, as shown in Figure 7.5. The fracturing operation is started with an injection rate of 0.0025 m^3/s, and the fluid injection is maintained for 20 min. The in-situ geological properties and geomechanical stresses are presented in Table 7.2. The XFEM model is a conglomerate of cohesive zone material and porous rock. The cohesive zone material is located at the centre of the computational domain around the perforation. It is surrounded by porous rock. The fluid is injected at a high injection rate such that when the fracture propagation criteria are reached, the fracture starts propagating and the fluid leaks into the surrounding porous rock. With the progression of time, the fracture is propagated, and the fracture profile is extracted and imported into the CFD module to study the proppant transport and distribution. The height of the fracture is assumed as constant for simplicity. The computational domain is discretised, and enriched elements are assigned for arbitrary fracture propagation based on the in-situ stress. The enriched elements consist of displacement and pore pressure degrees of freedom that aids in fracture propagation. Uniform pore pressure and initial stresses are defined based on the real field data shown in Table 7.2. The fluid flow and proppant transport are explicitly modelled using CFD technique, and the proppant distribution with fracture propagation is analysed at different time steps.

Table 7.2 Reservoir and geological properties

Property	**Value**
Porosity	0.10
Elastic Modulus	27.2 GPa
Permeability	2 mD
Poisson's ratio	0.22
Fluid viscosity	1 cP
Injection flow rate	0.0025 m^3/s
Stress (vertical, maximum horizontal, minimum horizontal)	(47.61 MPa, 54.42 MPa, 40.81 MPa)
Pore pressure	23.43 MPa

The rock geomechanical properties, such as Poisson's ratio, elastic modulus and rock tensile strength, play a critical role in the fracture initiation and propagation. Since these are material properties and are dependent on the characteristics of rock, thus it is a static parameter in the fracture propagation study. On the contrary, the controllable parameters in the hydraulic fracturing design are the fluid injection rates, fluid viscosity or fluid rheological properties, fluid leak-off, and type of proppants. Thus, an improved understanding of the effects of these parameters along with fluid-proppant interactions, proppant distribution in fracture initiation and fracture propagation can overcome the challenge of fracturing job failure in the petroleum industry.

The computational domain was discretised to add the enriched elements, and the mesh is shown in Figure 7.5. The mesh consists of 30,000 elements to accurately capture the fracture propagation. A very fine mesh is used surrounding the region where the perforation is located as shown in the zoomed image of Figure 7.5, because the large stress, pressure gradients and displacement are located there, and to accurately capture the fracture mechanics. As described earlier, the formation is modelled as a poroelastic material with the key rock mechanical and porous rock properties shown in Table 7.2. The traction-separation law is used, which is explained earlier in the methodology (section 3.5.3). The hydraulic fracturing fluid is assumed as incompressible with a viscosity of 1 cP. In order to model the in-situ stress and pore pressure, a geostatic step is used in Abaqus to achieve a stress equilibrium condition before a hydraulic fracture initiation. Following that in the next step, the fracturing fluid is injected at a sufficiently high rate so that the hydraulic pressure gradually increases and once the fracture propagation criteria are reached, the fracture starts propagating.

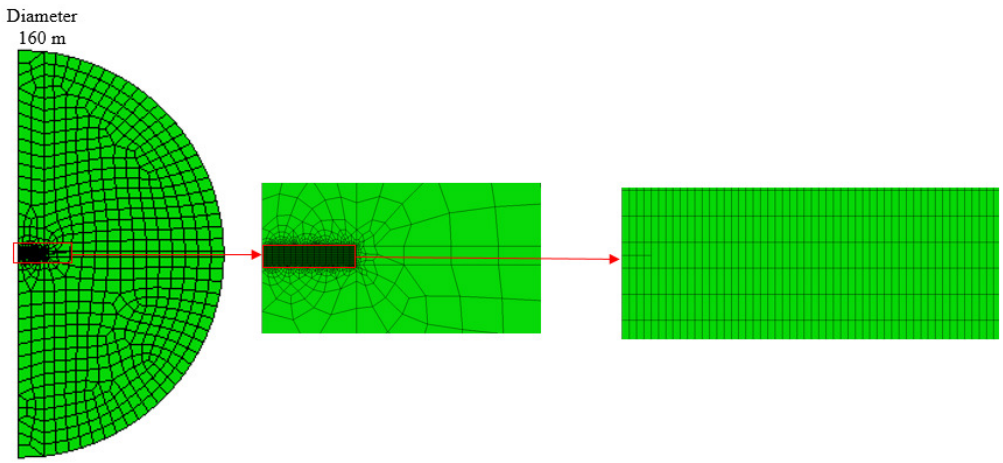

Figure 7.5 Computational domain and mesh

Next, to ensure the applicability of the proposed numerical model, the results obtained were compared with the real field data with the reservoir and geological parameters, as described in Table 7.2. The fracture initiation pressure from both numerical simulation and the published real field case results (Saberhosseini, Ahangari and Mohammadrezaei 2019) were compared. From Figure 7.6, the equivalent fracture pressure from the numerical XFEM simulation using the same parameters as stated in Table 7.2 is evaluated as 7497 psi or 51.69 MPa. Moreover, the actual fracture pressure from the field after 20 min of injection time is 7500 psi or 51.02 MPa, as stated in Saberhosseini, Ahangari and Mohammadrezaei (2019). Comparing the fracture initiation pressure using XFEM method and actual measured value provides the percentage error of 0.04%, which shows a good agreement. Thus, the current XFEM model can simulate the fracture mechanics accurately as verified against the zero-toughness analytical model and with the real field result. This represents that the current XFEM model can accurately simulate the fracture propagation and can be employed for detail investigation of proppant transport and fluid flow in dynamic fracture propagation.

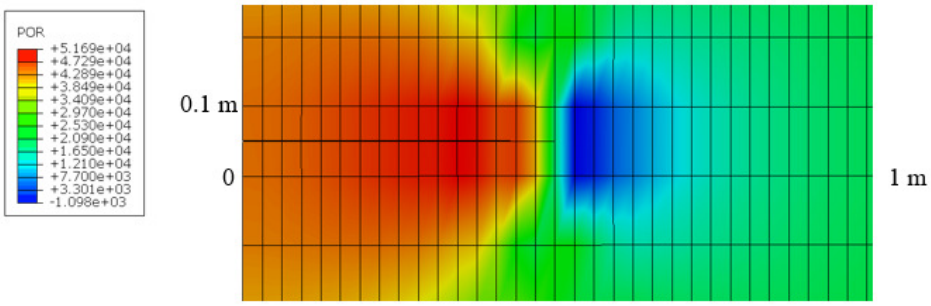

Figure 7.6 Fracture initiation pressure from XFEM model

7.2.2 Results of the base case

Next, a base case fracture propagation simulation using XFEM was run with the parameters in Table 7.2 and is discussed in this section to explain the applicability of the proposed model. The base case simulates a hydraulic fracture propagation from perforation based on the defined in-situ stress, pore pressure and injection parameters. When the fracture initiation criteria are met, the fracture propagates in the direction of minimum fracture resistance. The proposed model provides the fracture propagation at every time step and accounts for the injection pressure, in-situ stresses, pore pressure distribution, and fracture trajectory. This information is vital as it has a direct impact on the design and success of hydraulic fracturing operation.

The fracture geometries at different time step are illustrated in Figure 7.7, and the result of the fracture propagation using XFEM method with time is shown in Table 7.3. It can be seen from Figure 7.7 and Table 7.3 that once the fracture is initiated; the fracture propagates with time and as a result, the fracture length and fracture width increase. The fracture half-length increases abruptly towards the beginning as soon as the fracture is created. Subsequently, the fracture half-length gradually increases depending upon the injection flow rate and fluid leak-off.

Table 7.3 Fracture propagation at different time steps

Time (s)	Fracture half-length (m)	Fracture width (m)
0	0.25	0
1	1	0.003
2.5	1.94	0.004
5	3	0.0049
7	4.06	0.0055
11	5.125	0.0063
16	6.125	0.0078
21	7.19	0.0085
26	8.25	0.009
30	9.19	0.0095
60	10.2	0.016
1021	30	0.082
1200	33	0.085

Furthermore, to investigate the fluid flow and proppant transport with dynamic fracture propagation, the fracture profile from the XFEM at different time step and fluid properties were imported in Fluent and a detailed investigation using CFD proppant transport model was carried out. The DDPM model described earlier in section 3.2.3 is used for CFD modelling of proppant transport and distribution. The results from the proppant distribution at different time steps are shown in Figure 7.8. The fracture half-length and fracture width in Figure 7.8 at different time steps correspond to the fracture propagation length and fracture aperture from the XFEM fracture propagation model, and the height of the fracture is assumed as constant (0.5 m) for simplicity. It can be noticed from Figure 7.8 that as the fluid-proppant mixture or slurry is injected into the fracture, part of fracturing fluid leak-off from the surrounding fracture wall into the porous media. The remaining fluid transport the proppant in the slurry into the fracture. Thus, due to the complex hydrodynamics of proppants, proppant-fluid and inter-proppant interaction, the proppant deposits away from the wellbore at the fracture bottom and forms a proppant bed. As the injection time increases, it results in fracture further propagating and increased proppant distribution into the fracture. Thus, the current study aims to capture this coupled phenomenon, and the key results obtained from the base case simulation in terms of proppant volume fraction contour plot is illustrated in Figure 7.8.

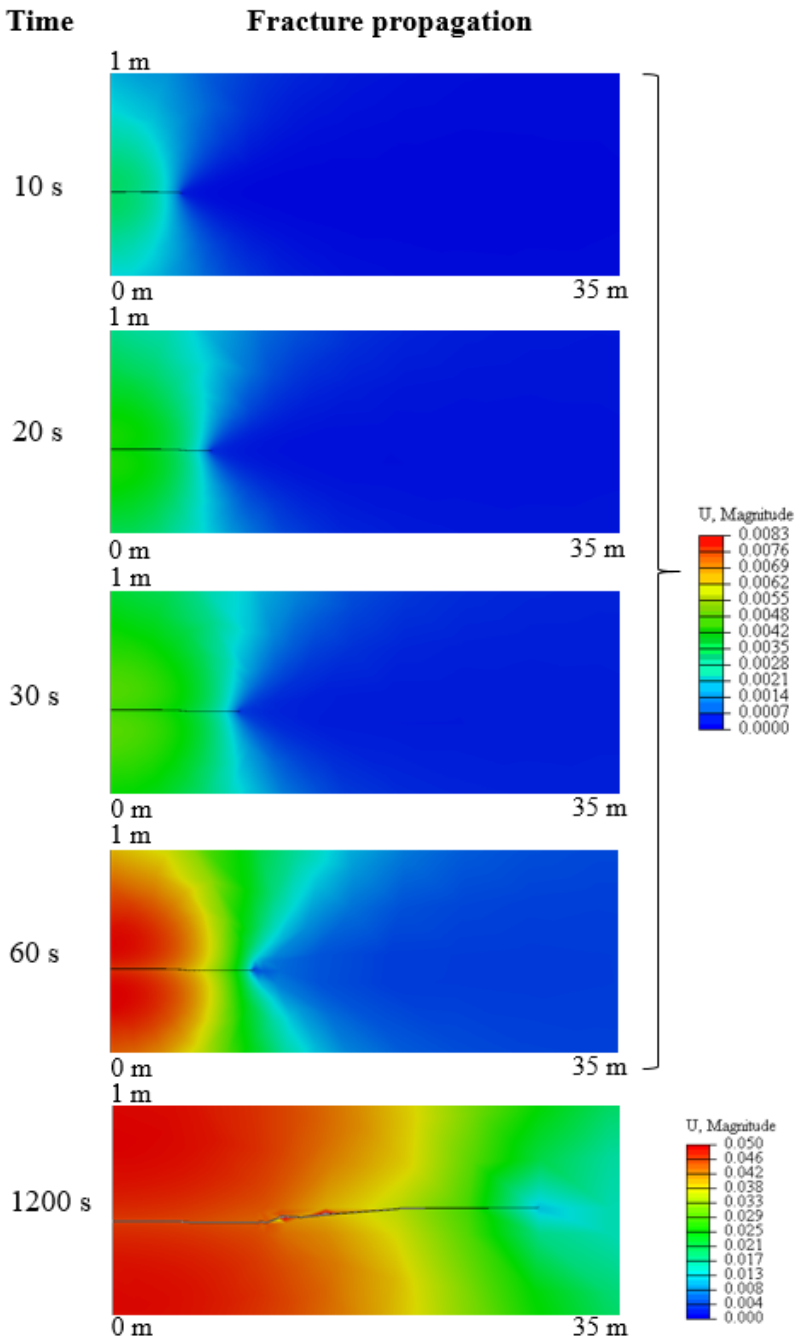

Figure 7.7 Fracture propagation at different time steps

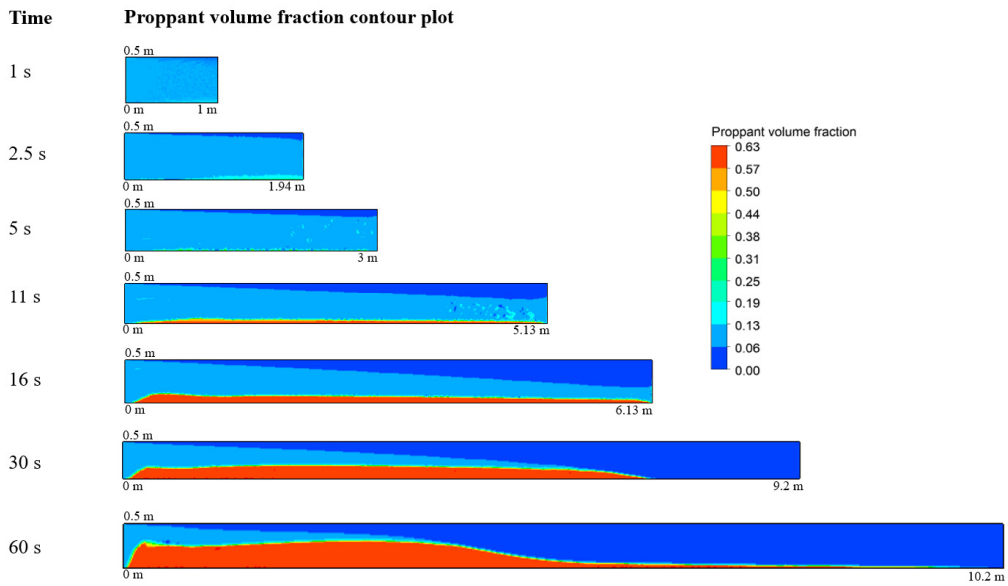

Figure 7.8 Proppant transport in dynamic fracture propagation at different time steps

In order to investigate in detail, the impact of flow properties in efficient proppant distribution and successful hydraulic fracturing design, different flow properties were varied. The role of injection rate, fluid viscosity and leak-off rate constant is analysed in the propagation of fracture and proppant distribution.

7.2.3 Fracture propagation as a function of injection rate

One of the most important controllable and yet essential parameters in the geometry of the fracture and its optimisation is the injection rate during operation. It is well-known that by increasing the injection rate, the dimensions of the fracture increase. Considering the overburden and underburden defined as barriers that surround the reservoir, the operation should be designed as if the mechanical and hydraulic integrity of these two barriers is guaranteed. The accurate evaluation of width is another critical parameter to the optimal design of the hydraulic fracturing because it directly dictates the size of proppant and also prevents the risk of proppant bridging and screen out. Proppants are used so that the induced fracture remains open and conducive. Moreover, by use of the validated numerical model, the real length of the induced fracture can be accurately estimated. Knowing this length can help to design in such a way that it can bypass the disturbed area around the wellbore wall. This disturbed area created after drilling and applying the drilling fluid can penetrate within the pores around the wellbore wall. Increasing the length of the fracture to pass this area can enhance the production.

Thus, an investigation was carried out at three different injection rates 0.001 m^3/s, 0.0025 m^3/s and 0.005 m^3/s to understand the fracture propagation and proppant distribution. The results are detailed in Table 7.4. Table 7.4 shows that with an increase in injection rate from 0.001 m^3/s to 0.005 m^3/s, the magnitude of fracture width and fracture half-length increases from 7.8 mm to 29 mm and 8 m to 12 m respectively. Therefore, the geometry of the induced fracture strongly depends on the difference in the injection rate.

Figure 7.9 details the comparison of proppant volume fraction at 60 s after injection for three different injection rates as described in Table 7.4. It can be interpreted from Figure 7.9 that with the increase in injection rate, due to the higher slurry velocity, it adds more turbulence in the flow which leads to greater proppant suspension ability in the fracturing fluid and consequently longer proppant transport. To quantitatively compare the results, the proppant volume fraction is calculated at two different cross-sectional planes located 2 m and 4 m from the inlet and plotted against the fracture height, as shown in Figure 7.10. It can be noted from Figure 7.10 that at x=2 m from the inlet higher proppant bed is seen with 0.001 m^3/s compared to 0.005 m^3/s, due to more significant amount of proppant depositing near the wellbore having a lower velocity and ability to suspend in the slurry. On the contrary, at higher injection rate, i.e. 0.005 m^3/s, the proppant is transported to a longer distance, as can be seen in Figure 7.10 @x=4 m from the inlet. This is one of the significant challenges in the oil industry, especially when using slick water for hydraulic fracturing in shales. The proppant tends to deposit quickly as soon as they are injected due to reduced ability of the slick water to suspend proppants. Thus, the unpropped section of the fracture closes down resulting in loss of efficiency and production. An effort to transport the proppant to a longer distance can lead to an improved hydraulic fracturing design.

Table 7.4 Fracture propagation with varying injection rate

Injection rate (bbl/min)	**Injection rate (m^3/s)**	**Fracture width (m)**	**Fracture half-length (m)**
0.4	0.0010	0.0078	8
1.0	0.0025	0.016	10
1.9	0.0050	0.029	12

Another frequently observed phenomenon seen during hydraulic fracturing that can lead to hydraulic fracturing design failure is that due to the proppant bridging, it can cause a fracture tip screen out. It means the proppant bed forms a bridge and does not allow the subsequent proppant injection to transport deeper into the fracture. This further result in an abrupt increase in pump pressure leading to hydraulic fracturing operation failure. This can be noticed in Figure 7.9 and Figure 7.10 that with low injection rate, the proppant bridge has started to form and gradually it will result in fracture tip screen out. One of the parameters that can aid in preventing fracture tip screen out is by adequately controlling the injection rate. Another important observation from Figure 7.10 is that near the wellbore (@x=2 m from the inlet) the proppant bed height for the lower injection rate case is greater compared with the higher injection rate case, due to the greater proppant deposition associated with lower injection rate, and higher proppant suspension in the higher injection rate case. On the contrary, away from the wellbore (@x=4 m from the inlet), the proppant bed height is greater for the higher injection rate case as compared to the lower injection rate case. This can be explained by as the proppant injected with lower injection rate case has the tendency to deposit quickly, so a majority of the proppants are deposited near to the wellbore. On the other hand, the proppant injected with a higher injection rate case tends to be suspended, transport longer into the fracture and deposit away from the wellbore. As a result, the higher proppant bed is noticed for the proppant injected with a higher injection rate.

Similarly, the proppant horizontal transport velocity is plotted with fracture height at 60 s after injection at 2 m and 4 m from the wellbore. It can be noticed from Figure 7.11 that near the wellbore the velocity profile of the cases q=0.0025 m^3/s and q=0.005 m^3/s are relatively similar. On the contrary, away from the wellbore, while the velocity of the case with q=0.001 m^3/s is low, the case with q=0.005 m^3/s still have higher velocity and thus ability to suspend proppant, resulting in more extended proppant transport. The results suggest that the increase in injection rate aids in more extended proppant transport by providing additional energy for the proppant suspension in the slurry.

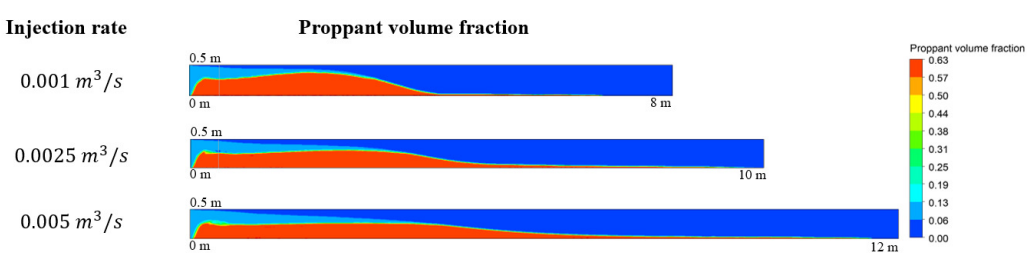

Figure 7.9 Proppant transport with dynamic fracture propagation at a varying injection rate

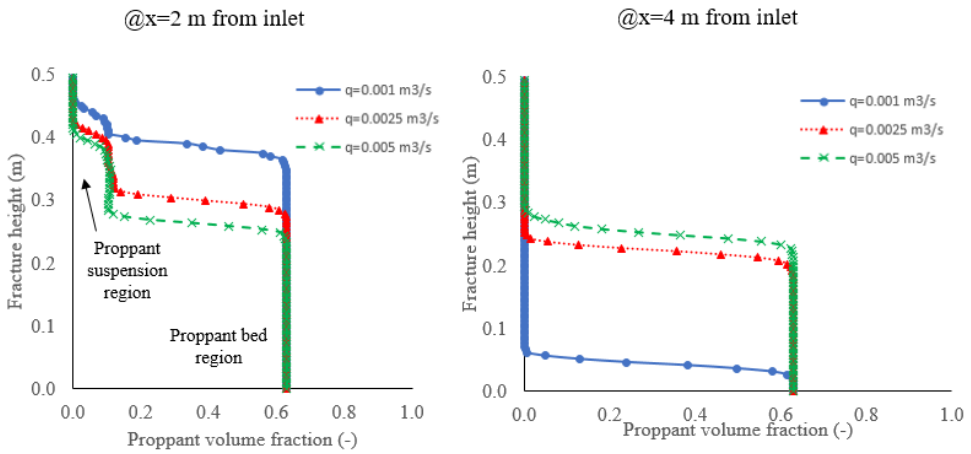

Figure 7.10 Comparison of proppant distribution against fracture height at two different locations for varying injection rates

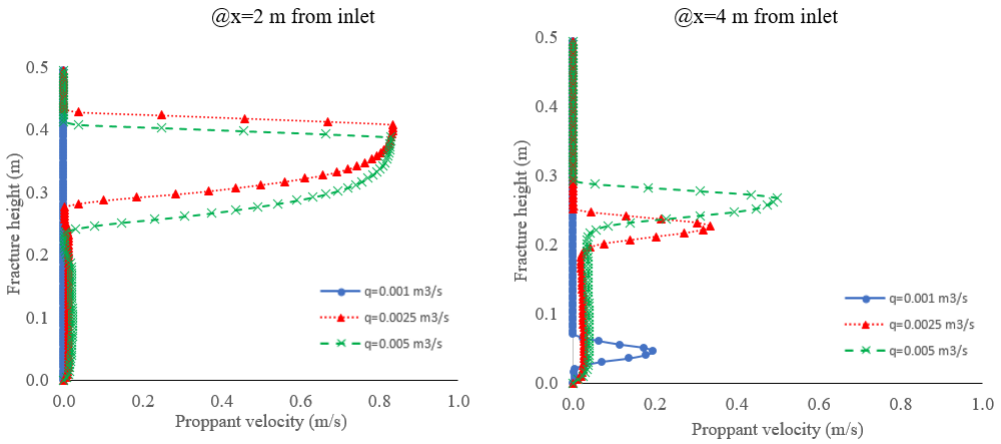

Figure 7.11 Comparison of proppant horizontal velocity against fracture height at two different locations for varying injection rates

Another innovative approach that can aid in the success of hydraulic fracturing design by preventing the fracture tip screen out and more extended proppant transport is injecting the proppants intermittently and controlling the injection rate. It means that if a continuous stream of proppant is injected with the fracturing fluid, depending upon the fracture height, the proppant bridge will start developing after some time and will eventually result in fracture tip screen out. However, if the proppant injection with fracturing fluid is followed by the pad fluid with no proppant (fluid injected after fracturing fluid not containing any proppants), the pad fluid will carry the proppant located towards the top of proppant bed and transport it further inside the fracture. This phenomenon can be observed in Figure 7.12, where the proppant suspended in the slurry was injected till the 60 s, and then the pad fluid is injected with no proppant for another 60

s. This intermittent injection is continued for two cycles, and the results are compared in Figure 7.12. To quantitatively understand the results of intermittent injection, the proppant distribution is compared against the fracture height at different time steps located at 2 m and 4 m from the wellbore and shown in Figure 7.13. The results from Figure 7.12 and Figure 7.13 show that when the proppants are injected in the slurry for the first 60 s, the proppant bridge started to build up in the form of proppant bed. Subsequently, when it is followed by the injection of pad fluid for the next 60 s, the deposited proppants are transported further long into the fracture with the pad fluid. This can be evident from the decrease of proppant bed height observed in Figure 7.13 at t=120 s suggesting that some of the proppants deposited earlier were transported further into the fracture. This cycle is repeated with the injection of proppants with the slurry for the next 60 s, and it can be noticed that for 180 s, nearly 60 % of the fracture is successfully propped as evident from Figure 7.12 and increase of proppant bed height in Figure 7.13. Areal sweep efficiency of proppant distribution can be further improved by subsequently following more intermittent injection cycles. This technique of intermittent injection can significantly improve the proppant distribution, enhance efficiency and fracture conductivity. The most significant advantage of using the intermittent injection and the proposed CFD-DEM DDPM model is that it provides an accurate prediction of proppant distribution and improved confidence to the petroleum engineers for a successful hydraulic fracturing design operation. This technique can help in overcoming the current challenge faced by the petroleum industry about low operational efficiency due to the unpropped fracture region. The unpropped region of the fracture closes down after the hydraulic pressure is removed.

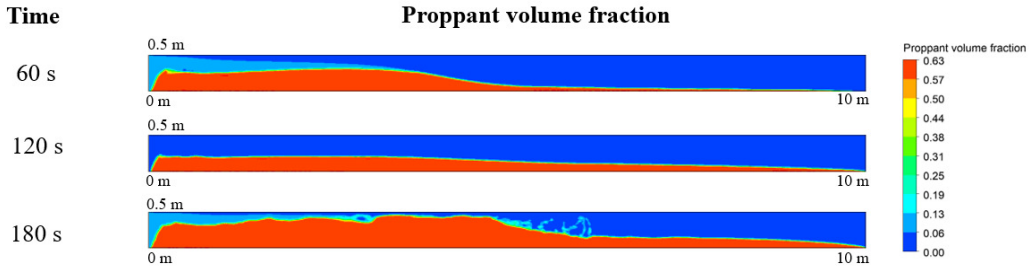

Figure 7.12 Proppant distribution at different time steps using intermittent injection.

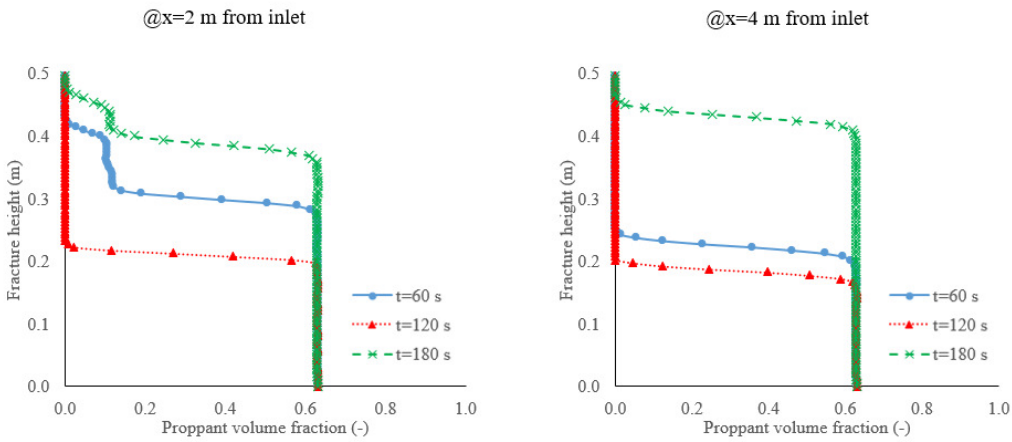

Figure 7.13 Comparison of proppant distribution against fracture height at two different locations for intermittent injection at different time steps

7.2.4 The impact of fracturing fluid viscosity on fracture propagation

The fluid rheology plays a significant role in the proppant suspension during hydraulic fracturing operation (Zhang, Gutierrez and Li 2017, Yi, Wu and Sharma 2018). Thus, in this section, the impact of fracturing fluid viscosity in fracture propagation and proppant distribution is studied. The viscosity of fracturing fluid is increased from 0.1 to 1 and 10 cP, and the results of fracture propagation are shown in Table 7.5. It can be interpreted from Table 7.5 that as viscosity is increased from 0.1 to 10 cP, a significant increase in fracture opening from 14.5 mm to 18 mm and fracture half-length from 9 m to 11 m is observed. This can be explained by as the viscosity of the fracturing fluid is increased, it results in higher wellbore pressure acting on the fracture surface area and consequently greater force leading to an increase in fracture opening.

Table 7.5 Effect of fluid viscosity on fracture propagation

Fluid viscosity (cP)	**Fluid viscosity (Pa.s)**	**Fracture width (m)**	**Fracture half-length (m)**
0.1	0.0001	0.0145	9
1	0.001	0.016	10
10	0.01	0.018	11

Next, the effect of viscosity was also investigated in terms of proppant distribution and fluid flow. The results of proppant transport with different viscosities are shown in Figure 7.14 in the form of a contour plot for proppant volume fraction. Figure 7.14 shows that fluid viscosity can substantially influence the proppant transport. The lower viscosity fluid possesses the poor ability for proppant suspension, and consequently, the proppants are deposited quickly after injection resulting in the formation of proppant bridge. This further leads to a substantial area of fracture remaining unpropped and eventually closing down when the hydraulic pressure is removed. On the contrary, the higher viscosity fracturing fluid due to its better proppant suspension ability can suspend the proppants for a longer period and thus resulting in more extended proppant transport inside the fracture.

Similar to the analysis of variation in injection rate, proppant volume fraction and proppant horizontal velocity are computed and compared for different fluid viscosities at 2 m and 4 m from the wellbore, as shown in Figure 7.15, and Figure 7.16. Proppant distribution in Figure 7.15 can be categorised into proppant bed and suspended proppants as shown. It can be seen that near the wellbore (@ 2 m from inlet), low viscosity fluid results in more significant proppant deposition as confirmed by the proppant bed almost reached the fracture height. This can further lead to a fracture tip screen out, as discussed earlier. On the contrary, for the high viscosity fluid, the proppant suspension region is substantially higher, and the proppant bed is minimal compared to other cases. However, away from the wellbore (@ 4 m from inlet), the low viscosity fluid has lower proppant bed and no proppant suspension region, as most of the proppant is deposited near the wellbore, and only a small number of proppants were able to reach this location. For the higher viscosity fluid, the proppants are still in suspension in good amount and tends to transport further deep into the fracture. This can be interpreted by the increasing viscous force contributes greater flow resistance and increases the amount of drag force on suspended proppants. This promotes the suspension ability of the proppants in the fluid and inhibits proppant deposition. Similar observations can also be noticed in Figure 7.16, where proppant horizontal velocity was compared for all the cases. Near the wellbore at 2 m from the inlet, although the low viscosity fracturing fluid possesses higher velocity compared to high viscosity fluid, it has poor proppant suspension ability and thus away from the wellbore at 4 m from the inlet, the proppant in lower viscosity fluid lags behind the proppants in higher viscosity fluid. Thus, the investigation of fluid viscosity on dynamic fracture propagation and proppant transport suggested that as the fluid viscosity increases it leads to a relatively longer fracture propagation and improved suspension ability of the proppants, which aids in better proppant distribution in the fracture domain. Correctly modelling the proppant distribution using the proposed model in an optimal fluid viscosity can help petroleum engineers to track the proppant distribution correctly and improve the hydraulic fracturing design.

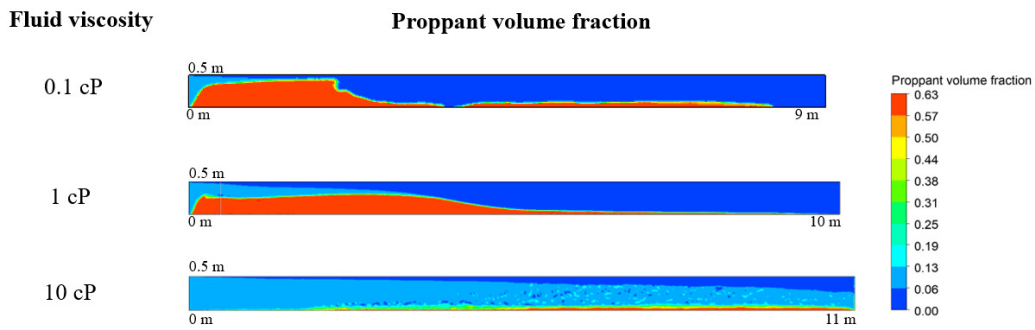

Figure 7.14 Effect of viscosity on proppant transport

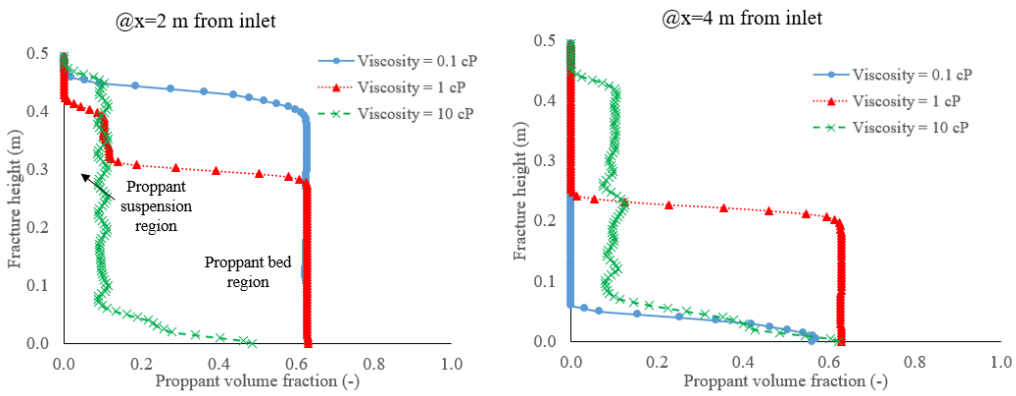

Figure 7.15 Effect of fluid viscosity on the proppant volume fraction

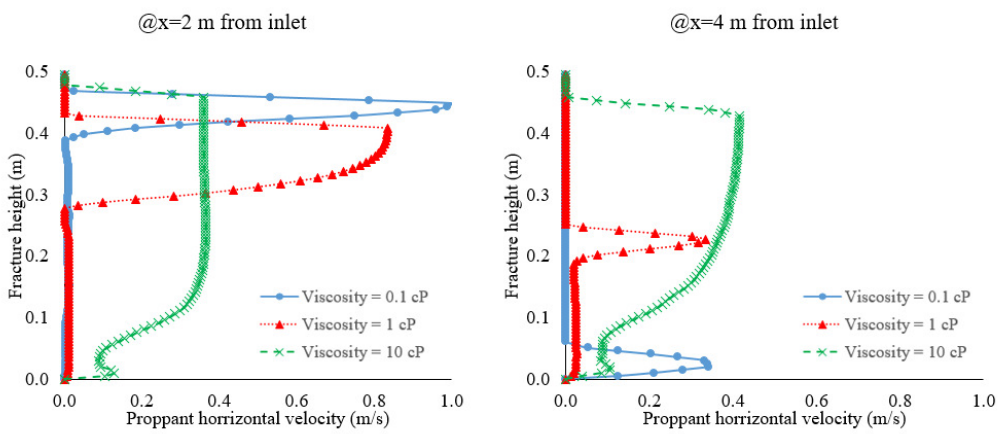

Figure 7.16 Effect of fluid viscosity on proppant horizontal velocity

7.2.5 Influence of leak-off coefficient

In the oil and gas industry, it is widely recognised that the amount of fluid leak-off can significantly influence the hydraulic fracturing operation. However, to the best of our knowledge, no reported studies have investigated the impact of fluid leakage from the fracture-matrix interface to surrounding porous rock in proppant distribution and fracture complexity. To analyse the dynamic effects of fluid leakage in proppant distribution and fracture propagation, the fluid leak-off rate constant was varied from 5.0E-11 m/kPa.s to 5.0E-9 m/kPa.s. Figure 7.17 shows the amount of fluid leakage for an increase in the non-dimensional fracture length with different leak-off constant and Figure 7.18 shows the fluid leak-off profile as the fracture propagates with different time steps. The results show that as the leak-off rate increases, more fluid seeps into the surrounding porous reservoir. Moreover, the maximum amount of injected fluid is lost in the reservoir within the 15-30% of fracture length. This directly affects the proppant suspension ability and increases the rate of proppant deposition.

The fluid leaks-off from the fracture wall to the surrounding porous rock, leaving the proppants in the slurry and thus most of the proppants deposits at the fracture bottom leading to poor distribution of proppant away from the wellbore. Thus, modelling dynamic fluid leak-off in the proppant transport physics is crucial for the accurate prediction of proppant distribution and successful hydraulic fracturing design. The results from the net fracture width and fracture half-length observed by varying the leak-off rates are reported in Table 7.6. Table 7.6 shows that as the amount of leak-off increases from 5.0E-11 m/kPa.s to 5.0E-9 m/kPa.s, it results in substantial lower fracture width from 18 mm to 10 mm and a relatively gradual reduction in fracture half-length from 11 m to 9.8 m. This can be explained by as the fluid leak-off increases from the fracture surface, it results in significantly lower pressure acting on the fracture wall that facilitates fracture propagation acting against the minimum principal stress. This consequently leads to lower fracture width.

Table 7.6 Fracture propagation with different leak-off coefficients

Leakoff constant (m/kPa.s)	**Fracture width (m)**	**Fracture half-length (m)**
5E-9	0.01	9.8
5E-10	0.016	10
5E-11	0.018	11

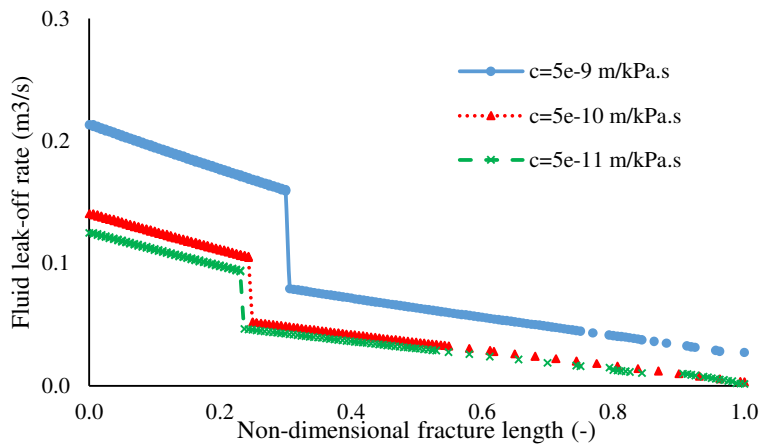

Figure 7.17 Fluid leak-off profile along fracture length with the different leak-off coefficients

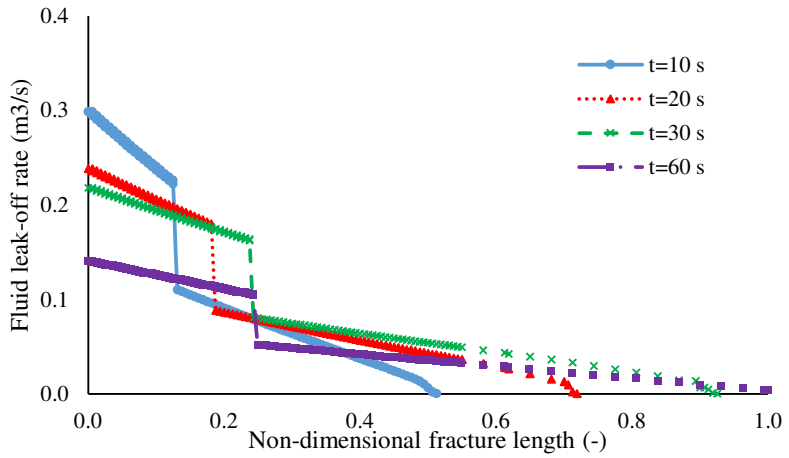

Figure 7.18 Fluid leak-off profile along fracture length at different time step

Next, the proppant distribution is investigated inside the fracture with varying leak-off rates. Fluid leakage from fracture-rock matrix interface characterises a pivotal role in the proppant suspension during hydraulic fracturing. As the fracturing fluid slurry enters into the fracture domain, the fracturing fluid leaks gradually through the fracture-rock matrix interface, and the remaining proppants in the slurry tend to deposit and form proppant bed at the fracture bottom. This can be evident in Figure 7.19 that illustrates the proppant volume fraction for the different leak-off rate constant. Figure 7.19 shows that a higher proppant bed is noticed for the higher leak-off case. This can be explained by as the fracturing fluid seeps to the surrounding porous rock leaving behind the proppant in the remaining slurry, proppants tend to settle quickly forming greater proppant bed and consequently higher chances of early fracture tip screen out. As explained earlier, the fracture tip screen out will then inhibit any further proppant transport into the fracture, and the unpropped section of the fracture will close down, resulting in loss of fracture conductivity. On the contrary, the lower fluid leak-off rate case results in less amount of fluid

leaking from the fracture to reservoir rock and thus can aid in proppant suspension with smaller proppant bed and more extended proppant transport into the fracture.

The effect of fluid leakage from the fracture-matrix interface on the proppant distribution is usually ignored by the existing proppant transport models, and it can be noticed from Figure 7.19 that it can lead to inaccurate determination of proppants and inefficient hydraulic fracturing design. To quantitatively investigate the effects of fluid leak-off on fracture propagation and proppant distribution, the plots of proppant volume fraction and horizontal velocity with a fracture height are computed at 2 m and 4 m from the wellbore and are shown in Figure 7.20 and Figure 7.21. It can be seen that the higher fluid leak-off case with constant 5.0E-9 m/kPa.s results in greater proppant bed deposition. This can be explained by a higher amount of fluid leaking-off from the fracture to reservoir matrix leaves the proppants inside the fracture. The settling velocity of the proppant becomes dominant to the horizontal transport velocity, and thus a more significant number of proppants tend to deposit. On the contrary, the lower leak-off rate case with constant 5.0E-11 m/kPa.s, due to smaller amount of fluid leakage from the fracture-matrix interface, results in suspending and transporting proppant longer into the fracture, and thus lower number of proppants are deposited. Furthermore, comparing the proppant horizontal velocity in Figure 7.21 suggests that the higher velocity is noticed from higher leak-off rate case with constant 5.0E-9 m/kPa.s, compared to the other two cases. This can be explained by the higher leak-off results in lower fracture width during fracture propagation, as explained earlier. Thus, due to the lower fracture width, the volumetric injection flow rate is greater for the higher leak-off case. However, it can be noticed that even with the higher velocity in the case of higher leak-off constant, the proppants tend to deposit early as the settling velocity is dominant over the horizontal transport velocity because of greater fluid leakage from the fracture-matrix interface. The results from the variation of leak-off rate on proppant distribution suggest that fracturing fluid leak-off is one of the significant factors that govern the proppant distribution, fracture geometry and fracture conductivity. It is essential to include it in accurately modelling the proppant transport physics and hydraulic fracturing design.

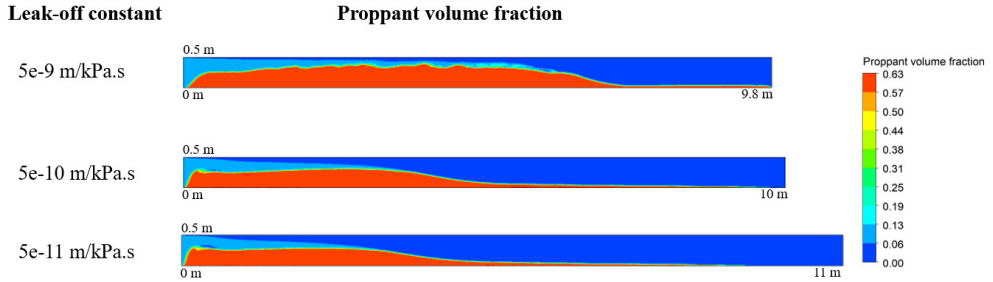

Figure 7.19 Proppant distribution with varying leak-off rate constant

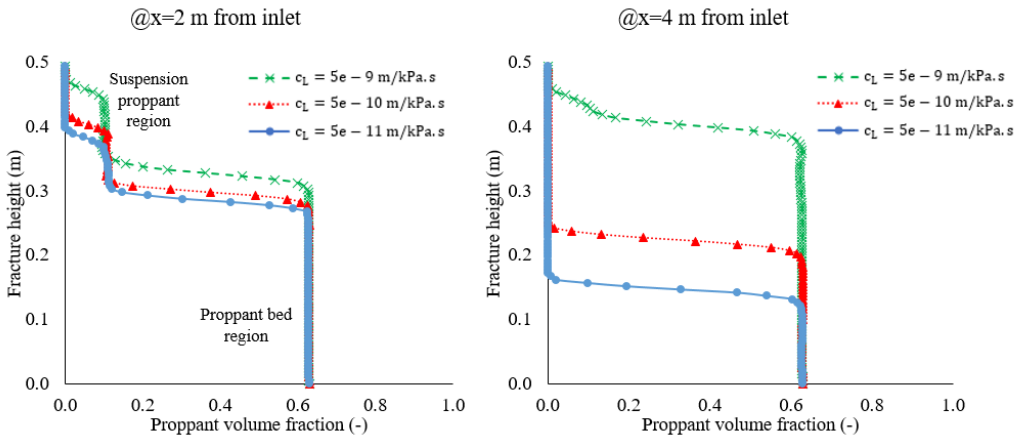

Figure 7.20 Effect of the fluid leak-off rate constant on the proppant volume fraction

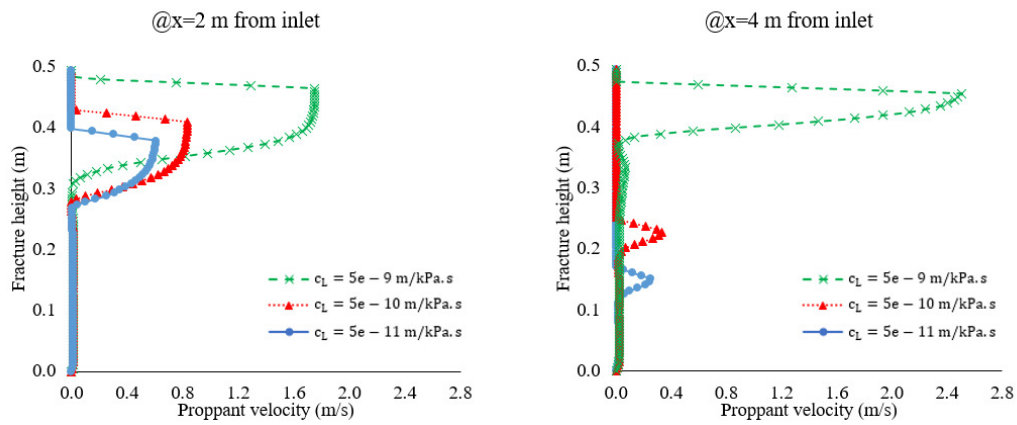

Figure 7.21 Effect of the fluid leak-off rate constant on proppant horizontal velocity

7.2.6 Application in petroleum engineering

A successful hydraulic fracturing operation is designed such that the fracture is initiated and propagated with minimum tortuosity and complexities around the wellbore. In addition, the successful transport and settling of proppants inside the fracture domain also add to the success of hydraulic fracturing. The unpropped section of fracture closes down due to the surrounding geomechanical stresses when the hydraulic pressure is removed. Thus, modelling accurately the fracture propagation coupled with proppant distribution is vital for the efficiency of hydraulic fracturing design. The propped fracture provides the desired conductivity and flow conduits for the reservoir fluids (oil or natural gas) to enter into the wellbore, and thus improve the production efficiency. Furthermore, another common failure in hydraulic fracturing design noticed in the oil industry is fracture tip screen out. This happens when proppant in fracturing fluid, create a bridge inside the fracture and prevents any further transport of proppant and fluid, resulting in a rapid

increase in pump pressure. Using advanced numerical models like the one proposed in the current study can aid in designing prevention of the fracture tip screen out and model accurately proppant transport physics with dynamic fracture propagation.

Lastly, the numerical modelling results in this research suggests that the reservoir characteristics and flow properties can significantly influence the fracture length, fracture width and proppant distribution inside the fracture. The coupled phenomenon of fluid flow, fracture propagation, proppant transport, fluid leakage, complex fluid-proppant and inter-proppant interactions can greatly influence the geomechanical stresses in the vicinity of the wellbore. This complex fracture mechanics and hydrodynamics of proppants cannot be modelled using analytical solutions or linear elastic models. Furthermore, the existing fracture propagation models use LEFM that assumes rock as a brittle material and neglect plastic deformations, which can be successfully modelled using the XFEM and CZM. Thus, the applicability of the proposed dynamic fracture propagation and fluid flow model with proppant transport and fluid leakage can help petroleum engineers to design the hydraulic fracturing operation with fewer limiting assumptions successfully.

7.3 Summary of the key findings

In this study, a fully integrated model is proposed to dynamically model the fracture propagation and proppant transport inside the fracture with fluid leak-off from the fracture sidewall. The fracture propagation is modelled using the extended finite element method, and the hydrodynamics of proppant transport is modelled using the computational fluid dynamics. The numerical modelling results were compared against the zero toughness analytical model and real field results, and a good agreement is obtained. The parametric study of injection rate, fluid viscosity and fluid leakage is conducted that influence fracture propagation and proppant distribution. The key conclusions obtained based on the parametric study are as follows-

1. Increase in injection rate aids in more extended proppant transport by providing additional energy for the proppant suspension in the slurry.
2. Proppant bridging is a frequently observed phenomenon seen during hydraulic fracturing depending upon the fracture height and width that can cause fracture tip screen out and lead to hydraulic fracturing design failure. Intermittent proppant injection technique is proposed and investigated to overcome this by controlling the injection rate. It is observed that this technique of intermittent proppant injection can significantly improve the proppant distribution, enhance areal sweep efficiency and fracture conductivity.
3. The investigation of fluid viscosity on dynamic fracture propagation and proppant transport suggested that as the fluid viscosity increases it leads to a relatively longer

fracture propagation and improved suspension ability of the proppants, which aids in better proppant distribution in the fracture domain. Correctly modelling the proppant distribution using the proposed model in an optimal fluid viscosity can help petroleum engineers to track the proppant distribution correctly and improve the hydraulic fracturing design.

4. The results from the variation of leak-off rate on proppant distribution suggest that fracturing fluid leak-off is one of the significant factors that govern the proppant distribution, fracture geometry and fracture conductivity. It is essential to include it in accurately modelling the proppant transport physics and hydraulic fracturing design. The higher leak-off rate can result in early proppant deposition and possibility of fracture tip screen out.

The fully coupled XFEM-CFD model for dynamic fracture propagation and proppant transport proposed in the current study overcomes the drawbacks of the existing proppant transport models by accounting for cohesive based traction-separation law for fracture mechanics and fluid leakage phenomenon through the fracture-rock matrix. These numerical modelling results suggest that coupling the effects of the fracture propagation, proppant transport, fluid leakage, complex fluid-proppant and inter-proppant interactions can significantly influence the geomechanical stresses in the vicinity of the wellbore. Thus, the current model aids petroleum engineers to successfully design the hydraulic fracturing operation and gain confidence in tracking and distribution of proppants inside the fracture.

Chapter 8: Conclusions and Recommendation for Future Work

In this research, an integrated numerical model is proposed to dynamically model the fracture propagation and proppant transport inside the fracture with fluid leak-off from the fracture sidewall. The fracture propagation is modelled using the extended finite element method, and the hydrodynamics of proppant transport is modelled using the computational fluid dynamics approach. Numerical simulation of proppant movement is studied within the hydraulic fracture using the DDPM model, which is a combination of Eulerian-Granular method and Discrete Element Method, in commercial computational fluid dynamics (CFD) software, ANSYS FLUENT. A user-defined function was defined in order to mimic and model the fluid leak-off rate in the porous reservoir through the hydraulic fracture. It was established by adding the momentum and mass source terms in the flow governing equations. The effect of fracture roughness on the hydrodynamics of proppant transport is also investigated in detail. The model was validated with the reported experimental study and show good agreement. This chapter summarises the key conclusions from this research and suggests some recommendations for future work.

8.1 Conclusions

The key objective of this research was to improve the hydraulic fracturing design in unconventional reservoirs by accurately modelling the proppant hydrodynamics, dynamic fracture propagation, fluid leak-off and fracture roughness. The main tasks achieved can be summarised as follows:

- A proppant transport model in hydraulic fractures was developed using the CFD based DDPM model which is a combination of Eulerian-Granular method and Discrete Element Method, that can accurately capture the inter-proppant, proppant-wall and proppant-fluid interactions. Furthermore, the proposed DDPM model can accurately predict the proppant transport and distribution in hydraulic fractures that can help petroleum engineers to design the hydraulic fracturing operation successfully.
- The fluid leak-off from the fracture wall to the surrounding porous rock was modelled using a user-defined function. This is done to mimic the fluid leak-off into the porous reservoir, leaving the proppant in the fracture. It was established by adding the momentum and mass source terms in the flow governing equations in order to provide a realistic proppant tracking and more accurate proppant transport.

- The results from the current simulation model were validated with the reported experimental study in terms of proppant bed height and proppant bed length and showed a good agreement.
- The Proppant transport model is applied in the rough hydraulic fractures using the Joint Roughness Coefficient (JRC) to establish a relationship between fracture roughness, proppant hydrodynamics and flow regime.
- An integrated hydraulic fracturing model is developed to dynamically model the fracture propagation and proppant transport inside the fracture with fluid leak-off from the fracture sidewall. The fully coupled CFD-XFEM model for dynamic fracture propagation and proppant transport proposed in the current research overcomes the drawbacks of the existing proppant transport models by accounting for cohesive based traction-separation law for fracture mechanics and fluid leakage phenomenon through the fracture-rock matrix. The fracture propagation is modelled using the extended finite element method, and the hydrodynamics of proppant transport is modelled using the computational fluid dynamics. The numerical modelling results were compared against the zero-toughness analytical model and real field results, and a good agreement is obtained.

The parametric study was performed to understand the proppant settling and transport mechanism by the variation in proppant properties (proppant diameter, proppant concentration), fluid properties (fluid viscosity, fluid injection rate), geomechanical properties (fracture width, fracture roughness, fracture height), fluid leakage and using foam as fracturing fluid. The following conclusions can be made based on the results presented in this dissertation:

- For low viscosity fluid like slick water, higher injection velocity can have higher proppant concentration in the suspension and result in transporting proppant to a greater distance inside the fracture. Increase in injection rate aids in more extended proppant transport by providing additional energy for the proppant suspension in the slurry.
- Proppant bridging is a frequently observed phenomenon seen during hydraulic fracturing depending upon the fracture height and width that can cause fracture tip screen out and lead to hydraulic fracturing design failure. Intermittent proppant injection technique is proposed and investigated to overcome this by controlling the injection rate. It is observed that this technique of intermittent proppant injection can significantly improve the proppant distribution, enhance areal sweep efficiency and fracture conductivity.
- The investigation of fluid viscosity on dynamic fracture propagation and proppant transport suggested that as the fluid viscosity increases it leads to a relatively longer fracture propagation and improved suspension ability of the proppants, which aids in

better proppant distribution in the fracture domain. Correctly modelling the proppant distribution using the proposed model in an optimal fluid viscosity can help petroleum engineers to track the proppant distribution correctly and improve the hydraulic fracturing design.

- The sensitivity analysis of proppant concentration shows that proppant concentration has a complex effect on proppant transport, such as proppant settling velocity and the rate of proppant bed build-up. The higher proppant concentration can help to reach the equilibrium height quickly, higher proppant velocity in the longitudinal direction and longer proppant bed length.
- The results show that small diameter proppant tends to remain suspended in the slurry, and larger diameter proppant tends to settle down quickly. Secondly, proppants with lower fracture width tends to form deposition dune quickly.
- The comparison of foam injection with water injection shows that foam has improved capability to suspend proppants and using foam as a fracturing fluid have the potential to mitigate the challenge of quick deposition of proppant in shale gas reservoirs.
- A comparison of the Eulerian-Granular method was made with the DEM method. The Eulerian-Granular method provides an approximate match with the DEM; however, the particle distribution rate in the Eulerian-Granular method is relatively higher than the DEM method. This was explained by the different ways in which particle-particle interaction is captured, and particle physics is handled in both these approaches. DEM provides a more accurate particle physics, but the computational time required is significantly higher. Considering the substantial simulation time required for the DEM method, and applicability for upscaling the model to field-scale hydraulic fractures, the current study suggests the need of a DDPM model that can be used for practical problems of petroleum engineering interests for proppant distribution and settling.
- The effect of fracture Joint Roughness Coefficient (JRC) was quantitatively investigated on proppant motion. When proppant transport in smooth fractures, the fracture walls employ substantial mechanical retardation effects on proppants resulting in a decrease of proppant horizontal transport velocity and greater proppant deposition in the form of bed. In contrast, when the proppants are transported in rough fractures, with the increase in fracture roughness the inter proppant and proppant-wall interactions dramatically increases, and consequently higher amount of proppants are suspended in the slurry resulting in greater proppant horizontal transport velocity. Furthermore, in terms of horizontal motion, proppants are inclined to transport to a longer distance away from the wellbore with the increase in fracture roughness. The mechanical interaction flow effects were found to be dependent on the proppant transport regime. When the proppant

transport in high viscosity fluids (i.e. at low proppant Reynolds number), no significant effect of fracture roughness in proppant transport is noticed. In contrast, for proppant transport in low viscosity fluids (i.e. at high proppant Reynolds number), the mechanical interaction effects become dominant with roughness and significantly increases proppant horizontal transport velocity.

- The results from the variation of leak-off rate on proppant distribution suggest that fracturing fluid leak-off is one of the significant factors that govern the proppant distribution, fracture geometry and fracture conductivity. It is essential to include it in accurately modelling the proppant transport physics and hydraulic fracturing design. The higher leak-off rate can result in early proppant deposition and possibility of fracture tip screen out.
- The simulation results suggest that neglecting the fracture roughness in the proppant transport model can result in over predicting the proppant bed length and underpredicting the proppant suspension layer by 10-15%. Furthermore, neglecting the fluid leak-off effect can result in under predicting the proppant bed height by 10-50% and over predicting the proppant suspension layer by 10-50%.

The key contribution to the knowledge of this research is the development of a model that dynamically integrates the fracture propagation, fluid flow and proppant transport with fluid leak-off in the rough hydraulic fractures and provide an improved hydraulic fracturing design. The novel feature of the model includes the following:

i. The present study models the effect of dynamic fluid leak-off from the fracture wall in the proppant hydrodynamics in order to accurately simulate the proppant-fracturing fluid interaction and inter-particle physics using the advanced computational methods.
ii. The present study proposes a 3D proppant transport model that captures the proppant physics in rough fractures using Joint Roughness Coefficient with detailed proppant-wall and inter-proppant interactions in order to improve the hydraulic fracturing design.
iii. The present study couples the fluid flow and proppant transport with the dynamic fracture propagation using CFD-XFEM method to track the proppants accurately and dynamically simulate the realistic phenomenon for an improved hydraulic fracturing design. The coupled CFD-XFEM model for dynamic fracture propagation and proppant transport proposed in the current research overcomes the drawbacks of the existing proppant transport models by accounting for cohesive based traction-separation law for fracture mechanics and fluid leakage phenomenon through the fracture-rock matrix.
iv. The present model can be used to prevent fracture tip screen out, which is a common failure in hydraulic fracturing design noticed in the oil industry. Fracture tip screen out

occurs when proppant in fracturing fluid, create a bridge inside the fracture and prevents any further transport of proppant and fluid, resulting in a rapid increase in pump pressure. Using advanced numerical models like the one proposed in the current study can aid in designing prevention of the fracture tip screen out and model accurately proppant transport physics with dynamic fracture propagation.

Considering the applicability of the DDPM model for rough fractures and dynamic fracture propagation, the current study suggests that the CFD-XFEM method can be used for practical problems of petroleum engineering interests for proppant distribution and settling. The numerical modelling results suggest that coupling the effects of the fracture propagation, proppant transport, fluid leakage, complex fluid-proppant and inter-proppant interactions can significantly influence the geomechanical stresses in the vicinity of the wellbore. This complex fracture mechanics and hydrodynamics of proppants cannot be modelled using analytical solutions or linear elastic models. Furthermore, the existing fracture propagation models use LEFM that assumes rock as a brittle material and neglect plastic deformations, which can be successfully modelled using the XFEM and CZM. The current study has enhanced the understanding of complex proppant transport phenomenon in hydraulic fractures with fluid leak-off by capturing the proppant-fracturing fluid interaction and inter-particle physics accurately using the advanced computational methods. Thus, the current model aids petroleum engineers to successfully design the hydraulic fracturing operation with fewer limiting assumptions successfully and gain confidence in tracking and distribution of proppants inside the fracture.

8.2 Recommendations for future work

The following recommendations for future research work have been identified from the present study:

i. For modelling the proppant transport in hydraulic fractures using Non-Newtonian fracturing fluid, one of the assumptions used was that the foam is dry and of high and uniform quality. It means no effect of foam drainage and foam microstructure is accounted for in the model. However, to improve the numerical modelling capability the wet foam characteristics with foam drainage can be investigated on proppant transport and distribution.

ii. The current CFD-XFEM model proposed for studying the proppant transport in dynamically propagating hydraulic fractures is explicitly modelled. An XFEM geomechanics solver based on cohesive traction law models the fracture propagation based on fracture mechanics, geomechanical stress and reservoir properties. A CFD

based solver models the proppant transport inside the fracture with fluid leaking off from the fracture-matrix interface. However, with the advancement of software programming, in future, an implicit integrated solver could be developed that can implicitly couple the multiphysics phenomenon of fracture propagation using XFEM and fluid flow with proppant transport using CFD based DDPM model.

iii. Probably the main limitation of our model is the current fracture propagation model assumes no variation in fracture height. Another key extension of our work is to investigate the XFEM model with the variation in height and integrate it with the CFD based DDPM model for proppant transport in hydraulic fractures. Furthermore, the model can be developed in fluid flow and proppant transport in multiple intersecting fractures and fracture network.

iv. In the present research, the spherical-shaped Rosin-Rammler proppant size distribution is used for the analysis. However, the naturally occurring sands or proppant used in slick water for hydraulic fracturing in unconventional reservoirs can be of irregular sizes. The proppant size irregularity and deviation from the spherical behaviour can influence the drag forces acting on the proppants. Thus, the current model can be extended to include the effect of irregular proppant size distribution in proppant hydrodynamics.

Chapter 9: References

ADACHI, J. and DETOURNAY, E., 2002. Self-similar solution of a plane-strain fracture driven by a power-law fluid. *International Journal for Numerical and Analytical Methods in Geomechanics,* 26(6), pp. 579-604

ADACHI, J.I., 2002. *Fluid-driven fracture in permeable rock.* [online] Ph.D. thesis, University of Minnesota.

ADACHI, J. et al., 2007. Computer simulation of hydraulic fractures. *International Journal of Rock Mechanics and Mining Sciences,* 44(5), pp. 739-757

ADAMCZYK, W.P. et al., 2014. Comparison of the standard Euler–Euler and hybrid Euler–Lagrange approaches for modeling particle transport in a pilot-scale circulating fluidized bed. *Particuology,* 15, pp. 129-137

ADVANI, S.H., LEE, T. and LEE, J., 1990. Three-dimensional modeling of hydraulic fractures in layered media: part I—finite element formulations. *Journal of Energy Resources Technology,* 112(1), pp. 1-9

ALAHMADI, Y.H. and NOWAKOWSKI, A.F., 2016. Modified shear stress transport model with curvature correction for the prediction of swirling flow in a cyclone separator. *Chemical Engineering Science,* 147, pp. 150-165

ALOTAIBI, M.A. and MISKIMINS, J.L., 2015. Slick water proppant transport in complex fractures: new experimental findings & scalable correlation. *Paper SPE-174828-MS, SPE Annual Technical Conference and Exhibition, 28-30 September, Houston, Texas, USA.* 28/09/2015. Society of Petroleum Engineers.

AL-QURAISHI, A.A. andCHRISTIANSEN, R.L., 1999. Dimensionless groups for interpreting proppant transport in hydraulic fractures. *Middle East Oil Show and Conference.* Society of Petroleum Engineers.

ANDERSON, T.B. and JACKSON, R., 1967. Fluid mechanical description of fluidized beds. Equations of motion. *Industrial & Engineering Chemistry Fundamentals,* 6(4), pp. 527-539

ANDREWS, M.J. and O'ROURKE, P.J., 1996. *The multiphase particle-in-cell (MP-PIC) method for dense particulate flows.*

BABCOCK, R., PROKOP, C. and KEHLE, R., 1967. Distribution of propping agent in vertical fractures. *Drilling and Production Practice.* American Petroleum Institute.

BAKKER, C., MEYER, C. and DEGLON, D., 2009. Numerical modelling of non-Newtonian slurry in a mechanical flotation cell. *Minerals Engineering,* 22(11), pp. 944-950

BANERJEE, S. and CHAN, A., 1980. Separated flow models—I. Analysis of the averaged and local instantaneous formulations. *International Journal of Multiphase Flow,* 6(1-2), pp. 1-24

BARENBLATT, G.I., 1962. The mathematical theory of equilibrium cracks in brittle fracture. *Advances in applied mechanics.* Elsevier. pp. 55-129

BARREE, R. and CONWAY, M., 1994. Experimental and numerical modeling of convective proppant transport. *SPE Annual Technical Conference and Exhibition, 25-28 September, New Orleans, Louisiana. Paper SPE-28564-MS.* Society of Petroleum Engineers.

BARTON, N. and CHOUBEY, V., 1977. The shear strength of rock joints in theory and practice. *Rock Mechanics,* 10(1-2), pp. 1-54

BASU, D., DAS, K., SMART, K. and OFOEGBU, G., 2015. Comparison of Eulerian-Granular and discrete element models for simulation of proppant flows in fractured reservoirs. *Paper IMECE2015-50050, ASME 2015 International Mechanical Engineering Congress and Exposition. Volume 7B: Fluids Engineering Systems and Technologies Houston, Texas, USA, 13-19 November, 2015.* American Society of Mechanical Engineers. pp. V07BT09A012

BEHR, A. et al., 2006. Consideration of damaged zone in a tight gas reservoir model with a hydraulically fractured well. *SPE Production & Operations,* 21(02), pp. 206-211

BELYADI, H., FATHI, E. and BELYADI, F., 2019. *Hydraulic fracturing in unconventional reservoirs: theories, operations, and economic analysis.* Gulf Professional Publishing.

BELYTSCHKO, T. and BLACK, T., 1999. Elastic crack growth in finite elements with minimal remeshing. *International Journal for Numerical Methods in Engineering,* 45(5), pp. 601-620

BENYAHIA, S., SYAMLAL, M. and O'BRIEN, T.J., 2005. Evaluation of boundary conditions used to model dilute, turbulent gas/solids flows in a pipe. *Powder Technology,* 156(2-3), pp. 62-72

BENZEGGAGH, M.L. and KENANE, M., 1996. Measurement of mixed-mode delamination

fracture toughness of unidirectional glass/epoxy composites with mixed-mode bending apparatus. *Composites Science and Technology,* 56(4), pp. 439-449

BIGGS, M.J. et al., 2008. Granular temperature in a gas fluidized bed. *Granular Matter,* 10(2), pp. 63-73

BLAZEK, J., 2015. *Computational fluid dynamics: principles and applications.* Butterworth-Heinemann.

BLOCKEN, B., CARMELIET, J. and STATHOPOULOS, T., 2007. CFD evaluation of wind speed conditions in passages between parallel buildings—effect of wall-function roughness modifications for the atmospheric boundary layer flow. *Journal of Wind Engineering and Industrial Aerodynamics,* 95(9-11), pp. 941-962

BLYTON, C.A., GALA, D.P. and SHARMA, M.M., 2015. A comprehensive study of proppant transport in a hydraulic fracture. *Paper SPE-174973-MS, SPE Annual Technical Conference and Exhibition, 28-30 September, Houston, Texas, USA.* Society of Petroleum Engineers.

BLYTON, C.A., GALA, D.P. and SHARMA, M.M., 2018. A Study of Proppant Transport with Fluid Flow in a Hydraulic Fracture. *SPE Drilling & Completion,* 33(04), pp. 307-323

BOKANE, A.B., JAIN, S. and CRESPO, F., 2014. Evaluation and Optimization of Proppant Distribution in Multistage Fractured Horizontal Wells: A Simulation Approach. *Paper SPE-171581-MS, SPE/CSUR Unconventional Resources Conference – Canada, 30 September–2 October, Calgary, Alberta, Canada.* Society of Petroleum Engineers.

BOKANE, A.B., JAIN, S., DESHPANDE, Y.K. and CRESPO, F., 2013. Transport and distribution of proppant in multistage fractured horizontal wells: a CFD simulation approach. *Paper SPE-166096-MS, SPE Annual Technical Conference and Exhibition, 30 September-2 October, New Orleans, Louisiana, USA.* Society of Petroleum Engineers.

BORONIN, S.A. and OSIPTSOV, A.A., 2010. Two-continua model of suspension flow in a hydraulic fracture. *Doklady Physics,* 55(4), pp. 199-202

BRANNON, H.D., WOOD, W.D. and WHEELER, R.S., 2006. Large scale laboratory investigation of the effects of proppant and fracturing fluid properties on transport. *Paper SPE-98005-MS, SPE International Symposium and Exhibition on Formation Damage Control, 15-17 February, Lafayette, Louisiana, USA.* Society of Petroleum Engineers.

BRIGGS, S., KARNEY, B.W. and SLEEP, B.E., 2017. Numerical modeling of the effects of roughness on flow and eddy formation in fractures. *Journal of Rock Mechanics and Geotechnical Engineering,* 9(1), pp. 105-115

BROWN, W.K. and WOHLETZ, K.H., 1995. Derivation of the Weibull distribution based on physical principles and its connection to the Rosin–Rammler and lognormal distributions. *Journal of Applied Physics,* 78(4), pp. 2758-2763

BURNS, A.D., FRANK, T., HAMILL, I. and SHI, J., 2004. The Favre averaged drag model for turbulent dispersion in Eulerian multi-phase flows. *5th international conference on multiphase flow, ICMF*. pp. 1-17

CARTER, B. et al., 2000. Simulating fully 3D hydraulic fracturing. *Modeling in geomechanics,* 200, pp. 525-557

CARTER, R., 1957. Derivation of the general equation for estimating the extent of the fractured area. *Appendix I of "Optimum Fluid Characteristics for Fracture Extension," Drilling and Production Practice, GC Howard and CR Fast, New York, New York, USA, American Petroleum Institute,* , pp. 261-269

CHANG, K., 2013. *Product Performance Evaluation using CAD/CAE: The Computer Aided Engineering Design Series.* Academic press.

CHEN, J., 2011. Simulation of multi-directional crack growth in braided composite T-piece specimens using cohesive models. *Fatigue & Fracture of Engineering Materials & Structures,* 34(2), pp. 123-130

CHEN, Z., 2013. An ABAQUS implementation of the XFEM for hydraulic fracture problems. *ISRM International Conference for Effective and Sustainable Hydraulic Fracturing, 20-22 May, Brisbane, Australia.* International Society for Rock Mechanics and Rock Engineering.

CHEN, Z. et al., 2009. Cohesive zone finite element-based modeling of hydraulic fractures. *Acta Mechanica Solida Sinica,* 22(5), pp. 443-452

CHIESA, M. et al., 2005. *Numerical simulation of particulate flow by the Eulerian–Lagrangian and the Eulerian–Eulerian approach with application to a fluidized bed.*

CHOBAN, E.R. et al., 2004. Microfluidic fuel cell based on laminar flow. *Journal of Power Sources,* 128(1), pp. 54-60

CHU, K. et al., 2017. Understand solids loading effects in a dense medium cyclone: effect of particle size by a CFD-DEM method. *Powder Technology,* 320, pp. 594-609

CHUNG, T., 2010. *Computational fluid dynamics.* Cambridge university press.

CIPOLLA, C.L., MACK, M.G. and MAXWELL, S.C., 2010. Reducing exploration and appraisal risk in low-permeability reservoirs using microseismic fracture mapping. *Canadian Unconventional Resources and International Petroleum Conference.* Society of Petroleum Engineers.

CLARK, P., HARKIN, M., WAHL, H. and SIEVERT, J., 1977. Design of a large vertical prop transport model. *SPE Annual Fall Technical Conference and Exhibition.* Society of Petroleum Engineers.

CLARK, P.E. and ZHU, Q., 1996. Convective transport of propping agents during hydraulic fracturing. *SPE Eastern Regional Meeting.* Society of Petroleum Engineers.

CLEARY, M.P., KAVVADAS, M. and LAM, K.Y., 1983. Development of a fully three-dimensional simulator for analysis and design of hydraulic fracturing. *SPE/DOE Low Permeability Gas Reservoirs Symposium, 14-16 March, Denver, Colorado, USA.* Society of Petroleum Engineers.

CLEARY, M. and FONSECA JR, A., 1992. Proppant convection and encapsulation in hydraulic fracturing: practical implications of computer and laboratory simulations. *SPE Annual Technical Conference and Exhibition.* Society of Petroleum Engineers.

CLIFTON, R. and WANG, J., 1988. Multiple fluids, proppant transport, and thermal effects in three-dimensional simulation of hydraulic fracturing. *Paper SPE-18198-MS, SPE Annual Technical Conference and Exhibition, 2-5 October, Houston, Texas.* Society of Petroleum Engineers.

COKLJAT, D. et al., 2006. Reynolds-stress model for Eulerian multiphase. *Progress in Computational Fluid Dynamics, An International Journal,* 6(1-3), pp. 168-178

CRANDALL, D., AHMADI, G. and SMITH, D.H., 2010. Computational modeling of fluid flow through a fracture in permeable rock. *Transport in Porous Media,* 84(2), pp. 493-510

CRISTIAN, M.S., PAULLO, M. and ROEHL, D., 2015. Continuation Methods for the Simulation of Rock Fracture with Cohesive Elements. *13th ISRM International Congress of Rock*

Mechanics, 10-13 May, Montreal, Canada. International Society for Rock Mechanics and Rock Engineering.

CUNDALL, P.A. and STRACK, O.D., 1979. A discrete numerical model for granular assemblies. *Geotechnique,* 29(1), pp. 47-65

DANESHY, A., 2011. Uneven distribution of proppants in perf clusters. *World Oil,* 232(4), pp. 75-76

DENG, S. et al., 2014. Simulation of shale–proppant interaction in hydraulic fracturing by the discrete element method. *International Journal of Rock Mechanics and Mining Sciences,* 70(Supplement C), pp. 219-228

DESHPANDE, Y.K., CRESPO, F., BOKANE, A.B. and JAIN, S., 2013. Computational fluid dynamics (CFD) study and investigation of proppant transport and distribution in multistage fractured horizontal wells. *Paper SPE-165952-MS, SPE Reservoir Characterization and Simulation Conference and Exhibition, 16-18 September, Abu Dhabi, UAE.* Society of Petroleum Engineers.

DI, Y. and TANG, H., 2018. Simulation of Multistage Hydraulic Fracturing in Unconventional Reservoirs Using Displacement Discontinuity Method (DDM). *Hydraulic Fracture Modeling.* Elsevier. pp. 41-74

DONALDSON, E.C., ALAM, W. and BEGUM, N., 2014. *Hydraulic fracturing explained: Evaluation, implementation, and challenges.* Elsevier.

DONTSOV, E.V. and PEIRCE, A.P., 2014. Slurry flow, gravitational settling and a proppant transport model for hydraulic fractures. *Journal of Fluid Mechanics,* 760, pp. 567-590

DONTSOV, E.V. and PEIRCE, A.P., 2015. A Lagrangian Approach to Modelling Proppant Transport with Tip Screen out in KGD Hydraulic Fractures. *Rock Mechanics and Rock Engineering,* 48(6), pp. 2541-2550

DREW, D.A., 1983. Mathematical modeling of two-phase flow. *Annual Review of Fluid Mechanics,* 15(1), pp. 261-291

DU, C.M., ZHAN, L., LI, J., ZHANG, X., CHURCH, S., TUSHINGHAM, K. and HAY, B., 2011. Generalization of dual-porosity-system representation and reservoir simulation of hydraulic fracturing-stimulated shale gas reservoirs. *SPE Annual Technical Conference and*

Exhibition. Society of Petroleum Engineers.

DUAN, Q. et al., 2009. Element-local level set method for three-dimensional dynamic crack growth. *International Journal for Numerical Methods in Engineering,* 80(12), pp. 1520-1543

ECONOMIDES, M.J. and NOLTE, K.G., 2000. *Reservoir stimulation.* Wiley New York.

EHSANI, M. et al., 2015. Effects of Restitution and Specularity Coefficients on Solid-Liquid Fluidized Bed Hydrodynamics. *Chemical Engineering & Technology,* 38(10), pp. 1827-1836

EKAMBARA, K. et al., 2009. Hydrodynamic simulation of horizontal slurry pipeline flow using ANSYS-CFX. *Industrial & Engineering Chemistry Research,* 48(17), pp. 8159-8171

ELGHOBASHI, S., 1991. Particle-laden turbulent flows: direct simulation and closure models. *Computational fluid Dynamics for the Petrochemical Process Industry.* Springer. pp. 91-104

EL-M. SHOKIR, E. and AL-QURAISHI, A.A., 2009. Experimental and numerical investigation of proppant placement in hydraulic fractures. *Petroleum Science and Technology,* 27(15), pp. 1690-1703

ENWALD, H., PEIRANO, E. and ALMSTEDT, A., 1996. Eulerian two-phase flow theory applied to fluidization. *International Journal of Multiphase Flow,* 22, pp. 21-66

ERGUN, S., 1952. Fluid flow through packed columns. *Chem.Eng.Prog.,* 48, pp. 89-94

FENG, Y. and GRAY, K., 2019. XFEM-based cohesive zone approach for modeling near-wellbore hydraulic fracture complexity. *Acta Geotechnica,* 14(2), pp. 377-402

FERZIGER, J.H. and PERIĆ, M., 2002. *Computational methods for fluid dynamics.* Springer.

FLUENT, A., 2009. 12.0 UDF Manual. *Ansys Inc,*

FRIEHAUF, K.E., 2009. *Simulation and design of energized hydraulic fractures.* [online] Ph.D. thesis, The University of Texas at Austin.

FRIES, T. and BAYDOUN, M., 2012. Crack propagation with the extended finite element method and a hybrid explicit–implicit crack description. *International Journal for Numerical Methods in Engineering,* 89(12), pp. 1527-1558

FU, P., JOHNSON, S.M. and CARRIGAN, C.R., 2013. An explicitly coupled hydro-

geomechanical model for simulating hydraulic fracturing in arbitrary discrete fracture networks. *International Journal for Numerical and Analytical Methods in Geomechanics,* 37(14), pp. 2278-2300

FUNG, R., VILAYAKUMAR, S. and CORMACK, D.E., 1987. Calculation of vertical fracture containment in layered formations. *SPE Formation Evaluation,* 2(04), pp. 518-522

GADDE, P.B., LIU, Y., NORMAN, J., BONNECAZE, R. and SHARMA, M.M., 2004. Modeling proppant settling in water-fracs. *Paper SPE-89875-MS, SPE Annual Technical Conference and Exhibition, 26-29 September, Houston, Texas.* Society of Petroleum Engineers.

GAURAV, A., DAO, E.K. and MOHANTY, K.K., 2010. Ultra-lightweight proppants for shale gas fracturing. *Tight Gas Completions Conference.* Society of Petroleum Engineers.

GEERTSMA, J. and DE KLERK, F., 1969. A rapid method of predicting width and extent of hydraulically induced fractures. *Journal of Petroleum Technology,* 21(12), pp. 1,571-1,581

GIACOMINI, A. et al., 2008. Numerical study of flow anisotropy within a single natural rock joint. *International Journal of Rock Mechanics and Mining Sciences,* 45(1), pp. 47-58

GIDASPOW, D., 1994. *Multiphase flow and fluidization: continuum and kinetic theory descriptions.* Academic press.

GIDASPOW, D., BEZBURUAH, R. and DING, J., 1991. Hydrodynamics of circulating fluidized beds: kinetic theory approach.

GÖKTEPE, S., ATALIK, K. and ERTÜRK, H., 2014. Comparison of single and two-phase models for nanofluid convection at the entrance of a uniformly heated tube. *International Journal of Thermal Sciences,* 80, pp. 83-92

GOLDHIRSCH, I., 2008. Introduction to granular temperature. *Powder Technology,* 182(2), pp. 130-136

GU, H., SIEBRITS, E. and SABOUROV, A., 2008. Hydraulic fracture modeling with bedding plane interfacial slip. *SPE Eastern Regional/AAPG Eastern Section Joint Meeting.* Society of Petroleum Engineers.

GU, Q. and HOO, K.A., 2014. Evaluating the performance of a fracturing treatment design. *Industrial & Engineering Chemistry Research,* 53(25), pp. 10491-10503

GU, M. and MOHANTY, K.K., 2014. Effect of foam quality on effectiveness of hydraulic fracturing in shales. *International Journal of Rock Mechanics and Mining Sciences,* 70(Supplement C), pp. 273-285

HADDAD, M. and SEPEHRNOORI, K., 2016. XFEM-based CZM for the simulation of 3D multiple-cluster hydraulic fracturing in quasi-brittle shale formations. *Rock Mechanics and Rock Engineering,* 49(12), pp. 4731-4748

HÖGBERG, J.L., 2006. Mixed mode cohesive law. *International Journal of Fracture,* 141(3-4), pp. 549-559

HOSSEINI, H., TSAU, J., PELTIER, E. and BARATI, R., 2018. Lowering Fresh Water Usage in Hydraulic Fracturing by Stabilizing scCO 2 Foam with Polyelectrolyte Complex Nanoparticles Prepared in High Salinity Produced Water. *Paper SPE-189555-MS, SPE International Conference and Exhibition on Formation Damage Control, 7-9 February, Lafayette, Louisiana, USA*. Society of Petroleum Engineers.

HU, X. et al., 2018. Effect of proppant addition schedule on the proppant distribution in a straight fracture for slick water treatment. *Journal of Petroleum Science and Engineering,* 167, pp. 110-119

ISHII, M. and HIBIKI, T., 2011. Drift-flux model. *Thermo-Fluid Dynamics of Two-Phase Flow*. Springer. pp. 361-395

ISLAM, M.R., 2014. *Unconventional gas reservoirs: evaluation, appraisal, and development.* Elsevier.

ISSA, R. and OLIVEIRA, P., 1993. Modelling of turbulent dispersion in two phase flow jets. *Engineering turbulence modeling and experiments,* 21993, pp. 947-957

IZADI, G., HOEINK, T., CRUZ, L. and COPELAND, D., 2017. Numerical Modeling of Proppant Transport in Complex Hydraulic Fracture Propagation. *SPE Annual Technical Conference and Exhibition.* Society of Petroleum Engineers.

JAIN, S., SOLIMAN, M., BOKANE, A., CRESPO, F., DESHPANDE, Y., KUNNATH AVEN, N. and CORTEZ, J., 2013. Proppant distribution in multistage hydraulic fractured wells: a large-scale inside-casing investigation. *Paper SPE-163856-MS, SPE Hydraulic Fracturing Technology Conference, 4-6 February, The Woodlands, Texas, USA*. Society of Petroleum Engineers.

JAKOBSEN, H.A., 2014. *Chemical reactor modeling: multiphase reactive flows.* Springer Science & Business Media.

JENKINS, J.T. and SAVAGE, S.B., 1983. A theory for the rapid flow of identical, smooth, nearly elastic, spherical particles. *Journal of Fluid Mechanics,* 130, pp. 187-202

JOHNSON JR, R.L. andGREENSTREET, C.W., 2003. Managing uncertainty related to hydraulic fracturing modeling in complex stress environments with pressure-dependent leakoff. *SPE Annual Technical Conference and Exhibition, 5-8 October, Denver, Colorado, USA.* Society of Petroleum Engineers.

JOHNSON, P.C. and JACKSON, R., 1987. Frictional–collisional constitutive relations for granular materials, with application to plane shearing. *Journal of Fluid Mechanics,* 176, pp. 67-93

JONES, W. and LAUNDER, B., 1972. The prediction of laminarization with a two-equation model of turbulence. *International Journal of Heat and Mass Transfer,* 15(2), pp. 301-314

KASSIS, S. andSONDERGELD, C.H., 2010. Fracture permeability of gas shale: Effect of roughness, fracture offset, proppant, and effective stress. *Paper SPE-131376-MS, International oil and gas conference and exhibition, 8-10 June, Beijing, China.* Society of Petroleum Engineers.

KERN, L., PERKINS, T. and WYANT, R., 1959. The mechanics of sand movement in fracturing. *Journal of Petroleum Technology,* 11(07), pp. 55-57

KESHAVARZI, R. and MOHAMMADI, S., 2012. A new approach for numerical modeling of hydraulic fracture propagation in naturally fractured reservoirs. *SPE/EAGE European Unconventional Resources Conference & Exhibition-From Potential to Production, 20-22 March, Vienna, Austria.*

KHOEI, A., VAHAB, M. and HIRMAND, M., 2016. Modeling the interaction between fluid-driven fracture and natural fault using an enriched-FEM technique. *International Journal of Fracture,* 197(1), pp. 1-24

KONG, B., FATHI, E. and AMERI, S., 2015. Coupled 3-D numerical simulation of proppant distribution and hydraulic fracturing performance optimization in Marcellus shale reservoirs. *International Journal of Coal Geology,* 147, pp. 35-45

KONG, X., MCANDREW, J. and CISTERNAS, P., 2016. CFD study of using foam fracturing fluid for proppant transport in hydraulic fractures. *Paper SPE-183549-MS, Abu Dhabi International Petroleum Exhibition & Conference, 7-10 November, Abu Dhabi, UAE.* Society of Petroleum Engineers.

KOSTENUK, N.H. andBROWNE, D.J., 2010. Improved proppant transport system for slick water shale fracturing. *Canadian Unconventional Resources and International Petroleum Conference.* Society of Petroleum Engineers.

KOU, R., MORIDIS, G.J. and BLASINGAME, T., 2018. Field Scale Proppant Transport Simulation and Its Application to Optimize Stimulation Strategy. *Paper URTEC-2878230-MS, SPE/AAPG/SEG Unconventional Resources Technology Conference, 23-25 July 2018, Houston, Texas, USA.* Society of Petroleum Engineers.

KURISON, C., KULELI, H.S. and MUBARAK, A.H., 2019. Unlocking well productivity drivers in Eagle Ford and Utica unconventional resources through data analytics. *Journal of Natural Gas Science and Engineering,* 71, pp. 102976

KURISON, C. et al., 2019. Reducing uncertainty in unconventional reservoir hydraulic fracture modeling: A case study in Saudi Arabia. *Journal of Natural Gas Science and Engineering,* 71, pp. 102948

LANGE, T. et al., 2013. Hydraulic fracturing in unconventional gas reservoirs: risks in the geological system part 1. *Environmental earth sciences,* 70(8), pp. 3839-3853

LECAMPION, B., 2009. An extended finite element method for hydraulic fracture problems. *Communications in Numerical Methods in Engineering,* 25(2), pp. 121-133

LI, P., ZHANG, X. and LU, X., 2018. Numerical simulation on solid-liquid two-phase flow in cross fractures. *Chemical Engineering Science,* 181, pp. 1-18

LI, T. and BENYAHIA, S., 2013. Evaluation of wall boundary condition parameters for gas–solids fluidized bed simulations. *AIChE Journal,* 59(10), pp. 3624-3632

LIU, Y., 2006. *Settling and hydrodynamic retardation of proppants in hydraulic fractures,*

LIU, Y. and SHARMA, M.M., 2005. Effect of fracture width and fluid rheology on proppant settling and retardation: an experimental study. *SPE annual technical conference and exhibition.* Society of Petroleum Engineers.

LOTH, E., 2010. *Particles, drops and bubbles: Fluid dynamics and numerical methods.* Cambridge University Press London.

LUN, C. et al., 1984. Kinetic theories for granular flow: inelastic particles in Couette flow and slightly inelastic particles in a general flowfield. *Journal of Fluid Mechanics,* 140, pp. 223-256

MACK, M., SUN, J. and KHADILKAR, C., 2014. Quantifying proppant transport in thin fluids: theory and experiments. *SPE Hydraulic Fracturing Technology Conference.* Society of Petroleum Engineers.

MAHDAVI, M., SHARIFPUR, M. and MEYER, J.P., 2015. CFD modelling of heat transfer and pressure drops for nanofluids through vertical tubes in laminar flow by Lagrangian and Eulerian approaches. *International Journal of Heat and Mass Transfer,* 88, pp. 803-813

MAKKAWI, Y.T., WRIGHT, P.C. and OCONE, R., 2006. The effect of friction and inter-particle cohesive forces on the hydrodynamics of gas–solid flow: a comparative analysis of theoretical predictions and experiments. *Powder Technology,* 163(1-2), pp. 69-79

MARINA, S. et al., 2015. Simulation of the hydraulic fracturing process of fractured rocks by the discrete element method. *Environmental Earth Sciences,* 73(12), pp. 8451-8469

MELENK, J.M. and BABUŠKA, I., 1996. The partition of unity finite element method: basic theory and applications. *Computer Methods in Applied Mechanics and Engineering,* 139(1-4), pp. 289-314

MENTER, F., 1993. Zonal two equation kw turbulence models for aerodynamic flows. *23rd fluid dynamics, plasmadynamics, and lasers conference.* pp. 2906

MOËS, N., DOLBOW, J. and BELYTSCHKO, T., 1999. A finite element method for crack growth without remeshing. *International Journal for Numerical Methods in Engineering,* 46(1), pp. 131-150

MOHAMMADNEJAD, T. and KHOEI, A., 2013. An extended finite element method for hydraulic fracture propagation in deformable porous media with the cohesive crack model. *Finite Elements in Analysis and Design,* 73, pp. 77-95

MOUKALLED, F., MANGANI, L. and DARWISH, M., 2016. The finite volume method in computational fluid dynamics. *An advanced introduction with OpenFoam® and Matlab®.Nueva York: Springer.Recuperado de http://www.gidropraktikum.narod.ru/Moukalled-et-al-FVM-*

OpenFOAM-Matlab.pdf,

MUDDE, R.F. and SIMONIN, O., 1999. Two-and three-dimensional simulations of a bubble plume using a two-fluid model. *Chemical Engineering Science,* 54(21), pp. 5061-5069

NGUYEN, V. et al., 2014. A combined numerical–experimental study on the effect of surface evolution on the water–sand multiphase flow characteristics and the material erosion behavior. *Wear,* 319(1-2), pp. 96-109

NIKOLOPOULOS, A. et al., 2017. Numerical investigation and comparison of coarse grain CFD–DEM and TFM in the case of a 1 MWth fluidized bed carbonator simulation. *Chemical Engineering Science,* 163, pp. 189-205

NOBLE, R. et al., 2019. FLUID FLOW THROUGH A FRACTURED POROUS RESERVOIR USING CFD MODELING. *Journal of Porous Media,* 22(5),

NORDGREN, R., 1972. Propagation of a vertical hydraulic fracture. *Society of Petroleum Engineers Journal,* 12(04), pp. 306-314

OGILVIE, S.R., ISAKOV, E. and GLOVER, P.W., 2006. Fluid flow through rough fractures in rocks. II: A new matching model for rough rock fractures. *Earth and Planetary Science Letters,* 241(3-4), pp. 454-465

OLSSON, R. and BARTON, N., 2001. An improved model for hydromechanical coupling during shearing of rock joints. *International Journal of Rock Mechanics and Mining Sciences,* 38(3), pp. 317-329

OSHER, S. and SETHIAN, J.A., 1988. Fronts propagating with curvature-dependent speed: algorithms based on Hamilton-Jacobi formulations. *Journal of computational physics,* 79(1), pp. 12-49

OSIPTSOV, A.A., 2017. Fluid mechanics of hydraulic fracturing: a review. *Journal of petroleum science and engineering,* 156, pp. 513-535

OUYANG, S., CAREY, G. and YEW, C., 1997. An adaptive finite element scheme for hydraulic fracturing with proppant transport. *International Journal for Numerical Methods in Fluids,* 24(7), pp. 645-670

PALISCH, T.T., VINCENT, M. and HANDREN, P.J., 2010. Slick water fracturing: food for

thought. *SPE Production & Operations,* 25(03), pp. 327-344

PATANKAR, N.A. and JOSEPH, D.D., 2001. Modeling and numerical simulation of particulate flows by the Eulerian–Lagrangian approach. *International Journal of Multiphase Flow,* 27(10), pp. 1659-1684

PATANKAR, N.A. et al., 2002. Power law correlations for sediment transport in pressure driven channel flows. *International Journal of Multiphase Flow,* 28(8), pp. 1269-1292

PATANKAR, S., 1980. *Numerical heat transfer and fluid flow.* CRC press.

PATEL, R.G. et al., 2017. Verification of Eulerian–Eulerian and Eulerian–Lagrangian simulations for turbulent fluid–particle flows. *AIChE Journal,* 63(12), pp. 5396-5412

PAUL, B. et al., 2018. 3D coupled HM–XFEM modeling with cohesive zone model and applications to non planar hydraulic fracture propagation and multiple hydraulic fractures interference. *Computer Methods in Applied Mechanics and Engineering,* 342, pp. 321-353

PEINKE, J. et al., 2006. *Progress in turbulence.* Springer Science & Business Media.

PEIRANO, E. and LECKNER, B., 1998. Fundamentals of turbulent gas-solid flows applied to circulating fluidized bed combustion. *Progress in Energy and Combustion Science,* 24(4), pp. 259-296

PEIRCE, A.P. and SIEBRITS, E., 2001. The scaled flexibility matrix method for the efficient solution of boundary value problems in 2D and 3D layered elastic media. *Computer Methods in Applied Mechanics and Engineering,* 190(45), pp. 5935-5956

PERKINS, T. and KERN, L., 1961. Widths of hydraulic fractures. *Journal of Petroleum Technology,* 13(09), pp. 937-949

PRESLEY, D. and TATARKO, J., 2009. *Principles of wind erosion and its control.* Kansas State University Agricultural Experiment Station and Cooperative Extension Service.

RABCZUK, T. et al., 2008. A new crack tip element for the phantom-node method with arbitrary cohesive cracks. *International Journal for Numerical Methods in Engineering,* 75(5), pp. 577-599

RASOULI, V. and HOSSEINIAN, A., 2011. Correlations developed for estimation of hydraulic parameters of rough fractures through the simulation of JRC flow channels. *Rock Mechanics and*

Rock Engineering, 44(4), pp. 447-461

RATERMAN, K.T. et al., 2018. Sampling a Stimulated Rock Volume: An Eagle Ford Example. *SPE Reservoir Evaluation & Engineering,* 21(04), pp. 927-941

REUGE, N. et al., 2008. Multifluid Eulerian modeling of dense gas–solids fluidized bed hydrodynamics: influence of the dissipation parameters. *Chemical Engineering Science,* 63(22), pp. 5540-5551

RIBEIRO, L.H.N., 2013. *Development of a three-dimensional compositional hydraulic fracturing simulator for energized fluids.* [online] Ph.D. thesis, The University of Texas at Austin.

RICCIO, A. et al., 2017. Modeling low velocity impact phenomena on composite structures. *Dynamic Response and Failure of Composite Materials and Structures.* Elsevier. pp. 129-158

RICHARDSON, J. and ZAKI, W., 1954. The sedimentation of a suspension of uniform spheres under conditions of viscous flow. *Chemical Engineering Science,* 3(2), pp. 65-73

ROOSTAEI, M. et al., 2018. Numerical simulation of proppant transport in hydraulic fractures. *Journal of Petroleum Science and Engineering,* 163, pp. 119-138

SABERHOSSEINI, S.E., AHANGARI, K. and MOHAMMADREZAEI, H., 2019. Optimization of the horizontal-well multiple hydraulic fracturing operation in a low-permeability carbonate reservoir using fully coupled XFEM model. *International Journal of Rock Mechanics and Mining Sciences,* 114, pp. 33-45

SAGAUT, P. and CAMBON, C., 2008. *Homogeneous turbulence dynamics.* Springer.

SAHAI, R., MISKIMINS, J.L. and OLSON, K.E., 2014. Laboratory results of proppant transport in complex fracture systems. *Paper SPE-168579-MS, SPE Hydraulic Fracturing Technology Conference, 4-6 February, The Woodlands, Texas, USA.* Society of Petroleum Engineers.

SANKARANARAYANAN, K. et al., 2002. Analysis of drag and virtual mass forces in bubbly suspensions using an implicit formulation of the lattice Boltzmann method. *Journal of Fluid Mechanics,* 452, pp. 61-96

SAVAGE, S. and JEFFREY, D., 1981. The stress tensor in a granular flow at high shear rates. *Journal of Fluid Mechanics,* 110, pp. 255-272

SCHOLS, R. andVISSER, W., 1974. Proppant bank buildup in a vertical fracture without fluid loss. *Paper SPE-4834-MS, SPE European Spring Meeting, 29-30 May, Amsterdam, Netherlands.* Society of Petroleum Engineers.

SETTARI, A., PUCHYR, P. and BACHMAN, R., 1990. Partially decoupled modeling of hydraulic fracturing processes. *SPE Production Engineering,* 5(01), pp. 37-44

SHAH, S.N., ASADI, M. and LORD, D.L., 1998. Proppant transport characterization of hydraulic fracturing fluids using a high pressure simulator integrated with a fiber optic/LED vision system. *SPE Annual Technical Conference and Exhibition.* Society of Petroleum Engineers.

SHAOUL, J.R., ROSS, M.J., SPITZER, W.J., WHEATON, S.R., MAYLAND, P.J. and SINGH, A.P., 2007. Massive hydraulic fracturing unlocks deep tight gas reserves in India. *European Formation Damage Conference, 30 May-1 June, Scheveningen, The Netherlands.* Society of Petroleum Engineers.

SHARMA, M.M. and GADDE, P.B., 2005. The impact of proppant retardation on propped fracture lengths. *SPE Annual Technical Conference and Exhibition.* Society of Petroleum Engineers.

SHI, F. et al., 2017. An XFEM-based method with reduction technique for modeling hydraulic fracture propagation in formations containing frictional natural fractures. *Engineering Fracture Mechanics,* 173, pp. 64-90

SIDDHAMSHETTY, P. et al., 2018. Feedback control of proppant bank heights during hydraulic fracturing for enhanced productivity in shale formations. *AIChE Journal,* 64(5), pp. 1638-1650

SIEBRITS, E. and PEIRCE, A.P., 2002. An efficient multi-layer planar 3D fracture growth algorithm using a fixed mesh approach. *International Journal for Numerical Methods in Engineering,* 53(3), pp. 691-717

SIMONIN, O. and VIOLLET, P., 1990. Modelling of turbulent two-phase jets loaded with discrete particles. *Phenomena in multiphase flows,* 1990, pp. 259-269

SIMONSON, E., ABOU-SAYED, A. and CLIFTON, R., 1978. Containment of massive hydraulic fractures. *Society of Petroleum Engineers Journal,* 18(01), pp. 27-32

SINGH, J.P., KUMAR, S. and MOHAPATRA, S., 2017. Modelling of two phase solid-liquid

flow in horizontal pipe using computational fluid dynamics technique. *International Journal of Hydrogen Energy,* 42(31), pp. 20133-20137

SINHA, N., 2013. *Towards RANS Parameterization of Vertical Mixing by Langmuir Turbulence in Shallow Coastal Shelves.* [online] Ph.D. thesis, University of South Florida. Available from: https://scholarcommons.usf.edu/etd/4945/

SMITH, M., BALE, A., BRITT, L., HAINEY, B. and KLEIN, H., 1997. Enhanced 2D Proppant Transport Simulation: The Key to Understanding Proppant Flowback and Post-Frac Productivity. *SPE Annual Technical Conference and Exhibition.* Society of Petroleum Engineers.

SPEIGHT, J.G., 2016a. *Handbook of Hydraulic Fracturing.* Wiley Online Library.

SPEIGHT, J.G., 2016b. *Deep shale oil and gas.* Gulf Professional Publishing.

STOLARSKA, M. et al., 2001. Modelling crack growth by level sets in the extended finite element method. *International Journal for Numerical Methods in Engineering,* 51(8), pp. 943-960

SUBRAMANIAM, S., 2013. Lagrangian–Eulerian methods for multiphase flows. *Progress in Energy and Combustion Science,* 39(2-3), pp. 215-245

SUKUMAR, N. and PRÉVOST, J., 2003. Modeling quasi-static crack growth with the extended finite element method Part I: Computer implementation. *International Journal of Solids and Structures,* 40(26), pp. 7513-7537

SURI, Y., ISLAM, S.Z. and HOSSAIN, M., 2019. A new CFD approach for proppant transport in unconventional hydraulic fractures. *Journal of Natural Gas Science and Engineering,* , pp. 102951

SURI, Y., ISLAM, S.Z. and HOSSAIN, M., 2020a. Numerical modelling of proppant transport in hydraulic fractures. *Fluid Dynamics & Material Processing,* 16(2), pp. 297-337

SURI, Y., ISLAM, S.Z. and HOSSAIN, M., 2020b. Effect of Fracture Roughness on the hydrodynamics of proppant transport in hydraulic fractures. *Journal of natural gas science and engineering,* , pp. 103401

SURI, Y., ISLAM, S.Z. and HOSSAIN, M., 2020c. Proppant transport in dynamically

propagating hydraulic fractures using CFD-XFEM approach. *International Journal of Rock Mechanics and Mining Sciences,* 131

SWAN, J.W. and BRADY, J.F., 2010. Particle motion between parallel walls: Hydrodynamics and simulation. *Physics of Fluids,* 22(10), pp. 103301

TALEGHANI, A.D. andOLSON, J.E., 2009. Analysis of multistranded hydraulic fracture propagation: an improved model for the interaction between induced and natural fractures. *SPE Annual Technical Conference and Exhibition, 4-7 October, New Orleans, Louisiana.* Society of Petroleum Engineers.

TAN, Q., 2011. *Dimensional analysis: with case studies in mechanics.* Springer Science & Business Media.

TEBOWEI, R., 2017. *Computational fluid dynamics (CFD) modelling of critical velocity for sand transport flow regimes in multiphase pipe bends.* [online] Ph.D. thesis, Robert Gordon University, Aberdeen.

TOMAC, I. and GUTIERREZ, M., 2014. *Fluid lubrication effects on particle flow and transport in a channel.*

TOMAR, V., ZHAI, J. and ZHOU, M., 2004. Bounds for element size in a variable stiffness cohesive finite element model. *International Journal for Numerical Methods in Engineering,* 61(11), pp. 1894-1920

TONG, S. andMOHANTY, K., 2017. Proppant Placement in Secondary Fractures. *Paper URTEC-2671549-MS, SPE/AAPG/SEG Unconventional Resources Technology Conference, 24-26 July, Austin, Texas, USA.* Society of Exploration Geophysicists, American Association of Petroleum Geologists, Society of Petroleum Engineers. pp. 1907-1918

TONG, S. and MOHANTY, K.K., 2016. Proppant transport study in fractures with intersections. *Fuel,* 181, pp. 463-477

TONG, S., SINGH, R. and MOHANTY, K.K., 2017. Proppant Transport in Fractures with Foam-Based Fracturing Fluids. *Paper SPE-187376-MS, SPE Annual Technical Conference and Exhibition, 9-11 October, San Antonio, Texas, USA.* Society of Petroleum Engineers.

TONG, S., SINGH, R. and MOHANTY, K.K., 2018. A visualization study of proppant transport in foam fracturing fluids. *Journal of Natural Gas Science and Engineering,* 52, pp. 235-247

TRYGGVASON, G. et al., 2001. A front-tracking method for the computations of multiphase flow. *Journal of computational physics,* 169(2), pp. 708-759

TSAI, K. et al., 2012. Advanced computational modeling of proppant settling in water fractures for shale gas production. *SPE Journal,* 18(01), pp. 50-56

VAN WACHEM, B. and ALMSTEDT, A., 2003. Methods for multiphase computational fluid dynamics. *Chemical Engineering Journal,* 96(1-3), pp. 81-98

VERSTEEG, H.K. and MALALASEKERA, W., 2007. *An introduction to computational fluid dynamics: the finite volume method.* Pearson Education.

WACHEM, B.G.M.V. et al., 2001. Comparative analysis of CFD models of dense gas–solid systems. *AIChE Journal,* 47(5), pp. 1035-1051

WANG, H., 2015. Numerical modeling of non-planar hydraulic fracture propagation in brittle and ductile rocks using XFEM with cohesive zone method. *Journal of Petroleum Science and Engineering,* 135, pp. 127-140

WANG, J., 2020. Continuum theory for dense gas-solid flow: A state-of-the-art review. *Chemical Engineering Science,* 215, pp. 115428

WANG, J., ELSWORTH, D. and MA, T., 2018. Conductivity evolution of proppant-filled hydraulic fractures. *Paper ARMA-2018-111, 52nd U.S. Rock Mechanics/Geomechanics Symposium, 17-20 June, Seattle, Washington.* American Rock Mechanics Association.

WANG, J., ELSWORTH, D. and DENISON, M.K., 2018. Propagation, proppant transport and the evolution of transport properties of hydraulic fractures. *Journal of Fluid Mechanics,* 855, pp. 503-534

WANG, J. et al., 2003. Bi-power law correlations for sediment transport in pressure driven channel flows. *International Journal of Multiphase Flow,* 29(3), pp. 475-494

WARPINSKI, N.R. et al., 2009. Stimulating unconventional reservoirs: maximizing network growth while optimizing fracture conductivity. *Journal of Canadian Petroleum Technology,* 48(10), pp. 39-51

WEN, C. and YU, Y., 1966. A generalized method for predicting the minimum fluidization velocity. *AIChE Journal,* 12(3), pp. 610-612

WENG, X. et al., 2011. Modeling of hydraulic-fracture-network propagation in a naturally fractured formation. *SPE Production & Operations,* 26(04), pp. 368-380

WU, C. and SHARMA, M.M., 2016. Effect of Perforation Geometry and Orientation on Proppant Placement in Perforation Clusters in a Horizontal Well. *Paper SPE-179117-MS, SPE Hydraulic Fracturing Technology Conference, 9-11 February, The Woodlands, Texas, USA.* Society of Petroleum Engineers.

WU, K., 2014. *Numerical modeling of complex hydraulic fracture development in unconventional reservoirs.* [online] Ph.D. thesis, The University of Texas at Austin.

WU, Y., 2015. *Multiphase fluid flow in porous and fractured reservoirs.* Gulf Professional Publishing.

XU, Y. and SUBRAMANIAM, S., 2010. Effect of particle clusters on carrier flow turbulence: A direct numerical simulation study. *Flow, Turbulence and Combustion,* 85(3-4), pp. 735-761

YAN, H. et al., 2019. Solid-Liquid Flow of Axial Flow Pump in Loop Reactor and Operating Control with Single Invert. *International Journal of Simulation Modelling,* 18(3), pp. 464-475

YANG, S., SIDDHAMSHETTY, P. and KWON, J.S., 2017. Optimal pumping schedule design to achieve a uniform proppant concentration level in hydraulic fracturing. *Computers & Chemical Engineering,* 101, pp. 138-147

YANG, T. et al., 2004. Influence of heterogeneity of mechanical properties on hydraulic fracturing in permeable rocks. *Rock Mechanics and Rock Engineering,* 37(4), pp. 251-275

YAO, Y., LIU, L. and KEER, L.M., 2015. Pore pressure cohesive zone modeling of hydraulic fracture in quasi-brittle rocks. *Mechanics of Materials,* 83, pp. 17-29

YEW, C.H. and WENG, X., 2014. *Mechanics of hydraulic fracturing.* Gulf Professional Publishing.

YI, S.S., WU, C. and SHARMA, M.M., 2018. Proppant Distribution Among Multiple Perforation Clusters in Plug-and-Perforate Stages. *SPE Production & Operations,* 33(04), pp. 654-665

ZENG, J., LI, H. and ZHANG, D., 2016. Numerical simulation of proppant transport in hydraulic fracture with the upscaling CFD-DEM method. *Journal of Natural Gas Science and*

Engineering, 33, pp. 264-277

ZHAN, J., SEETAHAL, S., CAO, J., HEJAZI, H., ALEXANDER, D., HE, R., ZHANG, K. and CHEN, Z., 2016. An Integrated Method to Characterize Shale Gas Reservoir Performance. *SPE Trinidad and Tobago Section Energy Resources Conference, 13-15 June, Port of Spain, Trinidad and Tobago*. Society of Petroleum Engineers.

ZHANG, G. and CHAO, K., 2018. Downward flow of proppant slurry through curving pipes during horizontal well fracturing. *Oil & Gas Science and Technology–Revue d'IFP Energies nouvelles,* 73, pp. 31

ZHANG, G., GUTIERREZ, M. and CHAO, K., 2019. Hydrodynamic and mechanical behavior of multi-particle confined between two parallel plates. *Advanced Powder Technology,* 30(2), pp. 439-450

ZHANG, G., GUTIERREZ, M. and LI, M., 2017. A coupled CFD-DEM approach to model particle-fluid mixture transport between two parallel plates to improve understanding of proppant micromechanics in hydraulic fractures. *Powder Technology,* 308, pp. 235-248

ZHANG, G., LI, M. and GUTIERREZ, M., 2016. Numerical simulation of proppant distribution in hydraulic fractures in horizontal wells. *Journal of Natural Gas Science and Engineering,*

ZHANG, G., LI, M. and GUTIERREZ, M., 2017. Simulation of the transport and placement of multi-sized proppant in hydraulic fractures using a coupled CFD-DEM approach. *Advanced Powder Technology,* 28(7), pp. 1704-1718

ZHANG, G. et al., 2015. Wall effects on spheres settling through non-Newtonian fluid media in cylindrical tubes. *Journal of Dispersion Science and Technology,* 36(9), pp. 1199-1207

ZHANG, J. and DUNN-NORMAN, S., 2015. Computational fluid dynamics (CFD) modeling of proppant transport in a plug and perf completion with different perforation phasing. *Paper URTEC-2169184-MS, Unconventional Resources Technology Conference, 20-22 July 2015, San Antonio, Texas, USA*. Society of Petroleum Engineers.

ZHANG, M., WU, C. and SHARMA, M., 2019. Proppant Placement in Perforation Clusters in Deviated Wellbores. *SPE/AAPG/SEG Unconventional Resources Technology Conference.* Unconventional Resources Technology Conference.

ZHANG, T. and SUN, S., 2019. A coupled Lattice Boltzmann approach to simulate gas flow and

transport in shale reservoirs with dynamic sorption. *Fuel,* 246, pp. 196-203

ZHANG, G.M. et al., 2010. Three-dimensional finite element simulation and parametric study for horizontal well hydraulic fracture. *Journal of Petroleum Science and Engineering,* 72(3–4), pp. 310-317

ZHELTOV, Y.P. andKHRISTIANOVIC, S.A., 1955. Formation of vertical fractures by means of highly viscous liquid. *4th world petroleum congress, 6-15 June, Rome, Italy.* World Petroleum Congress.

ZHIGAREV, V., MINAKOV, A., PLATONOV, D., DEKTEREV, D. and PRYAZHNIKOV, M., 2017. Testing of numerical simulation technique of concentrated suspensions agitation. *EPJ Web of Conferences.* EDP Sciences. pp. 00053

ZHONG, H. et al., 2015. The difference between specularity coefficient of 1 and no-slip solid phase wall boundary conditions in CFD simulation of gas–solid fluidized beds. *Powder Technology,* 286, pp. 740-743

ZHOU, L. and HOU, M.Z., 2013. A new numerical 3D-model for simulation of hydraulic fracturing in consideration of hydro-mechanical coupling effects. *International Journal of Rock Mechanics and Mining Sciences,* 60, pp. 370-380

ZIENKIEWICZ, O.C., TAYLOR, R.L. and ZHU, J., 2013. *The Finite Element Method: Its Basis and Fundamentals.* Butterworth-Heinemann.

Appendix A: User Defined Function (UDF) Code

```
/*
Title: User Defined Function Code - Fluid Leak-off from the fracture sidewall
Written by: Yatin Suri, Robert Gordon University, Aberdeen, U.K.
*/

# include "udf.h"

DEFINE_SOURCE(xmom_sourceC,c,t,dS,eqn)
{
real x[ND_ND];
real source;
float d;
float con;
cell_t c;

if (THREAD_ID(t) == 5) /* sidewall 1 */
{
begin_c_loop(c,t)
{
C_CENTROID(x,c,t);
d = x[0];
if (d<0.25)
{
con = (-0.1487*d+0.1407); /* fluid leak-off rate profile */
source = -1000*con*C_U(c,t)/C_VOLUME(c,t); /* fluid density = 1000 Kg/m3 */
dS[eqn] = -1000*con/C_VOLUME(c,t);
return source;
}
else
{
con = (-0.0637*d+0.0671);
source = -1000*con*C_U(c,t)/C_VOLUME(c,t);
dS[eqn] = -1000*con/C_VOLUME(c,t);
return source;
```

```
}
}
end_c_loop(c,t)
}
else if (THREAD_ID(t) == 9) /* sidewall 2 */
{
begin_c_loop(c,t)
{
C_CENTROID(x,c,t);
d = x[0];
if (d<0.25)
{
        con = (-0.1487*d+0.1407);
        source = -1000*con*C_U(c,t)/C_VOLUME(c,t);
        dS[eqn] = -1000*con/C_VOLUME(c,t);
        return source;
}
else
{
        con = (-0.0637*d+0.0671);
        source = -1000*con*C_U(c,t)/C_VOLUME(c,t);
        dS[eqn] = -1000*con/C_VOLUME(c,t);
        return source;
}
}
end_c_loop(c,t)
}
}

DEFINE_SOURCE(ymom_sourceC,c,t,dS,eqn)
{
        real x[ND_ND];
        real source;
        float d;
        float con;
        cell_t c;
```

```
if (THREAD_ID(t) == 5) /* sidewall 1 */
{
	begin_c_loop(c,t)
	{
		C_CENTROID(x,c,t);
		d = x[0];
		if (d<0.25)
		{
			con = (-0.1487*d+0.1407);
			source = -1000*con*C_V(c,t)/C_VOLUME(c,t);
			dS[eqn] = -1000*con/C_VOLUME(c,t);
			return source;
		}
		else
		{
			con = (-0.0637*d+0.0671);
			source = -1000*con*C_V(c,t)/C_VOLUME(c,t);
			dS[eqn] = -1000*con/C_VOLUME(c,t);
			return source;
		}
	}
	end_c_loop(c,t)
}
else if (THREAD_ID(t) == 9) /* sidewall 2 */
{
	begin_c_loop(c,t)
	{
		C_CENTROID(x,c,t);
		d = x[0];
		if (d<0.25)
		{
			con = (-0.1487*d+0.1407);
			source = -1000*con*C_V(c,t)/C_VOLUME(c,t);
			dS[eqn] = -1000*con/C_VOLUME(c,t);
			return source;
		}
		else
```

```
                {
                        con = (-0.0637*d+0.0671);
                        source = -1000*con*C_V(c,t)/C_VOLUME(c,t);
                        dS[eqn] = -1000*con/C_VOLUME(c,t);
                        return source;
                }
        }
        end_c_loop(c,t)
    }
}
DEFINE_SOURCE(zmom_sourceC,c,t,dS,eqn)
{
    real x[ND_ND];
    real source;
    float d;
    float con;
    cell_t c;

    if (THREAD_ID(t) == 5) /* sidewall 1 */
    {
        begin_c_loop(c,t)
        {
            C_CENTROID(x,c,t);
            d = x[0];
            if (d<0.25)
            {
                con = (-0.1487*d+0.1407);
                source = -1000*con*C_W(c,t)/C_VOLUME(c,t);
                dS[eqn] = -1000*con/C_VOLUME(c,t);
                return source;
            }
            else
            {
                con = (-0.0637*d+0.0671);
                source = -1000*con*C_W(c,t)/C_VOLUME(c,t);
                dS[eqn] = -1000*con/C_VOLUME(c,t);
                return source;
```

```
                }
            }
            end_c_loop(c,t)
        }
        else if (THREAD_ID(t) == 9) /* sidewall 2 */
        {
            begin_c_loop(c,t)
            {
                C_CENTROID(x,c,t);
                d = x[0];
                if (d<0.25)
                {
                    con = (-0.1487*d+0.1407);
                    source = -1000*con*C_W(c,t)/C_VOLUME(c,t);
                    dS[eqn] = -1000*con/C_VOLUME(c,t);
                    return source;
                }
                else
                {
                    con = (-0.0637*d+0.0671);
                    source = -1000*con*C_W(c,t)/C_VOLUME(c,t);
                    dS[eqn] = -1000*con/C_VOLUME(c,t);
                    return source;
                }
            }
            end_c_loop(c,t)
        }
}

DEFINE_SOURCE(mass_sourceC,c,t,dS,eqn)
{
real x[ND_ND];
real source;
float d;
float con;
cell_t c;
```

```
if (THREAD_ID(t) == 5) /* sidewall 1 */
{
begin_c_loop(c,t)
{
C_CENTROID(x,c,t);
d = x[0];
if (d<0.25)
{
con = (-0.1487*d+0.1407);
source = -1000*con/C_VOLUME(c,t);
dS[eqn] = -1000*con/(C_W(c,t)*C_VOLUME(c,t));
return source;
}
else
{
con = (-0.0637*d+0.0671);
source = -1000*con/C_VOLUME(c,t);
dS[eqn] = -1000*con/(C_W(c,t)*C_VOLUME(c,t));
return source;
}
}
end_c_loop(c,t)
}
else if (THREAD_ID(t) == 9) /* sidewall 2 */
{
        begin_c_loop(c,t)
        {
                C_CENTROID(x,c,t);
                d = x[0];
                if (d<0.25)
                {
                        con = (-0.1487*d+0.1407);
                        source = -1000*con/C_VOLUME(c,t);
                        dS[eqn] = -1000*con/(C_W(c,t)*C_VOLUME(c,t));
                        return source;
                }
                else
```

```
            {
                con = (-0.0637*d+0.0671);
                source = -1000*con/C_VOLUME(c,t);
                dS[eqn] = -1000*con/(C_W(c,t)*C_VOLUME(c,t));
                return source;
            }
        }
        end_c_loop(c,t)
}
}
```

Appendix B: Code for hydraulic fracture propagation using XFEM in Abaqus

```
*Heading
**
** Title: Code for Fracture Propagation Model using XFEM in 3D
** Written by: Yatin Suri, Robert Gordon University, Aberdeen, U.K.
**
** Important note- Units are in kN, kPa and m
**
*Preprint, echo=NO, model=NO, history=NO, contact=NO
**
*Node, nset=nall
     1,  80.62257390,    0.00000000,   -0.50000000
     2,  11.00000000,    0.00000000,   -0.50000000
     3,  10.00000000,   -1.00000000,   -0.50000000
     4,  10.00000000,  -80.00000000,   -0.50000000
     5,  10.00000000,    1.00000000,   -0.50000000
     6,   0.00000000,    1.00000000,   -0.50000000
     7,  10.00000000,   80.00000000,   -0.50000000
     8,   0.00000000,   80.00000000,   -0.50000000
     9,   0.00000000,   -1.00000000,   -0.50000000
    10,   0.00000000,  -80.00000000,   -0.50000000
    11,  71.32070160,    0.00000000,   -0.50000000
    12,  63.24361420,    0.00000000,   -0.50000000
    13,  56.23004150,    0.00000000,   -0.50000000
    14,  50.13994980,    0.00000000,   -0.50000000
    15,  44.85174560,    0.00000000,   -0.50000000
    16,  40.25984570,    0.00000000,   -0.50000000
    17,  36.27256010,    0.00000000,   -0.50000000
    18,  32.81028750,    0.00000000,   -0.50000000
    19,  29.80389210,    0.00000000,   -0.50000000
    20,  27.19335170,    0.00000000,   -0.50000000
    21,  24.92654230,    0.00000000,   -0.50000000
    22,  22.95820620,    0.00000000,   -0.50000000
    23,  21.24904250,    0.00000000,   -0.50000000
```

** not all nodes shown here for thesis

29500,	7.30839682,	-1.58381224,	0.00000000
29501,	7.11702728,	-1.58625770,	0.00000000
29502,	6.92277384,	-1.58581769,	0.00000000
29503,	6.72716713,	-1.58392525,	0.00000000
29504,	9.14244938,	-1.56609857,	0.00000000
29505,	9.31418133,	-1.62503588,	0.00000000
29506,	2.02526832,	-1.61477852,	0.00000000
29507,	2.59170699,	-1.60884953,	0.00000000
29508,	0.67754132,	-1.69337094,	0.00000000
29509,	7.88044405,	-1.59048343,	0.00000000
29510,	2.19526315,	-1.63143659,	0.00000000
29511,	2.38420486,	-1.62971568,	0.00000000
29512,	9.51877880,	-1.65878534,	0.00000000
29513,	0.46630436,	-1.68801403,	0.00000000
29514,	8.28288269,	-1.43081844,	0.00000000
29515,	1.62183774,	-1.43045950,	0.00000000
29516,	1.81304348,	-1.41970789,	0.00000000
29517,	8.84746838,	-1.38358915,	0.00000000

** not all nodes shown here for thesis

29980,	6.37959909,	-3.50799680,	0.00000000
29981,	2.67612839,	-2.90767217,	0.00000000
29982,	2.71996284,	-2.47821212,	0.00000000
29983,	4.51514769,	-4.52934885,	0.00000000
29984,	2.75553370,	-2.30482078,	0.00000000
29985,	4.26919746,	-4.30719423,	0.00000000
29986,	7.09932804,	-2.59978676,	0.00000000
29987,	6.50412035,	-2.38594460,	0.00000000
29988,	4.04924202,	-2.46942711,	0.00000000
29989,	3.45548344,	-2.45594764,	0.00000000
29990,	2.91662550,	-2.32353568,	0.00000000
29991,	2.92209220,	-2.70642257,	0.00000000
29992,	5.77452278,	-4.24255943,	0.00000000

```
29993,    4.41620922,   -3.40661192,    0.00000000
29994,    4.33618069,   -3.14331579,    0.00000000
29995,    6.04040194,   -3.33232164,    0.00000000
29996,    5.91486168,   -3.79355192,    0.00000000
29997,    4.07312059,   -2.98121381,    0.00000000
29998,    6.12655449,   -2.43644643,    0.00000000
29999,    5.85310745,   -2.44149470,    0.00000000
*Element, type=C3D8RP,elset=solid_eall
  1,     1,    11,   306,    86,  10001,  10011,  10306,  10086
  2,    11,    12,   307,   306,  10011,  10012,  10307,  10306
  3,    12,    13,   308,   307,  10012,  10013,  10308,  10307
  4,    13,    14,   309,   308,  10013,  10014,  10309,  10308
  5,    14,    15,   310,   309,  10014,  10015,  10310,  10309
  6,    15,    16,   311,   310,  10015,  10016,  10311,  10310
  7,    16,    17,   312,   311,  10016,  10017,  10312,  10311
  8,    17,    18,   313,   312,  10017,  10018,  10313,  10312
  9,    18,    19,   314,   313,  10018,  10019,  10314,  10313
 10,    19,    20,   315,   314,  10019,  10020,  10315,  10314
 11,    20,    21,   316,   315,  10020,  10021,  10316,  10315
 12,    21,    22,   317,   316,  10021,  10022,  10317,  10316
 13,    22,    23,   318,   317,  10022,  10023,  10318,  10317
 14,    23,    24,   319,   318,  10023,  10024,  10319,  10318
 15,    24,    25,   320,   319,  10024,  10025,  10320,  10319
 16,    25,    26,   321,   320,  10025,  10026,  10321,  10320
 17,    26,    27,   322,   321,  10026,  10027,  10322,  10321
 18,    27,    28,   323,   322,  10027,  10028,  10323,  10322
 19,    28,    29,   324,   323,  10028,  10029,  10324,  10323
 20,    29,    30,   325,   324,  10029,  10030,  10325,  10324

** not all elements shown here for thesis

12353,   29794,   29793,   29714,   29704,   29794,   29793,   29714,   29704
12354,   29695,   29716,   29793,   29794,   29695,   29716,   29793,   29794
12355,   29902,   29795,   29712,   29705,   29902,   29795,   29712,   29705
12356,   29647,   29661,   29679,   29678,   29647,   29661,   29679,   29678
12357,   29651,   29683,   29797,   29675,   29651,   29683,   29797,   29675
12358,   29798,   29599,   29601,   29642,   29798,   29599,   29601,   29642
```

```
 12359,   29900,   29644,   29672,   29696,  29900,  29644,  29672,  29696
 12360,   29705,   29904,   29673,   29908,  29705,  29904,  29673,  29908
 12361,   29905,   29902,   29705,   29908,  29905,  29902,  29705,  29908
 12362,   29718,   29905,   29908,   29706,  29718,  29905,  29908,  29706
**
*Nset, nset=_PickedSet13
   1,  4,  7,  8, 10, 78, 79, 80, 81, 82, 83, 84, 85, 86, 269, 270
 271, 272, 273, 274, 275, 276, 10001,   10004,   10007,   10008, 10010
 10078, 10079, 10080, 10081, 10082, 10083, 10084, 10085, 10086, 10269
 10270, 10271, 10272, 10273, 10274, 10275, 10276, 20001,   20004,   20007,   20008, 20020
 20078, 20079, 20080, 20081, 20082, 20083, 20084, 20085, 20086, 20269
 20270, 20271, 20272, 20273, 20274, 20275, 20276, 29001,   29004,   29007,   29008, 29029
 29078, 29079, 29080, 29081, 29082, 29083, 29084, 29085, 29086, 29269
 29270, 29271, 29272, 29273, 29274, 29275, 29276,
*Nset, nset=_PickedSet14
   6,  8,  9, 10, 182, 183, 184, 185, 186, 187, 188, 189, 190, 191, 192, 193
 194, 195, 196, 197, 198, 199, 200, 201, 202, 203, 204, 205, 206, 207, 208, 209
 210, 211, 212, 213, 214, 215, 216, 217, 218, 277, 278, 279, 280, 281, 282, 283
 284, 285, 286, 287, 288, 289, 290, 291, 292, 293, 294, 295, 296, 297, 298, 299
 300, 301, 302, 303, 304, 305
 10006, 10008, 10009, 10010, 10182, 10183, 10184, 10185, 10186, 10187, 10188
 10189, 10190, 10191, 10192, 10193, 10194, 10195, 10196, 10197, 10198, 10199
 10200, 10201, 10202, 10203, 10204, 10205, 10206, 10207, 10208, 10209, 10210
 10211, 10212, 10213, 10214, 10215, 10216, 10217, 10218, 10277, 10278, 10279
 10280, 10281, 10282, 10283, 10284, 10285, 10286, 10287, 10288, 10289, 10290
 10291, 10292, 10293, 10294, 10295, 10296, 10297, 10298, 10299, 10300, 10301
 10302, 10303, 10304, 10305
 29200, 29201, 29202, 29203, 29204, 29205, 29206, 29207, 29208, 29209, 29229
 29211, 29212, 29213, 29214, 29215, 29216, 29217, 29218, 29277, 29278, 29279
 29280, 29281, 29282, 29283, 29284, 29285, 29286, 29287, 29288, 29289, 29290
 29291, 29292, 29293, 29294, 29295, 29296, 29297, 29298, 29299, 29300, 29301
 29302, 29303, 29304, 29305
*enrichment,elset=solid_eall,interaction=lower,type=propagation crack, name=abc
*Solid Section, elset=solid_eall, material=Material-1, CONTROLS=CTR
**SECTION CONTROLS,NAME=CTR,INITIAL GAP OPENING=0.002
**
** MATERIALS
```

```
**
*Material, name=Material-1
*Elastic
27.2e+06, 0.22
*Permeability, specific=9.8
2.0e-8,0.1
*GAP FLOW
1.e-6
*FLUID LEAKOFF
 5.0e-10, 5.0e-10
*DAMAGE INITIATION,CRITERION=MAXS,tol=0.2
320.,320.,320.
*DAMAGE EVOLUTION,TYPE=ENERGY,MIXED MODE BEHAVIOR=BK,POWER=2.284
28.,28.,28.
*DAMAGE STABILIZATION
 1.e-5
**
*surface interaction,name=lower
1,0
** specific gravity of water
**
**
*INITIAL CONDITIONS, TYPE=RATIO
 nall,0.1
** Initial Porosity is 10%
*INITIAL CONDITIONS, TYPE=PORE
 nall, 23.46e+3
**
*INITIAL CONDITIONS, TYPE=STRESS
solid_eall, 47.61e+3, -54.42e+3, -40.81e+3
**
*initial condition,type=enrichment
1235,1,abc, 1.0, 0.0
1235,2,abc, 1.0,-1.0
1235,3,abc,-1.0,-1.0
1235,4,abc,-1.0, 0.0
```

```
1235,5,abc, 1.0, 0.0
1235,6,abc, 1.0,-1.0
1235,7,abc,-1.0,-1.0
1235,8,abc,-1.0, 0.0
**
*elset,elset=one
1235
**
** BOUNDARY CONDITIONS
**
** Name: BC-1 Type: Displacement/Rotation
*Boundary
_PickedSet13, 1, 1
_PickedSet13, 2, 2
nall, 3, 3
** Name: BC-2 Type: Displacement/Rotation
*Boundary
_PickedSet14, 1, 1
**
*Boundary,phantom=node
214  , 1,1
215  , 1,1
10214, 1,1
10215, 1,1
214  , 3,3
215  , 3,3
10214, 3,3
10215, 3,3
**
**
** STEP: Step-1
**
*Step, name=Step-1, nlgeom=YES, unsymm=YES
*geostatic
**
** Name: BC-2 Type: Pore pressure
*Boundary
```

```
_PickedSet13, 8, 8, 23.46e+3
**
** OUTPUT REQUESTS
**
** FIELD OUTPUT: F-Output-1
**
*Output, field
*node output
U,POR,PHILSM
*element output
S
**
*End Step
**
** STEP: Step-2
**
*Step, name=Step-2, nlgeom=YES, inc=1000000, unsymm=YES
*Soils, consolidation, end=PERIOD, utol=100000.00
** time in seconds
0.5, 1200., 0.000001, 10.0,
**
*cflow,phantom=edge
  214,  215,-0.0025
10214,10215,-0.0025
**
** Name: BC-2 Type: Pore pressure
*Boundary
_PickedSet13, 8, 8, 23.46e+3

**
** OUTPUT REQUESTS
**
** FIELD OUTPUT: F-Output-1
**
*Output, field, freq=200
*node output
U,
```

```
**POR,
PHILSM
*element output
S
PFOPENXFEM
LEAKVRTXFEM
LEAKVRBXFEM
ALEAKVRTXFEM
ALEAKVRBXFEM
PORPRES
GFVRXFEM
**
*Output, history,freq=20
*element output,elset=one
**PFOPENXFEM
LEAKVRTXFEM
**LEAKVRBXFEM
**ALEAKVRTXFEM
**ALEAKVRBXFEM
PORPRES
**GFVRXFEM
*End Step
```

Appendix C: Comparison of Eulerian-Granular model, CFD-DEM Model and DDPM model with the Experimental study

To compare the different numerical models of proppant transport in hydraulic fractures, all the three models namely Eulerian-Granular model, DEM Model and DDPM model are compared with the experimental results of Tong and Mohanty (2016) using the same experimental parameters and properties detailed in Table 4.1. Figure C.1 shows the comparison of all the three models with the experimental results for three different injection velocities 0.1 m/s, 0.2 m/s and 0.3 m/s after 20 s of injection time. Figure C.1 also shows the percentage error bars with the experimental results of ±10% in order to compare the results. It can be noted from Figure C.1 that the DEM model predicts the proppant distribution within ±10% of experimental results for all the three case of injection velocities. However, the DDPM model has a percentage error of within ±15% and Eulerian-Granular model has a percentage error of within ±20%. This can be explained by the different ways in which particle-particle and particle-wall interaction is captured in all these models. DEM method models the particle motion explicitly with a detailed inter-proppant and proppant-wall interaction and tends to capture the physical phenomenon close to reality as seen in Figure C.1. On the other hand, the Eulerian-Granular method is based on KTGF and considers the granular particles as continuous media. Thus, it describes more fluid-like behaviour for the proppants and results in higher particle distribution rate at fracture bottom. The DDPM model, since it is a combination of both the models, DEM and Eulerian-Granular model solves the mass and momentum conservation equations to model the continuous phase, and the proppant phase is modelled in the Lagrangian frame by tracking their motion using Newton's second law of motion like DEM model (Suri, Islam and Hossain 2019). The inter-proppant interaction is modelled by KTGF like Eulerian-Granular model, and the proppant-wall interaction is modelled using the Lagrangian method.

In terms of simulation time, the DEM Model shows the accurate proppant location, as it captures the complete particle micromechanics and tracks the individual particle and is computationally very expensive (around 10 times higher than the Eulerian-Granular model). On the other hand, Eulerian-Granular method provides proppant volume fraction, which can act as a substitute for the proppant position. One of the most significant advantages of using Eulerian-Granular method in proppant transport is that it is computationally economical compared with the DEM model. The DDPM model on the contrary, being a combination of both the models, DEM and Eulerian-Granular model, simulates the proppant transport in the order of three times of computational times compared to Eulerian-Granular model.

In general, from the comparison of all the proppant transport modelling techniques, it can be interpreted that DDPM model provides a reasonable approximation to the proppant particle physics inside the fracture in a reasonable computational time. Considering the significant simulation time required for the DEM method, and applicability for upscaling the model to field-scale hydraulic fractures, this comparison study suggests that DDPM model can be used for practical problems of petroleum engineering interests for proppant distribution and settling.

v=0.1 m/s

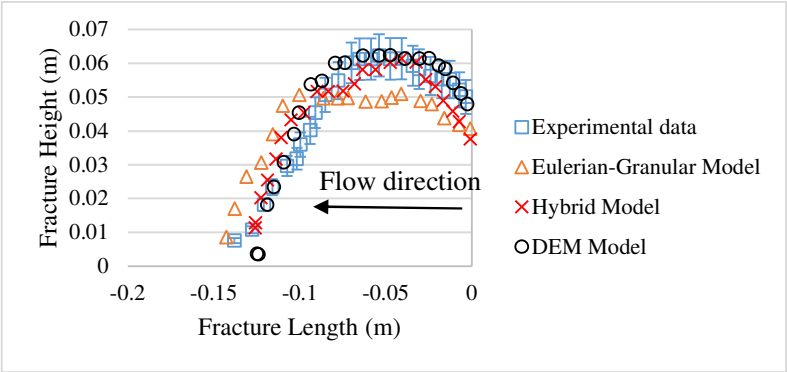

v=0.2 m/s

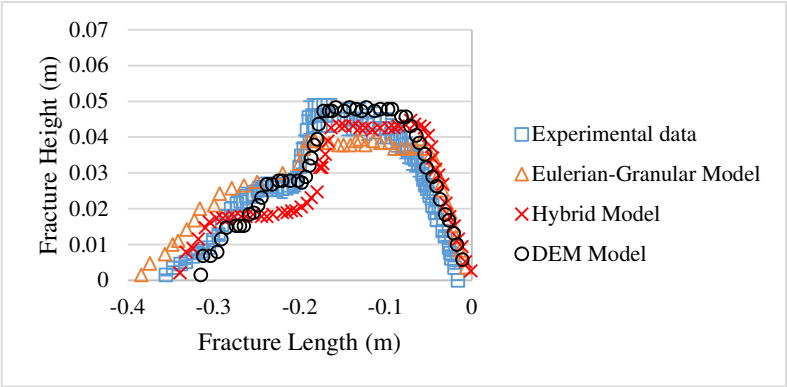

v=0.3 m/s

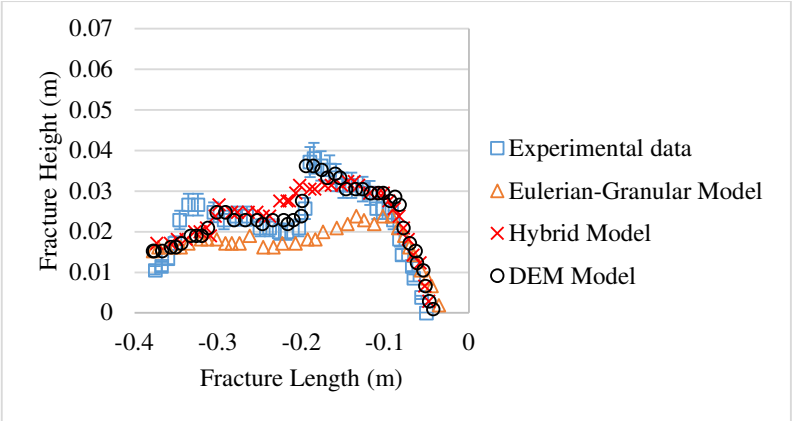

Figure C.1 Comparison of Eulerian-Granular Model, DEM Model and DDPM model with Experimental results

Appendix D: Publications

Journal publications

1. Suri, Y., Islam, S.Z., Hossain, M., 2019. A new CFD approach for proppant transport in unconventional hydraulic fractures. Journal of Natural Gas Science and Engineering, 102951. https://doi.org/10.1016/j.jngse.2019.102951
2. Suri, Y., Islam, S.Z. and Hossain, M., 2020. Numerical modelling of proppant transport in hydraulic fractures. Journal of Fluid Dynamics & Material Processing. vol.16, no.2, pp.297-337. https://doi.org/10.32604/fdmp.2020.08421
3. Suri, Y., Islam, S.Z., Hossain, M., 2020. Effect of Fracture Roughness on the hydrodynamics of proppant transport in hydraulic fractures. Journal of Natural Gas Science and Engineering, vol. 80, p.103401. https://doi.org/10.1016/j.jngse.2020.103401
4. Suri, Y., Islam, S.Z., Hossain, M., 2020. Proppant transport in dynamically propagating hydraulic fractures using CFD-XFEM approach. International Journal of Rock Mechanics and Mining Sciences, vol. 131, p.104356. https://doi.org/10.1016/j.ijrmms.2020.104356
5. Noble, R., Islam, S.Z., Droubi, G., Hossain, M., Stephen, K. and Suri, Y., 2019. Fluid flow through a fractured porous reservoir using CFD modeling. Journal of Porous Media, 22(5). https://doi.org/10.1615/JPorMedia.2019029084
6. Suri, Y., Islam, S.Z., Stephen, K., Donald, C., Thompson, M., Droubi, M.G., Hossain, M., 2020. Numerical Fluid Flow Modelling in Multiple Fractured Porous Reservoirs. Journal of Fluid Dynamics & Material Processing. vol.16, no.2, pp.245-266 https://doi.org/10.32604/fdmp.2020.06505

Conference Proceedings / Presentations

1. Two oral presentations entitled 'CFD-DEM and Two-Fluid Model coupled approach for numerical simulation of proppant transport and distribution in hydraulic fractures' and '3D CFD Modelling of Fluid Flow through Fractured Porous Reservoirs' were presented at the 3rd UK InterPore (International Society for Porous Media) Conference on Porous Media and the 1st Monash-Warwick PREFRAC Workshop on Hydraulic Fracturing at the University of Warwick on 04th-05th September 2017. https://warwick.ac.uk/fac/sci/eng/ukipcpm/
2. Oral presentation entitled 'A hybrid numerical model (CFD-DEM) for proppant transport in hydraulic fractures in shale gas reservoirs' was presented at the 4th Interpore

(International Society for Porous Media) UK annual conference at the University of Aberdeen on 10th-11th September 2018.
https://www.interpore.org/activities/national-chapters/uk/649-4th-uk-interpore-conference

3. Oral presentation entitled 'Effect of Fracture Roughness on Proppant Transport in Hydraulic Fractures using CFD-DEM model' was presented at the 32nd Scottish fluid flow meeting at the University of Dundee on 30th May 2019.
https://sites.dundee.ac.uk/sfmm-2019/wp-content/uploads/sites/121/2019/05/Book_of_abstractsSFMM2019UPDATE.pdf
4. Poster presentation entitled 'Proppant transport in hydraulic fractures in shale gas reservoirs' was presented at the IUTAM (International Union of Theoretical and Applied Mechanics) Symposium 2019 on 'Computational modelling of instabilities and turbulence in separated two-phase flows' at the University College Dublin (Ireland) on 10th-12th June 2019.
https://maths.ucd.ie/cfd2019/index.html

Awards

1. Top winner of Society of Petroleum Engineers (SPE) Bursary award 2018-2019, £3000 from the SPE Aberdeen section, UK on April 2019
2. Top winner of SPE Bursary award 2017-2018, £2500 from the SPE Aberdeen section, UK on March 2018
3. Winner of SPE Bursary award 2016-2017, £500 from the SPE Aberdeen section, UK on March 2017
4. Runner up of three minutes thesis competition held at Robert Gordon University, Aberdeen on 1st June 2018
5. PhD studentship award (2016-2019), Robert Gordon University, Aberdeen